

Advancement of bright-field hyperspectral X-ray tomographic imaging

A thesis submitted to The University of Manchester for the degree of
Doctor of Philosophy
in the Faculty of Science and Engineering

2023

Ryan L. Warr
Department of Materials in the School of Natural Sciences

Contents

Contents	2
List of figures	5
List of tables	19
Abstract	20
Declaration of originality	21
Copyright statement	22
Acknowledgements	23
Publications	24
1 Introduction	25
1.1 Aims and Objectives	29
1.2 Structure of the Thesis	30
1.3 References	30
2 Literature Review	33
2.1 From black and white to 'colour' X-ray CT	33
2.1.1 X-ray CT: basic principles	33
2.1.2 Limitations of XCT	35
2.1.3 Capturing spectral detail	36
2.1.4 Spectral markers	37
2.1.5 Dual-energy CT	38
2.2 Properties of spectroscopic imaging detectors	43
2.2.1 Energy-integrating detectors	43
2.2.2 Multispectral vs. Hyperspectral detectors	46
2.2.3 Challenges with spectroscopic detectors	49
2.3 Spectral image reconstruction	52
2.3.1 Intro to X-ray CT reconstruction	53
2.3.2 Analytic reconstruction - filtered back-projection	54
2.3.3 Iterative reconstruction algorithms	57
2.3.4 Extending to spectral reconstruction	59
2.3.5 Regularisation of iterative algorithms	61
2.4 Imaging modalities of energy-sensitive X-ray CT	64

2.4.1	Bright-field X-ray imaging	65
2.4.2	Applications of bright-field imaging	66
2.4.3	Evolution of dark-field energy-dispersive imaging	75
2.5	Summary	81
2.6	References	83
3	Materials and Methods	95
3.1	Laboratory X-ray scanning systems	95
3.2	Hyperspectral (HEXITEC) detector	97
3.2.1	HEXITEC calibration	101
3.2.2	Evaluation of HEXITEC characteristics	105
3.3	Sample preparation	112
3.3.1	Biological staining procedures	112
3.3.2	Phantom sample preparation	113
3.4	Data processing, reconstruction and analysis: Software and Hardware	115
3.4.1	Raw data processing	115
3.4.2	Image reconstruction: The Core Imaging Library	117
3.5	References	118
4	Enhanced hyperspectral tomography for bioimaging by spatio-spectral reconstruction	121
4.1	Introduction	124
4.2	Results	126
4.3	Discussion	135
4.4	Conclusion	136
4.5	Materials and methods	136
4.5.1	Phantom sample preparation	136
4.5.2	Biological sample preparation	137
4.5.3	X-ray detector	137
4.5.4	Data acquisition routines	137
4.5.5	Spectral CT data reconstruction	138
4.6	Acknowledgements	140
4.7	References	140
4.8	Supplementary Information	145
4.8.1	X-ray source properties	145
4.8.2	Spectral detector calibration	145
4.8.3	Powder phantom - phase 1 artefacts	146
4.8.4	Powder phantom - noise suppression	147
4.8.5	K-edge subtraction	148
5	Quantifying multiple stain distributions in bioimaging by hyperspectral X-ray tomography	150
5.1	Introduction	153

5.2	Methods	155
5.2.1	Biological sample and phantom preparation	155
5.2.2	Hyperspectral X-ray microCT imaging	157
5.2.3	Reconstruction routine	158
5.2.4	Volume registration	159
5.2.5	Spectral analysis routines	159
5.3	Results	160
5.4	Discussion	169
5.5	Conclusion	171
5.6	Acknowledgements	172
5.7	References	172
5.8	Supplementary Information	177
5.8.1	Hyperspectral energy-channel calibration and resolution calculation . .	177
5.8.2	Considerations on HEXITEC low concentration sensitivity	178
5.8.3	Factors affecting the quantification of chemical concentration	180
6	Conclusions and Future Work	182
6.1	Summary of Results and Conclusions	182
6.2	Future Directions	183
6.2.1	Optimisation and standardisation of quantitative hyperspectral analyses	183
6.2.2	Investigation of beam hardening reduction with hyperspectral CT . . .	184
6.2.3	Expanded hyperspectral applications with multi-detector arrays	184
6.2.4	High spatio-spectral resolution through correlative techniques	185
6.3	References	185

List of figures

1.1.1	Illustration of the concept of 'Black and White' versus 'Colour' imaging. (Bottom) Image of a typical Bremsstrahlung X-ray spectrum for a tungsten source target. Characteristic peaks due to fluorescence of tungsten are labelled. (Top) Distinction between the conventional 'energy-integrating' detectors, offering no energy-based insight, and the energy-sensitive systems. Hyperspectral imaging is capable of dividing the incident photon energies into many narrow channels, providing higher energy resolution over the 'few-channel' systems.	27
1.1.2	Example of a 'hypercube' data structure in remote surface mapping. (a) A conventional 2D greyscale image of a region of the Earth's surface. (b) The same region acquired as a HSI hypercube, where an additional spectral dimension is captured over hundreds of narrow bands. (c) Example of extracting spectral information from a pixel in the hypercube, allowing an individual spectral profile to be analysed [18].	28
2.1.1	Magnification of the projected image using a cone beam X-ray source. By moving the sample closer to the source, or the detector further away, the image recorded on the detector is magnified, improving spatial resolution. Labels defining the source-sample and sample-detector distances are included as (d_1) and (d_2) respectively.	35
2.1.2	Attenuation profiles as a function of energy for different chemical elements and materials. The mass attenuation values are shown across the hard X-ray range for each material. Sharp discontinuities occur at unique energies for each element, corresponding to the absorption edges. The K-edge energies for each element shown are quantified in the legend. Attenuation values extracted from the NIST online database [9].	37
2.1.3	Demonstration of the photoelectric effect. The diagram illustrates the different steps involved in photoelectric absorption. An incoming photon of sufficient energy is absorbed by an electron, and ejected as a photoelectron. The subsequent vacancy is filled by the transition of an electron from a higher atomic orbital, emitting an XRF photon of energy equal to the transition between states.	39
2.1.4	Variations of DECT geometries. 1) Dual-source scanning. 2) Rapid kV switching. 3) Dual-layer detector. 4) Sequential scans at two different kVp settings. Adapted from [19].	40

2.1.5	Workflow for the imaging of microDECT datasets. The images shown are of a mouse head, stained with an iodine-based contrast agent. A set of two scans, at high (80 kVp) and low (40 kVp) energy were acquired and reconstructed, before image conversion and filtering to reduce noise. A volume registration routine matched the orientation of the two datasets, before material decomposition was applied to separate the individual contributions of each material to the reconstructed volume, in this case hydroxyapatite (Material 1), iodine-stained soft tissue (Material 2) and the background (Material 3) [26].	42
2.2.1	Layout of a typical indirect scintillation detector. Incident X-ray photons interact with the scintillator crystal, with visible light photons emitted upon electron de-excitation in the crystal. Higher energy X-rays produce a greater number of visible light photons. The light signal is amplified and converted to an electrical output by photodiodes or photo-multiplier tubes (PMTs), where it is finally processed by an electronic integrating circuit.	44
2.2.2	Layout of a typical direct semiconductor detector. Incident X-ray photons interact with the semiconductor crystal, producing a charge cloud of electron-hole pairs. The free charges drift according to an externally applied electric field (E), creating a measurable current at the nearest pixel electrodes within the readout chip. Higher energy X-rays produce a greater number of e-h pairs, proportional to the incident photon energy. Electronic processing is then performed by the readout chip.	45
2.2.3	Measured absorption efficiency (DQE) variation for a range of typical detector semiconductor materials, as a function of energy. (Left) Multiple semiconductor materials compared for the same sensor thickness (curves for Ge and GaAs overlap). (Right) Commonly used thicknesses for commercial X-ray detectors [33].	47
2.2.4	Representation of the difference in spectral acquisition for multispectral and hyperspectral PCDs. Multispectral imaging detectors (top) record photon energies into one of several discrete energy bands, while hyperspectral detectors (bottom) have hundreds of narrow energy channels with much smaller width to allow for a continuous energy spectrum [45].	48
2.2.5	Illustration of the charge sharing effect encountered in hybrid pixel detectors. While the charge cloud of photon A diffuses into only one pixel, photon B has a charge cloud that interacts with a group of neighbouring pixels, distributing its charge [55].	51

2.2.6	Example case of how charge sharing corrections may be applied in spectroscopic data. (Left) An ideal case where a single photon event is fully recorded within a single detector pixel. (Middle) A charge-sharing event where a photon is incident between neighbouring elements, and the charge is shared unevenly. The event may be corrected using charge summing mode (Upper Right), where all charge is grouped and allocated to the highest charge-containing pixel in the cluster, or charge discrimination mode (Lower Right), where the entire event and all of its deposited charge is deleted.	52
2.3.1	Example of a Radon transform. Using the example of a Shepp-Logan simulated phantom (left), a sinogram is formed by acquiring 180 projections over a range of rotation angles. By performing a Radon transform, a sinogram is produced (right), displayed in projection space. Created using the <i>skimage</i> package in Python [60].	54
2.3.2	Back-projection of a chest phantom object (a). The graphics show back-projection of profiles acquired from 1 (b), 2 (c), 4 (d), 8 (e), and 720 (f) angular profiles. The final image shows significant blurring, highlighting the need for a filtration step to improve the reconstructed image sharpness [61].	55
2.3.3	Filtered back-projection of the same chest phantom object as in Fig. 2.3.2. The graphics show filtered back-projection of profiles acquired from 1 (b), 2 (c), 4 (d), 8 (e), and 720 (f) angular profiles. The application of a filter removes the blurring, improves image sharpness, and provides a reconstructed image much closer to the original object in (a) [61].	56
2.3.4	Test results for various reconstruction algorithms applied to spectral data of a palladium-filled carbon lattice. (Top) From left to right, reconstructions using FDK, SIRT and channel-linked SIRT methods. The iterative methods show significant spatial smoothing over FDK, with the channel-linked SIRT method the best for structural definition. (Bottom) Reconstructed spectra from a voxel where palladium signal was captured. The spectral noise is significantly lower for channel-linked SIRT compared to FDK, enabling a much clearer identification of the palladium K-edge (channel number 83) [78].	60
2.3.5	Illustration of the effect of varying the regularisation parameter using TV regularisation. The original image (centre) is shown, with a region of interest (dashed box) highlighted for magnified evaluation. Effects of a high value (left) and a low value regularisation parameter (right) are shown, illustrating the respective spatial smoothing and noise removal of the regularisation. Adapted from [81].	62

2.3.6	(Top) Design of the custom phantom, containing (a) quartz, (b) pyrite (c) galena and (d) gold. (Bottom) Columns showing the reconstruction, error and segmentation for a single channel (70) using two methods: channel-wise TV (Upper Row) and TNV (Lower Row). Reduced image errors and improved feature segmentation are achieved for the TNV method over channel-wise TV, where the pyrite central regions were poorly segmented with excessive smoothing. Adapted from [79].	63
2.3.7	Comparison of the denoising effects of TV and TGV based on an artificial test image containing a 'ramp' function on greyscale intensity. While both regularisers achieve strong denoising, the presence of staircasing artefacts are clear in TV, while such artefacts are eliminated completely using TGV [87].	63
2.4.1	A typical geometry for energy-sensitive bright-field CT imaging. The conventional set-up for absorption CT is used, whereby a sample is rotated in the presence of an incident X-ray beam, but collected by an energy-resolving detector placed on the beam axis. Also shown is a set of three spectra seen from various sections of the sample object, with clear absorption edges [92].	66
2.4.2	Representation of a typical multispectral (top) and hyperspectral (bottom) attenuation profile for molybdenum. The multispectral profile records single attenuation values for broad energy windows, while the hyperspectral detector is capable of effectively producing a continuous spectrum. Known positions of the K-edge for each element are overlaid as vertical dotted lines. All attenuation values were extracted from the NIST database [9]. . .	67
2.4.3	Hyperspectral analysis of a USB dongle. (a) Set of hyperspectral radiographs with an example set of absorption spectra. (b) Conventional radiograph image for comparison. (c) RGB image following spectral clustering. (d) K-edge absorption analysis including highlighted barium (blue) and tantalum (red). (e) and (f) show images created by applying fits to the absorbance spectra at 9.5 keV and 20-30 keV [93].	68
2.4.4	Relative concentration and distribution of Pd metal in a catalyst body. (a) Single voxel spectra showing the presence of the Pd absorption edge. Overlaid are linear fits applied to either side of the K-edge to measure the size of the step change ($\Delta\mu_0$). (b)-(d) Vertical and horizontal slices of the reconstructed volume mapping of $\Delta\mu_0$ values, as well as a 3D visualisation of the exterior. Adapted from [92].	69
2.4.5	Spectral CT 3D distribution of a gold-containing geological sample. (a) Greyscale slice of the ore sample acquired by integrating over the full spectral range. (b) Spectra highlighting the K-edges of gold and lead within the sample. (c) Spectra for quartz, pyrite and chalcopyrite. (d) Vertical slice with segmented gold (blue) and lead (red) voxels. (e) 3D reconstruction highlighting each phase [92].	70

2.4.6	3D rendering of a mouse aortic arch, with spectral subtraction. (a) The 3D volume produced after integrating over all 1024 energy bins. (b) 3D map following spectral subtraction of energy windows either side of the gold L_3 -edge. Some 'hotspots' appear to emerge, attributed to the presence of gold. Adapted from [99].	72
2.4.7	Multi-material mapping of a canine specimen. (a) Reconstructed greyscale image of the specimen, showing the kidney and abdomen, along with the circular calibration vials. (b) Colour map of the chemical stain distribution in the same image, with a legend mapping the colours to the element present. The unlabelled vial is that of a ferrous solution, matching the spectral properties of soft tissue. (c)-(e) Quantitative material maps, measured in terms of millimolar units. [105]	73
2.4.8	Illustration of the transformation in the 'TEDDI' setup. (a) Conventional geometry for a one detector, one collimator system, with one diffraction lozenge. (b) Example of a multiple-aligned vertical detector array. This produces multiple lozenges at different positions. (c) Multiple-aligned horizontal detector array with matched collimators. (d) 2D detector-collimator array, requiring sample motion in the one dimension [115].	77
2.4.9	Pinhole geometry for 'dark-field' hyperspectral imaging. (a) An off-axis pinhole projects scattered X-rays towards a spectroscopic detector, collecting diffraction patterns at each pixel. (b) Examples of diffraction patterns and a corresponding spatial mapping of the elements identified [122]. . . .	78
2.4.10	Scanning-probe imaging geometry for X-ray fluorescence measurement. A focused X-ray beam illuminates a columnar section of the sample, leading to excitation and emission of fluorescent X-rays, collected by the energy-dispersive detector (EDD). In addition is shown a conventional transmission detector (TD). The effect of re-absorption of some XRF signals by the black voxel highlighted is also shown [127].	80
3.1.1	Standard experimental set-up of the X-ray system within the 'Colour Bay' walk-in hutch, situated at the HMXIF. Key components (red circles) are the source, rotation/sample stage, and the detector. Additional components (blue dashed circles) may be included or varied to fine-tune the imaging procedure. These include a tube for reduction of X-ray scatter, and beam slits to collimate the incident beam.	96
3.1.2	Standard experimental set-up of the hyperspectral X-ray system within the 'High Flux Bay' walk-in hutch, situated at the HMXIF. Key components (red circles) are the source, rotation/sample stage, and the spectroscopic detector. The built-in energy-integrating detector is out of view, behind the HEXITEC along the same imaging plane.	97

3.2.1	Photographs of the HEXITEC hyperspectral detector. (a) Complete HEXITEC unit, with the CdTe sensor removed. Measurements of the full detector device are included. (b) Close-up of the CdTe sensor with scale included [4].	98
3.2.2	Diagram of the circuitry in each pixel of the HEXITEC ASIC. All core components, including the pre-amplifier, shaping, and filter electronics, as well as the peak-hold system, are labelled. In addition, the bias circuitry enables the detector to be held at a pre-defined voltage. A calibration circuit allows characterisation of the pixel electronics [10].	99
3.2.3	Photo of the HEXITEC system with the trigger controller installed. The cable connects directly to the HEXITEC, and runs through the trigger controller, before then connecting via USB to the sample stage PC. A magnified image of the triggering system (red box) is shown, with variable input based on trigger system. For all experiments, Input 2 was used.	100
3.2.4	Design of the experimental set-up for CT imaging using the HEXITEC in the commercial Nikon system. (Top) Ethernet connection from the HEXITEC transferred data to a computer, to be stored and viewed in the HEXITEC software. The trigger controller cable was connected between the HEXITEC and the HFB computer, containing the Inspect-X software (source and motor control) and IPC application linking all equipment. (Bottom) Interface developed using IPC, allowing the user to connect directly to Inspect-X and control the settings for the CT scan, as well as monitor source and sample settings. The output logged the progression of the full CT scan.	101
3.2.5	Global spectrum for emissions of ^{241}Am on to the metal foils of Ba and Tb. Peaks are highlighted and labelled for the relevant characteristic peaks of Ba and Tb, along with the photopeak from ^{241}Am	102
3.2.6	Linear fit calibration between channel number and energy for the identified characteristic peaks. In total, 5 data points were fitted with a linear fitting routine.	103
3.2.7	Effect of the COW method on the calibration dataset, containing spectral signals from Ba, Tb, and ^{241}Am . Pixels (60,20) and (20,60) were used to highlight initial differences with regards to spectral gain shift (Left), along with the same spectra after application of the COW method, showing better alignment (Right).	104

3.2.8	Demonstration of the bad pixel correction routine. Left Column: Top - Example flatfield image acquired at 50 kV, shown for a single energy channel (channel 120). Colour bar measures photon counts. Bad pixels appear as very low photon numbers for the given channel. Middle - Bad pixel map identifying all ineffective pixels that require correction. Bottom - The same flatfield image following correction of bad pixels. Right Column: Top - Example of a fully functioning pixel with good spectral response. Middle - Example of a poorly responding detector pixel. Bottom - The same ineffective pixel after correction.	105
3.2.9	Spectral resolution statistics based on the ^{241}Am photopeak. (Left) Histogram depicting the frequency distribution of FWHM values of the peak, measured for each pixel. Dead pixels were not included. (Right) Pixel map distribution of the FWHM values. Dead pixels were labelled as zeros. Many non-functioning pixels emerge at the detector edges due to leakage current and poor pixel bonding.	106
3.2.10	Variation in energy resolution as a function of peak energy and time. (Left) Average FWHM values for the five peaks considered in the calibration dataset. Error bars show one standard deviation. The Ba K_{β} peak shows poorer spectral response due to inconsistencies in the peak search algorithm. (Right) Energy resolution based on the ^{241}Am photopeak for several calibration datasets acquired over several years. Strong consistency in spectral resolution was observed. Full details on peak statistics, including the number of dead pixels identified, are included.	107
3.2.11	Single pixel (40,40) spectrum for a flatfield acquired at the scan settings of 60 kV and 0.1 mA. Significant pulse pile-up occurred, with very few low energy photon events recorded, and a number of events incorrectly assigned an initial photon energy beyond the maximum of 60 keV. Such effects are labelled and highlighted on the spectrum.	108
3.2.12	Reduction in pulse pile-up through changes in frame rate. A series of six flatfield images were acquired at 60 kV and 0.1 mA, with the global spectra for each flatfield shown. The frame rate used for each dataset is labelled. Also included is a plot comparing the global count rates as a function of frame rate.	110
3.2.13	Evaluation of the charge sharing discrimination (CSD) correction on a calibration dataset. Significant reduction in the low energy background was observed following CSD correction. Despite a large number of deleted events, the characteristic peaks (labelled) all increase in total counts registered. Other peaks have been labelled, including characteristic XRF signals from the detector materials (CdTe), as well as possible escape peaks due to the gamma emissions from the ^{241}Am source followed by XRF emissions of Tb and Ba.	111

3.3.1	Photographs of the stained biological specimens, each of which were chemically fixed and held in individual containers. Sample dimensions are overlaid. An approximation of the imaged section of each sample is highlighted (dashed box). All measurements are in mm.	113
3.3.2	(Left) Photograph of the multi-phase powder phantom, with each metal-based powder labelled. The external metal of the phantom is aluminium. (Right) Schematic of the phantom sample, with dimensions included.	114
3.3.3	Photographs of the chemical phantoms produced for spectral calibration using known chemical concentrations. Sample dimensions are overlaid, and are measured in mm. (Left) Two images of the iodine-based phantom, containing four interchangeable rods of differing concentration of the I_3^- ion (25.3, 50.6, 76.0 and 101.2 mg/ml). The second photograph shows the optional connector plate to hold the four containers in position. (Middle) The $BaSO_4$ phantom, containing three concentrations (100, 200, and 400 mg/ml), with corresponding concentration percentages labelled. (Right) The PTA phantom, with three concentrations (50, 100, and 200 mg/ml) as labelled on the container.	115
3.4.1	Implementation of the stripe reduction filter to minimise ring artefacts in hyperspectral imaging. (Left) Raw sinogram of the central image pixel, shown for a single energy channel, prior to any corrections. Stripes appear vertically (red dashed line) due to the same ineffective pixel in each projection. (Right) The same sinogram following ring artefact correction. A smooth, more natural sinogram is achieved, with less sharp changes between pixel columns. An example of a clear improvement in stripe reduction is highlighted (red arrow). Optical density values at the edge appear negative due to charge sharing effects.	117
4.2.1	Attenuation variation in the spectral dimension for a multi-phase powder phantom. (a) Set of four sinograms taken between channels 100-175 at equal spacing of 25 channels (corresponding average energies are shown - channel width 1.2 keV) for Scan A. A single discontinuity in the sinograms appears due to an interrupted scan. (b) The corresponding FDK reconstructions for each energy channel of the sinograms in (a). Three distinct regions are observed, corresponding to the three metal-based powders. The colour scale measures the attenuation, and is consistent across both images. Three ROIs are highlighted (white/blue squares, marked by numbers for each respective powder phase). (c) Average voxel spectra of powder phase ROI 1. A line signifying the theoretical position of the cerium K-edge is overlaid for comparison. (d) Comparison of measured absorption spectra (top) for ROIs 2 and 3 located in the zinc oxide and iron phases respectively, and the theoretical values (bottom) over the same spectral range.	127

4.2.2	Comparison of reconstruction algorithms. (a) Transverse and frontal slices, showing reconstructions for FDK of sample Scan A (left column), followed by Scan B reconstructions with FDK (middle column), and TV-TGV (right column). All reconstructed slices are shown for a single energy channel (42.27 keV - channel width 1.2 keV). Dashed lines indicate the positions from which spatial profiles were measured for each reconstruction. White arrows mark examples of streak artefacts due to photon starvation. ROIs in the ZnO phase (red - S) and the Al phase (white - Bg) are highlighted for use in CNR calculations. (b) Spatial profile across two powder phases for the same energy channel. (c) Absorption spectra for ROI 1 within the cerium powder region (blue square in (a)).	129
4.2.3	Reconstruction comparison using different image quality metrics. (a) Channelwise CNR calculations between the ZnO and the Al phase ROIs for an image slice in the transverse plane. Average values across the energy range were 27.44, 7.81 and 38.26 for FDK Scan A, FDK and TV-TGV Scan B respectively. (b) Channelwise RMSE values calculated using ROI 1 within the cerium phase. Values are calculated for all channels through comparison between Scan A and each respective Scan B reconstruction. . . .	130
4.2.4	Biological feature identification via regularised reconstruction. (a) Reconstructed slices for channel 120 (33.95 keV - channel width 1.2 keV), along both the axial and sagittal dimensions, following FDK (left column) and TV-TGV (right column) reconstruction. General noise reduction and smoothing due to TV regularisation is observed over all spatial regions. (b) Absorption spectra measured for a ROI in two sections of the sample (blue squares in (a) - lens and jaw). A line signifying the theoretical position of the iodine K-edge is overlaid for comparison. (c) Channelwise CNR calculations of the stained jaw using the signal ROI (red - S) and the background ROI (white - Bg), for the image slice shown in the sagittal plane. Average CNR values across the energy range were 8.91 and 35.97 for FDK and TV-TGV respectively.	132
4.2.5	Attenuation step size analysis for the iodine K-edge. (a) 3D visualisations of the step size in the absorption edge, $\Delta\mu_0$, corresponding to relative iodine concentration. Images are shown for the lizard head sample following both FDK (upper left) and TV-TGV (lower left) reconstruction. (b) Absorption spectra acquired within the jaw adductor muscle for the same ROI in each reconstructed volume. Linear fits were acquired and extrapolated to the extremities of the absorption edge, where the relative change in attenuation values were measured.	133

4.2.6	Lizard head segmentation comparison for hyperspectral and dual-energy imaging. Sagittal views of the segmented sample, producing maps of iodine-stained soft tissue (top row) and remaining hydroxyapatite (bottom row) bone structures. Results following K-edge subtraction for the TV-TGV reconstructed dataset (middle column) are directly compared to those following DECT acquisition of the same sample (left column), reduced to the same spatial resolution (137 μm). Labels indicate the successful segmentation of several iodine-stained soft tissue regions for the hyperspectral dataset, with similar structures identified in the DECT equivalent image. A comparison of HA maps show distinct bone structures observed across both datasets, as well as the accumulation of bone mineral in particular regions due to long term sample storage. Included is an example of a bone structure (quadrate) unidentified in TV-TGV segmentation. (Right column) Equivalent maps following FDK reconstruction of the hyperspectral dataset are also shown, with significant noise hiding a number of key features.	134
S1	Example incident source spectra measured by a single pixel of the hyperspectral detector. For each flatfield, a low-energy tail is observed due to the effect of charge sharing. (Left) Single flatfield projection measured prior to scanning the lizard head sample (50 kV, 0.7 W, and 120 s exposure time.) Sharp peaks appear due to the fluorescence of the Cd and Te materials within the detector. (Right) Single flatfield projection measured prior to scanning the long exposure powder phantom (60 kV, 6W, and 180 s exposure time).	146
S2	(Left) Example spectrum, measured in a single pixel, from the calibration source. Five arrows mark the peaks used for linear fitting, ranging from the $K_{\alpha,\beta}$ fluorescence peaks of Ba (farthest left) to the ^{241}Am γ -ray photopeak (farthest right). A large, low-energy tail is observed due to charge sharing. (Right) Distribution of FWHM values for the ^{241}Am peak, measured at 59.5 keV. Dead pixels were not considered.	146
S3	(Top) Spatial images of the FDK and TV-TGV reconstructions taken for Scan A and Scan B respectively. Images are shown for single energy channels, both before (top left) and after (top right) the Ce K-edge (40.443 keV). (Bottom) Line profiles taken across two phases, as marked on the spatial images (blue dotted line).	147
S4	RMSE values calculated by comparison of the Scan B reconstructions with the results of Scan A. Images shown are taken for single slices in the transverse (left) and frontal (right) planes, at energy 42.27 keV. Colour bars quantify the RMSE in each image, with scaling consistent within image planes for comparison.	148

S5	Example profile illustrating K-edge subtraction around the iodine absorption edge for a voxel in the stained lizard head. The theoretical position of the edge is marked for comparison (dotted line). The 'separation' (Sep.) determines the distance in energy (channels) away from the edge position, while the 'width' measures the energy (channel) range across which data is extracted (yellow bars). Identical values are used either side of the edge. Sizes of each parameter are not to scale.	149
5.1.1	Attenuation variation as a function of energy. Known values of the mass attenuation coefficient shown for a number of materials. Across the hard X-ray energy range, many elements exhibit sharp rises in attenuation at their absorption edge positions (K-edge energies given in legend), providing strong contrast relative to soft tissue or calcium (bone) structures. Values extracted from the NIST online database [15].	154
5.3.1	Voxel spectra analysis for double-stained hindlimb specimen. A) Single image slice in the sagittal plane across three monochromatic energy channels, following iterative reconstruction. A set of three regions-of-interest (ROIs) are highlighted for voxel spectra analysis. An enlarged image of a section of (A) - red box - is included to highlight ROI ₂ taken over one of the distinct material phases. ROIs _{1,3} cover a 3×3 voxel region, while a 2×2 pixel region is used for ROI ₂ , partially overlapping with surrounding material outside of the phase. B) Voxel spectra for each ROI, showing clear steps in attenuation. Known absorption edge positions (black dotted lines) confirm the presence of iodine and barium in the ROIs, while ROI ₃ shows a small iodine signal, having partially diffused into the calcium-containing bone.	161
5.3.2	Elemental segmentation of hindlimb by K-edge subtraction. A) Elemental difference maps shown for the hyperspectral image slice shown in the sagittal plane (left). Colour bar for elemental difference maps is measured in terms of attenuation change, $\Delta\mu$, as determined by KES of narrow energy windows (5 channels, ~1.1 keV width total) either side of each absorption edge. B) 3D volume mapping for elemental maps of iodine-, barium- and calcium-containing regions (top, middle, bottom respectively). C) Virtual cross-section from a high spatial resolution XCT scan of the mouse hindlimb, showing the equivalent image slice following volume registration. Labels indicate the three material phases with expected stain uptake regions.	162

5.3.3 Spectral analysis for a triple-stained forelimb specimen. A) Elemental difference maps shown for the hyperspectral image slice shown in the coronal plane (left). Colour bar for elemental difference maps is measured in terms of attenuation change, $\Delta\mu$. Arrows are included to highlight distinct soft tissue regions stained by each chemical, confirmed as hair (pink), vasculature (blue), skin (green) and muscle (white). B) Reconstructed cross-section from a high spatial resolution DECT scan of the mouse forelimb, following basis material decomposition. The image slice matches that shown in the hyperspectral dataset, following volume registration. Labels indicate regions containing tungsten and calcium (green), as well as those containing iodine and barium (magenta). DECT decomposition fails to fully segment all elements into distinct phases. The dashed region and asterisk highlight the area below the elbow joint where PTA did not fully stain. C) Reconstructed cross-section slice in the coronal plane of the triple-stained mouse forelimb. ROIs are shown for five distinct regions of the specimen, to analyse average voxel spectra. All ROIs cover 3×3 pixels, apart from ROI₃, which covers a 2×2 region. D) Voxel spectra for the ROIs selected in (C). Known K-edge positions are overlaid, with ROIs 1, 2 and 3 matching the K-edges for iodine, barium and tungsten respectively (top). Two ROIs, 4 and 5, show the presence of both iodine and tungsten contrast agents (bottom). 163

- 5.3.4 **Design and spectral analysis of chemical phantoms.** A) Illustration of the phantom layout for each contrast agent (left), with chemical concentrations labelled in units of mg/ml. The I_2KI phantom is labelled as iodine to highlight that the concentrations represent aqueous I_3^- . Reconstructed image slices for each of the respective chemical phantoms (right), with orientation matched to the concentrations labelled. The $BaSO_4$ phantoms appear heterogeneous due to partial sinking and separation of the barium sulphate crystals from the agarose base. Images are measured in terms of 'standardised intensity' value, with the same overall scaling range. B) Reconstructed slices of each chemical phantom, shown in the axial plane, for two energy channels, taken just before (left column) and just after (right column) the relevant K-edge position. ROIs covering each chemical phase are highlighted and numbered, from which spectral plots were extracted. Minor ring artefacts appear on the PTA reconstructed phantom. C) Voxel spectra showing attenuation as a function of energy for the ROIs highlighted in (B). The attenuation values were averaged over the full ROI. Known K-edge positions of the phantom's heavy element are overlaid. D) Fitted relationship for each chemical phantom, based on the average K-edge step change over six vertical slices through the sample depth. Error bars measure the standard deviation across the slices analysed. A line of best fit is applied for each phantom following linear interpolation. E) Fitted relationship between chemical concentration and 'standardised intensity' value in each phantom phase following conventional XCT imaging. Values were calculated for the central slice reconstruction. Phantom datasets were scanned at 80 kV and 100 μA with a Zeiss Xradia MicroXCT-400. Standardised intensity values are based on 2% agarose and air, as the barium phantom uses an agarose base. 167
- 5.3.5 **Distribution and concentration of contrast agents.** A) 3D volume maps quantifying the stain distribution of iodine (top) and barium (bottom) in the soft tissue and blood vessels respectively within the double-stained mouse hindlimb. Some low concentrations regions (white arrow) with a systematic pattern of voxels are attributed to ring artefacts or general noise. B) Histogram detailing the statistical breakdown of concentration distribution on a voxel-by-voxel basis for each chemical stain of the sample in (A). C) Volume maps for the triple-stained mouse forelimb, showing absolute concentration values in each voxel for iodine (top), $BaSO_4$ (middle) and PTA (bottom). D) Concentration distribution histogram for each stain within the sample in (C). 168

S1	Energy calibration using the ^{241}Am radioactive source. (Left) Single pixel (40, 40) plot of the calibration spectra, measuring photon counts as a function of channel number. The highest energy peak at 59.5 keV ^{241}Am photopeak is labelled, as well as the XRF peaks produced from Ba and Tb metal foils upon exposure to the ^{241}Am source. (Right) Matching of the channel number for each XRF peak and the ^{241}Am photopeak to their known energy values, enabling a linear relationship between channel number and energy to be determined.	178
S2	Measurement of the resolution statistics using the ^{241}Am photopeak. (Left) Histogram of the frequency distribution for FWHM values measured at 59.5 keV based on the ^{241}Am photopeak, over the full detector pixel array. Dead pixels were not included. (Right) Pixel map of the FWHM distribution. Dead pixels were set to a value of zero.	179
S3	Extended concentration statistics for double-stained mouse hindlimb specimen. Histogram statistics are shown, detailing the concentration distribution of iodine (top) and BaSO_4 (bottom) over all voxels in the reconstructed volume. A total of 250 histogram bins are used over the full concentration range for both plots.	179
S4	Extended concentration statistics for triple-stained mouse forelimb specimen. Histogram statistics are shown, detailing the concentration distribution of iodine (top), BaSO_4 (middle) and PTA (bottom) over all voxels in the reconstructed volume. A total of 150 histogram bins are used over the full concentration range for iodine and BaSO_4 , while 250 bins are used for PTA. The sharp increase in voxel frequency for the lowest concentration bin in the PTA plot is attributed to the effect of ring artefacts within the final reconstructed volume.	180

List of tables

3.2.1	Summary of the technical specifications for the HEXITEC detector system. Detector specification values obtained from the HEXITEC data sheet [5] and relevant published literature on the device development [4, 6–8].	98
5.3.1	Sample preparation and scan settings. A full list of the different contrast agents and scan settings for each biological sample and phantom included in this paper.	160

Abstract

X-ray computed tomography (CT) has become a powerful tool for 3D evaluation of samples, expanding from healthcare applications to security scanning, archaeology, and non-destructive testing across a range of industries. To date, the majority of X-ray systems implement 'black and white' imaging, providing insight into the relative electron density of structures, but no further material discrimination is achievable. With the creation of pixelated energy-sensitive X-ray detectors, previously lost energy-based information may now be captured, providing both spatial and spectral detail about the sample at every pixel. The development of hyperspectral sensors in recent years has enabled this spectral dimension to be recorded and visualised with excellent energy resolution. Characteristic features of elements within a sample, such as absorption edges and fluorescence peaks, may now be used as fingerprints for chemical mapping across a full reconstructed volume.

Hyperspectral imaging offers a wide range of imaging modalities, enabling exploration in the direct X-ray beam (bright-field) and off-axis (dark-field), for full flexibility in the range of chemical and crystallographic properties that may be studied. Bright-field imaging provides an appealing alternative to conventional X-ray CT given the simple requirement to replace the old detector for a hyperspectral one. However, despite the significant potential of bright-field hyperspectral CT, the technique is still in its infancy, and requires further advancement in a number of areas.

This thesis focuses on advancing the field of bright-field imaging in terms of the reconstruction, analysis, and wider applications of the technique moving forward. Limited studies to date have explored the reconstruction techniques required to handle hyperspectral datasets. With the additional spectral dimension, 4D datasets emerge. The benefit of high energy resolution, however, is counteracted by poor signal-to-noise ratio. A novel form of regularised iterative reconstruction algorithm is described, and evaluated in a research study on both a phantom sample and stained biological specimen. The extent of noise removal is assessed, with a scan time reduction of $36\times$ possible without loss of image quality.

Advancements in the range of bright-field spectral analyses are also explored. The ability to extract quantitative information on chemical concentration and distribution is evaluated for the field of bioimaging, through a research study on multiple simultaneous contrast agent staining. The extraction of absolute chemical concentration values in each voxel are shown for double- and triple-stained specimens, performed for the first time in hyperspectral CT via absorption edge fitting of a set of calibration phantoms. Finally, potential routes for the further development of hyperspectral imaging are discussed.

Declaration of originality

I hereby declare that no portion of the work referred to in the thesis has been submitted in support of an application for another degree or qualification of this or any other university or other institute of learning.

Ryan L. Warr

Copyright statement

- i The author of this thesis (including any appendices and/or schedules to this thesis) owns certain copyright or related rights in it (the “Copyright”) and he has given The University of Manchester certain rights to use such Copyright, including for administrative purposes.
- ii Copies of this thesis, either in full or in extracts and whether in hard or electronic copy, may be made *only* in accordance with the Copyright, Designs and Patents Act 1988 (as amended) and regulations issued under it or, where appropriate, in accordance with licensing agreements which the University has from time to time. This page must form part of any such copies made.
- iii The ownership of certain Copyright, patents, designs, trademarks and other intellectual property (the “Intellectual Property”) and any reproductions of copyright works in the thesis, for example graphs and tables (“Reproductions”), which may be described in this thesis, may not be owned by the author and may be owned by third parties. Such Intellectual Property and Reproductions cannot and must not be made available for use without the prior written permission of the owner(s) of the relevant Intellectual Property and/or Reproductions.
- iv Further information on the conditions under which disclosure, publication and commercialisation of this thesis, the Copyright and any Intellectual Property and/or Reproductions described in it may take place is available in the University IP Policy (see <http://documents.manchester.ac.uk/DocuInfo.aspx?DocID=24420>), in any relevant Thesis restriction declarations deposited in the University Library, The University Library’s regulations (see <http://www.library.manchester.ac.uk/about/regulations/>) and in The University’s policy on Presentation of Theses.

Acknowledgements

Firstly I wish to thank the EPSRC for funding this research.

I would like to thank my supervisors, Professor Philip Withers and Professor Robert Cernik, for their support, knowledge and guidance throughout the course of my PhD. They allowed me the freedom to explore the wonderful world of colour imaging, providing excellent expertise from the sidelines.

In addition, I am extremely grateful for all the staff and students, past and present, based at The Henry Moseley X-ray Imaging Facility, some of whom I am happy to call my friends. Thank you for providing a positive work environment, where we have all had the opportunity to collaborate and produce some excellent research over the years. I wish you all the best in your future endeavours.

I would also like to thank my fellow PhD colleague, flatmate, and close friend, Sam Johnston for all his support as we have gone along this PhD journey together. We have navigated the bumpy road of research, and I'm grateful to have had you there to experience and discuss it all, typically over a pint or two!

Finally, I would like to thank all those close to me who have supported me along my academic journey, through my undergrad and PhD at The University of Manchester for the last 8 years. To my dear friends from back home, and those who have joined our ever-growing group, I can't thank you enough for all the help you provided me during my PhD, both emotionally and mentally, particularly as we all battled our way through the pandemic and lockdown. I couldn't ask for a better bunch of friends.

And to my parents, siblings, and partners over the years, thank you so much for being there and helping me in every way possible to get where I am today. It has not always been easy, but having you all there has enabled me to get through the tough times, and find the light on the other side.

Publications

1. **Warr, R.**, Handschuh, S., Glösmann, M., Cernik, R. J., Withers, P. J., Quantifying multiple stain distributions in bioimaging by hyperspectral X-ray tomography. *Scientific Reports* **12**, 21945 (2022). <https://doi.org/10.1038/s41598-022-23592-0>
2. **Warr, R.**, Ametova, E., Cernik, R. J., Fardell, G., Handschuh, S., Jørgensen, J. S., Papoutsellis, E., Pasca, E., Withers, P. J., Enhanced hyperspectral tomography for bioimaging by spatio-spectral reconstruction. *Scientific Reports* **11**, 20818 (2021). <https://doi.org/10.1038/s41598-021-00146-4>
3. Jørgensen, J. S., Ametova, E., Burca, G., Fardell, G., Papoutsellis, E., Pasca, E., Thielemans, K., Turner M., **Warr, R.**, Lionheart, W. R. B. and Withers, P. J., Core Imaging Library - Part I: a versatile Python framework for tomographic imaging. *Phil. Trans. R. Soc. A.* **379**, 20200192 (2021) <https://doi.org/10.1098/rsta.2020.0192>
4. Papoutsellis, E., Ametova, E., Delplancke, C., Fardell, G., Jørgensen, J. S., Pasca, E., Turner, M., **Warr, R.**, Lionheart, W. R. B. and Withers, P. J., Core Imaging Library - Part II: multichannel reconstruction for dynamic and spectral tomography. *Phil. Trans. R. Soc. A.* **379**, 20200193 (2021) <https://doi.org/10.1098/rsta.2020.0193>

Chapter 1

Introduction

The discovery of X-rays by Wilhelm Röntgen in 1895 marked the beginning of a new era of imaging, through the use of ionising radiation to determine the structural composition of objects by acquiring radiographic images [1]. By evaluating the intensity values recorded across a radiographic film, structural properties of materials could begin to be analysed. X-ray imaging enabled internal features to be identified and distinguished, by virtue of their difference in atomic electron density, without the need for destruction of the object. As a result, a form of non-invasive imaging was developed.

In the following years, the most significant advancement of X-ray imaging emerged in the 1970s, as the transition from 2D to 3D X-ray imaging was achieved through the development of a clinical X-ray computed tomography (CT) system by Sir Godfrey Hounsfield [2]. The fundamental design of any X-ray CT system includes the use of an X-ray source, X-ray detector and a sample stage. For clinical imaging of patients or living biological organisms, the detector and source rotate around the the region to be imaged, with the 'specimen' remaining fixed in position. In contrast, for benchtop CT systems, which often aim to achieve high-resolution studies of various materials and structures, the X-ray source and detector are fixed in position, while the sample is rotated on a rotation stage [3]. In each case, multiple 2D image projections ('radiographs') are acquired at a range of angles over 360°, and then recombined using a computational reconstruction algorithm to produce a detailed 3D map of the internal structure. Originally, acquisition time was slow, as narrow pencil beams were used, covering only a small region of the object per image. Therefore, as well as rotating the full gantry (source plus detector) for each projection of the CT scan, there was often a need to translate the system in order to cover a larger imaging field. Nevertheless, the first generation CT scanners proved the tremendous potential of X-ray imaging, both for clinical and benchtop research.

Nowadays, the technique of X-ray CT has found use in a wide range of research and application fields, including: medical imaging [4], metrology [5], industrial failure analysis [6], geoscience [7], and security scanning [8]. The transition from 2D to 3D X-ray imaging has undergone a number of technological advancements throughout its evolution, with a wide array of scanning configurations depending on application, yet the same basic principles are adopted. The conventional method of determining internal composition and structure of objects based purely on X-ray attenuation differences has often been referred to as 'Black and White' imaging, referencing the commonly used colour scale observed in clinical radiographic images comparing e.g. bone vs. tissue. This is due to their use of 'energy-

integrating' X-ray detectors. Typically, these are scintillation devices, whereby incident photons interact with the detector material, generating a set of visible light pulses, which are then amplified and converted to an electronic signal which may be measured for a single detector pixel [9, 10]. As highlighted in the name, regardless of photon energy, the total signal is simply integrated in each pixel, and therefore any energy-based information about the incident photons is lost.

In recent years, the development of 'colour' X-ray CT techniques have emerged, referencing the ability to extract additional information related to the chemical composition of objects under investigation. Much like the visible range of the electromagnetic spectrum has observable colours, based on their different wavelength (energy), a similar analogy may be applied to the X-ray spectrum. An example depiction of this analogy is shown in Fig. 1.1.1. Commonly in X-ray research, a wide range of energies are utilised as a polychromatic beam, and therefore if the precise energy of each incident photon is recorded, a full colour 'spectrum' may be constructed. The result is that direct insight on the distribution and range of photon energies is obtained, following interaction with the object being studied. Figure 1.1.1 also differentiates the two main categories of colour imaging, referred to as 'spectral' (or multispectral) and 'hyperspectral', based on the number of energy windows (channels) the polychromatic photon spectrum can be divided into. By accessing the previously 'lost' energy-based information, a wide range of chemical, crystallographic, and structural characteristics of an object may be unlocked, in addition to the 3D volumetric mapping. With the development of energy-sensitive X-ray detectors, such spectral properties may be measured, simply by replacing the conventional 'integrating' X-ray detectors used before. This offers a wealth of information, due to the presence of characteristic spectral markers, appearing in the form of edges and peaks on the energy spectrum. The example shown in Fig. 1.1.1 shows such markers, in this case due to characteristic fluorescence peaks emitted by a tungsten X-ray source target. Markers such as these may be used to directly evaluate the chemical composition of objects through energy-sensitive imaging.

Despite the introduction of 2D energy-resolved X-ray imaging as early as 1971, analysing crystal structure of metal foils [11], and 3D investigations in 1990 using 'energy-dispersive tomography' [12], it is only with the rapid development of pixellated, spectroscopic detectors from the 1990s through the 21st century that has enabled significant advancement in spectral studies across many research fields. However, many areas of energy-sensitive research still remain untapped. Much of the research into spectroscopic imaging has focused on the 'few-channel' spectral systems, offering coarse energy resolution. For the high energy resolution hyperspectral detectors, many gaps in the research applications, data processing, reconstruction and analysis of hyperspectral work remain.

The concept of hyperspectral imaging (HSI) was first proposed in the 1980s outside of X-ray imaging, emerging in the field of remote sensing of the Earth's surface by aircraft and spacecraft. This form of imaging 'spectrometry' largely utilised the visible, near-infrared, or ultraviolet portions of the electromagnetic spectrum, and was capable of analysing the chemical composition and structure of the surface materials based on the different propor-

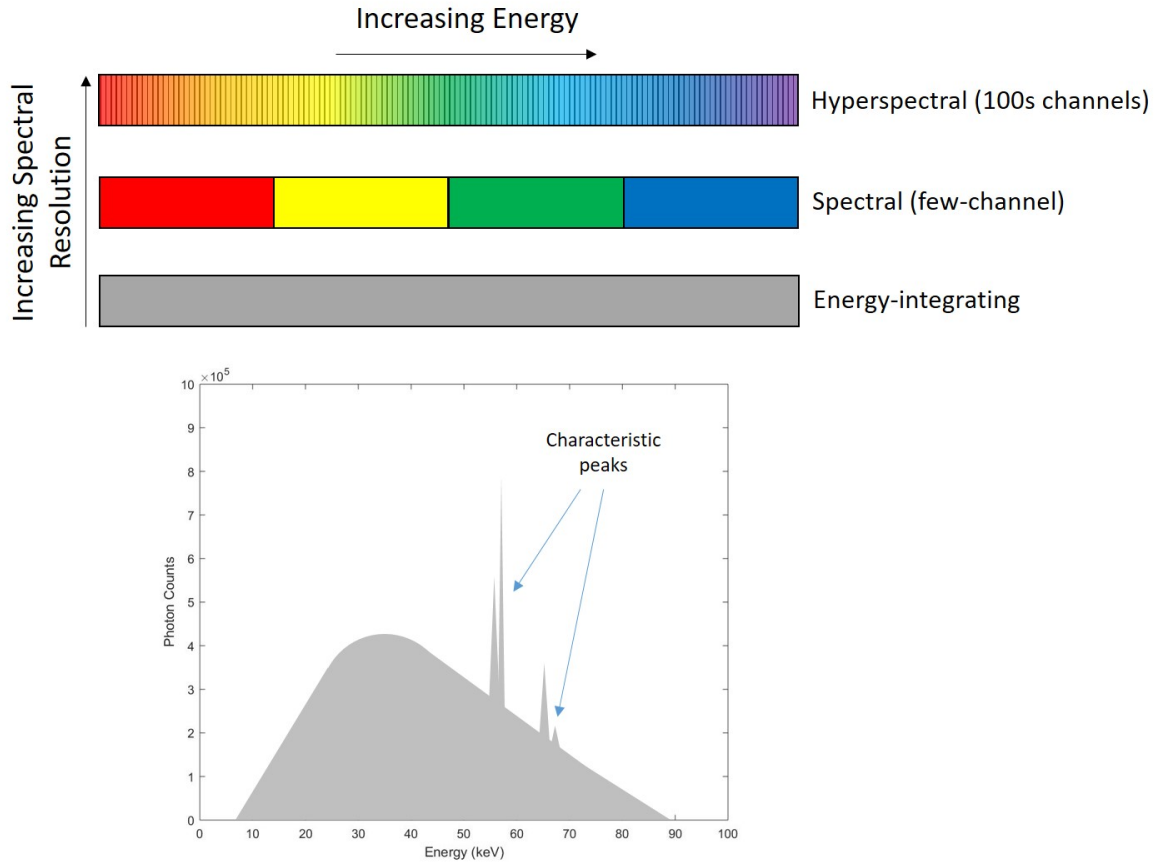


Figure 1.1.1. Illustration of the concept of 'Black and White' versus 'Colour' imaging. (Bottom) Image of a typical Bremsstrahlung X-ray spectrum for a tungsten source target. Characteristic peaks due to fluorescence of tungsten are labelled. (Top) Distinction between the conventional 'energy-integrating' detectors, offering no energy-based insight, and the energy-sensitive systems. Hyperspectral imaging is capable of dividing the incident photon energies into many narrow channels, providing higher energy resolution over the 'few-channel' systems.

tions to which objects reflect, absorb, and emit the incident radiation [13]. The original definition of the imaging technique was described as "the acquisition of data in hundreds of spectral bands simultaneously" [14], and it was the ability to capture these distinct spectral signatures which enabled such specific mapping and material identification to be possible. With this technique, remote mapping of minerals in rocks, soil, and vegetation was achievable over vast areas. HSI now finds application in a wide field of study, ranging from archaeology and food quality control, to forensic analysis and medical diagnosis [15, 16].

The principle of HSI, much like in hyperspectral X-ray CT, as will be explained in this thesis, builds on the concept of accessing an additional dimension of spectral information. As such, rather than a standard 2D spatial image, datasets in HSI become a 3D data 'block', sometimes referred to as a 'hypercube', of size $n_1 \times n_2 \times d$. As shown in Fig. 1.1.2, this additional dimension essentially accumulates a set of energy-based layers, corresponding to equally-spaced wavelengths of the electromagnetic spectrum. Hence for an image of $n_1 \times n_2$ pixels, each pixel would contain a vector of d spectral channels. Therefore, by analysing individual voxels, spectral profiles of the imaged region may be evaluated, and insight on chemical composition extracted. In the case of HSI, measurements of reflectance, absorbance or fluorescence profiles are obtainable, allowing surface structure, texture and

molecular composition to be determined [15, 17, 18].

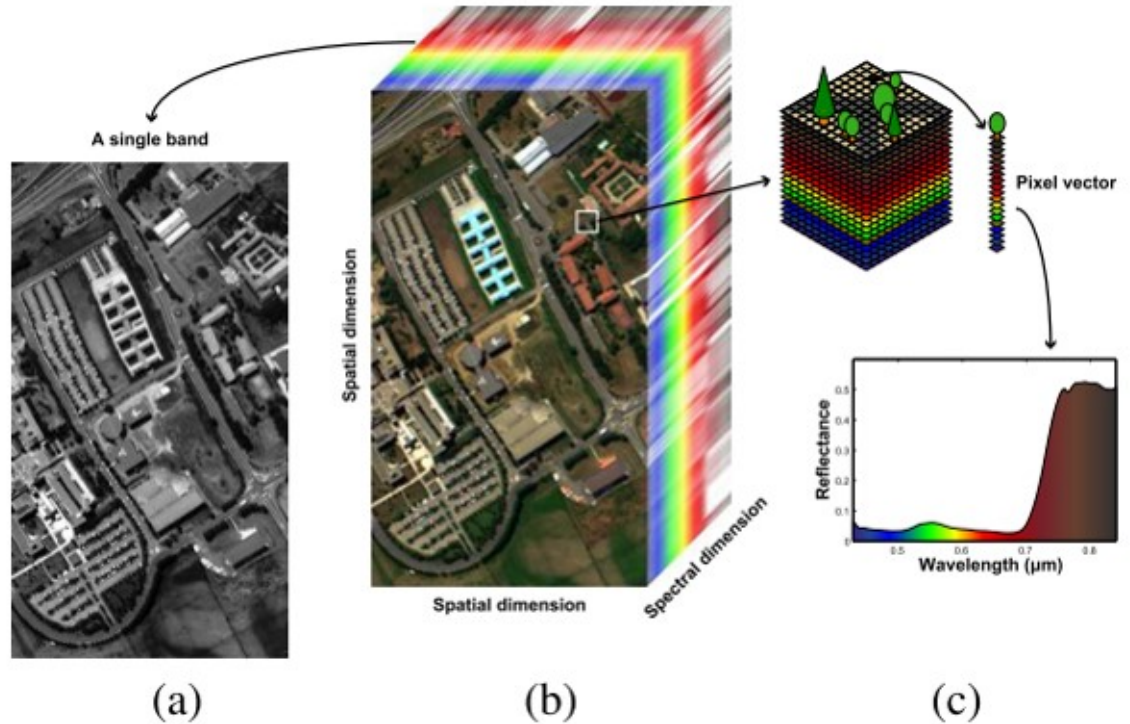


Figure 1.1.2. Example of a 'hypercube' data structure in remote surface mapping. (a) A conventional 2D greyscale image of a region of the Earth's surface. (b) The same region acquired as a HSI hypercube, where an additional spectral dimension is captured over hundreds of narrow bands. (c) Example of extracting spectral information from a pixel in the hypercube, allowing an individual spectral profile to be analysed [18].

One of the key challenges faced in HSI, however, is the trade-off between high spatial and high spectral image resolution. While one possible solution is the acquisition of two image sets, one at high spatial and one at high spectral resolution, this introduces the complexity of image alignment and fusion [19, 20]. Therefore, typically the focus has largely been on the development of image enhancement techniques, to extract the maximum information from a single data acquisition [21].

Similar issues emerge in the case of hyperspectral imaging for X-ray CT. As will be discussed in this thesis, despite excellent spectral resolution, poor spatial resolution is a defining characteristic of hyperspectral X-ray detectors, compared to their energy-integrating counterparts. As with HSI, outside of multi-modal acquisitions and image fusion, a crucial aspect of advancing the technique is improving the ability to extract more information from poorer data quality.

Given the high energy resolution of hyperspectral X-ray detectors, full spectral profiles become accessible, and with it a range of imaging modalities have been developed, focused on assessing chemical or crystallographic properties of a sample. The choice of modality depends on the type of spectral marker to be identified, but is broadly split into two categories: 'bright-field' (absorption edges) and 'dark-field' (scattered fluorescence/diffraction peaks). This PhD research was focused on the bright-field category, and how we can advance the various aspects of the full hyperspectral imaging process.

1.1 Aims and Objectives

In the case of a laboratory-based setup, where polychromatic cone beams are used, hyperspectral imaging is still in its early stages of development across several steps of the imaging process. One of the main weaknesses of hyperspectral imaging emerges as a result of its key strength: the ability to measure the energy of each individual photon requires increased signal processing, limiting the detector count rate to levels significantly below that of energy-integrating systems [22]. A logical solution to such an issue is to simply increase exposure time, though this is inefficient due to increased scan times, and inapplicable to cases where X-ray dose is important, such as clinical studies. An alternative for handling noisy data is through improved post-processing and reconstruction routines, in order to extract the maximum information from the limited existing data. To date, few studies have explored reconstruction routines for the 4D nature of energy-sensitive imaging, with even less so designed specifically for the hyperspectral imaging sensors [23].

This work first aims to address the research gap of hyperspectral reconstruction methods. The research focuses on the application of a novel algorithm built to handle the complex nature of hyperspectral data, through the method of 'regularisation'. That is, through handling the spatial and spectral components separately, an optimised reconstruction may be obtained to compensate for noisy 4D datasets. Previous work in both conventional and multispectral X-ray CT has shown the capability of regularised algorithms to handle complex datasets [24, 25]. Through application to both a phantom sample and a real-world biological specimen, this work assesses the capacity for improved elemental mapping following the use of the novel algorithm, and how they compare to the existing methods.

Following the construction of a routine capable of improving the data quality of hyperspectral acquisitions, the crucial next step of the process is extraction and interpretation of all energy-based information in the bright-field regime, available within the spectral profiles measured in each pixel. As such, another objective of the research is the evaluation and development of both qualitative and quantitative spectral analyses applicable to the bright-field modality. Much of the current research in hyperspectral imaging to date has been qualitative in its chemical analysis, with quantitative research largely focused on few-channel multispectral imaging [26, 27]. This work aims to assess the quantitative results which may be extracted from the full attenuation profiles of hyperspectral X-ray CT.

Given the infancy of hyperspectral imaging, a wide range of research fields remain untapped, where non-destructive elemental analysis would benefit. In this research, emphasis is given on one of the major fields believed to be the first future realm of mainstream colour imaging: the life sciences. Both clinical and biological research utilises highly-attenuating contrast agents to differentiate soft tissue, and therefore offers a prime case for energy-sensitive imaging to map such materials. Therefore, an overarching theme of this research is a focus on mapping the inhomogeneous distribution of contrast agents utilised in the field of bioimaging. In particular, the higher energy resolution of hyperspectral over multispectral imaging enables full flexibility in the imaging of multiple simultaneous chemicals. The

work covered in this thesis explores a range of biological specimens, varying in the number and type of applied chemical stains. Full evaluation of the stain distribution and interaction becomes possible with hyperspectral CT, and is assessed for multiple case studies.

In summary, the objectives within this PhD include:

1. The development of novel spectral, 4D reconstruction routines for bright-field hyperspectral CT, and assessment of image quality improvement compared to the conventional algorithms used within X-ray CT.
2. Evaluation of the extent of qualitative and quantitative spectral analyses achievable from bright-field spectral profiles.
3. Exploration of the bioimaging applications for bright-field hyperspectral CT in the case of multiple inhomogeneous chemical staining.

1.2 Structure of the Thesis

Following the introduction, **Chapter 2** provides a detailed literature review describing the transition from 'black and white' to 'colour' X-ray CT imaging. The chapter covers the key technological advancements in X-ray detector systems to enable energy-sensitive acquisitions, as well as a review of existing X-ray CT reconstruction algorithms. Finally, the different modalities of energy-sensitive imaging are explored, along with some of the main applications to date. **Chapter 3** details the materials, equipment and experimental approach for the work conducted within the various research chapters. **Chapter 4** provides the first research study, on the development of a novel 4D spectral reconstruction algorithm aimed at producing hyperspectral volumes with high image quality, enabling improved spectral analysis. The study assesses the algorithm through a phantom sample and stained biological specimen. **Chapter 5** covers a secondary research study, investigating the quantitative mapping of chemical concentrations for biological specimens stained with multiple contrast agents across a number of soft tissue structures. The work discusses a first instance of direct extraction of chemical concentration of inhomogeneously distributed stains in bioimaging using hyperspectral X-ray CT. Finally, **Chapter 6** summarises the results achieved and the conclusions drawn, alongside a discussion of potential future work.

1.3 References

¹W. Rontgen, "On a new kind of rays", *Science* **3**, 227–231 (1896).

²G. N. Hounsfield, "Computerized transverse axial scanning (tomography): Part I. Description of system", *British Journal of Radiology* **46**, 1016–1022 (1973).

- ³P. J. Withers, C. Bouman, S. Carmignato, V. Cnudde, D. Grimaldi, C. K. Hagen, E. Maire, M. Manley, A. D. Plessis, and S. R. Stock, “X-ray computed tomography”, *Nature Reviews Methods Primers* **1**, 1–21 (2021).
- ⁴G. Wang, H. Yu, and B. De Man, “An outlook on x-ray CT research and development”, *Medical Physics* **35**, 1051–1064 (2008).
- ⁵J. M. Warnett, V. Titarenko, E. Kiraci, A. Attridge, W. R. Lionheart, P. J. Withers, and M. A. Williams, “Towards in-process x-ray CT for dimensional metrology”, *Measurement Science and Technology* **27**, 1–14 (2016).
- ⁶P. Lall, S. Deshpande, J. Wei, and J. Suhling, “Non-Destructive Crack and Defect Detection in SAC Solder Interconnects”, *Electronic Components and Technology Conference (ECTC)*, 2014 IEEE 64th, 1449–1456 (2014).
- ⁷F. Mees, R. Swennen, M. V. Geet, and P. Jacobs, “Applications of X-ray computed tomography in the geosciences”, *Geological Society, London, Special Publications* **215**, 1–6 (2003).
- ⁸G. Zentai, “X-ray imaging for homeland security”, in *Ieee workshop on imaging systems and techniques proceedings* (2008), pp. 1–6.
- ⁹J. G. Rocha and S. Lanceros-Mendez, “Review on X-ray detectors based on scintillators and CMOS technology”, *Recent Patents on Electrical Engineering* **4**, 16–41 (2011).
- ¹⁰N. Faderl, “Fast decay solid-state scintillators for high-speed x-ray imaging”, in *Proc. spie 11159, electro-optical and infrared systems: technology and applications xvi*, October 2019 (2019), p. 10.
- ¹¹J. Chwaszczewska, S. Szarras, Z. Szmid, and M. Szymczak, “Application of semiconductor detectors in crystal structure investigations”, *Physica Status Solidi (a)* **4**, 619–626 (1971).
- ¹²G. Harding, “Energy-dispersive X-ray diffraction tomography”, *Physics in Medicine and Biology* **35**, 33–41 (1990).
- ¹³A. F. Goetz, “Three decades of hyperspectral remote sensing of the Earth: A personal view”, *Remote Sensing of Environment* **113**, S5–S16 (2009).
- ¹⁴A. F. Goetz, G. Vane, J. E. Solomon, and B. N. Rock, “Imaging spectrometry for earth remote sensing”, *Science* **228**, 1147–1153 (1985).
- ¹⁵G. Lu and B. Fei, “Medical hyperspectral imaging: a review”, *Journal of Biomedical Optics* **19**, 010901 (2014).
- ¹⁶A. Schneider and H. Feussner, “Diagnostic procedures”, in *Biomedical engineering in gastrointestinal surgery*, 1st (Academic Press, 2017) Chap. 5, pp. 87–220.

- ¹⁷F. Vasefi, N. MacKinnon, and D. L. Farkas, “Hyperspectral and Multispectral Imaging in Dermatology”, in *Imaging in dermatology* (Elsevier Inc., 2016) Chap. 16, pp. 187–201.
- ¹⁸P. Ghamisi, N. Yokoya, J. Li, W. Liao, S. Liu, J. Plaza, B. Rasti, and A. Plaza, “Advances in Hyperspectral Image and Signal Processing: A Comprehensive Overview of the State of the Art”, *IEEE Geoscience and Remote Sensing Magazine* **5**, 37–78 (2017).
- ¹⁹E. W. Mowle and C. J. Dennehy, “The Landsat-6 Satellite: An Overview”, in *Ntc ’91 - national telesystems conference proceedings*, March (1991), pp. 1–6.
- ²⁰M. Moeller, T. Wittman, and A. L. Bertozzi, “A variational approach to hyperspectral image fusion”, *Algorithms and Technologies for Multispectral, Hyperspectral, and Ultra-spectral Imagery XV* **7334**, 73341E (2009).
- ²¹I. Amro, J. Mateos, M. Vega, R. Molina, and A. K. Katsaggelos, “A survey of classical methods and new trends in pansharpening of multispectral images”, *Eurasip Journal on Advances in Signal Processing* **2011**, 1–22 (2011).
- ²²R. Ballabriga, J. Alozy, M. Campbell, E. Frojdh, E. H. Heijne, T. Koenig, X. Llopart, J. Marchal, D. Pennicard, T. Poikela, L. Tlustos, P. Valerio, W. Wong, and M. Zuber, “Review of hybrid pixel detector readout ASICs for spectroscopic X-ray imaging”, *Journal of Instrumentation* **11**, 1–31 (2016).
- ²³D. Kazantsev, J. S. Jørgensen, M. S. Andersen, W. R. Lionheart, P. D. Lee, and P. J. Withers, “Joint image reconstruction method with correlative multi-channel prior for x-ray spectral computed tomography”, *Inverse Problems* **34**, 1–27 (2018).
- ²⁴E. Y. Sidky, C. M. Kao, and X. Pan, “Accurate image reconstruction from few-views and limited-angle data in divergent-beam CT”, *Journal of X-Ray Science and Technology* **14**, 119–139 (2006).
- ²⁵D. S. Rigie and P. J. La Rivière, “Joint reconstruction of multi-channel, spectral CT data via constrained total nuclear variation minimization”, *Physics in Medicine and Biology* **60**, 1741–1762 (2015).
- ²⁶R. Symons, B. Krauss, P. Sahbaee, T. E. Cork, M. N. Lakshmanan, D. A. Bluemke, and A. Pourmorteza, “Photon-counting ct for simultaneous imaging of multiple contrast agents in the abdomen: an in vivo study”, *Medical Physics* **44**, 5120–5127 (2017).
- ²⁷S. Si-Mohamed, V. Tatard-Leitman, A. Laugerette, M. Sigovan, D. Pfeiffer, E. J. Rummeny, P. Coulon, Y. Yagil, P. Douek, L. Bousset, and P. B. Noël, “Spectral photon-counting computed tomography (spcct): in-vivo single-acquisition multi-phase liver imaging with a dual contrast agent protocol”, *Scientific Reports* **9**, 1–8 (2019).

Chapter 2

Literature Review

The following chapter details the relevant theory and literature which form the foundation of the research covered in this thesis. The transition from conventional (black and white) X-ray CT imaging to the latest developments in spectral (colour) imaging is discussed in detail. A journey through the key elements of recording, processing, and analysing data are covered. The technical developments in spectroscopic imaging detectors are compared to their energy-integrating counterparts, as is also reviewed in the field of spectral image reconstruction. An exploration is made of the various reconstruction algorithms designed to overcome the inclusion of an additional, energy-based dimension, and the complexities this brings.

Focus is then directed onto the main X-ray imaging modalities that become available with the use of an energy-sensitive detector, particularly for hyperspectral imaging. A review of the fields of study utilising the bright-field geometry is made, and how the work in this thesis aims to fill some of the gaps in the research to date. Alternative modalities, such as those in the 'dark-field' regime, are then briefly discussed to evaluate the versatility of the hyperspectral method.

2.1 From black and white to 'colour' X-ray CT

2.1.1 X-ray CT: basic principles

As mentioned in Chapter 1, the fundamental design of a benchtop X-ray CT system involves the use of an X-ray source, sample stage, and X-ray detector. X-rays are generated through the use of an X-ray tube, whereby electrons are accelerated from an electron source (cathode) to a target material (anode) via an applied electric field. Electrons ejected from the cathode travel through the tube, according to the applied field, and interact with the anode material. The majority of electron interactions with the anode target simply involve the absorption of the kinetic energy by the anode, resulting in heating of the target. Where instead the electrons interact with the anode atoms, electromagnetic radiation in the form of X-rays may be formed. In cases where electrons are decelerated by the electric fields of the anode atoms, kinetic energy is transformed to X-ray radiation of a wide-energy range, known as bremsstrahlung radiation [1, 2]. In a perfect interaction, all energy is converted to a single photon, defining the maximum X-ray photon energy achievable. However, in most

instances, the energy is lost over multiple interactions, and therefore a continuous range of X-ray energies form the final bremsstrahlung spectrum produced by the X-ray tube.

For lab-based imaging, the X-ray tube emits photons as a cone beam over a range of energies up to the accelerating voltage of the electrons within the source. This forms the 'polychromatic' X-ray spectrum, sometimes known as a 'white beam'. Most X-ray tubes use tungsten as the anode 'target' material, producing spectra similar to that shown in Fig. 1.1.1. Alternatively, X-ray sources may be utilised at synchrotron facilities, where several experimental CT beamlines are placed tangentially to a central electron storage ring. With the X-ray source typically up to hundreds of meters from the object of interest, the incident beam is often highly parallel, such that no magnification of the sample takes place, regardless of the geometry of the system. Additional flexibility is provided by synchrotrons in that monochromatic X-ray beams may be extracted, set to a specifically selected energy. Monochromatic systems can offer advantages such as the avoidance of certain artefacts present in polychromatic sources [3]. A key advantage to synchrotron facilities is the significantly higher flux achievable compared to a lab-based source, which can be highly beneficial in reducing overall scan time to the order of seconds [4].

The most common imaging modality for X-ray CT is absorption X-ray CT (XCT), whereby a 3D map is reconstructed with contrast between features based on the different attenuation coefficients of materials within a sample. Therefore, the technique provides a means of feature differentiation based on electron density variation of the sample composition. For a given object, the transmitted intensity of the X-ray beam decreases exponentially while travelling along its ray path. The degree of intensity loss by the incident beam is determined by the attenuation coefficient, μ of the object material. For a single, homogeneous material, the loss of intensity, I for an X-ray travelling through an object of thickness, x may be determined by the Beer-Lambert law

$$I(x) = I_0 e^{-\mu x} \quad (2.1)$$

where I_0 defines the unattenuated X-ray beam intensity [2]. In many cases, however, samples may contain a number of inhomogeneously distributed materials, each with their own attenuation coefficient. Therefore, when considering spatial variations in attenuation over an X-ray path length, l the Beer-Lambert law becomes

$$I(l) = I_0 e^{-\int_0^l \mu(x) dx} \quad (2.2)$$

where the attenuation coefficient, μ now varies as a function of spatial position. The result is that XCT produces the conventional "black and white" X-ray images, where higher electron density materials (e.g. bone) appear brighter than surrounding, lower density materials (e.g. fat, muscle), when measured in terms of absorbance. For cone-beam XCT, the level of detail of observed features is directly influenced by the geometrical setup. As shown in Fig.

2.1.1, by adjusting the source-sample (d_1) and sample-detector (d_2) distances, one can alter the geometric magnification (M) of the system, which affects the final spatial resolution. An increased magnification results in improved spatial resolution, such that smaller features may be distinguished and differentiated from the surrounding phases. The value of M may be calculated using the following equation:

$$M = \frac{d_1 + d_2}{d_1}. \quad (2.3)$$

An influential factor in the achievable spatial resolution is the pixel size of the X-ray detector. The pixel size, combined with the magnification, directly determine the resulting voxel size in 3D following spatial reconstruction. A larger initial pixel size will require an increased magnification to achieve the desired spatial resolution [5, 6]. On the other hand, increased magnification reduces the detector field of view (FOV), limiting the size of object which can be fully captured, therefore a trade-off emerges between resolution and sample size.

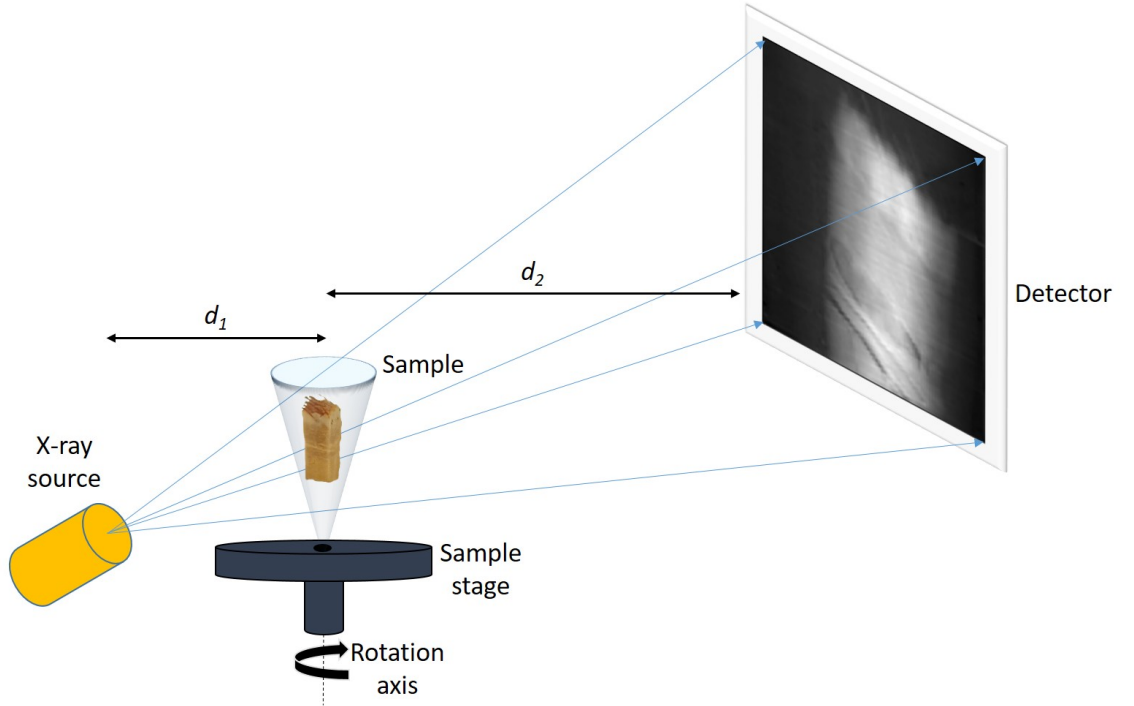


Figure 2.1.1. Magnification of the projected image using a cone beam X-ray source. By moving the sample closer to the source, or the detector further away, the image recorded on the detector is magnified, improving spatial resolution. Labels defining the source-sample and sample-detector distances are included as (d_1) and (d_2) respectively.

2.1.2 Limitations of XCT

While the dominant modalities of X-ray CT have been highly successful in providing levels of detail and insight never before seen for non-invasive imaging of materials, they have often solely relied on singular pieces of information for structure determination, such as density variation. As such, one may be able to distinguish internal structures depending on im-

age quality and contrast, however material identification is impossible without prior knowledge of composition. As a result, the task of separation (segmentation) of internal features based only on changes in greyscale intensity values can be subjective and limited by factors such as image noise and reconstruction artefacts.

An additional factor to consider in the case of imaging with a polychromatic source, is the emergence of imaging artefacts, particularly those caused by 'beam hardening', the cause and effect of which is described below.

The previously defined Beer-Lambert law shown in Equation 2.2 assumes the X-ray beam to be monochromatic, and therefore attenuation is a constant value. In using a polychromatic beam, however, attenuation changes as a function of energy, and therefore a more accurate definition of the Beer-Lambert law becomes

$$I(l) = \int_0^{E_{max}} I_0(E) e^{-\int_0^l \mu(E,x) dx} dE \quad (2.4)$$

where the energy dependence of the attenuation, $\mu(E)$ is accounted for, for the full bremsstrahlung spectrum up to the maximum photon energy, E_{max} [2]. By examining the attenuation change over the hard X-ray range (>10 keV), the effect of the energy dependence becomes clear. Figure 2.1.2 shows the mass attenuation coefficient values for a number of elements, as well as soft tissue, for energies up to 100 keV. It should be noted that the mass attenuation coefficient is simply a scaling of μ by the density ρ of the absorbing material. It becomes clear that attenuation significantly decreases as energy is increased in all materials, and that low-energy X-ray photons are more strongly attenuated than high-energy photons. This preferential absorption of low-energy photons leads to a shift in the mean X-ray energy towards harder radiation, causing the 'beam hardening' phenomenon. Without correction, the observed result in reconstructed volumes is the presence of 'cupping' or 'streaks' artefacts [7, 8].

2.1.3 Capturing spectral detail

When acquiring XCT data with a polychromatic beam, one of the defining characteristics of the incident X-ray photons are their different energies. Despite the aforementioned beam hardening issues of using a polychromatic beam for lab-based X-ray imaging, the upside lies in the increased photon flux, such that scan times may be reduced, compared to the use of a monochromatic beam. While energy-integrating detectors effectively disregard the photon energy information contained within the incident spectrum, significant amounts of information relating to the chemical or crystallographic properties of the sample under inspection may be obtained by utilising a system capable of measuring photon energies. Energy-sensitive detection was first theorised and implemented as early as 1971 in the field of diffraction imaging [10], enabling crystal structure analysis to be performed with the use of a polychromatic source. By processing each detected photon individually,

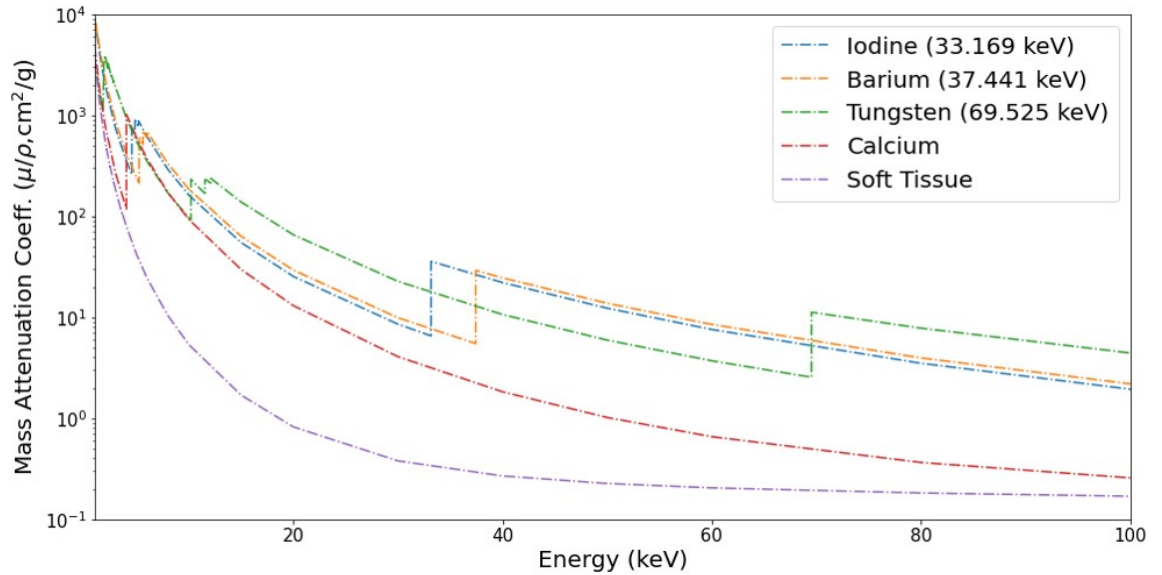


Figure 2.1.2. Attenuation profiles as a function of energy for different chemical elements and materials. The mass attenuation values are shown across the hard X-ray range for each material. Sharp discontinuities occur at unique energies for each element, corresponding to the absorption edges. The K-edge energies for each element shown are quantified in the legend. Attenuation values extracted from the NIST online database [9].

an energy spectrum may be constructed, providing additional information based on X-ray interaction with a sample object. The attenuation response observed across the spectral range is strongly influenced by the type of X-ray photon interaction with the sample. For the hard X-ray range, the predominant interaction is the photoelectric effect, due to a higher photoelectric effect cross-section [11]. In this regime, the magnitude of the interaction is directly proportional to the 4th power of the atomic number, Z and inversely proportional to the 3rd power of the photon energy, E [12]. This relationship is observed in the attenuation profiles for each individual element of the periodic table, whereby the attenuation coefficient for each material varies as a function of energy, as shown previously in Fig. 2.1.2. These attenuation characteristics are exactly known and well documented, and have also been evaluated for several common materials, such as soft tissue and bone, offering useful information for clinical CT studies [9].

2.1.4 Spectral markers

A notable feature of the elemental attenuation profiles are the large step rises in attenuation at specific energies, due to photoelectric absorption. The phenomena of the photoelectric effect is the dominant form of photon interaction with matter, within the hard X-ray range. Its principle is shown in Fig. 2.1.3. These 'absorption edges' occur at unique energies for each element, corresponding to the binding energies of the core-electron states, and are typically referred to as K-, L- and M-edges, relating to the electron shells from which a photoelectron is ejected [13]. Given that each element has a unique atomic structure, the binding energies, and resultant absorption edges, are also unique to each element, therefore each edge acts as a 'fingerprint' specific to the element that produced it. This illustrates the first of a type of 'spectral marker' that may be used as a form of elemental identification. An ad-

ditional marker also emerges as a secondary effect of photoelectric absorption, due to X-ray 'fluorescence' (XRF), whereby secondary, fluorescent X-ray photons are emitted from an atom following photoelectric interaction. Following the ejection of the photoelectron, a 'vacancy' remains, and the atom becomes ionised, producing an unstable atomic structure. To stabilise the atom, an electron from a higher atomic orbital will transition to the lower orbital to fill the vacancy. During transition, an XRF photon is emitted at an energy equal to the transition between the two atomic orbitals. As such, the emitted radiation is also characteristic of the interacting element, and appears as a peak at the corresponding XRF energy. The characteristic nature of such emissions was discovered by Henry Moseley, in a series of experiments which related XRF spectra to the underlying atomic charge of a given element [14, 15]. Similar to absorption edges, XRF peaks are labelled according to the orbitals they transition from and to. For example, a K_{α} peak corresponds to a transition of an L-shell electron to a K orbital, while a K_{β} is measured if the transition is from the M-shell to a K orbital. With the presence of two distinct types of spectral marker available, any form of energy-sensitive detection immediately provides access to these, and therefore offers the ability to measure and map them back to the element from which they originated. This introduces the concept of 'colour' imaging, used as an analogy to help better define the process of energy-sensitive imaging. Visible light has a range of wavelengths (energies) that we observe as a spectrum of colour, or when combined as a whole is observed as white. We can apply the same principle to X-rays. If we can capture and observe the full range of X-ray wavelengths from a polychromatic beam, these detectors can then effectively capture the full X-ray 'colour range', even if invisible to the naked eye. Add in the ability to measure and unambiguously identify chemicals based on spectral markers at unique energies, and energy-sensitive imaging can help to bring full colour X-ray volume imaging to life. In the following sections, the transitional steps taken in the evolution from 'black and white' to 'colour' X-ray imaging are discussed, starting with a modality developed to handle similar attenuation in soft tissue structures: the introduction of Dual-Energy CT (DECT).

2.1.5 Dual-energy CT

The modality of DECT was first conceptualised and explored in the 1970s [16–18], with the idea that additional information may be extracted from a sample by scanning at different X-ray energies. The key reasoning behind this centres around the attenuation differences as a function of energy, as shown in Fig. 2.1.2. By employing a scan approach at two specifically chosen X-ray energies, improved contrast may be achieved by exploiting these attenuation differences. While synchrotron studies are capable of using two monochromatic beams, a lab source itself is still typically polychromatic, however it is chosen such that the peak (and thus the most photons) has the desired energy of choice. As a result, scan conditions are typically termed based on the incident beam 'peak kilovoltage', given as units of kVp. A number of experimental geometries and DECT imaging designs have been implemented since the technique was first explored. A summary of these designs are shown in Fig. 2.1.4. Each technique offers both benefits and drawbacks, and therefore the choice

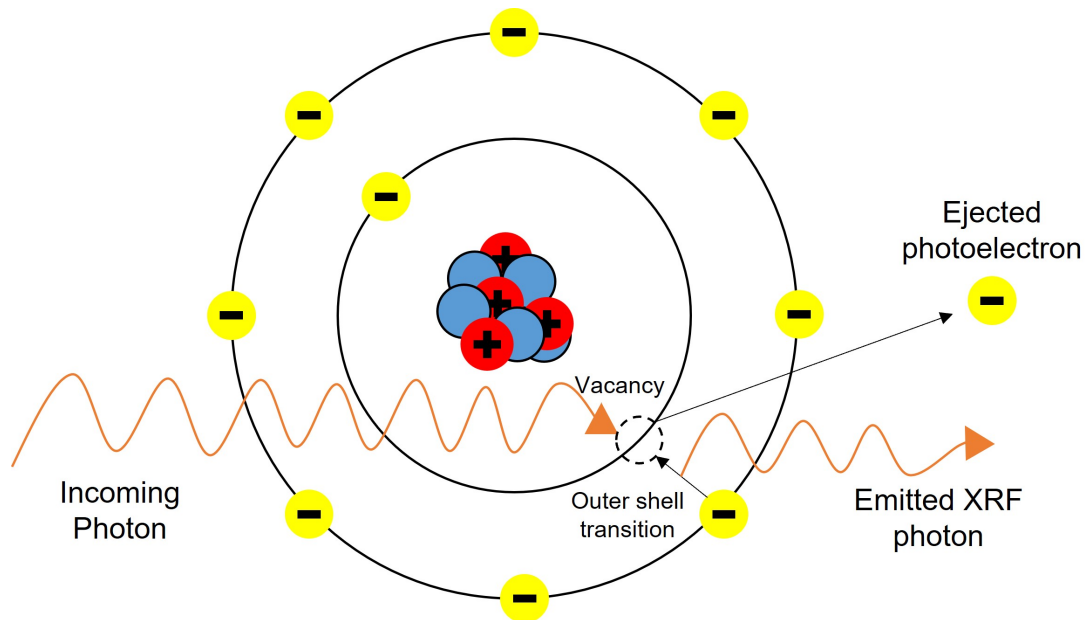


Figure 2.1.3. Demonstration of the photoelectric effect. The diagram illustrates the different steps involved in photoelectric absorption. An incoming photon of sufficient energy is absorbed by an electron, and ejected as a photoelectron. The subsequent vacancy is filled by the transition of an electron from a higher atomic orbital, emitting an XRF photon of energy equal to the transition between states.

of system may depend on the type of study conducted, or the equipment available. Given its simplicity, the use of two sequential scans at differing tube voltages was one of the first explored (technique 4). Such a design does not require additional CT hardware, however can create issues due to the additional scan time and dose required to effectively collect two CT scans. Further, for clinical imaging, motion artefacts due to patient movement may degrade image quality for longer scan acquisitions. The same may be said for the technique of rapid voltage switching (technique 2), with a slower rotation speed required to capture images at both voltages. If feasible, the dual source geometry (technique 1) offers a useful, faster imaging solution that may be optimised to improve image contrast based on the patient or object under investigation. The application of a dual-layer detector (technique 3) is a newer DECT design and implements a type of energy-resolving detector system. By using two detector materials, with different spectral response, high- and low-energy photons are selectively absorbed by a single layer, such that the X-ray tube need only scan at a single beam voltage. Therefore it offers advantages in terms of overall scan time and patient dose. The main complications emerge in the complex detector design, and more sophisticated reconstruction routines required to resolve the spectral information. Several studies have conducted thorough reviews of the various DECT modalities available, and how they compare in terms of dose, temporal resolution, and image contrast [19–21].

While DECT aims to overcome the issue of similar contrast in soft tissue by exploiting the differences in attenuation across the energy range, it is common to further aid the feature definition in structures through the application of contrast agents. That is, by administering a dense chemical stain into the patient or sample of interest, contrast in a specific region, or regions, may be significantly enhanced by the presence of the chemical. This is particularly common in the medical and bioimaging field, where a vast range of contrast agents are used to provide improved feature definition in specific soft tissue structures. A recent review by

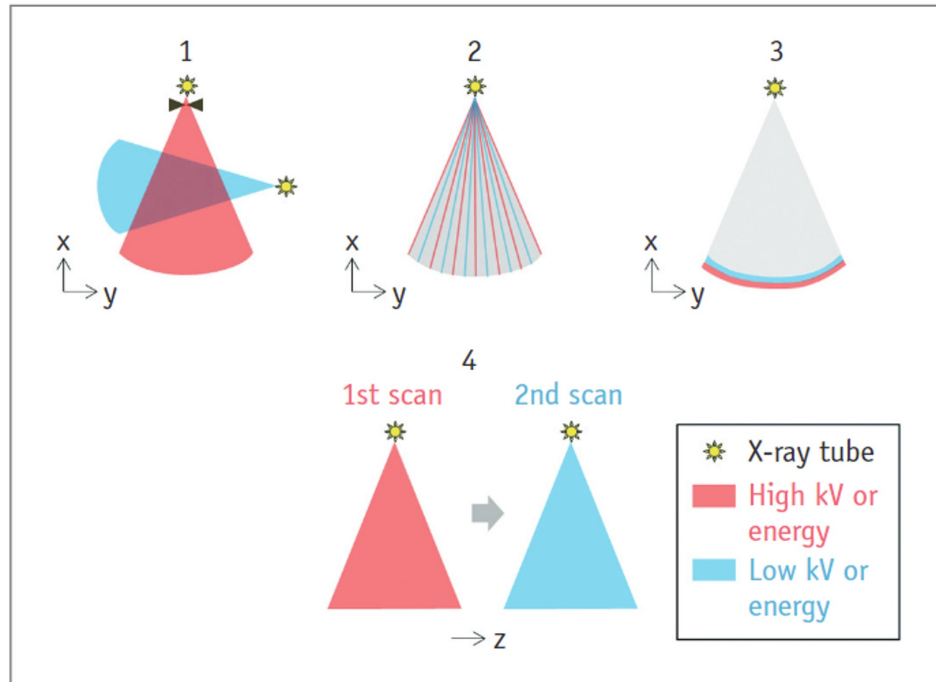


Figure 2.1.4. Variations of DECT geometries. 1) Dual-source scanning. 2) Rapid kV switching. 3) Dual-layer detector. 4) Sequential scans at two different kVp settings. Adapted from [19].

Koç *et al.* provided an extensive report of contrast agents used for X-ray tomography, including their production, staining protocols, and wide-ranging applications in bioimaging [22]. In addition, an evaluation of the use of X-ray CT in the life sciences was conducted by Rawson *et al.*, reviewing the latest capabilities in the field of life science imaging. The article highlights the accomplishments in extending from 2D through to 3D and 4D tools for imaging of biological specimens, including the latest extension into DECT and lab-based spectral imaging [23]. Below, a brief summary is provided of how contrast agents are utilised for improved soft tissue imaging in techniques such as DECT, as well as the wider potential following the latest developments of energy-sensitive, spectral X-ray detectors.

By using contrast agents, the attenuation profile of interest during scanning now contains a distinct spectral marker, in the form of an absorption edge, within the X-ray diagnostic energy range. This creates a sharp difference in attenuation at energies either side of the edge. Therefore, the source scan settings may be tailored around these edges, choosing kVp values that lie either side of a K-edge, producing a non-negligible difference in attenuation. Chemical stains, such as iodine-, tungsten- and barium-based compounds, are all commonly used, and the presence of their absorption edges (see Fig. 2.1.2) provide a significant boost over the natural attenuation of soft tissue phases. The use of these stains has also opened up a wider range of imaging applications for DECT, particularly in the field of *ex vivo* bioimaging. That is, investigations involving an organ or section of tissue extracted from the whole organism, and studied externally. The clear benefit to *ex vivo* studies is that X-ray dose is no longer of concern, and therefore the scan settings may be optimised to improve image quality. Further, a wider range of chemical staining procedures may be tested, with no risk involved in the use of toxic contrast agents for example. Several studies have explored the different material segmentation and soft tissue analysis achievable with DECT.

Badea *et al.* investigated the ability to estimate vascular, tissue and air fractions within rodent lungs, in a three-part study, involving a simulation, followed by *ex vivo* and *in vivo* experiments [24]. By using an iodine-based contrast agent, combined with a fast imaging routine utilising a dual-source setup, the work successfully showed potential for volumetric distribution evaluation for future clinical pulmonary studies. The use of an iodinated-contrast media was also applied in a study characterising coronary atherosclerotic plaque [25], and was capable of differentiating calcified from non-calcified plaque. Poor spatial resolution, however, limited the technique from identifying the more vulnerable plaque regions. The work by Handschuh *et al.* [26] evaluated a number of biological specimens using a range of contrast agents in *ex vivo* studies, to assess the potential of DECT as a technique for high resolution material identification in fixed biological samples. One of the key elements of the work is that the method was a 'microDECT' modality, as a commercial, lab-based microCT setup was used for the scan acquisitions. This ensured the achievable spatial resolution was still on par with conventional XCT, reaching below 10 μm , to provide excellent feature definition. The other fundamental component of the DECT workflow, as is the case for many spectral studies, was the use of a spectral separation method to segment the components due to each material. Here, the method of 'material decomposition' was used, which is common in DECT, and also other forms of spectral analysis, due to its success in the separation of individual materials present in the acquired data. Its fundamental principle lies in the fact that the attenuation of an X-ray beam, energy E , can be described by a linear combination of the attenuation coefficients, $\mu(E)$ of the materials through which it passes:

$$\mu(E) = \sum_a f_a(E) A_a \quad (2.5)$$

where f_a is the energy-dependent basis function which describes each material's attenuation, and A_a is the line integral over the material a , which act as weightings for each base. This is essentially a decomposition of all the individual contributing attenuation coefficients into a set of 'basis pairs'. The contributions to the summation are primarily from the combination of photoelectric and Compton interactions. The concept of 'photo-Compton' decomposition was an approach first theorised in 1976 for X-ray CT [27]. If K-edge discontinuities are present, these must also be taken into account as additional factors. By solving for the weights for each individual beam projection, one may decompose the raw data into individual basis maps, highlighting contributions of each factor spatially. The steps taken from raw data to final material decomposition are shown in Fig. 2.1.5. The two datasets are converted to Hounsfield units, a dimensionless unit typically used as the standard for comparing CT image intensity values [28]. Image filtering is applied to reduce noise and improve feature definition [24], before 'volume registration' is performed to align and match the orientations of the two DECT reconstructed datasets at high and low energy. Finally, decomposition may be performed, producing a segmented image with mapping of the materials present, such as iodine (contrast agent), hydroxyapatite (bone) and air. The work by Handschuh *et al.* successfully showed the high resolution mapping of several soft tissue

structures, reaching voxel sizes down to $2\ \mu\text{m}$, with DECT highly effective in the differentiation of a single contrast agent within soft tissue regions from the unstained bone structures. The study also explored the possibility of dual-staining, in this case using iodine and tungsten contrast agents for different regions. The work showed for the first time the capability of dual-stain imaging for a lab-based microDECT setup, with previous studies using synchrotron-based monochromatic beams. The dual-staining procedure was successful for DECT due to the distinct and clear spectral separation in the K-edges of iodine and tungsten (see Fig. 2.1.2), producing significant attenuation differences. More closely-spaced absorption edges, however, such as that of iodine and barium, would struggle to be separated in the DECT regime, due to their spectral similarity.

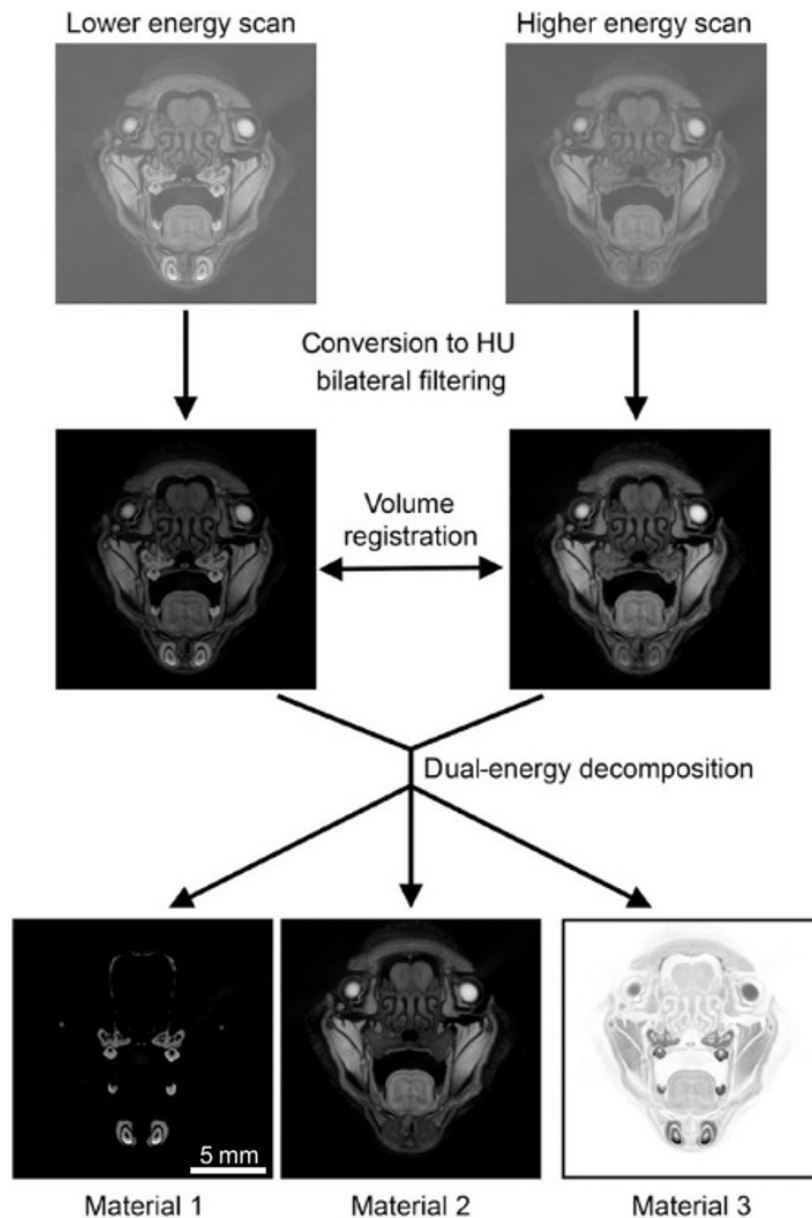


Figure 2.1.5. Workflow for the imaging of microDECT datasets. The images shown are of a mouse head, stained with an iodine-based contrast agent. A set of two scans, at high (80 kVp) and low (40 kVp) energy were acquired and reconstructed, before image conversion and filtering to reduce noise. A volume registration routine matched the orientation of the two datasets, before material decomposition was applied to separate the individual contributions of each material to the reconstructed volume, in this case hydroxyapatite (Material 1), iodine-stained soft tissue (Material 2) and the background (Material 3) [26].

As discussed, the ability to utilise a commercial CT system for DECT ensures that high

spatial resolution is achievable, and simple elemental segmentation is possible, giving a layer of chemical information not possible with conventional XCT. Therefore, DECT offers an excellent entry point for obtaining additional spectral information in addition to the spatial reconstructed volume, for a means of non-destructive elemental mapping. However, several modalities of DECT require a complex geometry, with additional hardware needed to avoid the issue of long scan times using a single X-ray source. For clinical imaging, radiation dose is a crucial factor in determining the optimum acquisition routine, and therefore DECT can be limited in its field of application. One of the notable outcomes of DECT reviews in recent years has been the agreement that the emerging technology of energy-sensitive X-ray detectors is a promising move forward in material identification [19, 20]. The ability to acquire all spectral information in a single scan offers a potential solution for reducing X-ray dose, though the technological limitations are highlighted as the current roadblock in the modality. As will be discussed in the following section, the introduction of energy-sensitive detectors, capable of resolving the spectral information incident upon them, has developed through different routes. A variety of detector systems offering their own advantages and disadvantages, compared to the conventional, 'energy-integrating' detector technology have been produced. The key aim with these new detector designs is the ability to resolve the spectral information available with greater precision and higher resolution, to match what is currently achievable in the spatial domain.

2.2 Properties of spectroscopic imaging detectors

In the following section, a breakdown is made of the technological developments that enabled a transition to pixelated detector systems, capable of resolving the energy information of incident photons. Below, the basic principles of conventional, energy-integrating detectors are discussed, followed by a review of the key changes which enabled energy-sensitive, spectral detectors to be created.

2.2.1 Energy-integrating detectors

For conventional XCT systems, which covers most commercial laboratory set-ups, the detector used is an energy-integrating technology. That is, they work by integrating the light generated by X-ray interactions within the detector material over a given timeframe (exposure). This produces a resultant image based on variable intensities due to X-rays passing through materials of differing properties. The most common style of integrating detector is the scintillation detector, which uses a scintillating crystal such as NaI, CsI, LaBr₃, etc. [29]. These materials are so-called inorganic scintillators, as they are crystals grown for such purposes as X-ray imaging. These crystals interact with incident X-rays, resulting in the emission of many visible light photons for each interacting X-ray photon. The proportion of X-ray-to-light conversion varies with scintillator material and detector design, and can be estimated, as derived elsewhere [30]. The light photons are then amplified and pro-

cessed by the detector electronics. The materials are chosen for their high efficiency and high conversion rates for photon detection. This form of detection is known as ‘indirect detection’ and is considered to be a two-step process: X-ray to light conversion, followed by detection in pixelated photodiodes [31]. As a result, performance with regards to resolution and detection efficiency can be limited by one or both stages. The process of indirect detection is shown in Fig. 2.2.1. One such way in which conversion efficiency of indirect systems may be improved is the addition of an ‘activator’ material within the inorganic scintillator crystal. These are small impurities added to the crystal, which adapt the energy structure. For pure crystals, the size of the ‘band gap’ between the crystal material’s electron states is often large, such that the emitted photons are few, and do not lie within the visible light range. The presence of activators create additional energy states within the crystal, such that de-excitation of electrons may take place in smaller steps, emitting a larger number of photons at lower energies (longer wavelengths), shifting them towards the visible light spectrum. Common activator materials include the use of thallium or sodium, creating e.g. NaI(Tl), CsI(Tl) and CsI(Na) doped scintillator crystals [31].

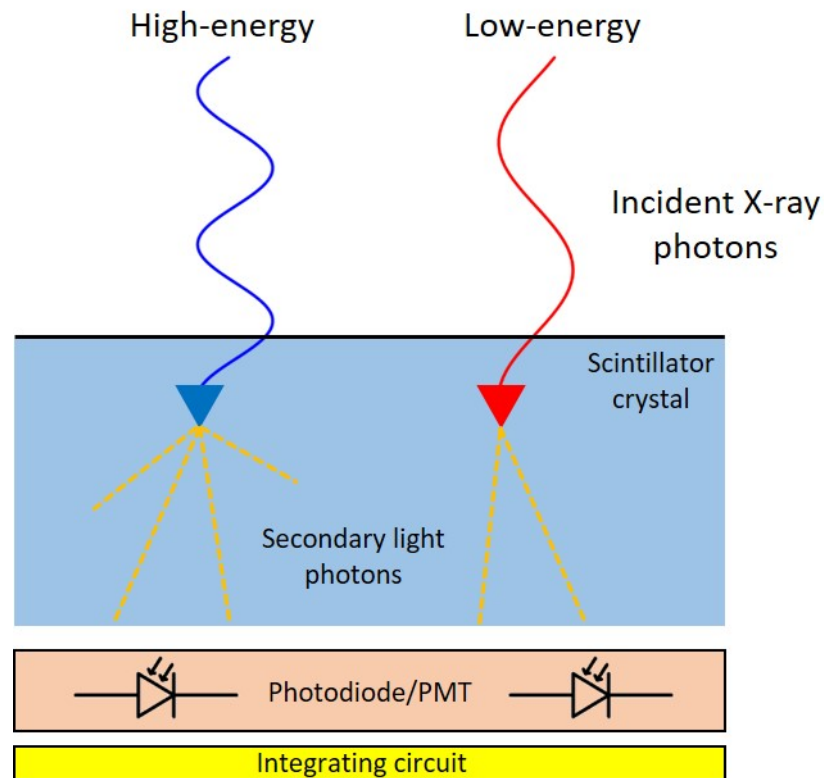


Figure 2.2.1. Layout of a typical indirect scintillation detector. Incident X-ray photons interact with the scintillator crystal, with visible light photons emitted upon electron de-excitation in the crystal. Higher energy X-rays produce a greater number of visible light photons. The light signal is amplified and converted to an electrical output by photodiodes or photo-multiplier tubes (PMTs), where it is finally processed by an electronic integrating circuit.

Alternatively, one may switch to a ‘direct’ detection method, whereby X-ray signal measurement is a one-step process. This is achievable through the replacement of a scintillation crystal and light conversion system, with a semiconductor crystal sensor. The resultant detector design resembles the layout shown in Fig. 2.2.2, consisting of the semiconductor ‘sensor’ chip, and an electronic readout chip. Here, the interaction of incident X-ray pho-

tons with the crystal leads to the generation of electron-hole (e-h) pairs. The interaction varies by sensor material, with predominant interactions including Compton scatter and photoelectric absorption. The e-h pairs form as a charge cloud, which drift to the nearest pixel connection via an externally applied electric field. The direction of the external field will determine which charge carrier is processed by the readout chip, and is typically decided based on the charge mobility properties for the given semiconductor. A higher mobility, corresponding to an increased charge velocity under the applied electric field, is an important factor when considering the optimum semiconductor material [32, 33]. The readout chip is an electronic processing component, most commonly being an application specific integrated circuit (ASIC). The ASIC is a 2D matrix matching the pixel design of the sensor chip. Direct detectors have much higher X-ray electron conversion rates and collection speeds (count rates) than indirect systems, as has been extensively reviewed elsewhere [31]. Other factors including the semiconductor material and thickness also influence the detector properties, including working energy range, detective quantum efficiency (DQE) - output signal-to-noise ratio (SNR) vs. input SNR - and charge effects. These will be explored further when evaluating the transition to semiconductor sensor designs for energy-sensitive systems.

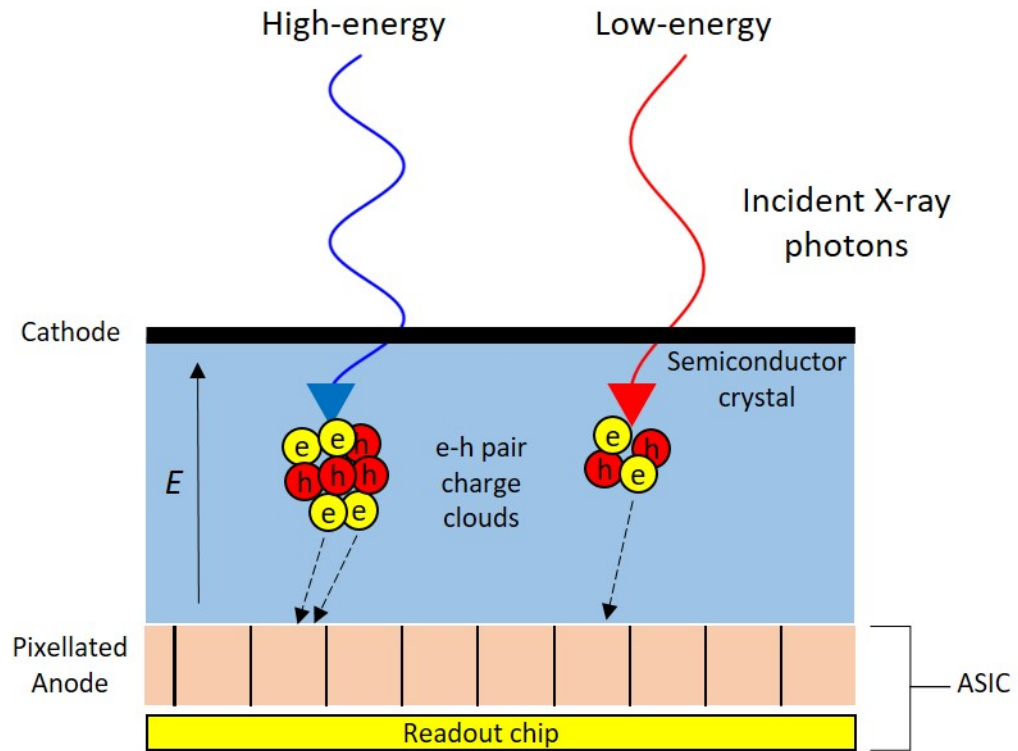


Figure 2.2.2. Layout of a typical direct semiconductor detector. Incident X-ray photons interact with the semiconductor crystal, producing a charge cloud of electron-hole pairs. The free charges drift according to an externally applied electric field (E), creating a measurable current at the nearest pixel electrodes within the readout chip. Higher energy X-rays produce a greater number of e-h pairs, proportional to the incident photon energy. Electronic processing is then performed by the readout chip.

The use of an integration process has a number of limitations. One such issue is the presence of ‘dark current’ noise [34]. This is the intrinsic noise due to leakage current detected as signal in the absence of incident radiation. By integrating all signal collectively, dark current is often included and can result in poorer signal-to-noise ratio (SNR). Further

to this, the signal contributed by each photon is weighted proportional to its energy, thus higher energy photons provide a higher contribution than low-energy photons. This leads to an inaccurate representation of effects such as beam hardening, due to the uneven weighting [35]. Most prominent of all is that, by integrating a number of photons over a given time-frame, only the total effect is measured. As a result, information regarding each individual photon, such as its energy, is lost. Therefore, it is not possible to extract any insight with regards to the materials with which the X-rays have interacted. These issues are overcome with the use of energy-resolving detection systems.

The creation of energy-resolving systems, also referred to as energy-sensitive, energy-discriminating, photon-counting, or spectroscopic, builds on direct detection technology, with the use of a semiconductor crystal connected to a readout chip to process the electric current generated. The key step to extracting the additional energy-based information is the use of sufficiently fast readout circuits, with very low dead time. In an ideal photon-counting system, there is zero dead time, defined as the time after a photon event when no new signal can be recorded as a separate event. At a minimum, this value must be much smaller than the average time between incident photon signals for a given pixel [33]. The other condition of an ideal energy-resolving system is that the charge cloud of e-h pairs is assigned to a single detector pixel [36]. With the aim of developing systems to meet these requirements, two main types of photon-counting detectors (PCDs) were developed, differing in their hardware, spatial, and spectral characteristics. These are referred to here onwards as 'multispectral' and 'hyperspectral'.

2.2.2 Multispectral vs. Hyperspectral detectors

One of the first developments of a pixelated energy-resolving system came directly as a spin-off project from the work at the European Organization for Nuclear Research (CERN): the development of the Medipix detector, a form of multispectral detector [37]. A multispectral detector counts every single photon which arrives at a pixel based on its electrical output generated when energy is deposited. This works by means of amplifying the charge deposited in the detector electrode. Due to the electronic linearity, the initial deposited charge produces a signal with a peak amplitude directly proportional to the incident photon energy, therefore the incident energy may be determined [38]. In the case of multispectral detection, the charge is compared to a set of reference values and each photon is binned into a specific energy threshold window, before the detector increments digitally. The threshold windows concern a set of pre-defined energy ranges, forming the 'channels' within which X-ray photons are stored depending on their detected charge. Therefore, one may tune such a detector to count only photons within a desired range, e.g. 15-20 keV, 20-25 keV, etc. By allowing each pixel to contain a number of these windows, it is possible to perform spectroscopic imaging, particularly suited for materials of known prior composition. Alternatively, these detectors may instead be used as an improved form of dual-energy CT by applying low-energy thresholds, whereby all photons of energies equal to and above the threshold are stored. Thus, this creates independent projection datasets with increasing lower bounds via

individual acquisitions e.g. 10 keV and above, 20 keV and above, etc. This can offer more flexibility yet is considerably more time consuming. Some systems also offer a 'Spectroscopic' mode, whereby the detector groups pixels into clusters, reducing the pixel size, but enabling additional threshold channels to be set, improving the energy resolution at the cost of spatial resolution [39].

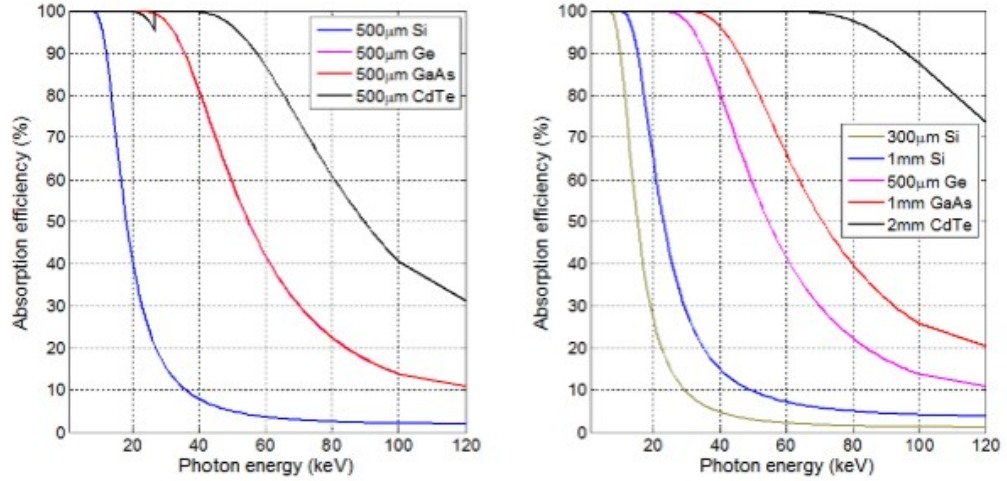


Figure 2.2.3. Measured absorption efficiency (DQE) variation for a range of typical detector semiconductor materials, as a function of energy. (Left) Multiple semiconductor materials compared for the same sensor thickness (curves for Ge and GaAs overlap). (Right) Commonly used thicknesses for commercial X-ray detectors [33].

The family of Medipix detectors has evolved over the years, with a recent review by Bal-labriga summarising the key hardware changes from the first design in 1998, comprising a 64×64 pixel array at a pixel size of $170 \mu\text{m}$, to the Medipix4 currently under production, with a 320×320 matrix and $70 \mu\text{m}$ pixel size [40]. The latest designs offer up to eight threshold windows, with increased thresholds resulting in finer energy ranges. The choice of sensor material for the Medipix range has largely involved the use of silicon, with the Medipix3 constituting a $300 \mu\text{m}$ thick layer. The sensors vary in their energy-resolving properties, based on crystal material, as well as thickness. One such factor is the DQE (absorption efficiency), which for some materials, such as silicon, sees a significant decrease in the hard X-ray range, as illustrated in Fig. 2.2.3. As efficiency falls, so too does the SNR as fewer photons are successfully processed as detected signal. Thus overall image quality is reduced. The DQE also directly influences the working energy range of the detector, as lower DQE leads to degraded spectroscopic performance, meaning silicon-based detectors such as the Medipix is more well-suited to energies of $\leq 50 \text{ keV}$ [41]. In contrast, high-Z sensor materials, such as CdTe, maintain a very high DQE throughout the hard X-ray range, enabling a much greater working energy range up to approximately 200 keV [42].

The use of CdTe has been implemented in the development of hyperspectral detector systems, named as such due to the significant increase in energy channels within which photons are binned. Compared to the multispectral detectors, hyperspectral devices enable very high energy resolution, such that single photons may be binned into hundreds of narrow energy channels. As such, the transition from multispectral to hyperspectral moves the spec-

tral domain from a set of discrete windows, to effectively a continuous energy spectrum, as illustrated in Fig. 2.2.4. One such hyperspectral detector which makes use of the CdTe semiconductor sensor is the High energy X-ray imaging technology (HEXITEC) detector, which was used as the energy-sensitive system within this research project. The current design of the HEXITEC comprises an 80×80 pixel array, with a pixel pitch of $250 \mu\text{m}$ ($200 \mu\text{m}$ pixel size with a $50 \mu\text{m}$ inter-pixel gap), forming a $2 \text{ cm} \times 2 \text{ cm}$ detection area. By using a 1mm CdTe sensor, the detector has a working energy range of 4-200 keV, ideal for the typical beam voltages used for lab-based research [43, 44]. Further details of the detector and its operation characteristics are described in Chapter 3.

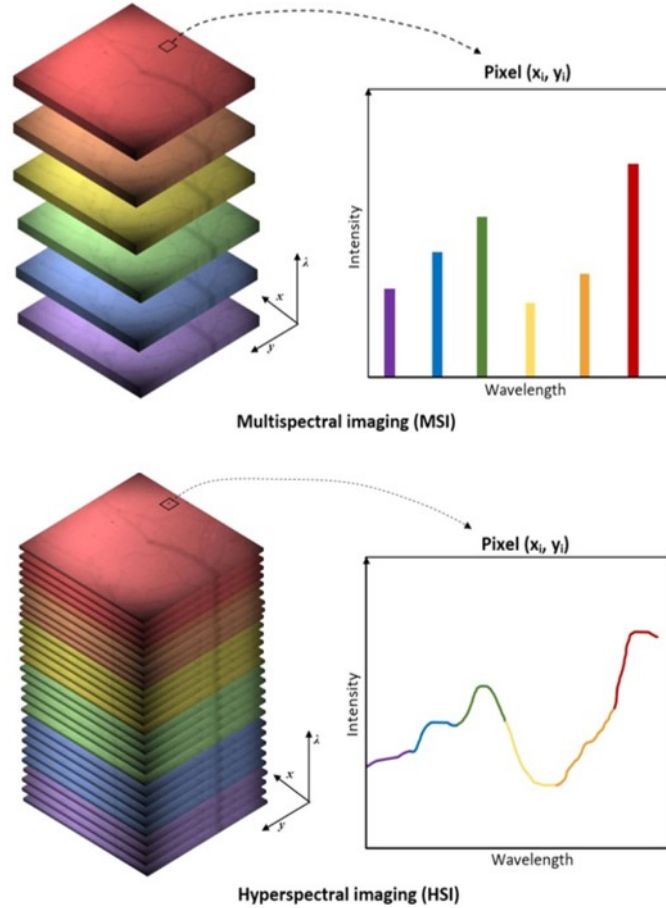


Figure 2.2.4. Representation of the difference in spectral acquisition for multispectral and hyperspectral PCDs. Multispectral imaging detectors (top) record photon energies into one of several discrete energy bands, while hyperspectral detectors (bottom) have hundreds of narrow energy channels with much smaller width to allow for a continuous energy spectrum [45].

There are several benefits to the creation of PCDs. Firstly, there is the ability to eliminate the aforementioned dark current signal, due to the ability to set a 'noise threshold'. That is, by setting a threshold above the noise of the detector electronics, no leakage current will be recorded as a true event. Therefore, in theory no dark current offset image needs to be acquired and corrected as part of the detector calibration [46]. In addition, the architecture of PCDs is such that every photon event is given an equal weighting of one. Combined with the availability of multiple energy threshold windows, this enables optimisation of radiographic imaging by applying energy-dependent weighting to improve SNR, boost contrast in particular features, or improve X-ray dose efficiency [47, 48]. Further, the detectors allow a very high dynamic range, defined as the range of exposures a detector can record be-

tween minimum detection and complete saturation. PCDs are capable of a dynamic range ratio on the order to 10^6 , compared to energy-integrating, flat-panel detectors which offer a dynamic range ratio on the order of 10^3 [38]. Most importantly, however, PCDs offer the ability to quantize the signal generated by incident photons, based on the aforementioned relationship between photon energy and deposited charge, unlocking a layer of spectral information. Therefore, identification of spectral markers, such as absorption edges and fluorescence peaks, becomes achievable by accessing the spectral dimension. The amount of information which may be extracted depends on the characteristics of the detector, as well as its spectral type. For example, one of the key differences between these PCD systems is the energy resolution. Hyperspectral detectors are designed to achieve a much higher resolution in the spectral dimension, with the HEXITEC capable of up to 800 eV at 60 keV [44], making the identification of several spectrally similar markers possible within a single hyperspectral acquisition. In contrast, many multispectral systems operate at a 5-10 keV resolution at a similar X-ray voltage, but can achieve resolution down to ~ 2 keV for soft X-rays below 10 keV, particularly through the use of a Si sensor, as is the case for the Medipix range [33]. Markers may still be identified by a sudden rise/drop in signal intensity due to a K-edge or XRF peak, but precise matching of their energies is not possible. As such, the detectors are better suited for studies where prior knowledge of sample composition is known. This is further reinforced by the need for pre-defined thresholds to set the energy window positions. For multispectral systems however, the reduced energy resolution is often counterbalanced by an improved spatial resolution, as smaller pixel size and larger pixel arrays are possible. Hence, samples with smaller features may be studied without the need for significant magnification through the geometrical setup of the X-ray scan.

Despite the significant advantages offered by energy-resolving X-ray detector devices, there are several challenges associated with the technology of PCDs, and the resultant spectral information they produce.

2.2.3 Challenges with spectroscopic detectors

Two of the most prominent effects related to the electronic processing of incident photon events are: pulse pile-up, and charge sharing [46]. Pulse pile-up describes the phenomena of multiple photon events being recorded during the same read-out cycle of the electronics. As such, rather than being registered as individual events, the current generated by each photon is combined and read out as if it emerged from a single photon. With the energy determination based on the proportional relationship between incident photon energy and charge pulse amplitude, coincident photon events may lead to spectral distortion as the single pulse will record a photon energy equal to the sum of the two incident energies [49]. The impact of pulse pile-up is that image quality is deteriorated, as image noise increases due to fewer individual photon events contributing to the recorded radiograph. In addition, the achievable energy resolution decreases, as an inaccurate spectral photon distribution is measured. The effect is particularly an issue in cases of high photon flux, beyond the count rate of the detector. Low density samples or instances where no sample is present (e.g. flat-

field correction acquisitions) are most strongly affected, as little attenuation of the incident beam takes place [50]. In PCD devices, pulse pile-up is minimised in designs containing smaller pixels, as well as increased readout rates [51]. However, a secondary effect within direct conversion detectors, known as charge sharing, can lead to a trade-off between the two.

Charge sharing emerges due to the creation of charge clouds following interaction of the incident photon with the semiconductor material. As previously discussed, a number of e-h pairs, with a number proportional to the photon energy, are produced, with the desired charge carrier directed towards the nearest pixel element by an external electric field for pulse readout. Depending on the choice of sensor materials, the size of the charge cloud will vary, but will increase in size as it drifts towards the pixel electrodes. Studies by Seller, Veale *et al.* [43, 44] quote that for the 1 mm CdTe sensor used in the HEXITEC detector, the initial cloud starts at approximately 10 μm in size, but can diffuse up to a size of 100-200 μm when under a typical bias voltage applied to the detector (~ 500 V). Other factors including fluorescence and Compton scattering (partial energy transfer from a photon interaction with an electron in an atom) may also have an effect, due to a photon interacting with the semiconductor material and depositing energy at several sites [52, 53]. If the charge cloud is produced near the edges of multiple detector elements, the signal may be induced in several neighbouring pixels, leading to a sharing of the total charge between pixels, as shown in Fig. 2.2.5. In the case of the HEXITEC, with a 50 μm inter-pixel gap between the 200 μm pixels, the charge cloud is of similar size to the gap, and therefore the chances of charge sharing are high. As a result, an example photon event of e.g. 100 keV, may be split between four neighbouring pixels, with pixels recording charge equal to 10, 20, 30, and 40 keV respectively. The distribution of the charge across pixels is unknown, and therefore leads to a random distortion of the spectral profile in each pixel. The effect of the phenomena is typically observed as a low-energy background, with a significant number of incorrectly registered photon events around the soft X-ray energy range (< 10 keV) [44]. The spectral profile can also be further distorted by an additional form of detector 'cross-talk', due to the type of detector interaction with the photons. For silicon detectors, most photons interact by Compton scattering, and small portions of the scattered energy can transition to a new detector element, measuring as a separate, low-energy event. Similarly, in CdTe detectors, where photoelectric absorption is the dominant interaction, part of the deposited photon energy may be released in the form of fluorescence X-rays. If then absorbed by the detector elements, signals are registered at the energy of the fluorescence of the detector materials, such as cadmium and tellurium [49, 54], as well as their related escape peaks (incident photon energy minus the energy of the generated XRF peak) [52]. As such, each recorded signal fails to correctly represent the energy of the incident photon. For characteristic peaks, these may interfere with the ability to identify other spectral markers within the same energy region.

A number of routines have been implemented into spectroscopic systems to correct for charge sharing. Two of the most common correction routines are illustrated in Fig. 2.2.6.

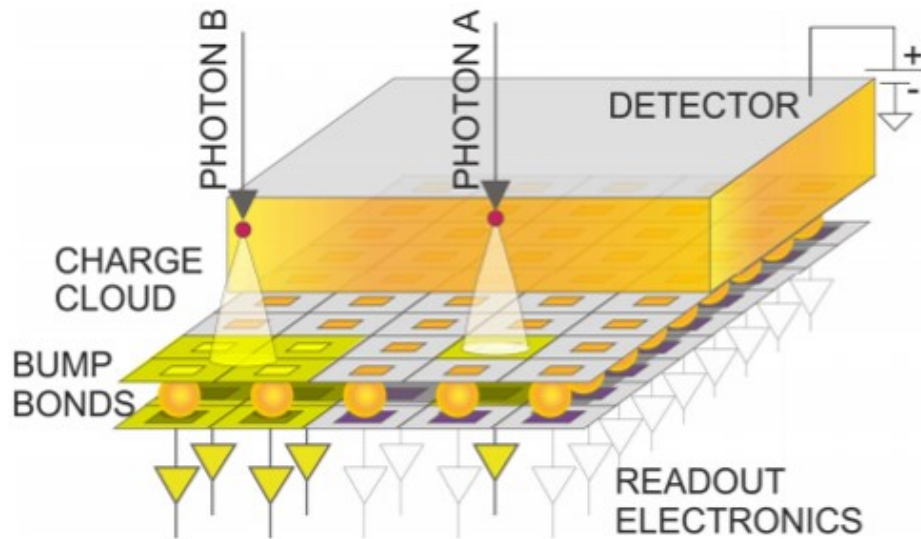


Figure 2.2.5. Illustration of the charge sharing effect encountered in hybrid pixel detectors. While the charge cloud of photon A diffuses into only one pixel, photon B has a charge cloud that interacts with a group of neighbouring pixels, distributing its charge [55].

First is the use of a 'Charge Summing Mode' (CSM). Here, pixels are grouped in clusters of e.g. 2×2 , 3×3 , etc. When a charge is deposited within a cluster, the relative signal measured in each of the neighbouring pixels is evaluated, and the total charge is allocated to the pixel with the largest initial charge deposit. This way, all of the charge due to the incident photon is maintained, and recorded as a single event for a single pixel. However, in the case of the Medipix detectors, this comes at the cost of spatial resolution, as the pixel cluster signal is combined, summing additional noise in quadrature along with the incident photon signal [56]. Further, summing over a defined set of pixels cannot guarantee that the full charge will be captured, leading to some spectral distortion. An alternative correction method is the use of a 'Discrimination' routine. That is, for any photon events which span multiple pixels, the signals are deleted and the events are not recorded, removing all cases of charge sharing. For the HEXITEC, this is implemented by evaluating each frame of data over sets of 3×3 or 5×5 pixel regions, where multiple neighbouring pixels measure a charge over the low-energy threshold [44]. The correction may be applied during acquisition, or performed as a post-processing step to the raw data. An obvious downside to such a correction lies in that a proportion of the incident X-ray flux is being thrown away, which is particularly significant in cases of high charge sharing occupancy. The work by Veale *et al.* [44] notes that for cases of high X-ray flux, the ability to fully correct for charge sharing may not be possible due to the high occupancy, and it is most effective in cases where occupancy does not exceed 11% in a single frame of data. Alternatively, X-ray flux may be reduced to limit the effect, however an increase in exposure time may be required as a result to achieve the desired levels of SNR for image quality purposes.

Due to the issue of increased signal processing of single photon events, maximum count rate is also limited, particularly in the case of the HEXITEC, where a limit of 0.001 Mcps/pixel is achievable, without degradation in spectroscopic performance [44]. This is

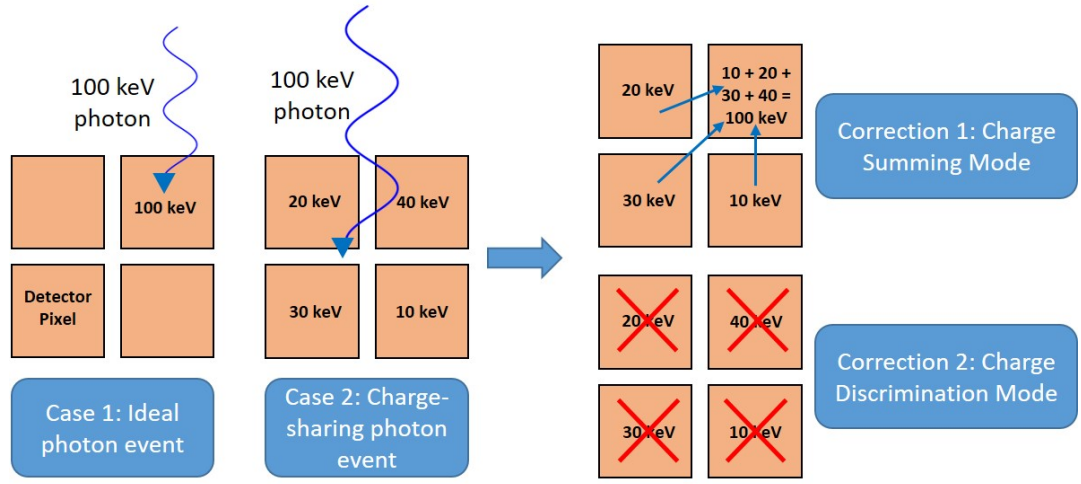


Figure 2.2.6. Example case of how charge sharing corrections may be applied in spectroscopic data. (Left) An ideal case where a single photon event is fully recorded within a single detector pixel. (Middle) A charge-sharing event where a photon is incident between neighbouring elements, and the charge is shared unevenly. The event may be corrected using charge summing mode (Upper Right), where all charge is grouped and allocated to the highest charge-containing pixel in the cluster, or charge discrimination mode (Lower Right), where the entire event and all of its deposited charge is deleted.

significantly below the rates possible with multispectral systems [33], with both far below the rates of energy-integrating detectors. This is due to the increased readout requirements for binning of photon events into narrow energy channels. The result is that, for example, a 60s exposure time per projection with the HEXITEC would limit a 200 channel spectrum to only a few hundred counts per energy bin [43, 44]. Therefore, when taking statistical noise into account, extracting the desirable information from every individual bin can be complex. It is possible to improve the channel-by-channel signal by increasing the overall exposure, however there are instances (such as medical imaging) whereby there are upper limits on X-ray dose. As such, each energy channel can be very noisy, to the point where characteristic signals may be hidden beneath the noise, becoming difficult to extract in post-processing and analysis. It has previously been shown that the SNR for K-edge imaging is dependent on the atomic number of the element under observation [50], as well as object diameter and X-ray tube voltage. Thus preliminary tests may be taken to optimise the system for the sample of interest. Despite this, limitations in SNR still exist, and as such there is reliance on the reconstruction and post-processing steps to extract element-specific information even in the absence of high SNR data.

2.3 Spectral image reconstruction

While crucial to ensure the correct detector system is chosen and optimised for the materials and research fields of interest, equally important is the ability to efficiently handle and analyse the data to extract the desired information. As energy-resolving detectors have been developed over time, so too have the methods in which to collect, reconstruct, and maximise the usage of this additional, spectral dimension. In the following section, an introduction to reconstruction in the context of X-ray CT imaging is provided, highlighting the types of reconstruction algorithm available. The transition to reconstruction algorithms for

spectral datasets is then discussed, with an evaluation of existing methods, noting some example applications and any limitations.

2.3.1 Intro to X-ray CT reconstruction

The aim of X-ray CT reconstruction is the creation of a representative 3D volume of the original object, using the set of 2D projection data taken of the object over a range of rotation angles. As shown in Equation 2.4, the intensity of an X-ray beam may be directly described by the Beer-Lambert law, as the X-ray passes through an inhomogeneous material of varying attenuation. Therefore, for a tomographic scan, the attenuation as a function of position may be determined in theory by measuring a large number of intensity (transmission) values at each rotation angle, with each 2D image representing a series of line integrals through the 3D volume being scanned.

As mentioned previously in Section 2.1.2, however, an assumption is typically made in that the X-ray beam is monochromatic, and therefore commonly Equation 2.2 is used. In the case of synchrotron radiation, the use of monochromatic X-rays is easily achievable through the use of a monochromator, isolating the beam to the desired single energy, with no concerns of increased scan time due to the significantly higher flux compared to laboratory X-ray tubes. Outside of synchrotron facilities, polychromatic beams are commonplace, and therefore the previously described issues of beam hardening emerge. Given that in most cases beam hardening may be corrected for prior to or following image acquisition, this issue is typically ignored and the monochromatic Beer-Lambert law is used. In this scenario, a simple rearrangement of Equation 2.2 provides the calculation of the absorption, or projection, values, via a negative-log transformation,

$$-\log \frac{I}{I_0} = \int_0^l \mu(x) dx \quad (2.6)$$

where the equation is equivalent to the Radon transform, first introduced in 1917, showing that the image may be defined as a series of line integrals through an object for all ray paths, across many acquisition angles [57]. The additional division of $\frac{I}{I_0}$ represents the 'flatfield' correction of the image, whereby variations in pixel sensitivity and non-uniformity of the detector are corrected for, eliminating fixed pattern noise from the images [58]. The resulting output of the Radon transform over a series of rotation angles produces a 'sinogram', with an example case shown in Fig. 2.3.1, where a Shepp-Logan phantom image is used [59], simulating an X-ray CT acquisition. Therefore, the sinogram provides a graphical representation of the Radon transform of the imaged object. In modern CT systems, the sinogram occupies a 3D space, with one sinogram for each row of detector pixels.

With the Radon transform describing the distribution in attenuation for each angular projection and detector pixel position, it logically follows that in order to return a 2D image of the original object, an inverse of the Radon transform must be performed. This forms the basis

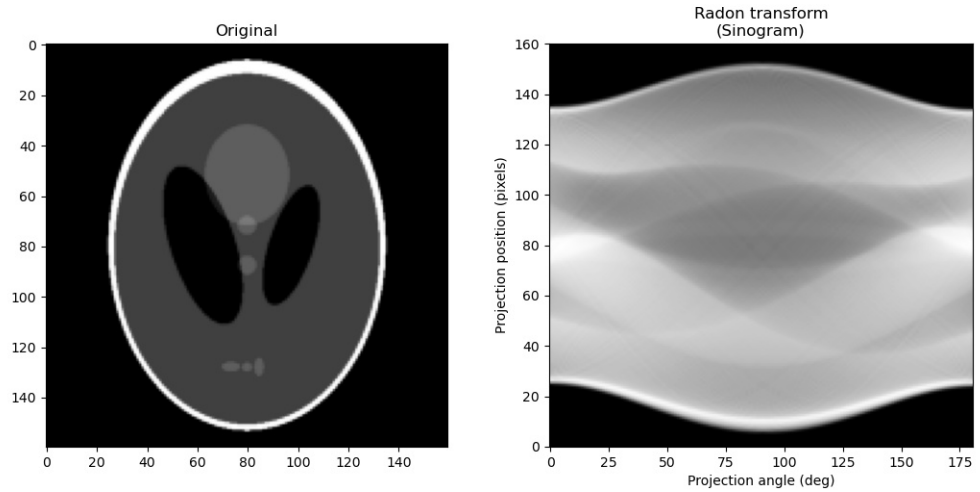


Figure 2.3.1. Example of a Radon transform. Using the example of a Shepp-Logan simulated phantom (left), a sinogram is formed by acquiring 180 projections over a range of rotation angles. By performing a Radon transform, a sinogram is produced (right), displayed in projection space. Created using the *skimage* package in Python [60].

of X-ray CT reconstruction.

The most simplistic case of X-ray CT image reconstruction applies in the case of a 2D parallel beam geometry, as was used for many early X-ray CT scanners, and is found in the majority of synchrotron radiation sources. Here, each X-ray beam moves linearly, parallel to the X-ray detector, with no geometric effects such as magnification taking place. In this scenario, only projections over 180° are required, as the X-rays capture all necessary information to reconstruct the original image, with the following 180° only producing exact copies of the original projections. Below, a breakdown is made of the types of reconstruction algorithm available in X-ray CT.

2.3.2 Analytic reconstruction - filtered back-projection

For X-ray CT image reconstruction, there are two main types of reconstruction routine: analytic and iterative. For parallel beam geometries, the most popular reconstruction method utilised is the analytic method of Filtered Back-Projection (FBP). For many years, FBP has been the standard routine for X-ray CT image reconstruction, largely due to its simplicity and low computational intensity. The application of FBP contains two key steps: 'back-projection' of data across image space for each rotation angle, and the application of a filter to improve reconstructed image sharpness. In the back-projection step, the measured detector values are applied back along the detector ray path, assigning an average attenuation value to each pixel on the path [61]. In this case the simplistic case of parallel beam geometry is assumed, such that the back-projected operation takes place over the same ray paths as those in the original projection step. By applying the method at each projection angle, and summing all allocated attenuation values, a back-projected image may be formed. An example of the back-projection process, without the addition of the 'filter' step, is shown in Fig. 2.3.2. As observed in the final image (Fig. 2.3.2f) even after a sufficient number of

attenuation profiles (720) are back-projected, the final reconstructed image contains significant blurring. The reason for this may be explained by the Fourier slice theorem (FST), which describes how for a set of projection angles, the distribution of spatial frequencies of the object may be fully described in the Fourier domain, through the application of a Fourier transform at each angle. Greater detail may be found elsewhere on the concept of the FST, and how the method of back-projection may be mathematically derived from it [62]. In short, low spatial frequency components of an image, which describe the bulk image and smooth regions, are over-represented, while higher spatial frequencies, which correspond to the details and sharp edges, are under-represented.

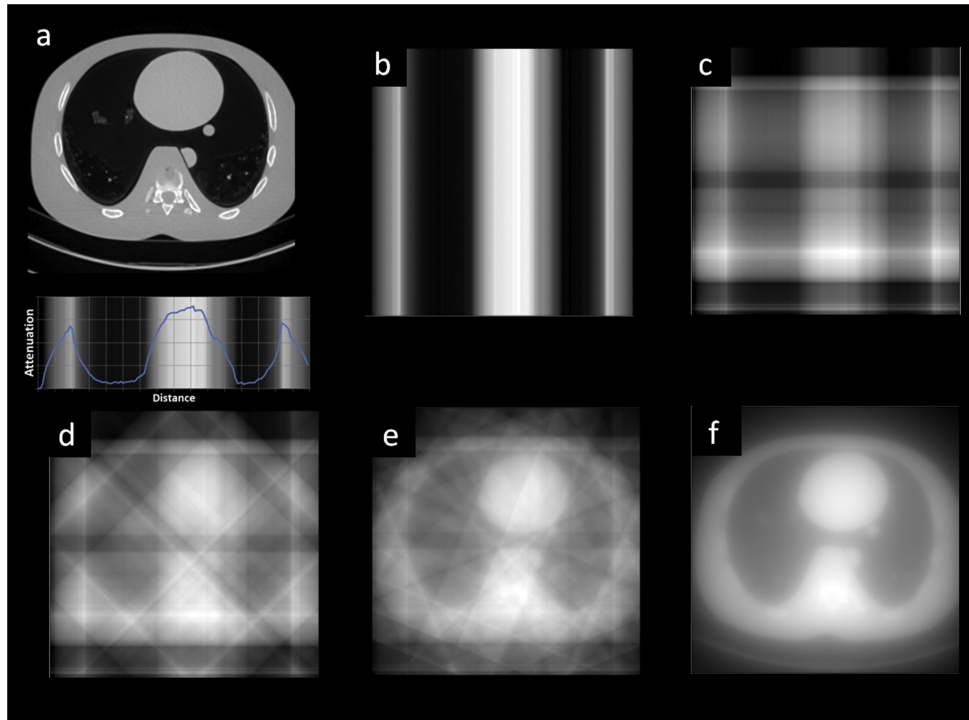


Figure 2.3.2. Back-projection of a chest phantom object (a). The graphics show back-projection of profiles acquired from 1 (b), 2 (c), 4 (d), 8 (e), and 720 (f) angular profiles. The final image shows significant blurring, highlighting the need for a filtration step to improve the reconstructed image sharpness [61].

By applying a spatial frequency filter to the projection data, prior to back-projection, the blurring effect may be minimised, and an improved reconstructed image quality is achieved. A common filter of choice is the ramp filter, aimed at suppressing low spatial frequencies, increasing the relative contribution of high spatial frequencies [63]. The result of applying a filtration step is shown in Fig. 2.3.3 for the same phantom object as in Fig. 2.3.2, with a clear improvement in image sharpness and feature contrast.

As explained previously, FBP describes the 'ideal' case of parallel-beam geometry. Adaptations of the algorithm have enabled equivalent reconstruction routines to be applied in other geometries, including the cone-beam X-ray sources typically found in laboratory set-ups. In this case, the Feldkamp-Davis-Kress (FDK) algorithm is the approximate cone-beam equivalent to FBP, and is the conventional method used for the majority of X-ray CT reconstruction [64]. For all forms of FBP reconstruction, the main advantage lies in its simplicity [65]. In most cases, no parameters require adjustment or optimisation, requiring a matter of minutes to fully reconstruct a 3D volume. Many commercial systems have built the FDK

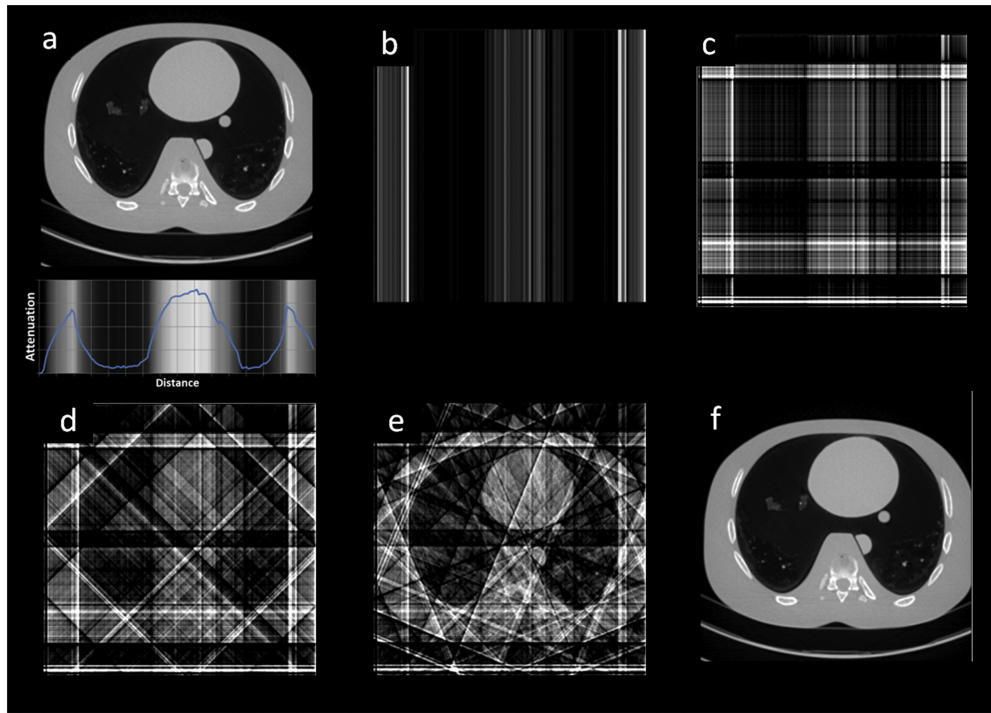


Figure 2.3.3. Filtered back-projection of the same chest phantom object as in Fig. 2.3.2. The graphics show filtered back-projection of profiles acquired from 1 (b), 2 (c), 4 (d), 8 (e), and 720 (f) angular profiles. The application of a filter removes the blurring, improves image sharpness, and provides a reconstructed image much closer to the original object in (a) [61].

method into their software as the default reconstruction tool [66], offering it as an easily accessible and robust solution which requires very low computing power.

However, analytic routines like FDK are also severely limited in their capacity, and struggle outside of ideal imaging conditions. For example, these methods require 'complete' data, with a large number of angular projections, to maintain high image quality following reconstruction. In the case of an undersampled (low projection dataset), 'aliasing' artefacts can emerge, reducing image quality [2]. Further, the full angular range is required, with FDK incapable of dealing with limited angle datasets without resulting in severe image distortion. The application of a filter in FDK also introduces issues particularly in the case of noisy data. For clinical systems, where dose considerations or time constraints may require faster scans, the SNR may be limited, and while a ramp filter may reduce blur in the reconstruction process, it is also known to propagate and enhance image noise present in the raw data signal, resulting in a "mottled" appearance in the reconstructed volume [61, 67]. In addition, FBP methods are very inflexible in their design, which while adding to their simplicity and convenience, makes them insufficient for more complex imaging geometries or scan routines. These algorithms offer no ability to exploit prior knowledge of the imaging, which otherwise may be used to reduce image artefacts.

While FBP-based methods have been commonplace in X-ray CT reconstruction throughout its technological advancement over the decades, so too has the creation of iterative reconstruction algorithms, aimed at providing improved image quality, and the flexibility to accommodate complex imaging geometries, limited angular ranges, and more.

2.3.3 Iterative reconstruction algorithms

Some of the first reconstruction algorithms discussed for X-ray imaging were those implementing iterative routines, emerging even before the development of the first clinical CT scanner [68]. Due to their increased computational requirements, they were not applicable to most instances of X-ray imaging at the time, and therefore simpler alternatives, such as that of FBP, were introduced and became the standard. Alongside the rapid technological advancements in CT imaging over recent years, significant theoretical progress has also been made in the field of tomographic reconstruction. A wide range of advanced, flexible iterative algorithms are now available, aimed at overcoming the challenges faced by analytic methods, as well as offering additional advantages, at the cost of increased computational complexity. In all cases, the algorithms aim to solve the 'inverse problem'.

To understand the iterative approach to X-ray CT reconstruction, the imaging process may be viewed as a linear system,

$$Ku = b \quad (2.7)$$

where the measurements recorded may be defined by the physical conditions of the imaging system, and the given parameters of the system. For X-ray CT, K is the imaging operator, which can vary with geometry, experimental set-up, modality etc., u contains the image property values, and b provides the projections, or measured data. Therefore, given the conditions of the imaging system are known, and a set of recorded projections have been acquired, the aim is to solve the inverse problem to recover the parameters of the original image, such that

$$u = K^{-1}b. \quad (2.8)$$

In an ideal system, Equation 2.8 may be easily solved and the original image values reproduced. However, in a real imaging system, factors such as variable noise in b , assumptions within the model, the fact that K is not typically a square matrix, and other errors mean no direct inversion is possible. Therefore, given no exact solution, the standard approach is to find a solution to u such that Ku gives the closest possible result to b . This is referred to as the 'least-squares minimisation' problem:

$$\min_u \|Ku - b\|_2^2 = \sum_i ((Ku)_i - b_i)^2. \quad (2.9)$$

In order to find the best possible value for u , an iterative method may be employed, whereby an initial estimate value is chosen, the difference between Ku (computed projection data) and b (measured projection data) is determined, and the value of u is then updated, beginning the next iteration. The process is repeated until a convergence is found at the optimum

value [2, 69]. Below, a few of the most popular iterative algorithms are described, with their basic principles. Greater mathematical background to each algorithm may be found elsewhere [70].

One of the earliest iterative reconstruction routines implemented in image reconstruction was that of the Algebraic Reconstruction Technique, typically referred to as ART. Though the concept has existed in numerical linear algebra since the 1930s [71], its first implementation in X-ray CT was demonstrated in 1970 [68]. The algorithm aimed to solve the system of linear equations for each X-ray image (see Equation 2.7) over the series of angular projections. With each iteration of ART, an approximate solution of the system was calculated, before evaluating the difference between computed and measured terms for each projection, and applying this as a correction to the next iteration, until a convergence is met. One key advantage of the ART algorithm, and many of the following iterative methods developed thereafter, was the ability to incorporate prior knowledge. For example, given the knowledge that any image was non-negative in its solution, ART enabled any calculated solutions to immediately set negative values to zero, increasing the speed of convergence to a solution [65]. For ART, typically a relaxation parameter was applied to the correction, which was found to yield improved SNR. However, the parameter also slowed convergence, increasing computation time.

The computational cost of ART was its main disadvantage, due to the application of the method on a single projection basis. That is, each correction was applied to a single projection at a time, therefore iterating on a step-by-step basis. As such, faster algorithms were developed which were capable of updating all data across all projections simultaneously, such as the Simultaneous Iterative Reconstruction Technique (SIRT), first developed in 1972 [72]. The method allowed an average correction to be determined for each single voxel by evaluating all projections and accumulating the required changes first, before applying the correction at the end of the iteration. SIRT provided improved reconstructed image quality over ART, though required a long time in order to achieve convergence [70]. For both ART and SIRT, the ability of these algorithms to reach an optimised solution is also largely set by the user, in the form of the number of iterations. While improved SNR may often be achieved over methods like FDK, the solutions are typically found to smooth towards an ideal solution, before divergence and poorer image quality beyond a certain number of iterations. Given that the optimum number of iterations is often unknown, increased computational time may be required to determine the smoothest image reconstruction.

One such algorithm aimed at reaching a faster convergence, despite no additional stopping criterion, is that of the Conjugate Gradient Least Squares (CGLS) algorithm, which uses the results from all previous iterations to aid the next step of the algorithm [73]. CGLS typically converges to an optimum solution in much fewer iterations than ART or SIRT [74], however additional constraints such as non-negativity cannot be included to further improve the iterative process [75].

Both in the case of analytic and iterative algorithms, the application to conventional X-ray CT imaging aims to reconstruct a matrix of spatial data built over a series of 2D projections taken over a given angular range, providing a 3D matrix of raw data profiles. In order to expand such methods into spectral reconstruction routines, the additional dimension of energy-based information must be taken into account. As will be discussed below, the step is not particularly complex, but brings with it issues including computational cost and the manner of how to treat a spectral dimension compared to the spatial dimensions.

2.3.4 Extending to spectral reconstruction

For multispectral or hyperspectral imaging, the linear systems in XCT are extended into the spectral dimension. As the dataset is split into a number of energy channels (hundreds in the case of hyperspectral CT) the inversion problem becomes extended. With multiple ($N > 2$) energy channels registering data, one may acquire a very large set (N) of these linear equations,

$$K_i u_i = b_i, i = 1, \dots, N. \quad (2.10)$$

In essence, the minimisation problem to be solved is the same, but must now be solved for every energy channel, increasing the computational cost. Methods like FDK may simply be extended to reconstruct spectral data, by treating each energy channel as a separate dataset, and reconstructing on a channel-by-channel basis. However, with the flexibility of iterative algorithms, it is possible to exploit the multichannel nature of spectral datasets to improve the final reconstruction. Multichannel or multi-modal reconstruction methods provide a more connected route for reconstructing images with multiple material phases, due to the fact that these algorithms do not treat each channel as an individual, but instead uses them as a form of ‘prior knowledge’ or reference. These methods base their principles around structural or spectral similarity between the different datasets (whether it be neighbouring energy channels or entirely different imaging modalities). Therefore, if one can assume or have knowledge on the relation between the u_i , then this may be exploited to help solve each individual inversion problem. For example, multi-modality reconstruction methods have been utilised for combined positron emission tomography-magnetic resonance imaging (PET-MRI) data acquisitions [76, 77]. In these cases, structural similarities in the functional and anatomical data collected mean that a joint reconstruction may be applied, for example based on similar edge positions or orientations.

There are two main methods to approach the joint reconstruction problem. First, one may acquire *a priori* knowledge of some of u_i to serve as a reference point for the reconstruction of the other channels or modalities. In a study of hyperspectral image reconstruction, one study adopts a channel-wise iterative method, whereby the reconstructed image produced in the previous energy channel is used as the starting (reference) vector for the next [78]. This is a deterministic approach, as the reference is automatically known and selected. Fig. 2.3.4

illustrates an example of applying such an algorithm to spectral data, acquired when imaging a lattice carbon structure containing palladium metal. Included are results from three methods of reconstruction. The first uses the conventional method of FDK, while the other two methods are based on the SIRT algorithm, described above in Section 2.3.3. On top of simply using the standard SIRT routine, the study evaluates a ‘channel-linked’ SIRT algorithm, where neighbouring channels are used to determine the reference estimate. As well as the improved spatial smoothing observed for the channel-linked SIRT reconstruction, a graph is included to highlight the ‘energy smoothing’ achieved as well. It is clear that the spectral noise is significantly reduced across energy channels compared to the conventional FDK algorithm. Due to the high degree of spectral similarity from one channel to the next, these ‘linked’ reconstruction methods work well for spectral data.

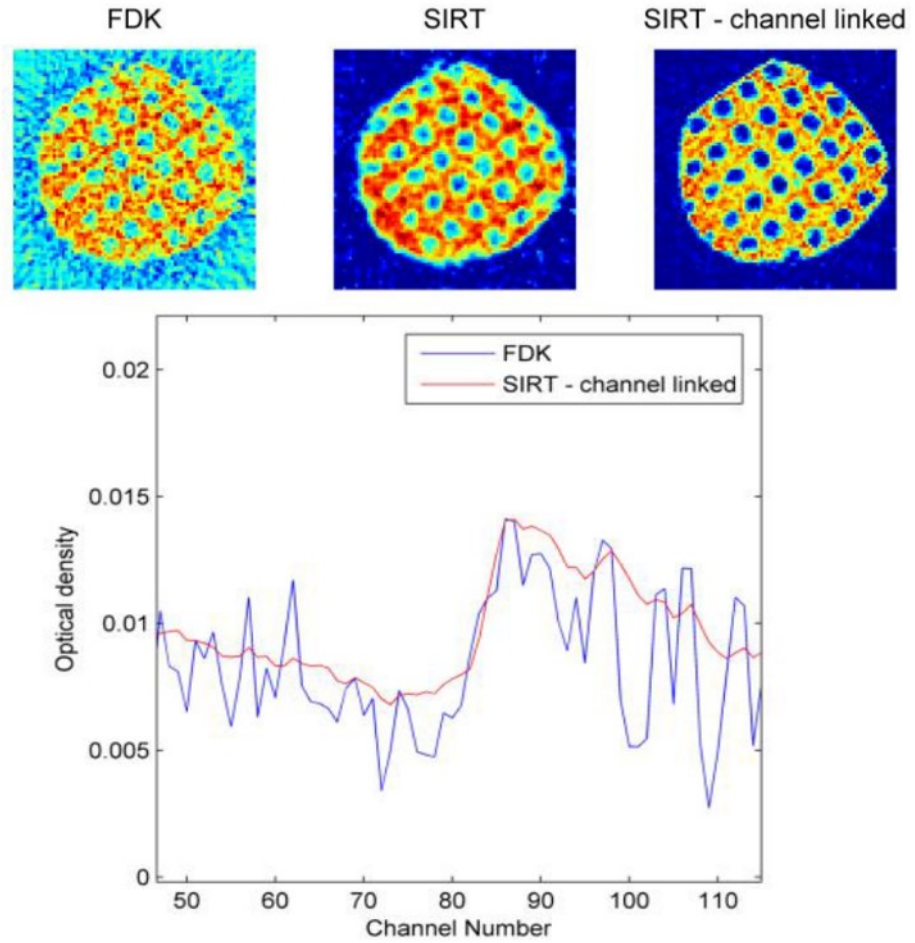


Figure 2.3.4. Test results for various reconstruction algorithms applied to spectral data of a palladium-filled carbon lattice. (Top) From left to right, reconstructions using FDK, SIRT and channel-linked SIRT methods. The iterative methods show significant spatial smoothing over FDK, with the channel-linked SIRT method the best for structural definition. (Bottom) Reconstructed spectra from a voxel where palladium signal was captured. The spectral noise is significantly lower for channel-linked SIRT compared to FDK, enabling a much clearer identification of the palladium K-edge (channel number 83) [78].

An alternative approach is to reconstruct each energy channel simultaneously, using each other to support the reconstruction process. As such, it is possible to produce all image property values, u_i across all channels. One study by Kazantsev *et al.* generalises this method for the case of hyperspectral imaging, where an arbitrarily large number of energy channels may be used [79]. Here, an iterative reconstruction algorithm is used, with all

channels reconstructed jointly. A suitable channel is taken from the previous iteration of the reconstruction to be used as a reference point for the next. The method aims to obtain reference channels with preference shown towards those with a high SNR. This condition can result in better image quality in the final reconstructions. Further, the work introduces the concept of combining the iterative algorithm with a 'regularising' term to improve overall image quality.

2.3.5 Regularisation of iterative algorithms

Due to the higher levels of noise associated with spectral datasets, the majority of 4D reconstruction algorithms involve the use of a 'regularised' iterative routine. Regularisation refers to an additional parameter which can be used to enforce regularity of the model solutions. For example, a regularising term may be used to force image sparsity (similarity) or smoothness, or alternatively as a means to improve image sharpness and edge definition. The choice and value of the regularisation parameter often results in a trade-off between noise minimisation and optimised data fitting.

One of the most popular and common types of regularisation is based on the Total Variation (TV) method. TV is a useful technique in image processing due to its noise removal and edge-preserving capabilities. TV measures the variation of an image by means of calculating the absolute gradient of the overall image signal [80]. This factor can be used as an additional regularising term in a non-linear, least-squares minimisation problem, such that the iterative routine becomes

$$\min_u \|Ku - b\|_2^2 + \lambda \cdot TV(u) \quad (2.11)$$

where λ is a weighting parameter acting on the TV applied to u . As explained in Section 2.3.3, the minimisation problem compares the pixel signal, u with the acquired projection data, b once the signal has been forward-projected by operator K . Hence the aim is to minimise any variance between the two terms in the least-squares problem in order to best fit the data. The regulariser will act to force a given condition on this solution. For any regularising term, a weighting parameter is included to enable precise control of the regulariser's impact. The size of λ has a significant effect on the overall minimisation result. The effects of varying the regularisation parameter are illustrated in Fig. 2.3.5 for a sample photo. By selecting a high value of λ , the influence of the minimisation is small compared to the regulariser, resulting in large amounts of noise removal (spatial smoothing) at the cost of correctly modelling the data fit. Conversely a low λ results in extensive noise but maintains edge-preservation.

For the case of multi-channel regularisation, one can use a channel-wise TV, whereby the sum of the TV norm is taken for each channel. The use of TV has previously been shown to be efficient at image denoising, while also effective at coping with undersampled CT data [82]. TV regularisation is most ideally suited to piece-wise structures, where sharp edge

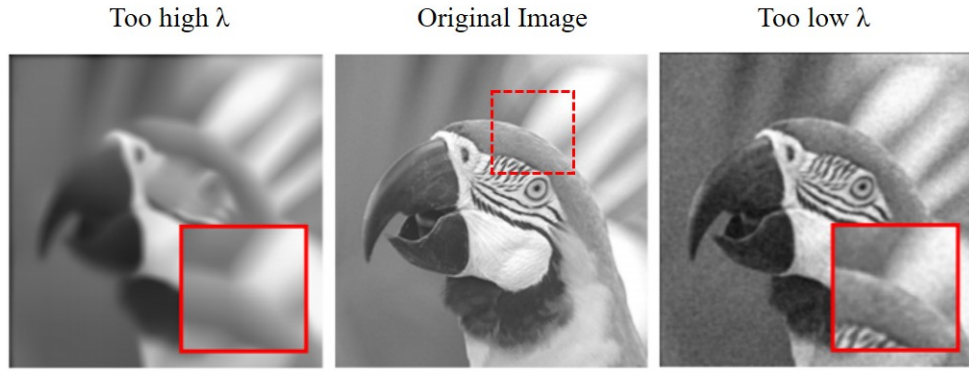


Figure 2.3.5. Illustration of the effect of varying the regularisation parameter using TV regularisation. The original image (centre) is shown, with a region of interest (dashed box) highlighted for magnified evaluation. Effects of a high value (left) and a low value regularisation parameter (right) are shown, illustrating the respective spatial smoothing and noise removal of the regularisation. Adapted from [81].

boundaries exist. As a consequence, however, TV is known to introduce 'staircasing' artefacts, such that in the process of denoising images, the resulting reconstruction can appear 'blocky', particularly in smooth areas that also contain slanted regions [83]. This introduces an issue with hyperspectral reconstructions, where the attenuation profiles of the spectral dimension often include slants or discontinuities due to absorption edges. As such, a number of modified versions of TV have been developed to overcome such deficiencies.

An adaptation to the TV regulariser is the use of Total Nuclear Variation (TNV), which promotes reconstructions that contain common structures and similar edge locations, and therefore works well for multichannel images, where structural similarity is expected across energy channels [84].

In the aforementioned work by Kazantsev, the channel-wise TV and TNV methods are directly compared for a simulated hyperspectral reconstruction of a multi-phase phantom [79]. The results of the reconstructions for the four-phase phantom (containing quartz, pyrite, galena and gold) are shown in Fig. 2.3.6. It becomes clear that TNV offers greatly improved spatial resolution and noise reduction over the conventional channel-wise TV method. Errors are significantly reduced, with much cleaner feature segmentation, though some misclassification still occurs. This in part is due to the fact that both TV and TNV suffer from a loss of contrast, particularly for small features which the methods struggle to preserve [83, 85]. Further, despite its improved performance, TNV only enables a single regularisation parameter to be simultaneously applied to both the spatial and spectral dimensions.

A novel version of TV which may cope with the spectral profiles observed in hyperspectral X-ray CT is that of the Total Generalised Variation (TGV). As described in its name, TGV offers a less restrictive approach to image reconstruction. The use of TGV has been shown to be effective in image denoising, while capable of promoting both sharp edge features as well as gradual changes in image intensity across smoother regions. The method achieves this by taking into account higher order derivatives of the image data [86]. Further, TGV avoids the issue of staircasing artefacts compared to TV, as highlighted on a test

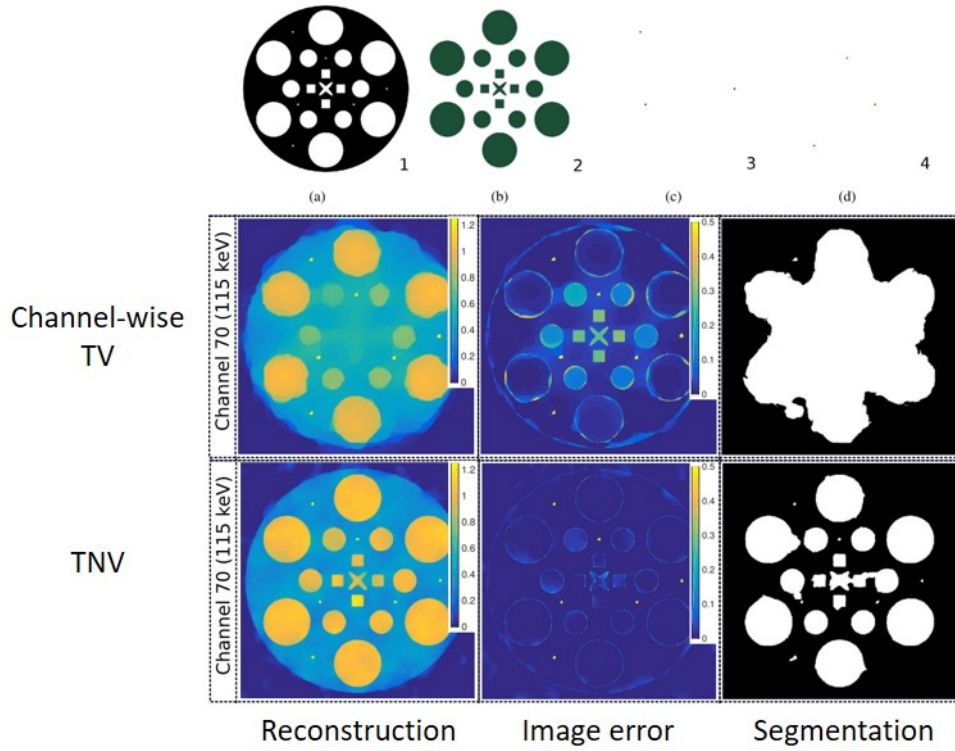


Figure 2.3.6. (Top) Design of the custom phantom, containing (a) quartz, (b) pyrite (c) galena and (d) gold. (Bottom) Columns showing the reconstruction, error and segmentation for a single channel (70) using two methods: channel-wise TV (Upper Row) and TNV (Lower Row). Reduced image errors and improved feature segmentation are achieved for the TNV method over channel-wise TV, where the pyrite central regions were poorly segmented with excessive smoothing. Adapted from [79].

image in Fig. 2.3.7, and has been observed to work well in the case of reconstructing 'natural' looking images, such as those found in biology or clinical CT, with a demonstration of this shown for Magnetic Resonance Imaging (MRI) [87]. In the case of spectral imaging, TGV also offers the flexibility of application to a single dimension, such that regularisation may be optimised separately to achieve improved spatial and spectral image quality.

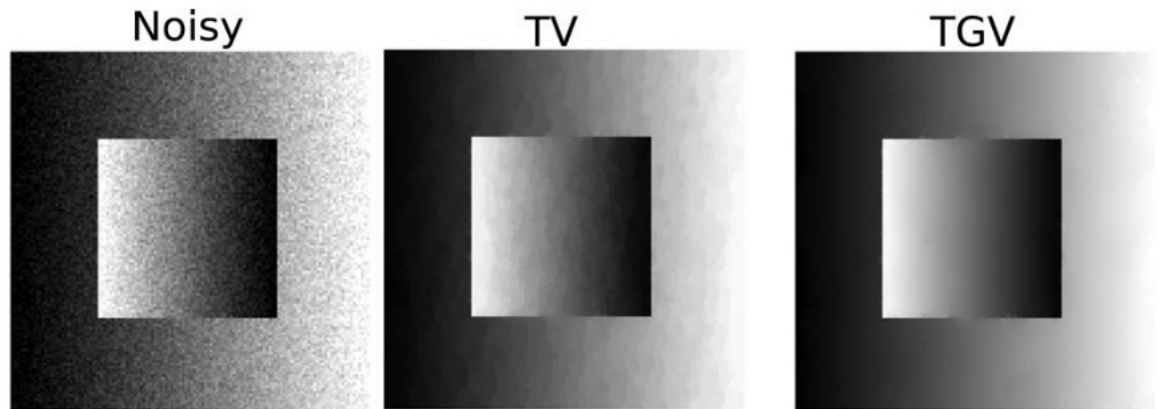


Figure 2.3.7. Comparison of the denoising effects of TV and TGV based on an artificial test image containing a 'ramp' function on greyscale intensity. While both regularisers achieve strong denoising, the presence of staircasing artefacts are clear in TV, while such artefacts are eliminated completely using TGV [87].

For hyperspectral imaging, several factors must be taken into account when trying to achieve the optimum reconstruction:

- The aforementioned limits in detector count rate mean noisy datasets are common, therefore strong denoising is required for both the spatial and spectral domains.
- Spatial resolution is poor, which can result in some image features spanning only a few pixels. Hence the ability to maintain strong image contrast is crucial.
- The high spectral resolution through the availability of hundreds of energy channels brings with it large datasets, thus increased complexity in reconstruction algorithms also brings about significantly larger computational cost.
- Often the needs of the spatial and spectral dimensions vary in the level of smoothing and edge preservation required, so a multi-modal approach may be required to satisfy each dimension separately.

Taking into account all requirements above, specific designs of iterative reconstruction algorithm are needed to deal with the issues encountered in hyperspectral CT. To date, very few research studies have developed algorithms catered to the needs of hyperspectral imaging, with most studies focused on simulation investigations, or case studies involving multispectral (few-channel) datasets [79, 84, 88, 89]. Other investigations meanwhile have focused on alternative imaging modalities, such as Positron Emission Tomography or MRI [76, 77, 87]. Some work has explored the application of a multi-regularising approach, to tackle the challenge of optimising a combined spatio-spectral reconstruction, and demonstrates its effectiveness over FBP for up to 12 energy channels and low projection datasets [90]. However, such studies are still limited to simulated phantoms, while also using a simpler parallel beam geometry. The case studies described in this thesis, Chapters 4 and 5, aim to lay the foundations for advanced hyperspectral cone-beam reconstruction algorithms, through direct testing on physical experimental samples.

2.4 Imaging modalities of energy-sensitive X-ray CT

The development of hybrid pixel detectors over recent years has had dramatic impacts on the field of spectroscopic imaging. Due to the chemical and crystallographic insight achievable, wide-ranging applications have become available, across a number of research fields. Different imaging modalities have been developed to explore samples of varying feature size and composition. As detector design has improved and higher intensity X-ray sources have become more readily available, techniques have become more refined, reducing acquisition times, as well as improving resolution in both the spatial and spectral domains.

Imaging modes of energy-sensitive systems are commonly split into two main subsections: 'bright-field' and 'dark-field'. As will be discussed below, these modes are split based on

their difference in experimental geometries (on-axis vs. off-axis detector), as well as the type of characteristic spectral markers they aim to record.

First, a review of bright-field X-ray CT is conducted. Available to both multispectral and hyperspectral detector systems, bright-field mode is regarded as the most simple in terms of its imaging geometry and the manner in which chemical properties of the sample may be extracted. Applications of the technique, across fields including geology, chemical catalysis, and bioimaging are reviewed. The current state of the art is established, in the extent of chemical discrimination possible, as well as the various spectral analysis performed with the energy-based properties, particularly with hyperspectral sensors.

Finally, a brief exploration is made into the evolution of dark-field techniques, aimed at recording characteristic scattered photons, including both diffraction and X-ray fluorescence. The main advantages and limitations of the technique are reviewed, and how they can complement bright-field imaging.

2.4.1 Bright-field X-ray imaging

By placing the pixelated energy-resolving detector onto the axis of the incident beam, it is possible to access the ‘bright-field’ and collect conventional radiographs. This allows for the collection of information via bright-field energy-sensitive CT. As discussed in Section 2.2.2, multispectral and hyperspectral detectors are capable of identifying the energy of incident X-ray photons through the evaluation of the generated charge in the respective detector system. While multispectral detectors typically match the incident charge to one of a set of 2-8 pre-defined threshold values to provide broad energy resolution, hyperspectral detectors are capable of building an entire X-ray absorption spectrum in each pixel, owing to its high energy resolution. Therefore, each pixel of the hyperspectral system enables full attenuation profiles to be observed and analysed in each pixel.

By taking radiographs across a full range of projection angles, a reconstructed spectra dataset will produce a 4D volume (3D spatial + 1D spectral), where chemical properties of the imaged object may be extracted, predominantly through the analysis of spectral markers, as described in Section 2.1.4. In most cases, it is the identification of absorption edges which are the focus of bright-field imaging. As such, bright-field CT is also often referred to as ‘K-edge CT’, due to the fact that it is ionisation of electrons from the K-shell which are the most commonly observed identifiers of elemental composition. This allows for analysis which is analogous to X-ray absorption spectroscopy, a technique used in the evaluation of chemical species based on the sharp rise in attenuation close to electronic binding energy values [91]. An illustration of the conventional K-edge CT set-up is shown in Fig. 2.4.1 for a lab-based geometry with a cone-beam source. Here the figure illustrates the typical pixel-by-pixel output expected for a hyperspectral detector, where continuous attenuation profiles are displayed as a function of energy.

A comparison of typical profiles for both multispectral and hyperspectral data is shown in

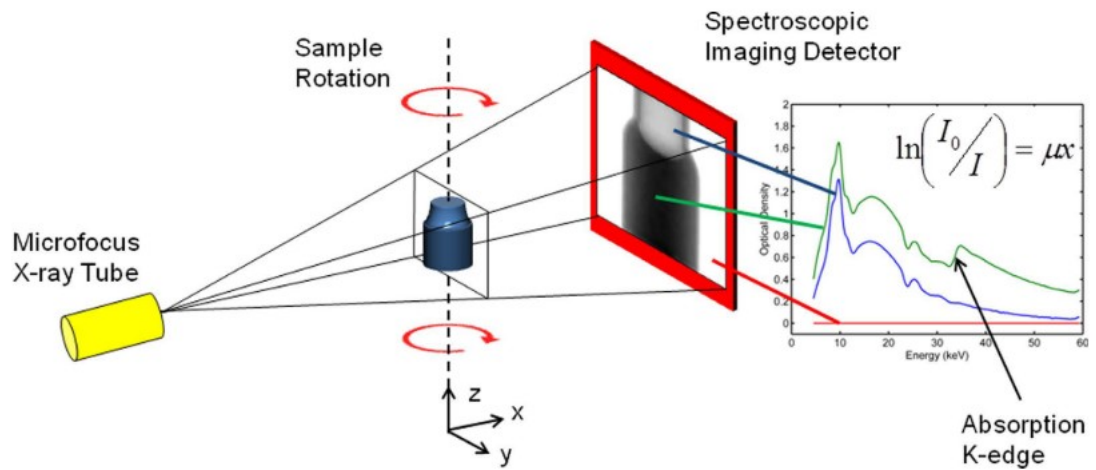


Figure 2.4.1. A typical geometry for energy-sensitive bright-field CT imaging. The conventional set-up for absorption CT is used, whereby a sample is rotated in the presence of an incident X-ray beam, but collected by an energy-resolving detector placed on the beam axis. Also shown is a set of three spectra seen from various sections of the sample object, with clear absorption edges [92].

Fig. 2.4.2 for known attenuation values of molybdenum, with an absorption K-edge at 20.0 keV. Multispectral profiles contain few data points, with broad energy windows. As such, the presence of K-edges are less clearly defined. This is highlighted by the lack of a sharp attenuation rise as the K-edge value is passed. In contrast, the hyperspectral profile produces a spectrum close to continuous. Hundreds of narrow energy windows allow precise matching of the measured K-edge to its known value.

2.4.2 Applications of bright-field imaging

Many of the early lab-based studies using hyperspectral detectors evaluated the range of materials that may be identified and segmented based purely on the identification of their elemental absorption edge markers. A proof of concept study used a tungsten target tube to separate and identify the different materials in a wireless USB dongle [93]. Using the 80×80 array, $250 \mu\text{m}$ pixel size, CdTe-based HEXITEC detector, a number of 2D radiographs were acquired, collecting 30s exposures over a range of 400 spectral channels. By employing spectral decomposition and 'clustering' methods, aimed at segmenting energy-based signals and grouping them by signal similarity [94], it was possible to map out the distinct object features based on spectral similarities alone, as shown in Fig. 2.4.3c. In order to then identify elements present in the sample, the absorption edges were isolated and mapped to the corresponding elements in the radiographs. Here, the K-edges of both barium (37.4 keV) and tantalum (67.4 keV) were used to spatially map the elements within the printed circuit board of the dongle, as shown in Fig. 2.4.3d.

Further analysis demonstrated how the full attenuation profile enables additional image segmentation, outside of the absorption edges present. Fits to the low-energy portion of the spectra in Fig. 2.4.3a were performed, extracting additional electronic components in the 2D maps. A Gaussian fit to the peak at 9.5 keV and a linear fit in the 20-30 keV region highlighted such components, as shown in Fig. 2.4.3e and f. Such analysis demonstrated a

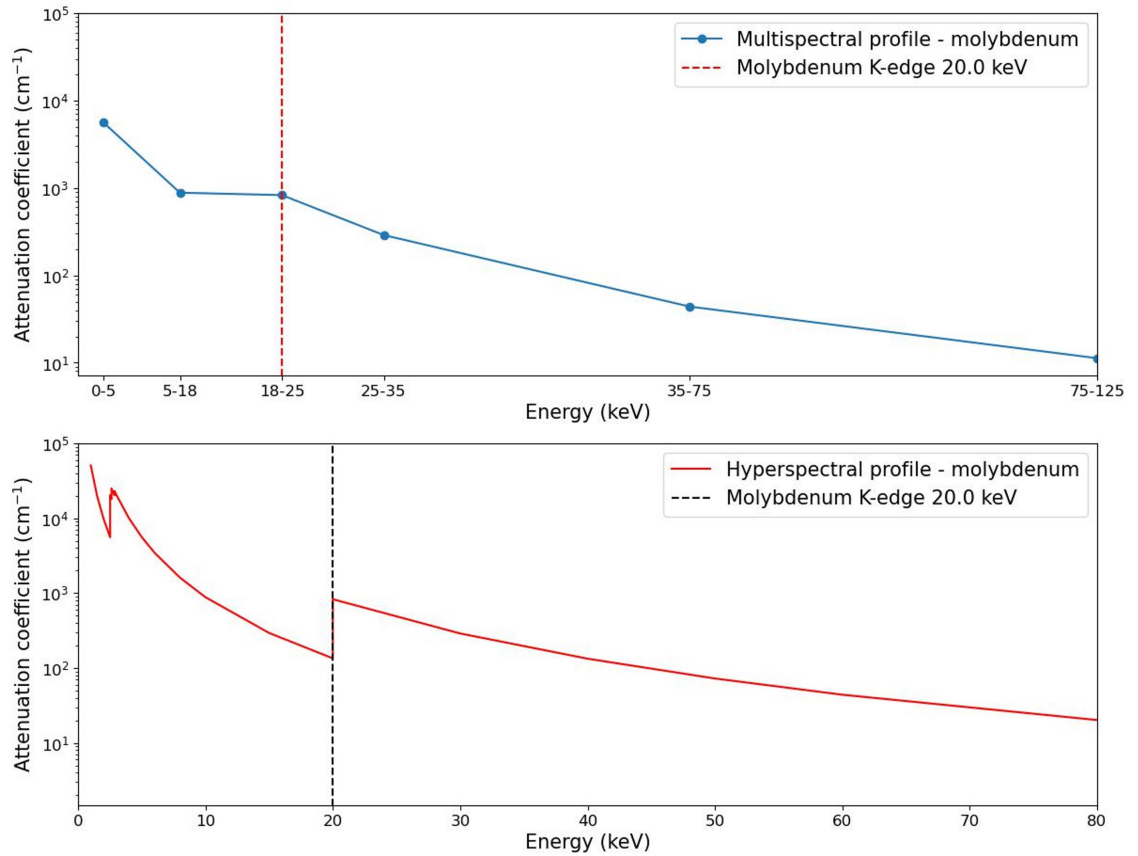


Figure 2.4.2. Representation of a typical multispectral (top) and hyperspectral (bottom) attenuation profile for molybdenum. The multispectral profile records single attenuation values for broad energy windows, while the hyperspectral detector is capable of effectively producing a continuous spectrum. Known positions of the K-edge for each element are overlaid as vertical dotted lines. All attenuation values were extracted from the NIST database [9].

novel aspect to energy-dispersive imaging, allowing visualisation of previously unseen features in conventional radiographs (Fig. 2.4.3b). While lower density materials may still be identifiable using the correct analysis techniques, such as the use of spectral clustering to separate the plastic casing from the higher density segments, the imaging method is better suited to heavy elements. The work defines a lower boundary for the spectral sensitivity of the system, through which characteristic edges and fluorescence peaks may be identified, as $Z \geq 29$. In contrast to the lower density components of such samples, these heavier elements require no *a priori* knowledge of the composition to confirm chemical identity.

Two applications of bright-field hyperspectral CT were performed by Egan *et al.* [92], including a study on the distribution of palladium (Pd) in a Pd-loaded catalyst pellet, while the research field of geoscience was explored by imaging a mineralised core taken from a geothermal vein. The work also presented two forms of spectral analysis, to extract additional characteristics of the sample, outside of solely confirming an element's presence.

Chemical catalysis offers an excellent field of research for energy-sensitive imaging, due to the presence of high-attenuation metal and metal oxides used for large-scale, industrial catalysis. Hyperspectral imaging offers a direct route to mapping the distribution of such metals, loaded onto the catalyst body, which can have a significant effect on the efficiency of the chemical processes to which they are utilised [95]. In the study by Egan *et al.*, an ab-

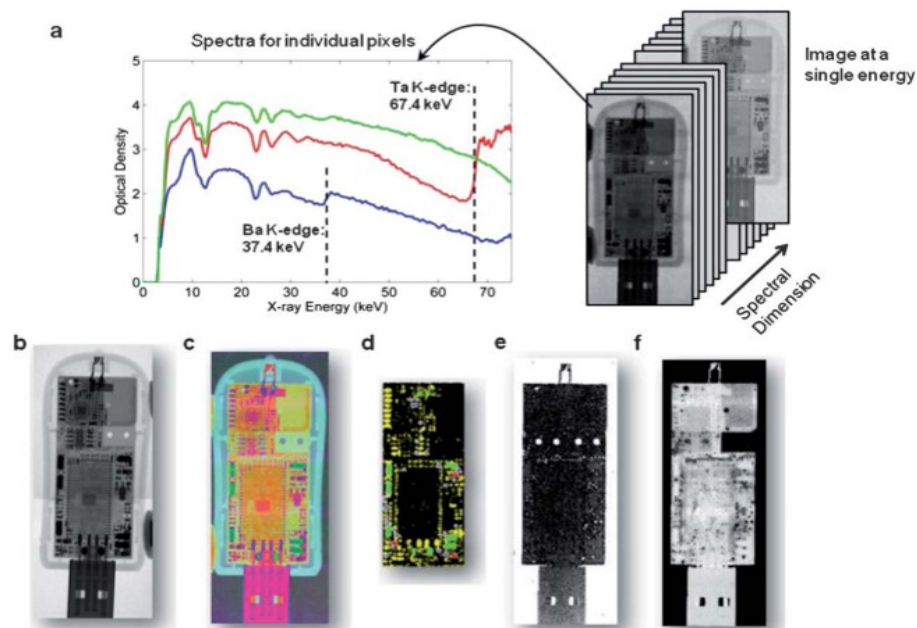


Figure 2.4.3. Hyperspectral analysis of a USB dongle. (a) Set of hyperspectral radiographs with an example set of absorption spectra. (b) Conventional radiograph image for comparison. (c) RGB image following spectral clustering. (d) K-edge absorption analysis including highlighted barium (blue) and tantalum (red). (e) and (f) show images created by applying fits to the absorbance spectra at 9.5 keV and 20-30 keV [93].

sorption step matching the K-edge of Pd (24.350 keV) was clearly identified through analysis of single voxel absorption spectra.

To evaluate the relative distribution of Pd as a function of position, a novel technique was used to perform semi-quantitative analysis. As shown in Fig. 2.4.4a, least-squares fitting of linear functions either side of the Pd K-edge was performed and extrapolated to the K-edge position. Subtraction of the two fits at the K-edge energy provided a relative measure of absorption step size for every pixel, labelled $\Delta\mu_0$. In addition, the technique decoupled any contributions from the catalyst body. This was an important factor, given that the body could not be assumed to have homogeneous density. Therefore distribution of the Pd metal was more accurately measured by isolating its contribution to the total absorption. Further, $\Delta\mu_0$ is stated to be directly proportional to phase concentration, hence through a voxel-by-voxel fitting, spatial mapping of Pd concentration across the volume was achieved. This showed that the Pd had a tendency to build up at the periphery of the pellet, as well as appearing in ‘hotspots’ around voids (see Fig. 2.4.4b-d). The technique of absorption step size fitting demonstrates one form of spectral analysis directly available due to the high energy resolution in hyperspectral imaging detectors. However, the work also notes that the technique in its current form offers a simply qualitative metric, mapping relative differences in chemical concentration. Calculation of absolute concentration values as a function of position would require measurement of various standard samples of known concentration to establish a precise relationship. Nevertheless, the study once more demonstrated additional characteristics available from the spectral profiles alone.

A secondary, and more commonly utilised, form of spectral analysis was also evaluated in the study. That is, the method of ‘K-edge subtraction’. The geological core sample was ex-

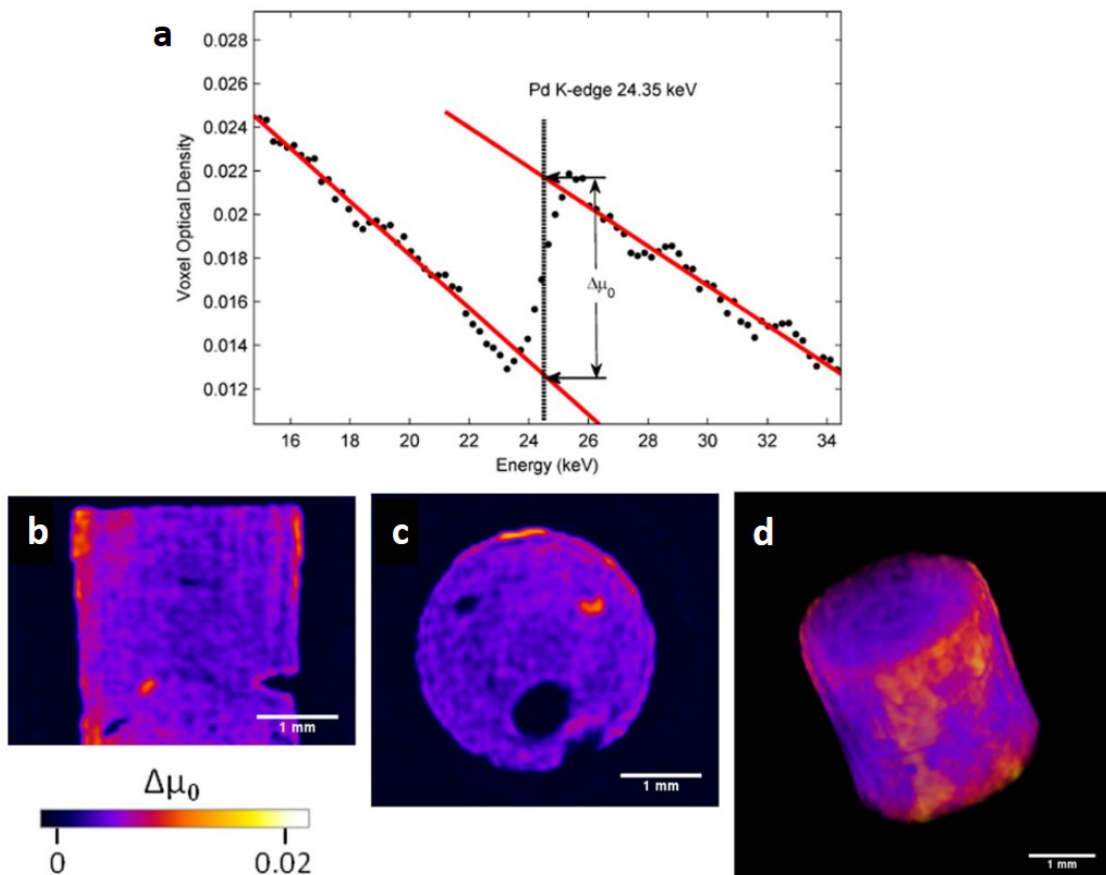


Figure 2.4.4. Relative concentration and distribution of Pd metal in a catalyst body. (a) Single voxel spectra showing the presence of the Pd absorption edge. Overlaid are linear fits applied to either side of the K-edge to measure the size of the step change ($\Delta\mu_0$). (b)-(d) Vertical and horizontal slices of the reconstructed volume mapping of $\Delta\mu_0$ values, as well as a 3D visualisation of the exterior. Adapted from [92].

amined with hyperspectral CT to non-invasively map in 3D the range of mineral and elemental phases present. Collected from a gold-rich vein, a deeper understanding of the distribution of mineral inclusions within such ores can be crucial in developing efficient extraction processes. Heavier elements in the sample were easily identifiable as inclusions in the reconstructed images from their greyscale intensity differences alone, relative to the surrounding phases. Through analysis of individual voxel spectra, the precise mapping of both gold and lead phases was possible through matching of the measured absorption edges to the known K-edge values (Au - 80.7 keV, Pb - 88.0 keV), as shown in Fig. 2.4.5a, b and d. To directly segment these phases, a ‘K-edge subtraction’ (KES) analysis was employed, whereby images at energies above and below the edge were subtracted from one another, isolating the individual elemental contributions. The result of mapping the elemental phases in 3D is shown in Fig. 2.4.5e. Using standard greyscale contrast, these phases would be difficult to segment in XCT due to a high degree of density similarity, but segmentation becomes a simple task using methods such as KES. In order to map the remaining low density material phases present, a combination of prior knowledge on the ores’ composition, as well as the availability of full attenuation profiles, was used to fully characterise the sample. Phases including quartz (SiO_2) and pyrite (FeS_2) contain low Z elements from which absorption edges were below the sensitivity of the detector. However, by evaluating linear fits of the optical density gradient for each phase, as shown in Fig. 2.4.5c, a spectral threshold-

ing tool was formed. The relative density differences between the phases became visible, and enabled a form of 3D mapping even in the absence of characteristic markers.

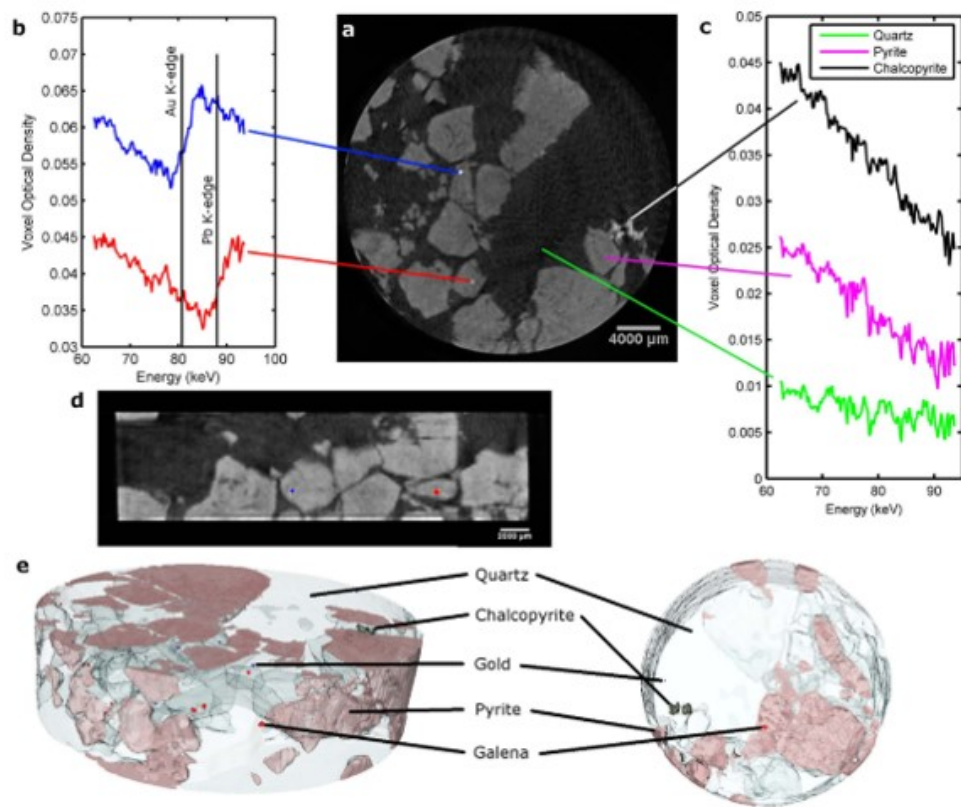


Figure 2.4.5. Spectral CT 3D distribution of a gold-containing geological sample. (a) Greyscale slice of the ore sample acquired by integrating over the full spectral range. (b) Spectra highlighting the K-edges of gold and lead within the sample. (c) Spectra for quartz, pyrite and chalcopyrite. (d) Vertical slice with segmented gold (blue) and lead (red) voxels. (e) 3D reconstruction highlighting each phase [92].

Aspects of the preprocessing and reconstruction routine highlighted some of the issues commonly encountered with hyperspectral, as well as conventional, X-ray CT data. A correction to align the pixel-by-pixel spectral response was performed, known as Correlation Optimised Warping [96]. A further correction to remove ring artefacts was applied to the sinograms before reconstruction. Ring artefacts are common in microtomography, and are predominantly due to non-functioning or poor pixel response. This may be due to one or two defective pixels registering erroneous signal values. These can often be corrected via a flat-field correction, however other causes such as variations in scintillator thickness for energy-integrating detectors can mean further correction is required [97]. Once reconstructed, these errors appear as concentric rings around the centre of rotation point, leading to reduced image quality. In this paper, a wavelet based Fourier filter was applied to minimise the effect, as described elsewhere [98].

The work by Egan *et al.* was some of the first to demonstrate the potential of hyperspectral imaging for multiple simultaneous chemical mapping with hyperspectral X-ray CT. With increased energy resolution, the technique stands out over multispectral imaging for its ability to provide the user with full attenuation profiles of the 3D volume. As such, hyperspectral tomography eliminates the uncertainty associated with fine-tuning the energy thresholds of broader spectral windows, as is required with multispectral systems. Here, markers

such as K-edges may unambiguously be distinguished, identified and mapped based on precise matching of the observed to known edge positions for each element present. In contrast, multispectral imaging is limited by the choice of energy windows, and may lead to difficulty in segmenting multiple chemicals with narrowly-spaced K-edges, also highlighted as a significant barrier to the wider application of DECT, as discussed in Section 2.1.5.

An exploration into the hyperspectral measurement of markers in the softer X-ray regime was performed by Boone *et al.*, in the field of bioimaging [99]. The work aimed to spectrally segment gold nanoparticles from calcification in a case of atherosclerosis in the aortic arch of a mouse specimen. The study used the SLcam, a silicon-based hyperspectral detector designed for high energy resolution in the soft X-ray range. The detector contains a 264×264 pixel array, with pixel size of $48 \times 48 \mu\text{m}$, and an achievable energy resolution of approximately 150 eV at 5 keV [100]. The working energy range is quoted as 5-40 keV, but falls to below 10% quantum efficiency at the upper boundary. Prior knowledge of Ca, Zn and the Au nanoparticles were confirmed via 2D micro-XRF. Here, the L-edges of Au, along with the Zn K-edge, were the characteristic markers of interest for the study, all falling in the 9.5-15.0 keV range [9].

The SLcam was noted to suffer from severe limits in count rate, below $10 \text{ counts s}^{-1} \text{ pixel}^{-1}$, and therefore two methods of SNR improvement were implemented. First, exposure times of 20 minutes were used across the 180 projections, for a total scan time of 60 hours. Second, from the 1024 total energy bins in each pixel profile, select groups of channels were combined to total widths of 1.25-2.50 keV to improve image noise, producing a quasi-multispectral dataset. The groupings were selected to each contain specific characteristic markers, and enabled a form of KES to be applied. The authors were able to identify 'hotspots' of gold accumulation, following subtraction of regions either side of the gold L_3 -edge (Fig. 2.4.6b), despite the complex geometry of the sample, illustrated by the full energy-integrated volume (Fig. 2.4.6a). However, the poor SNR, combined with a voxel size of $16 \mu\text{m}$, meant the authors could not confidently distinguish noise from chemical signal in the 3D rendering, and were unable to identify Zn or Ca from spectral markers alone. Combined with the need to operate at a temperature of -20°C to maintain the high energy resolution, the current technology limits of silicon-based hyperspectral systems were highlighted.

In the identification, segmentation and mapping of single or multiple simultaneous high-density contrast agents, both multispectral and hyperspectral systems have proven competent in performance. Given the full *a priori* knowledge of the heavy metal elements contained in such staining agents, multispectral detectors may be finely tuned to set the broad threshold energy windows at appropriate points, ensuring no overlap in absorption edge markers.

A simulated phantom study by Ghadiri *et al.* presented a 'K-edge ratio' tool for multiple chemical discrimination [101], aimed towards future applications of targeted staining and diagnosis of multiple simultaneous organs. Using the sharp rise in attenuation either side

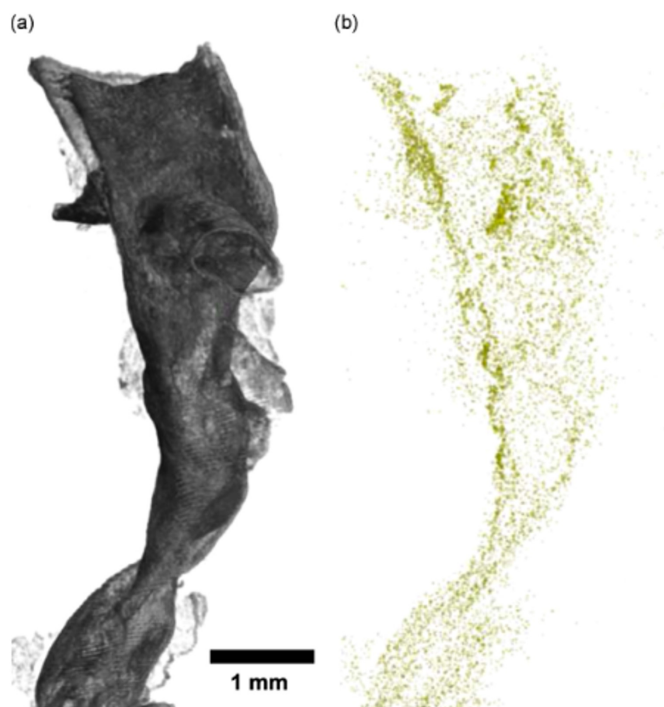


Figure 2.4.6. 3D rendering of a mouse aortic arch, with spectral subtraction. (a) The 3D volume produced after integrating over all 1024 energy bins. (b) 3D map following spectral subtraction of energy windows either side of the gold L_3 -edge. Some 'hotspots' appear to emerge, attributed to the presence of gold. Adapted from [99].

of every K-edge, the method calculated ratios of energy bins and used them as a tool for thresholding multiple elemental signals. While successful segmentation of several elements (such as Gd, Hf and Au) was possible, effects such as photon starvation and beam hardening became prominent with multiple high density materials present. Further, the acquisition protocol was found to be case-specific with regards to the positioning of energy thresholds, and did not perfectly map physical experimental conditions with regards to noise and detector efficiency.

Several studies have sought to utilise multispectral CT for the mapping of multiple contrast agents in real-world experimental cases, applied to both phantom samples and biological specimens. Studies of anthropomorphic phantoms, modelling a colon [102] and abdominal aortic aneurysm [103], applied gadolinium- and iodine-based contrast agents to evaluate the feasibility of photon-counting detectors in the multiple mapping of targeted stains. Using a material decomposition approach, as described in detail in Section 2.1.5, maps of each respective element were successfully established and provided clearly distinguished contrast-enhanced regions. Such proof-of-concept studies emphasise the potential for such detectors to benefit the field of clinical imaging, while they also discussed the established approach for quantification of chemical density in such spectral data.

In order to conduct quantitative measurements of the elemental concentrations, a range of approaches have been adopted. It has previously been shown in DECT [26] that a linear relationship may be determined between chemical concentration and CT number (in Hounsfield Units), therefore calculation of absolute values is achievable given a preliminary scan of a known concentration phantom. Similar work has been performed in a multispec-

tral setting to confirm the same linear relationships may be established [104]. Studies by Muenzel and Dangelmaier correlated the CT values to the relative chemical concentrations using lookup tables [102, 103]. An *in vivo* study by Symons *et al.* performed the calibration procedure through the acquisition of phantoms and a stained animal specimen using the same X-ray scan settings and chemical concentrations [105]. As shown in Fig. 2.4.7a-b, direct conversion from CT number in the greyscale image to a full multi-material map was achieved using material decomposition. Using the values recorded in the circular vials of I, Gd, Bi (oral agent) and a ferrous solution mimicking soft tissue, quantitative measurements of concentration were mapped to the reconstructed image (Fig. 2.4.7c-e). The work showed the spectral applicability of studying multiply-stained specimens at sufficiently low dose and chemical concentration level for *in vivo* study. Further multispectral studies, on the *in vivo* contrast-enhancing stain distribution within white rabbits, have further emphasised the current state of the art for photon-counting devices [106, 107]. The ability to probe biological processes and enhance the identification of specific soft tissue regions, all within a single CT scan, confirms the potential for spectral imaging moving forward.

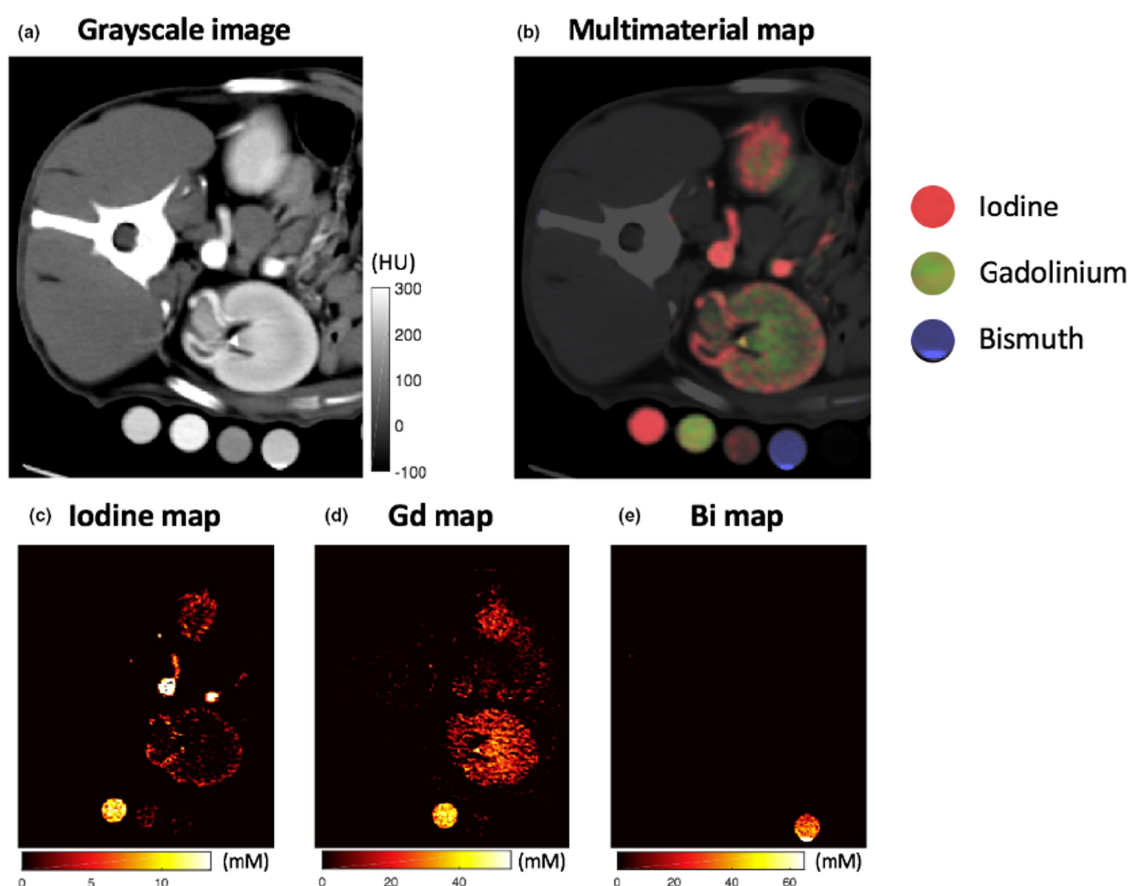


Figure 2.4.7. Multi-material mapping of a canine specimen. (a) Reconstructed grayscale image of the specimen, showing the kidney and abdomen, along with the circular calibration vials. (b) Colour map of the chemical stain distribution in the same image, with a legend mapping the colours to the element present. The unlabelled vial is that of a ferrous solution, matching the spectral properties of soft tissue. (c)-(e) Quantitative material maps, measured in terms of millimolar units. [105]

It is important to note that in virtually all multispectral cases of bright-field, K-edge imaging, the contrast agents are selected such that there is large spectral separation between the respective K-edges. Such an approach is logical, given the poorer energy resolution com-

pared to hyperspectral systems. Neighbouring elements become very difficult to separate, and therefore can limit the applicability of the technique. One study did seek to test the limits of such spectral segmentation, successfully separating iodine ($Z = 53$) from barium ($Z = 56$) contrast agents, despite only a 4 keV difference in absorption edge position [108].

A particular point of note, and perhaps limitation to the existing technology, is the applicability of bright-field imaging in the absence of absorption edge markers. Such situations emerge in two scenarios. First, where the K-edge is outside of the working range of the detector, as discussed in recent studies [92, 93]. It should be noted that while this is predominantly the case for low-density materials, with edges below the sensitivity limit of the detector, the same can also apply for the very high-density elements, where DQE of the sensor is too low to obtain significant signal for identification of characteristic signals. Second, in the cases where spectral concentration is too low in a single voxel, or ROI, to distinguish an absorption edge from the surrounding background noise. For the latter, improved reconstruction routines, as described in Section 2.3.5, offer one possible solution, but often cannot extract such signals in the presence of significant noise.

One alternative to direct segmentation through K-edge mapping is through the analysis of relative attenuation gradients for hyperspectral absorption profiles, as briefly shown in the geological core work [92]. Low-density materials may still be differentiated through their rate of change of attenuation as a function of energy, provided a large enough energy range is available to measure such changes. If profiles are mapped in terms of attenuation coefficient, then in theory identification of elements may be achievable through matching of the measured values to the theoretical profiles over the same range. However, spectral distortions due to charge sharing and pulse pile up (see Section 2.2.3) are known to alter the profiles, such that precise matching is not always achievable.

A study by Yokhana *et al.* has sought to test the potential for bone densitometry calculations and soft tissue mapping, in the absence of contrast agents [109]. Using the CdTe-based, multispectral PiXirad detector [110], two energy ranges were studied (21-40 keV and 27-40 keV). By evaluating the two overlapping ranges, a distinct shift in linear attenuation coefficient was observed in each phase of a bone phantom, due to the different average energy of each range. As a result, a linear relationship was determined between density and attenuation coefficient. An automatic segmentation of phases was then performed by plotting frequency distributions of attenuation values over the reconstructed image, and performing fits to the peaks corresponding to each phase. As a further proof of concept, the same principle was then applied to a mouse embryo, successfully segmenting bone from soft tissue in the absence of contrast agent staining, in addition to calculating bone density within the specimen. The work further expanded the potential applications for bright-field imaging using energy-sensitive detectors.

Summary of bright-field imaging

In summary, the ease of transition from a conventional, energy-integrating system to an energy-sensitive detector becomes trivial when imaging in the bright-field. The geometry remains identical, and simply requires replacing one detector for another. Several studies in the last decade have demonstrated the potential for both multispectral and hyperspectral detectors to distinguish and map single, or multiple, simultaneous chemical species in a range of samples. Geology, catalysis, and biological staining have all been shown as applicable fields for elemental study using photon-counting detectors in transmission mode.

The subject of bioimaging, and analysis of multiple staining regimes, has dominated the multispectral research field, given the prior knowledge of staining elements and ease in optimising the threshold energy window positions. The pros and cons of the two detector formats were highlighted through the review of the above literature. In cases of prior knowledge, multispectral detector systems stand out. Typically offering higher spatial resolution and improved SNR owing to their broader energy windows, elemental mapping becomes a simple task if thresholds are chosen correctly. The poorer energy resolution only becomes an issue in cases where spectrally similar elements are present in a sample, making segmentation difficult. Yet, one study has proven this to still be achievable [108].

In contrast, while lacking in spatial resolution and SNR, hyperspectral imaging sensors offer no such issues in spectral segmentation. In the case of CdTe detectors, such as that of the HEXITEC, a large working energy range ensures the majority of high-density elements may be simultaneously mapped from their absorption edges alone, with no prior knowledge required. Additional spectral analyses become available from the continuous attenuation profiles in each voxel, with KES and step size fitting offering unique qualitative insight on chemical distribution with high spectral precision. Outside of the HEXITEC studies previously discussed, little work has been conducted in the bright-field regime for real-world investigations using hyperspectral systems. Given the low counts in each energy channel, the requirement of increased dose to improve SNR limits the ability to perform *in vivo* studies, without the aid of advanced reconstruction routines. Combined with the limited detector array size, the technology is still in its infancy in terms of hardware development. Nevertheless, there is significant scope for further exploitation of the spectral data offered by systems such as the HEXITEC. No studies have previously performed quantitative analysis on the absorption edges, as has been investigated in multispectral systems. Given the large imaging bandwidth available with the HEXITEC, studies in bioimaging offer an exciting opportunity to study a wide range of simultaneous contrast agents in various combinations, in order to evaluate stain interaction, binding properties, and concentration distribution.

2.4.3 Evolution of dark-field energy-dispersive imaging

Given its ability to acquire multiple forms of characteristic signal by moving off-axis from the incident X-ray beam, a number of hyperspectral studies have instead been conducted in

the so-called dark-field regime to exploit such flexibility. The result is the potential to unlock additional chemical and crystallographic insight. Below a brief summary of the evolution of dark-field imaging is provided for energy-sensitive detectors, and some of the work conducted to date.

Tomographic energy-dispersive diffraction imaging

As early as 1987, Kosanetzky *et al.* had proposed the idea of combining X-ray computed tomography with diffraction in order to spatially map the crystallographic properties of plastics and biological material [111]. Soon after, Harding proposed the novel technique of ‘energy-dispersive X-ray diffraction tomography’, in which diffraction properties of plastics could be obtained directly from X-ray scatter using a polychromatic source [112].

While typical X-ray diffraction is based on the wavelength-dependent Bragg diffraction law, Harding’s team utilised the energy-dispersive form of Bragg’s law,

$$E \approx \frac{12.398n}{2d \sin \theta} \quad (2.12)$$

where lattice spacing d and Bragg diffraction angle θ are measured in Angstroms and degrees respectively, and n is the diffraction order, while X-ray energy, E is given in keV and relates to the wavelength via the photon energy formula,

$$\lambda \approx \frac{12.398n}{E} \quad (2.13)$$

Equation 2.13 highlights the transition from angle-dispersive diffraction (ADD), in which monochromatic (fixed wavelength) X-rays collect diffraction patterns over a range of Bragg angles, to energy-dispersive diffraction (EDD), where irradiation with polychromatic X-rays result in a full diffraction spectrum for a fixed angle [113]. Thus, EDD experiments highlighted the ability to simply transition from monochromatic imaging, which produced conventional intensity versus angle plots, to a qualitatively equivalent plot of intensity versus energy.

The evolution of spectral diffraction geometries is shown in Fig. 2.4.8. The technique is based around defining a specific region of the sample from which diffracted photons originate. Defined as a ‘gauge volume’ (diffraction lozenge), this region size and position is determined by the intersection of the X-ray beam and a collimator between the sample and detector (Fig. 2.4.8a) [114, 115]. Diffraction patterns are collected as the sample is translated in all three spatial dimensions, building a 3D volume without the need for reconstruction algorithms. As such, equivalent tomographic results are achieved, hence the name ‘Tomographic energy-dispersive diffraction imaging’ (TEDDI) to highlight its similarities, yet clear distinction, from conventional X-ray CT. The result is that each voxel contains crystallographic information. The downside is that spatial resolution is limited by the size of the

lozenge, while scan times are on the order of several hours, even with synchrotron radiation. Extending to multiple collimator systems, either in 1D or a full 2D array (Fig. 2.4.8b-d) significantly helps the latter [116–118]. Applications of the technique have included studying the chemical processes in cement [119], ferrite micro-structure [120], and analysis of metal alloys [121].

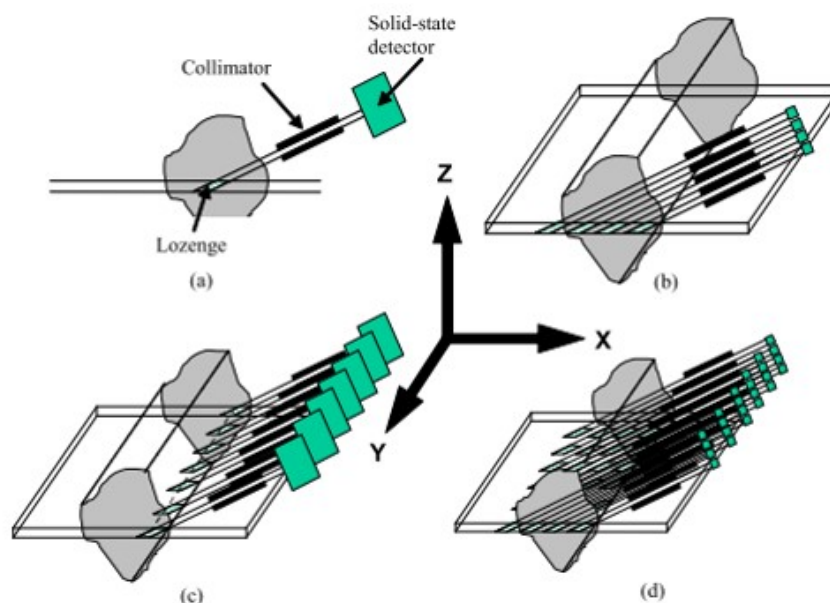


Figure 2.4.8. Illustration of the transformation in the 'TEDDI' setup. (a) Conventional geometry for a one detector, one collimator system, with one diffraction lozenge. (b) Example of a multiple-aligned vertical detector array. This produces multiple lozenges at different positions. (c) Multiple-aligned horizontal detector array with matched collimators. (d) 2D detector-collimator array, requiring sample motion in the one dimension [115].

Dark-field imaging with pixelated spectroscopic sensors

As the development and wider use of pixelated spectroscopic detectors came to the fore, so too did adaptations to the geometries and techniques involved with imaging diffraction patterns within samples. A simpler geometry avoids the need for collimation through the use of a pinhole placed off-axis to act as an aperture [122], projecting the diffracted signals onto the detector. The novel technique is termed 'dark-field' due to its ability to provide composition insight outside of the conventional 'bright-field' orientation. The work by Egan *et al.* described a set-up, as illustrated in Fig. 2.4.9a, whereby the pinhole was placed at a low 2θ angle (typically between 1° and 5°), and the detector collected individual EDD patterns at each individual pixel, providing information on the physio-chemical structure. In this case, the detector was the 80×80 pixel HEXITEC detector.

Upon integrating over specific spectral bands where identifiable diffraction or fluorescence peaks are observed, materials in the sample can be spatially mapped and colour-coded to highlight elements and phases present (Fig. 2.4.9b). Further, in-detail analysis of the diffraction spectra allows refinement and calculation of the crystallographic properties, such as lattice parameters, crystallite size, and any preferred orientation. The pinhole aperture in this technique offers the additional benefit of geometric magnification (reported here to

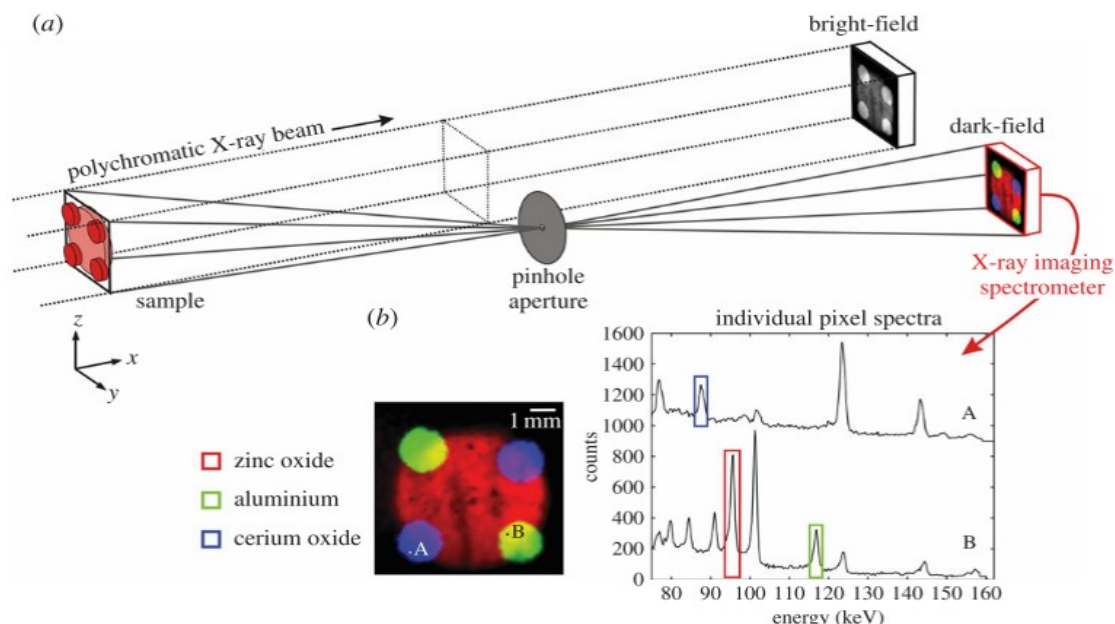


Figure 2.4.9. Pinhole geometry for ‘dark-field’ hyperspectral imaging. (a) An off-axis pinhole projects scattered X-rays towards a spectroscopic detector, collecting diffraction patterns at each pixel. (b) Examples of diffraction patterns and a corresponding spatial mapping of the elements identified [122].

be between $0.1\text{--}10\times$), allowing for larger samples, or ‘zoomed-in’ region-of-interest (ROI) studies to be conducted [122]. The work employed the conventional CT approach of rotating the sample through a number of projections, using filtered back-projection to build up complete, 3D volumes. The effectiveness of the technique was illustrated by imaging an aluminium alloy friction stir weld (FSW), commonly used in the aerospace industry [123].

The study, conducted at beamline I12 of Diamond Light Source, UK, demonstrated a significant improvement in the acquisition times, producing 6400 pixel images in 2–5 minute exposures. With no flux limitations to the technique, this form of dark-field imaging offered an experimental setup applicable to both laboratory and synchrotron sources. This was shown by a follow-up lab-based study, where once more an FSW was analysed, collecting a full-field powder diffraction pattern across the sample volume [124]. In this case, the laboratory X-ray tube provided a flux of roughly 4×10^6 photons $\text{s}^{-1} \text{mm}^{-2} \text{keV}^{-1}$, several orders of magnitude weaker than that provided by the synchrotron source. As a result, exposure times were increased to 30 minutes per image to ensure observable signals could still be recorded.

Recent pinhole-based, polychromatic diffraction studies using the HEXITEC detector have reviewed the benefits of hyperspectral systems for fields where bright-field imaging is not possible. A lab-based study on the accumulation of amyloid plaque in mice brains evaluated the potential for future *in vivo* studies, absent of contrast-enhancing stains [125], measuring broad diffraction patterns with total scan times on the order of minutes. A synchrotron study by Connolley *et al.* measured the chemical changes in the charge and discharge of a Zn-MnO₂ battery cell [126]. Here, the time resolution remained on the order of minutes. An attempt at improving SNR was made through the use of a twin-detector regime, placed at equal 2θ angles either side of the bright-field axis. However, challenges

in aligning each dataset to the same ROI of the cell prevented an improved signal in the final data.

The notable limitations to the latest dark-field methods emerge from the use of pinhole apertures. While the use of a pinhole offers greatly enhanced spatial resolution, larger apertures and shorter pinhole-detector distances introduce diffraction peak-width broadening [124]. This limits the technique to studying widely spaced Bragg peaks (larger lattice parameters). The issue of longer exposure times may be simply offset by an increase in X-ray flux, with high-powered X-ray tubes (1-2 kW) widely available for lab-based research, with no concerns regarding the count rate limit of the HEXITEC while in a dark-field geometry [124]. Despite some of the technical limitations in its current development, the ability to directly image and map crystallographic properties in 2D (and 3D following sample rotation) offers significant promise in the field of hyperspectral imaging, particularly when considered part of a multi-modal approach with bright-field imaging.

Energy-dispersive X-ray fluorescence CT (dark-field)

An alternative, or additional, characteristic marker available is that of X-ray fluorescence peaks. Fluorescence signals make for an excellent form of elemental analysis due to the fact these secondary X-rays emit isotropically, and thus a detector placed at any angle will collect these characteristic peaks, enabling spectral analysis. When collected by an energy-dispersive detector (EDD), an energy-resolved intensity pattern allows observation of fluorescent peaks at specific energies, providing immediate identification of the constituent elements within the imaged sample. A typical geometry for energy-dispersive X-ray fluorescence CT (EDXRF-CT) is shown in Fig. 2.4.10, whereby the EDD is placed at a right-angle to the sample object, parallel to the incident beam. The ability to obtain elemental information purely based on an inherent property of matter allows one to effectively eliminate the polychromatic bremsstrahlung radiation. As discussed in Section 2.2.3, fluorescence peaks often emerge in the bright-field spectra due to secondary interaction of the incident photons with the detector materials. Moving the detector out of the direct beam essentially removes the ‘background’ bremsstrahlung component, leaving only the fluorescence signals. In the case of a focused-beam, whereby the sample is much larger than the beam itself, one must perform raster scanning by translating the sample to collect signal from the full volume. This is then repeated once the sample is rotated by a specific angle, building a set of 2D data which can be mathematically reconstructed for 3D volume mapping. The set-up may also be accompanied by a secondary detector placed in the conventional bright-field position, collecting additional attenuation data. Fig. 2.4.10 also depicts one of the largest limiters of XRF-CT: the effect of self-absorption.

Depending on the sample size and position of the focused, incident beam relative to the sample, both incident and fluorescent X-rays may suffer from attenuation from the sample itself before reaching the detector. That is, while absorption is a fundamental feature in non-destructive imaging, this is a disadvantage when one seeks to extract weaker signals

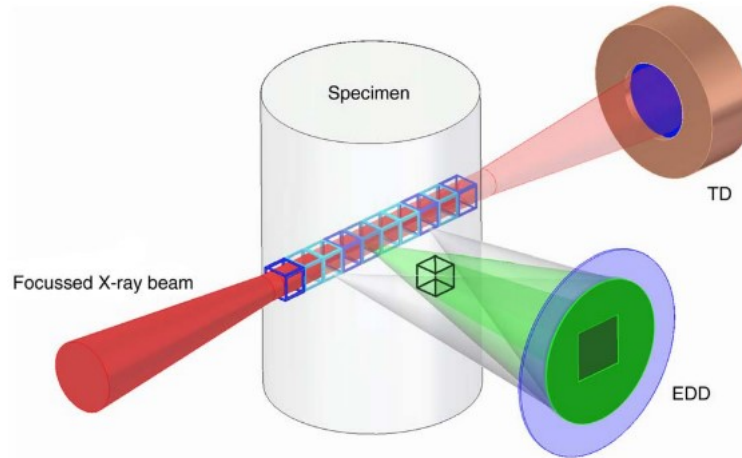


Figure 2.4.10. Scanning-probe imaging geometry for X-ray fluorescence measurement. A focused X-ray beam illuminates a columnar section of the sample, leading to excitation and emission of fluorescent X-rays, collected by the energy-dispersive detector (EDD). In addition is shown a conventional transmission detector (TD). The effect of re-absorption of some XRF signals by the black voxel highlighted is also shown [127].

such as elemental fluorescence. One of the early reports concerning attenuation issues in fluorescence tomography breaks down the three key stages in fluorescence scanning where issues can arise [128]:

1. Incident radiation is absorbed by the medium up to the point in question within the sample, based on the absorption coefficients for the given photon energy.
2. A characteristic emission of fluorescent X-rays occurs, via interaction with the element present, based on the fluorescence coefficient.
3. Each fluorescent X-ray is subsequently absorbed by the media between the point in question and the detector, based on the absorption coefficients at the fluorescent photon energy.

De Jonge and Vogt conducted a review of hard X-ray fluorescence tomography, highlighting the core areas of limitation for the modality, as well as fields of study in which it can excel [127]. One of the key points noted is that “despite the conceptual simplicity, XRF tomography has not yet found general application, mostly due to technical challenges and analytical complexities.” The key limitation being the aforementioned self-absorption, which the authors suggest is prominent for elements lighter than potassium ($Z = 19$) and samples with a size greater than $20\ \mu\text{m}$. Thicker samples with heavier elements (in the range between Fe and As) have however been successfully reconstructed with filtered back-projection, without the need for self-absorption corrections [129, 130], comfortably reconstructing samples of diameters into the hundreds of microns.

The other key issue of this dark-field technique, as with the diffraction pinhole modality adopted by Egan *et al.* [122], is the long scan times for lab-based experiments. Most X-ray sources are limited to lower power, often sacrificing high flux in favour of improved focal spot size (and hence spatial resolution) to improve image quality. As such, exposure times for energy-dispersive systems extend to several minutes per image to reach sufficient

SNR, such that chemical markers may be identified from the recorded energy spectra measured. Further to this, some EDXRF systems also employ a pinhole geometry in order to improve spatial resolution. Consequently, X-ray flux is reduced further, while FOV is narrowed based on the sample-pinhole-detector distances. While enabling higher resolution through geometric magnification of the sample, the limited size of existing spectral detectors typically requires the use of raster scanning to image larger samples or multiple ROIs.

It is these issues of long scan times, as well as the effects of self-absorption, which have limited the appeal of EDXRF-CT as a general use imaging modality. However, by limiting the sample size, along with the use of light elements, it is possible to find far-reaching applications in multiple research fields.

Monochromatic synchrotron EDXRF investigations into low-energy components of an unstained fish specimen revealed Br, Zn and Ca by direct integration of the XRF peaks [131]. In the same study up to six low density metals, all with peaks in the 4-14 keV range, were successfully discriminated and mapped to electronic components within a SIM card. The non-destructive advantages of EDXRF-CT were reviewed for the fields of environmental and planetary science, and once more highlighted the issues of self-absorption and scan time as the main limiters to its wider appeal [132]. A comprehensive review into the EDXRF applications within the life sciences reaches the same conclusions, but notes that continued improvements in detector technology will enable faster scan times and general use in lab-based environments [133]. Such lab studies have been evaluated using a polychromatic source with the HEXITEC detector, with material-specific mapping of spectrally similar elements achievable for XRF emission peaks up to 30 keV, including the mapping of high density materials such as lead [134].

2.5 Summary

In summary, this chapter has mapped the evolution from conventional black and white X-ray CT to the world of colour imaging modalities in the 21st century. Through the rapid advancement in pixelated, energy-sensitive detector hardware, lost energy-based information can now be exploited to extract chemical insight which previously required additional characterisation methods on top of X-ray CT.

From the earliest steps into spectral imaging through DECT, the transition to energy-sensitive techniques now relies only on the replacement of an energy-integrating detector with that of a multispectral or hyperspectral sensor. The technological differences and acquisition routines of dual-energy [20], multispectral, and hyperspectral detectors [33] were discussed, along with the common challenges associated with the collection of spectroscopic data. In particular, the count rate limits and poor SNR observed in hyperspectral imaging provide a stumbling block in its widespread application.

Where compromises in scan time or sample selection cannot overcome the spectral challenges, developments in 4D reconstruction routines have stepped in. This chapter sum-

marised the range of analytic and iterative routines commonly implemented in XCT, and the required adjustments needed to handle the additional spectral dimension. To date, very few studies have built established hyperspectral reconstruction frameworks [78, 79]. The work in this thesis aims to fill this research gap through the exploration of regularised reconstruction algorithms in 4D.

The bright-field imaging modality has been reviewed, with several applications across geology, catalysis and the life sciences. The field of bioimaging has been shown as of particular interest, given the prominent use of high contrast stains. While multispectral imaging of stained specimens has proven efficient in multi-stain mapping [106–108], the need to define energy thresholds requires prior optimisation and can limit the ideal choice of stains to those spectrally distinct from one another. As such, full flexibility in exploring new stain combinations becomes restricted. Hyperspectral imaging removes the need for prior knowledge and optimisation, offering full attenuation profiles for complete analysis of any characteristic markers available, regardless of spectral similarity. Despite this, the area of bioimaging in the bright-field hyperspectral regime remains largely untapped, and offers a unique opportunity to explore variations in staining procedures, such as the interaction between overlapping contrast agents. Quantitative analysis, as has been performed in multispectral studies [105–107], has to date not been investigated with hyperspectral data, outside of a single analysis of relative chemical distribution [92]. Full attenuation profiles in each voxel enable precise fitting to extract deeper chemical information about the sample composition and elemental concentration. Advancements in this area represent an opportunity for further exploration to be conducted as part of the work in this thesis.

Finally, a brief review of the alternative modalities offered by hyperspectral systems was conducted. These dark-field modalities provide an additional layer of characteristic signals beyond what is possible with conventional X-ray and multispectral CT. Given its infancy, these modalities and their widespread application fields constitute entire research projects of their own, outside the scope of this thesis.

2.6 References

- ¹W. J. Duffin, *Electricity and Magnetism*, 4th editio (McGraw-Hill Book Company, 1990).
- ²T. M. Buzug, *Computed Tomography: From Photon Statistics to Modern Cone-Beam CT*, 1st (Springer-Verlag, Berlin, 2008), pp. 32–48, 201–207.
- ³P. J. Withers, C. Bouman, S. Carmignato, V. Cnudde, D. Grimaldi, C. K. Hagen, E. Maire, M. Manley, A. D. Plessis, and S. R. Stock, “X-ray computed tomography”, *Nature Reviews Methods Primers* **1**, 1–21 (2021).
- ⁴S. R. Stock, *MicroComputed Tomography*, 2nd (CRC Press, 2019), p. 389.
- ⁵G. T. Barnes, M. V. Yester, and M. A. King, “Optimizing Computed Tomography (CT) Scanner Geometry”, *Application of Optical Instrumentation in Medicine VII* **173**, 225–237 (1979).
- ⁶P. J. Friedman and R. H. Greenspan, “Observations on Magnification Radiography”, *Radiology* **92**, 549–557 (1969).
- ⁷A. J. Duerinckx and A. Macovski, “Polychromatic Streak Artifacts in Computed Tomography Images”, *Journal of Computer Assisted Tomography* **2**, 481–487 (1978).
- ⁸Y. Tan, K. Kiekens, F. Welkenhuyzen, J.-p. Kruth, and W. Dewulf, “Beam hardening correction and its influence on the measurement accuracy and repeatability for CT dimensional metrology applications”, *Ndt*, 355–362 (2012).
- ⁹J. H. Hubbell and S. M. Seltzer, *Tables of x-ray mass attenuation coefficients and mass energy-absorption coefficient*, 2004.
- ¹⁰J. Chwaszczewska, S. Szarras, Z. Szmid, and M. Szymczak, “Application of semiconductor detectors in crystal structure investigations”, *Physica Status Solidi (a)* **4**, 619–626 (1971).
- ¹¹L. Grodzins, “Optimum energies for x-ray transmission tomography of small samples. Applications of synchrotron radiation to computerized tomography I”, *Nuclear Instruments and Methods In Physics Research* **206**, 541–545 (1983).
- ¹²H. Arslan, “Photon attenuation parameters for some tissues from Geant4 simulation, theoretical calculations and experimental data: a comparative study”, *Nuclear Science and Techniques* **30**, 1–10 (2019).
- ¹³Robert J. Gould and Y.-D. Jung, “The energies and structure of x-ray K-absorption edges”, *The Astrophysical Journal* **373**, 271–276 (1991).

- ¹⁴H. Moseley, “Xciii. the high-frequency spectra of the elements”, The London, Edinburgh, and Dublin Philosophical Magazine and Journal of Science **26**, 1024–1034 (1913).
- ¹⁵H. Moseley, “Lxxx. the high-frequency spectra of the elements. part ii”, The London, Edinburgh, and Dublin Philosophical Magazine and Journal of Science **27**, 703–713 (1914).
- ¹⁶M. R. Millner, W. D. McDavid, R. G. Waggener, M. J. Dennis, W. H. Payne, and V. J. Sank, “Extraction of information from CT scans at different energies”, Medical Physics **6**, 70–71 (1979).
- ¹⁷H. K. Genant and D. Boyd, “Quantitative bone mineral analysis using dual energy computed tomography”, Investigative Radiology **12**, 545–551 (1977).
- ¹⁸G. D. Chiro, R. A. Brooks, R. M. Kessler, G. S. Johnston, A. E. Jones, J. R. Herdt, and W. T. Sheridan, “Tissue Signatures with Dual-Energy Computed Tomography”, Radiology **131**, 521–523 (1979).
- ¹⁹H. W. Goo and J. M. Goo, “Dual-energy CT: New horizon in medical imaging”, Korean Journal of Radiology **18**, 555–569 (2017).
- ²⁰T. R. Johnson, “Dual-energy CT: general principles”, American journal of roentgenology **199**, 3–8 (2012).
- ²¹S. Faby, S. Kuchenbecker, S. Sawall, D. Simons, H.-P. Schlemmer, M. Lell, and M. Kachelrieß, “Performance of today’s dual energy CT and future multi energy CT in virtual non-contrast imaging and in iodine quantification: A simulation study”, Medical Physics **42**, 4349–4366 (2015).
- ²²M. M. Koç, N. Aslan, A. P. Kao, and A. H. Barber, “Evaluation of X-ray tomography contrast agents: A review of production, protocols, and biological applications”, Microscopy Research and Technique **82**, 812–848 (2019).
- ²³S. D. Rawson, J. Maksimcuka, P. J. Withers, and S. H. Cartmell, “X-ray computed tomography in life sciences”, BMC Biology **18**, 1–15 (2020).
- ²⁴C. T. Badea, X. Guo, D. Clark, S. M. Johnston, C. D. Marshall, and C. A. Piantadosi, “Dual-energy micro-CT of the rodent lung”, American Journal of Physiology - Lung Cellular and Molecular Physiology **302**, 1088–1097 (2012).
- ²⁵T. Soeda, S. Uemura, Y. Morikawa, K. I. Ishigami, S. Okayama, S. J. Hee, T. Nishida, K. Onoue, S. Somekawa, Y. Takeda, H. Kawata, M. Horii, and Y. Saito, “Diagnostic accuracy of dual-source computed tomography in the characterization of coronary atherosclerotic plaques: Comparison with intravascular optical coherence tomography”, International Journal of Cardiology **148**, 313–318 (2011).

- ²⁶S. Handschuh, C. J. Beisser, B. Ruthensteiner, and B. D. Metscher, “Microscopic dual-energy CT (microDECT): a flexible tool for multichannel ex vivo 3D imaging of biological specimens”, *Journal of Microscopy* **267**, 3–26 (2017).
- ²⁷R. Alvarez and A. Macovski, “Energy-selective reconstructions in X-ray computerized tomography”, *Physics in Medicine and Biology* **21**, 733–744 (1976).
- ²⁸G. Hounsfield, “Computed medical imaging.”, *Journal of Computer Assisted Tomography* **4**, 665–674 (1980).
- ²⁹M. Nikl, “Scintillation detectors for x-rays”, *Measurement Science and Technology* **17**, 37–54 (2006).
- ³⁰D. J. Robbins, “On Predicting the Maximum Efficiency of Phosphor Systems Excited by Ionizing Radiation”, *Journal of The Electrochemical Society* **127**, 2694 (1980).
- ³¹G. Prekas, H. Sabet, H. H. Bhandari, G. Derderian, F. Robertson, H. Kudrolli, C. J. Stapels, J. Christian, S. Kleinfelder, S. Cool, L. J. D’Aries, and V. V. Nagarkar, “Direct and indirect detectors for X-ray photon counting systems”, *IEEE Nuclear Science Symposium Conference Record*, 1487–1493 (2012).
- ³²A. Owens and A. Peacock, “Compound semiconductor radiation detectors”, *Nuclear Instruments and Methods in Physics Research, Section A: Accelerators, Spectrometers, Detectors and Associated Equipment* **531**, 18–37 (2004).
- ³³R. Ballabriga, J. Alozy, M. Campbell, E. Frojdh, E. H. Heijne, T. Koenig, X. Llopart, J. Marchal, D. Pennicard, T. Poikela, L. Tlustos, P. Valerio, W. Wong, and M. Zuber, “Review of hybrid pixel detector readout ASICs for spectroscopic X-ray imaging”, *Journal of Instrumentation* **11**, 1–31 (2016).
- ³⁴S. B. Mahato, J. De Ridder, G. Meynants, G. Raskin, and H. Van Winckel, “Characterization of the per-pixel dark current and activation energy of a large format CMOS image sensor”, 112 (2018).
- ³⁵P. M. Shikhaliev, “Beam hardening artefacts in computed tomography with photon counting, charge integrating and energy weighting detectors: A simulation study”, *Physics in Medicine and Biology* **50**, 5813–5827 (2005).
- ³⁶B. Mikulec, “Development of segmented semiconductor arrays for quantum imaging”, *Nuclear Instruments and Methods in Physics Research, Section A: Accelerators, Spectrometers, Detectors and Associated Equipment* **510**, 1–23 (2003).
- ³⁷M. Campbell, E. H. M. Heijne, G. Meddeler, E. Pemigotti, and W. Snoeys, “Readout for a 64x64 pixel matrix with 15-bit single photon counting”, *Nuclear Science Symposium, 1998. IEEE* **1**, 189–191 (1998).

- ³⁸D. Pacella, “Energy-resolved X-ray detectors: The future of diagnostic imaging”, Reports in Medical Imaging **8**, 1–13 (2015).
- ³⁹R. Ballabriga, J. Alozy, G. Blaj, M. Campbell, M. Fiederle, E. Frojdh, E. H. M. Heijne, X. Llopart, M. Pichotka, S. Procz, L. Tlustos, and W. Wong, “The medipix3RX: A high resolution, zero dead-time pixel detector readout chip allowing spectroscopic imaging”, Journal of Instrumentation **8**, 10.1088/1748-0221/8/02/C02016 (2013).
- ⁴⁰R. Ballabriga, M. Campbell, and X. Llopart, “An introduction to the Medipix family ASICs”, Radiation Measurements **136**, 106271 (2020).
- ⁴¹J. P. Ronaldson, R. Zainon, N. J. A. Scott, S. P. Gieseg, A. P. Butler, P. H. Butler, and N. G. Anderson, “Toward quantifying the composition of soft tissues by spectral CT with Medipix3”, Medical Physics **39**, 6847–6857 (2012).
- ⁴²J. W. Scuffham, M. D. Wilson, P. Seller, M. C. Veale, P. J. Sellin, S. D. Jacques, and R. J. Cernik, “A CdTe detector for hyperspectral SPECT imaging”, Journal of Instrumentation **7**, 10.1088/1748-0221/7/08/P08027 (2012).
- ⁴³P. Seller, S. Bell, R. J. Cernik, C. Christodoulou, C. K. Egan, J. A. Gaskin, S. Jacques, S. Pani, B. D. Ramsey, C. Reid, P. J. Sellin, J. W. Scuffham, R. D. Speller, M. D. Wilson, and M. C. Veale, “Pixellated Cd(Zn)Te high-energy X-ray instrument”, Journal of Instrumentation **6**, 1–11 (2011).
- ⁴⁴M. C. Veale, P. Seller, M. Wilson, and E. Liotti, “HEXITEC: A High-Energy X-ray Spectroscopic Imaging Detector for Synchrotron Applications”, Synchrotron Radiation News **31**, 28–32 (2018).
- ⁴⁵L. Giannoni, F. Lange, and I. Tachtsidis, “Hyperspectral imaging solutions for brain tissue metabolic and hemodynamic monitoring: Past, current and future developments”, Journal of Optics (United Kingdom) **20**, 10.1088/2040-8986/aab3a6 (2018).
- ⁴⁶D. Walter, U. Zscherpel, and U. Ewert, “Photon Counting and Energy Discriminating X-Ray Detectors - Benefits and Applications”, 19th World Conference on Non-Destructive Testing, Proceedings, 1–10 (2016).
- ⁴⁷T. G. Schmidt, “Optimal ”image-based” weighting for energy-resolved CT”, Medical Physics **36**, 3018–3027 (2009).
- ⁴⁸J. Berglund, H. Johansson, M. Lundqvist, B. Cederström, and E. Fredenberg, “Energy weighting improves dose efficiency in clinical practice: implementation on a spectral photon-counting mammography system”, Journal of Medical Imaging **1**, 031003 (2014).
- ⁴⁹M. J. Willemink, M. Persson, A. Pourmorteza, N. J. Pelc, and D. Fleischmann, “Photon-counting CT: Technical principles and clinical prospects”, Radiology **289**, 293–312 (2018).

- ⁵⁰E. Roessl, B. Brendel, K. J. Engel, J. P. Schlomka, A. Thran, and R. Proksa, “Sensitivity of photon-counting based K-Edge Imaging in X-ray computed tomography”, *IEEE Transactions on Medical Imaging* **30**, 1678–1690 (2011).
- ⁵¹T. Flohr, M. Petersilka, A. Henning, S. Ulzheimer, J. Ferda, and B. Schmidt, “Photon-counting CT review”, *Physica Medica* **79**, 126–136 (2020).
- ⁵²M. C. Veale, S. J. Bell, D. D. Duarte, A. Schneider, P. Seller, M. D. Wilson, and K. Iniewski, “Measurements of charge sharing in small pixel CdTe detectors”, *Nuclear Instruments and Methods in Physics Research, Section A: Accelerators, Spectrometers, Detectors and Associated Equipment* **767**, 218–226 (2014).
- ⁵³K. Iniewski, H. Chen, G. Bindley, I. Kuvvetli, and C. Budtz-Jørgensen, “Modeling charge-sharing effects in pixellated CZT detectors”, *IEEE Nuclear Science Symposium Conference Record* **6**, 4608–4611 (2007).
- ⁵⁴M. Krumrey, M. Gerlach, F. Scholze, and G. Ulm, “Calibration and characterization of semiconductor X-ray detectors with synchrotron radiation”, *Nuclear Instruments and Methods in Physics Research, Section A: Accelerators, Spectrometers, Detectors and Associated Equipment* **568**, 364–368 (2006).
- ⁵⁵A. Krzyzanowska, G. W. Deptuch, P. Maj, P. Grybos, and R. Szczygiel, “Characterization of the Photon Counting CHASE Jr., Chip Built in a 40-nm CMOS Process with a Charge Sharing Correction Algorithm Using a Collimated X-Ray Beam”, *IEEE Transactions on Nuclear Science* **64**, 2561–2568 (2017).
- ⁵⁶E. Frojdh, R. Ballabriga, M. Campbell, M. Fiederle, E. Hamann, T. Koenig, X. Llopart, D. D. P. Magalhaes, and M. Zuber, “Count rate linearity and spectral response of the Medipix3RX chip coupled to a 300 μ m silicon sensor under high flux conditions”, *Journal of Instrumentation* **9**, 10.1088/1748-0221/9/04/C04028 (2014).
- ⁵⁷J. Radon, “On the Determination of Functions From Their Integral Values Along Certain Manifolds”, *IEEE Transactions on Medical Imaging* **5**, 170–176 (1986).
- ⁵⁸V. Van Nieuwenhove, J. De Beenhouwer, F. De Carlo, L. Mancini, F. Marone, and J. Sibbers, “Dynamic intensity normalization using eigen flat fields in X-ray imaging”, *Optics Express* **23**, 27975 (2015).
- ⁵⁹L. A. Shepp and B. F. Logan, “The Fourier Reconstruction of a Head Section”, *IEEE Transactions on Nuclear Science* **21**, 21–43 (1974).
- ⁶⁰S. Van Der Walt, J. L. Schönberger, J. Nunez-Iglesias, F. Boulogne, J. D. Warner, N. Yager, E. Gouillart, and T. Yu, “Scikit-image: Image processing in python”, *PeerJ* **2014**, 1–18 (2014).

- ⁶¹R. Schofield, L. King, U. Tayal, I. Castellano, J. Stirrup, F. Pontana, J. Earls, and E. Nicol, “Image reconstruction: Part 1 – understanding filtered back projection, noise and image acquisition”, *Journal of Cardiovascular Computed Tomography* **14**, 219–225 (2020).
- ⁶²S. Zhao, K. Yang, and K. Yang, “Fan beam image reconstruction with generalized fourier slice theorem”, *Journal of X-Ray Science and Technology* **22**, 415–436 (2014).
- ⁶³G. N. Ramachandran and A. V. Lakshminarayanan, “Three-dimensional reconstruction from radiographs and electron micrographs: application of convolutions instead of Fourier transforms.”, *Proceedings of the National Academy of Sciences of the United States of America* **68**, 2236–2240 (1971).
- ⁶⁴L. Feldkamp, L. C. Davis, and J. Kress, “Practical cone-beam algorithm”, *Journal of the Optical Society of America* **1**, 612–619 (1984).
- ⁶⁵A. C. Kak and M. Slaney, *Principles of Computerized Tomographic Imaging*, 1st (IEEE Press, 1988), pp. 275–296.
- ⁶⁶P. Gajjar, J. S. Jørgensen, J. R. Godinho, C. G. Johnson, A. Ramsey, and P. J. Withers, “New software protocols for enabling laboratory based temporal CT”, *Review of Scientific Instruments* **89**, 10.1063/1.5044393 (2018).
- ⁶⁷Mark Tseytlin, A. Dhami, S. S. Eaton, and G. R. Eaton, “Comparison of Maximum Entropy and Filtered Back-Projection Methods to Reconstruct Rapid-Scan EPR Images”, *Journal of Magnetic Resonance* **184**, 157–168 (2007).
- ⁶⁸R. Gordon, R. Bender, and G. T. Herman, “Algebraic Reconstruction Techniques (ART) for three-dimensional electron microscopy and X-ray photography”, *Journal of Theoretical Biology* **29**, 471–481 (1970).
- ⁶⁹R. C. Nelson, S. Feuerlein, and D. T. Boll, “New iterative reconstruction techniques for cardiovascular computed tomography: How do they work, and what are the advantages and disadvantages?”, *Journal of Cardiovascular Computed Tomography* **5**, 286–292 (2011).
- ⁷⁰M. Lohvithee, “Iterative reconstruction technique for cone-beam computed tomography with limited data”, PhD thesis (2016).
- ⁷¹S. Kaczmarz, “Angenäherte auflösung von systemen linearer Gleichungen”, *International Bulletin of the Polish Academy of Sciences and Letters* **35**, 355–357 (1937).
- ⁷²P. Gilbert, “Iterative Methods for the Three-dimensional Reconstruction of an Object from Projections”, *Journal of Theoretical Biology* **36**, 105–117 (1972).

- ⁷³M. Hestenes and E. Stiefel, “Methods of conjugate gradients for solving linear systems”, *Journal of Research of the National Bureau of Standards* **49**, 409 (1952).
- ⁷⁴S. L. Fisher, “Improved identification of illicit materials using an X-ray backscattering technique”, PhD thesis (University of Manchester, 2021), pp. 150–151.
- ⁷⁵J. Nagy and Z. Strakos, “Enforcing nonnegativity in image reconstruction algorithms”, *Proceedings SPIE Mathematical Modeling, Estimation, and Imaging* **4121**, 182–190 (2000).
- ⁷⁶M. J. Ehrhardt, K. Thielemans, L. Pizarro, D. Atkinson, S. Ourselin, B. F. Hutton, and S. R. Arridge, “Joint reconstruction of PET-MRI by exploiting structural similarity”, *Inverse Problems* **31**, 1–23 (2015).
- ⁷⁷J. Rasch, E. M. Brinkmann, and M. Burger, “Joint reconstruction via coupled Bregman iterations with applications to PET-MR imaging”, *Inverse Problems* **34**, 1–39 (2018).
- ⁷⁸C. K. Egan, S. D. M. Jacques, M. D. Wilson, M. C. Veale, P. Seller, R. A. Pattrick, P. J. Withers, and R. J. Cernik, “3D elemental mapping of materials and structures by laboratory scale spectroscopic X-ray tomography”, *Journal of Physics: Conference Series* **849**, doi.org/10.1088/1742-6596/849/1/012013 (2017).
- ⁷⁹D. Kazantsev, J. S. Jørgensen, M. S. Andersen, W. R. Lionheart, P. D. Lee, and P. J. Withers, “Joint image reconstruction method with correlative multi-channel prior for x-ray spectral computed tomography”, *Inverse Problems* **34**, 1–27 (2018).
- ⁸⁰L. I. Rudin, S. Osher, and E. Fatemi, “Nonlinear total variation based noise removal algorithms”, *Physica D* **60**, 259–268 (1992).
- ⁸¹J. C. De los Reyes, C. B. Schönlieb, and T. Valkonen, “Bilevel Parameter Learning for Higher-Order Total Variation Regularisation Models”, *Journal of Mathematical Imaging and Vision* **57**, 1–25 (2017).
- ⁸²E. Y. Sidky, C. M. Kao, and X. Pan, “Accurate image reconstruction from few-views and limited-angle data in divergent-beam CT”, *Journal of X-Ray Science and Technology* **14**, 119–139 (2006).
- ⁸³T. Chan, S. Esedoglu, F. Park, and A. Yip, “Recent Developments in Total Variation Image Restoration”, in *Mathematical methods in scattering theory and biomedical engineering: proc. of the 7th int. workshop (nymphaio, greece, 8–11 september 2005)* (2005), pp. 1–8.
- ⁸⁴D. S. Rigie and P. J. La Rivière, “Joint reconstruction of multi-channel, spectral CT data via constrained total nuclear variation minimization”, *Physics in Medicine and Biology* **60**, 1741–1762 (2015).

- ⁸⁵E. Ametova, G. Burca, S. Chilingaryan, G. Fardell, J. S. J rgensen, E. Papoutsellis, E. Pasca, R. Warr, M. Turner, W. R. Lionheart, and P. J. Withers, “Crystalline phase discriminating neutron tomography using advanced reconstruction methods”, *Journal of Physics D: Applied Physics* **54**, 10.1088/1361-6463/ac02f9 (2021).
- ⁸⁶K. Bredies, K. Kunisch, and T. Pock, “Total generalized variation”, *SIAM Journal on Imaging Sciences* **3**, 492–526 (2010).
- ⁸⁷F. Knoll, K. Bredies, T. Pock, and R. Stollberger, “Second Order Total Generalized Variation (TGV) for MRI”, *Magnetic Resonance in Medicine* **65**, 480–491 (2011).
- ⁸⁸R. Foygel Barber, E. Y. Sidky, T. Gilat Schmidt, and X. Pan, “An algorithm for constrained one-step inversion of spectral CT data”, *Physics in Medicine and Biology* **61**, 3784–3818 (2016).
- ⁸⁹Q. Xu, A. Sawatzky, M. A. Anastasio, and C. O. Schirra, “Sparsity-regularized image reconstruction of decomposed K-edge data in spectral CT”, *Physics in Medicine and Biology* **59**, 64–79 (2014).
- ⁹⁰O. Semerci, N. Hao, M. E. Kilmer, and E. L. Miller, “Tensor-based formulation and nuclear norm regularization for multienergy computed tomography”, *IEEE Transactions on Image Processing* **23**, 1678–1693 (2014).
- ⁹¹J. Evans, *X-ray absorption spectroscopy for the chemical and materials sciences* (2018), pp. 10–20.
- ⁹²C. K. Egan, S. D. M. Jacques, M. D. Wilson, M. C. Veale, P. Seller, A. M. Beale, R. A. D. Patrick, P. J. Withers, and R. J. Cernik, “3D chemical imaging in the laboratory by hyperspectral X-ray computed tomography”, *Scientific Reports* **5**, 1–9 (2015).
- ⁹³S. D. M. Jacques, C. K. Egan, M. D. Wilson, M. C. Veale, P. Seller, and R. J. Cernik, “A laboratory system for element specific hyperspectral X-ray imaging”, *Analyst* **138**, 755–759 (2013).
- ⁹⁴B. Vekemans, K. Janssens, L. Vincze, A. Aerts, F. Adams, and J. Hertogen, “Automated Segmentation of μ -XRF Image Sets”, *X-Ray Spectrometry* **26**, 333–346 (1997).
- ⁹⁵A. M. Beale, S. D. M. Jacques, J. A. Bergwerff, P. Barnes, and B. M. Weckhuysen, “Tomographic energy dispersive diffraction imaging as a tool to profile in three dimensions the distribution and composition of metal oxide species in catalyst bodies”, *Angewandte Chemie - International Edition* **46**, 8832–8835 (2007).
- ⁹⁶G. Tomasi, F. Van Den Berg, and C. Andersson, “Correlation optimized warping and dynamic time warping as preprocessing methods for chromatographic data”, *Journal of Chemometrics* **18**, 231–241 (2004).

- ⁹⁷W. Vågberg, J. C. Larsson, and H. M. Hertz, “Removal of ring artifacts in microtomography by characterization of scintillator variations”, *Optics Express* **25**, 23191–23198 (2017).
- ⁹⁸B. Münch, P. Trtik, F. Marone, and M. Stampanoni, “Stripe and ring artifact removal with combined wavelet-Fourier filtering”, *Optical Society of America* **17**, 8567–8591 (2009).
- ⁹⁹M. N. Boone, J. Garrevoet, P. Tack, O. Scharf, D. P. Cormode, D. V. Loo, E. Pauwels, M. Dierick, L. Vincze, and L. V. Hoorebeke, “High spectral and spatial resolution x-ray transmission radiography and tomography using a color x-ray camera”, *Nuclear Instruments and Methods in Physics Research, Section A: Accelerators, Spectrometers, Detectors and Associated Equipment* **735**, 644–648 (2014).
- ¹⁰⁰O. Scharf, S. Ihle, I. Ordavo, V. Arkadiev, A. Bjeoumikhov, S. Bjeoumikhova, G. Buzanich, R. Gubzhokov, A. Günther, R. Hartmann, M. Kühbacher, M. Lang, N. Langhoff, A. Liebel, M. Radtke, U. Reinholz, H. Riesemeier, H. Soltau, L. Strüder, A. F. Thünemann, and R. Wedell, “Compact pnccd-based x-ray camera with high spatial and energy resolution: a color x-ray camera”, *Analytical Chemistry* **83**, 2532–2538 (2011).
- ¹⁰¹H. Ghadiri, M. R. Ay, M. B. Shiran, H. Soltanian-Zadeh, and H. Zaidi, “K-edge ratio method for identification of multiple nanoparticulate contrast agents by spectral ct imaging”, *British Journal of Radiology* **86**, 10.1259/bjr.20130308 (2013).
- ¹⁰²D. Muenzel, M. Bartels, F. K. Kopp, B. Brendel, R. Proksa, and P. Douek, “Spectral photon-counting ct : initial experience with dual – contrast agent k-edge colonography”, *Radiology* **283** (2017).
- ¹⁰³J. Dangelmaier, D. Bar-Ness, H. Daerr, D. Muenzel, S. Si-Mohamed, S. Ehn, A. A. Fingerle, M. A. Kimm, F. K. Kopp, L. Boussel, E. Roessl, F. Pfeiffer, E. J. Rummeny, R. Proksa, P. Douek, and P. B. Noël, “Experimental feasibility of spectral photon-counting computed tomography with two contrast agents for the detection of endoleaks following endovascular aortic repair”, *European Radiology* **28**, 3318–3325 (2018).
- ¹⁰⁴S. Si-Mohamed, D. Bar-Ness, M. Sigovan, V. Tatard-Leitman, D. P. Cormode, P. C. Naha, P. Coulon, L. Rasclé, E. Roessl, M. Rokni, A. Altman, Y. Yagil, L. Boussel, and P. Douek, “Multicolour imaging with spectral photon-counting ct: a phantom study”, *European Radiology Experimental* **2**, 10.1186/s41747-018-0063-4 (2018).
- ¹⁰⁵R. Symons, B. Krauss, P. Sahbaee, T. E. Cork, M. N. Lakshmanan, D. A. Bluemke, and A. Pourmorteza, “Photon-counting ct for simultaneous imaging of multiple contrast agents in the abdomen: an in vivo study”, *Medical Physics* **44**, 5120–5127 (2017).

- ¹⁰⁶D. P. Cormode, S. Si-Mohamed, D. Bar-Ness, M. Sigovan, P. C. Naha, J. Balegamire, F. Lavenne, P. Coulon, E. Roessl, M. Bartels, M. Rokni, I. Blevis, L. Boussel, and P. Douek, “Multicolor spectral photon-counting computed tomography: in vivo dual contrast imaging with a high count rate scanner”, *Scientific Reports* **7**, 1–11 (2017).
- ¹⁰⁷S. Si-Mohamed, V. Tatard-Leitman, A. Laugere, M. Sigovan, D. Pfeiffer, E. J. Rummeny, P. Coulon, Y. Yagil, P. Douek, L. Boussel, and P. B. Noël, “Spectral photon-counting computed tomography (spcct): in-vivo single-acquisition multi-phase liver imaging with a dual contrast agent protocol”, *Scientific Reports* **9**, 1–8 (2019).
- ¹⁰⁸N. G. Anderson, A. P. Butler, N. J. Scott, N. J. Cook, J. S. Butzer, N. Schleich, M. Firsching, R. Grasset, N. De Ruiter, M. Campbell, and P. H. Butler, “Spectroscopic (multi-energy) CT distinguishes iodine and barium contrast material in MICE”, *European Radiology* **20**, 2126–2134 (2010).
- ¹⁰⁹V. S. K. Yokhana, B. D. Arhatari, T. E. Gureyev, and B. Abbey, “Soft-tissue differentiation and bone densitometry via energy-discriminating X-ray microCT”, *Optics Express* **25**, 29328 (2017).
- ¹¹⁰R. Bellazzini, G. Spandre, A. Brez, M. Minuti, M. Pinchera, and P. Mozzo, “Chromatic x-ray imaging with a fine pitch cdte sensor coupled to a large area photon counting pixel asic”, in , Vol. 8 (Feb. 2013).
- ¹¹¹J. Kosanetzky, B. Knoerr, G. Harding, and U. Neitzel, “X ray diffraction measurements of some plastic materials and body tissues”, *Medical Physics* **14**, 526–532 (1987).
- ¹¹²G. Harding, “Energy-dispersive X-ray diffraction tomography”, *Physics in Medicine and Biology* **35**, 33–41 (1990).
- ¹¹³C. Crews, P. S. Kenny, D. O’Flynn, and R. D. Speller, “Multivariate calibration of energy-dispersive X-ray diffraction data for predicting the composition of pharmaceutical tablets in packaging”, *Journal of Pharmaceutical and Biomedical Analysis* **151**, 186–193 (2018).
- ¹¹⁴C. Hall, P. Barnes, J. K. Cockcroft, S. L. Colston, D. Häusermann, S. D. M. Jacques, A. C. Jupe, and M. Kunz, “Synchrotron energy-dispersive X-ray diffraction tomography”, *Nuclear Instruments and Methods in Physics Research, Section B: Beam Interactions with Materials and Atoms* **140**, 253–257 (1998).
- ¹¹⁵K. H. Khor and R. J. Cernik, “A new, rapid 3D tomographic energy dispersive diffraction imaging system for materials characterization and object imaging (rapid TEDDI)”, *AIP Conference Proceedings* **879**, 1747–1750 (2007).

- ¹¹⁶P. Barnes, A. C. Jupe, S. L. Colston, S. D. M. Jacques, A. Grant, T. Rathbone, M. Miller, S. M. Clark, and R. J. Cernik, “A new three-angle energy-dispersive diffractometer”, Nuclear Instruments and Methods in Physics Research, Section B: Beam Interactions with Materials and Atoms **134**, 310–313 (1998).
- ¹¹⁷P. Barnes, S. Colston, B. Craster, C. Hall, A. Jupe, S. Jacques, J. Cockcroft, S. Morgan, M. Johnson, D. O’connor, and M. Bellotto, *Time-and space-resolved dynamic studies on ceramic and cementitious materials* (2000), pp. 167–177.
- ¹¹⁸C. Hall, S. L. Colston, A. C. Jupe, S. D. M. Jacques, R. Livingston, A. O. Ramadan, A. W. Amde, and P. Barnes, “Non-destructive tomographic energy-dispersive diffraction imaging of the interior of bulk concrete”, Cement and Concrete Research **30**, 491–495 (2000).
- ¹¹⁹A. Jupe, X. Turrillas, P. Barnes, S. Colston, and C. Hall, “Fast in situ x-ray-diffraction studies of chemical reactions: A synchrotron view of the hydration of tricalcium aluminate”, Physical Review B - Condensed Matter and Materials Physics **53**, R14697–R14700 (1996).
- ¹²⁰R. J. Cernik, R. Freer, C. Leach, C. Mongkolkachit, P. Barnes, S. Jacques, K. Pile, and A. Wander, “Direct correlation between ferrite microstructure and electrical resistivity”, Journal of Applied Physics **101**, 10.1063/1.2735400 (2007).
- ¹²¹R. J. Cernik, C. C. Hansson, C. M. Martin, M. Preuss, M. Attallah, A. M. Korsunsky, J. P. Belnoue, T. S. Jun, P. Barnes, S. Jacques, T. Sochi, and O. Lazzari, “A synchrotron tomographic energy-dispersive diffraction imaging study of the aerospace alloy ti 6246”, Journal of Applied Crystallography **44**, 150–157 (2011).
- ¹²²C. K. Egan, S. D. M. Jacques, M. D. Wilson, M. C. Veale, P. Seller, and R. J. Cernik, “Dark-field hyperspectral X-ray imaging”, Proceedings of the Royal Society A **470**, 1–9 (2014).
- ¹²³R. S. Mishra, M. W. Mahoney, Y. Sato, and Y. Hovanski, “Friction stir welding and processing”, Materials Science and Engineering: R: Reports **50**, 1–78 (2005).
- ¹²⁴C. K. Egan, S. D. M. Jacques, M. D. Wilson, M. C. Veale, P. Seller, P. J. Withers, and R. J. Cernik, “Full-field energy-dispersive powder diffraction imaging using laboratory x-rays”, Journal of Applied Crystallography **48**, 269–272 (2015).
- ¹²⁵E. Dahal, B. Ghammraoui, M. Ye, J. C. Smith, and A. Badano, “Label-free X-ray estimation of brain amyloid burden”, Scientific Reports **10**, 1–6 (2020).

- ¹²⁶T. Connolley, O. V. Magdysyuk, S. Michalik, P. K. Allan, M. Klaus, P. H. Kamm, F. G. Moreno, J. A. Nelson, M. C. Veale, and M. D. Wilson, “An operando spatially resolved study of alkaline battery discharge using a novel hyperspectral detector and x-ray tomography”, *Journal of Applied Crystallography* **53**, 1434–1443 (2020).
- ¹²⁷M. D. De Jonge and S. Vogt, “Hard X-ray fluorescence tomography-an emerging tool for structural visualization”, *Current Opinion in Structural Biology* **20**, 606–614 (2010).
- ¹²⁸J. P. Hogan, R. A. Gonsalves, and A. S. Krieger, “Fluorescent Computer Tomography : A Model for Correction of X-Ray Absorption”, *Transactions on Nuclear Science* **38**, 1721–1727 (1991).
- ¹²⁹N. K. Blute, D. J. Brabander, H. F. Hemond, S. R. Sutton, M. G. Newville, and M. L. Rivers, “Arsenic sequestration by ferric iron plaque on cattail roots”, *Environmental Science and Technology* **38**, 6074–6077 (2004).
- ¹³⁰S. A. Kim, T. Punshon, A. Lanzirotti, L. Li, J. M. Alonso, J. R. Ecker, J. Kaplan, and M. L. Guerinot, “Localization of iron in arabidopsis seed requires the vacuolar membrane transporter vit1”, *Science* **314**, 1295–1298 (2006).
- ¹³¹I. Ordavo, S. Ihle, V. Arkadiev, O. Scharf, H. Soltau, A. Bjeoumikhov, S. Bjeoumikhova, G. Buzanich, R. Gubzhokov, A. Günther, R. Hartmann, P. Holl, N. Kimmel, M. Kühbacher, M. Lang, N. Langhoff, A. Liebel, M. Radtke, U. Reinholz, H. Riesemeier, G. Schaller, F. Schopper, L. Strüder, C. Thamm, and R. Wedell, “A new pnccd-based color x-ray camera for fast spatial and energy-resolved measurements”, *Nuclear Instruments and Methods in Physics Research, Section A: Accelerators, Spectrometers, Detectors and Associated Equipment* **654**, 250–257 (2011).
- ¹³²P. Bleuet, P. Gergaud, L. Lemelle, P. Bleuet, R. Tucoulou, P. Cloetens, J. Susini, G. Delette, and A. Simionovici, “3d chemical imaging based on a third-generation synchrotron source”, *TrAC - Trends in Analytical Chemistry* **29**, 518–527 (2010).
- ¹³³M. J. Pushie, I. J. Pickering, M. Korbas, M. J. Hackett, and G. N. George, “Elemental and chemically specific x-ray fluorescence imaging of biological systems”, *Chemical Reviews* **114**, 8499–8541 (2014).
- ¹³⁴C. K. Egan, M. D. Wilson, M. C. Veale, P. Seller, S. D. M. Jacques, and R. J. Cernik, “Material specific X-ray imaging using an energy-dispersive pixel detector”, *Nuclear Instruments and Methods in Physics Research, Section B: Beam Interactions with Materials and Atoms* **324**, 25–28 (2014).

Chapter 3

Materials and Methods

This chapter details the equipment used and samples created in order to conduct the X-ray scanning, reconstruction and analysis for the research conducted in this thesis. Two lab-based X-ray scanning systems were utilised throughout the research, both based in the Henry Moseley X-ray Imaging Facility (HMXIF) at the University of Manchester. As described below, each system required its own level of testing, development, and optimisation in order to implement the bright-field imaging modality with the energy-sensitive detector. This chapter provides a breakdown of the experimental systems used, and details the workflow developed to enable spectral X-ray CT for both a custom-built and commercial X-ray system.

For Chapters 4 and 5, the same hyperspectral detector (HEXITEC) was used for all energy-sensitive studies. This chapter describes in depth a full characterisation of the HEXITEC detector used in the experimental work, including all calibration and pre-processing steps applied prior to any X-ray scan acquisition. The properties are compared to the ideal working conditions and parameters of a standard HEXITEC system. Performance of the detector is further evaluated through analysing the various forms of detector 'cross-talk', including pulse pile-up and charge sharing, as previously discussed in Section 2.2.3.

Full details are also provided for the samples used in Chapters 4 and 5, including all biological specimens and their staining procedures, as well as each custom-made phantom object.

3.1 Laboratory X-ray scanning systems

The first X-ray system used was the custom-built, walk-in "Colour Bay" system, designed for different modalities of spectroscopic X-ray imaging and tomography. A photograph of the standard set-up is shown in Fig. 3.1.1. A work bench was installed to allow for adjustments of the imaging set-up, depending on the desired imaging mode. The fundamental system set-up contained the three key components required for X-ray tomography: an X-ray source, a rotation/sample stage, and an X-ray detector. Additional components such as tubing to reduce X-ray scatter, and beam slits for collimation of the incident beam, were also available. For the Colour Bay, a GE ISOVOLT Titan E generator was installed. A Comet 225HP/11 X-ray tube was used, with a Tungsten target for X-ray generation. A spot size of 1 mm was used, with a maximum achievable power of 1800 W, and a full working energy range from 5 – 225 kV. The source was controlled via a control panel, which enabled ad-

justment of both beam voltage and current, with a lower limit of 5 kV and 0.1 mA, equating to a power of 0.5 W. The X-ray tube was water-cooled with a heat exchange chiller. Full product specifications of both the generator and X-ray tube may be found elsewhere [1, 2]. The sample stage consisted of three individual motor stages: a rotation stage to conduct full 360° rotation of a sample for X-ray CT acquisition, and two translation stages for vertical and horizontal movement required prior to, or during, scanning. The stages were controlled by a programmable ‘Galil Motion Control’ box [3], with custom scripts developed in MATLAB to allow full user control of the sample position. Such scripts were updated by the author (Ryan Warr) to ensure full working operation.

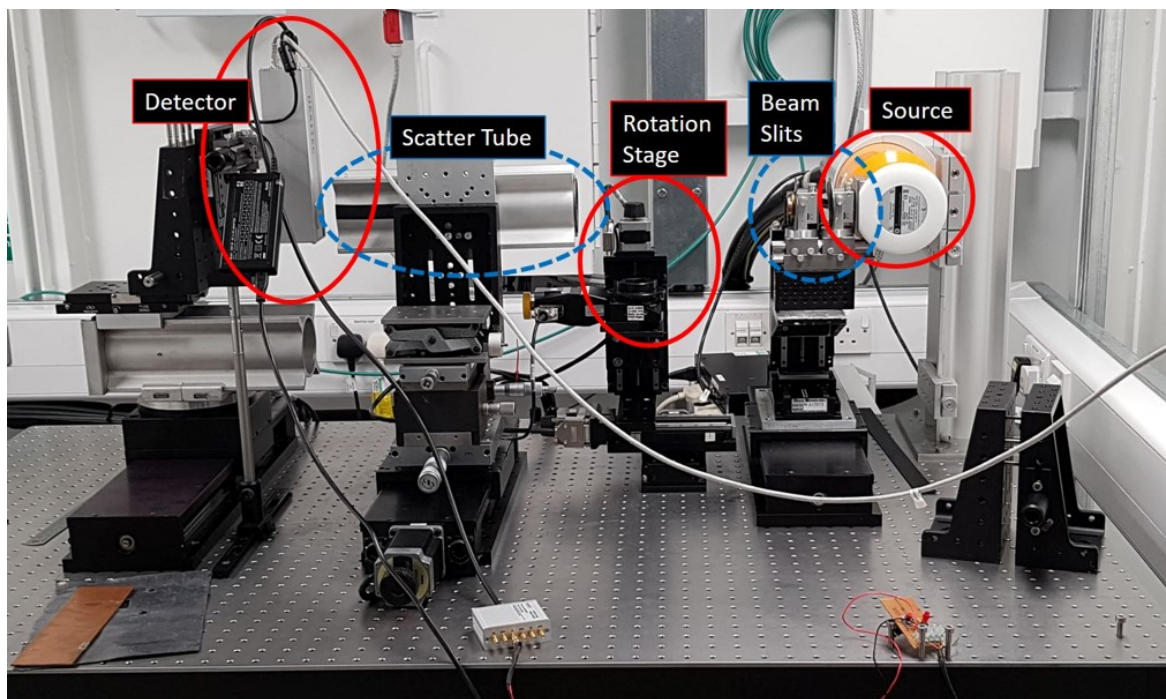


Figure 3.1.1. Standard experimental set-up of the X-ray system within the ‘Colour Bay’ walk-in hutch, situated at the HMXIF. Key components (red circles) are the source, rotation/sample stage, and the detector. Additional components (blue dashed circles) may be included or varied to fine-tune the imaging procedure. These include a tube for reduction of X-ray scatter, and beam slits to collimate the incident beam.

A secondary walk-in bay known as the “High Flux Bay” (HFB) was used, containing a conventional flat-panel, energy-integrating detector for XCT. The HFB, also based at the HMXIF, was a commercial Nikon 320/225 kV XTEK system, with interchangeable X-ray sources to suit the needs of the user. For all work in this thesis, the 225 kV source was used, with X-ray current stable down to 10 μ A. Full flexibility in X-ray source settings, along with sample stage and detector motion control, were enabled by the Nikon Inspect-X software. In order to conduct spectroscopic imaging within the Nikon system, the HEXITEC detector was installed in a parallel configuration with the source and sample stage, as shown in Fig. 3.1.2, such that the source, sample and detector were all aligned along the same bright-field imaging plane.

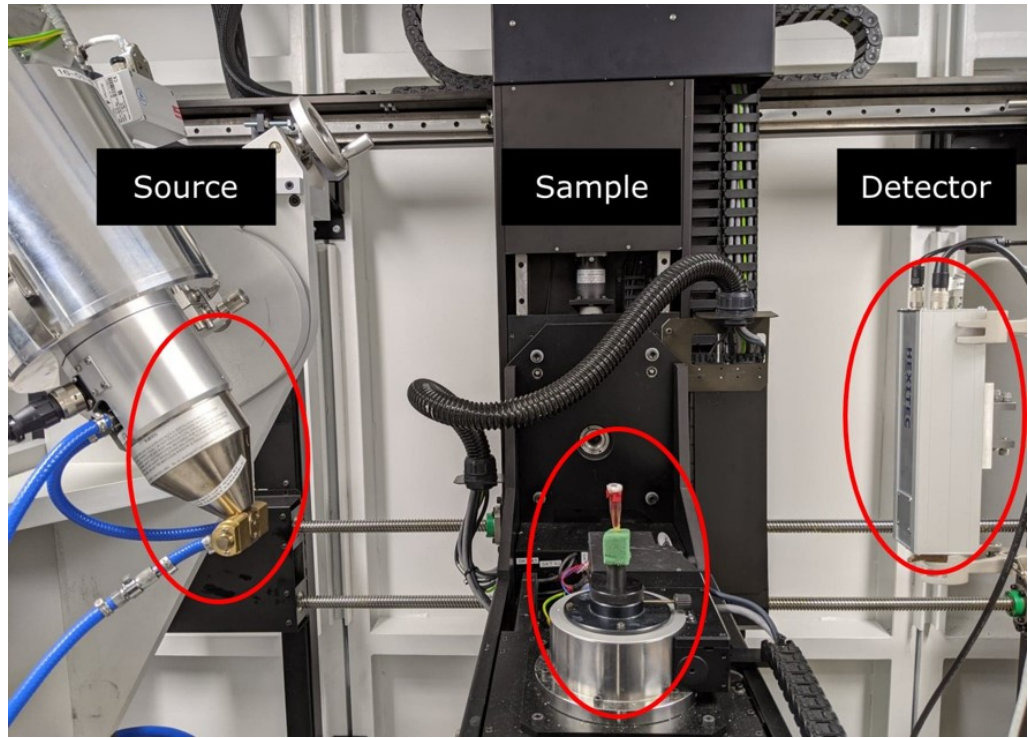


Figure 3.1.2. Standard experimental set-up of the hyperspectral X-ray system within the 'High Flux Bay' walk-in hutch, situated at the HMXIF. Key components (red circles) are the source, rotation/sample stage, and the spectroscopic detector. The built-in energy-integrating detector is out of view, behind the HEXITEC along the same imaging plane.

3.2 Hyperspectral (HEXITEC) detector

All experimentation and research concerning energy-sensitive X-ray tomographic imaging was performed using the HEXITEC hyperspectral detector system. The HEXITEC is a pixelated, single photon counting (SPC) X-ray detector designed to process and measure incident photon energy at a high resolution, as well as the position on a pixel-by-pixel basis. A photograph of the HEXITEC device is shown in Fig. 3.2.1. The detector sensor chip consisted of a 1 mm thick CdTe single-crystal semiconductor, which was bump-bonded to an application specific integrated circuit (ASIC), producing a total detection area of $2\text{ cm} \times 2\text{ cm}$. The pixel array consisted of 80×80 pixels, with a pixel pitch of $250\text{ }\mu\text{m}$ ($200\text{ }\mu\text{m}$ pixel pad with a $50\text{ }\mu\text{m}$ inter-pixel gap [4]). An additional 1 mm aluminium plate can also be added as a filter over the detector sensor. Table 3.2.1 provides a summary of the main characteristics of the HEXITEC detector, with specifications taken from the HEXITEC specification data sheet [5], articles related to the development of the detector system, and a 2016 review of currently available spectral detector systems [4, 6–8]. The table therefore provided optimum working parameters for the detector, however some aspects of the detector, such as energy resolution, vary over time and thus required testing for the specific device. Such investigations are described in greater detail below in Section 3.2.1. The system ran off a 12 V power supply, while data transfer was performed using a GigE Ethernet connection from the device to a control PC, where the HEXITEC software was installed and enabled raw spectroscopic images to be viewed.

When an incident X-ray photon reaches the HEXITEC sensor and interacts with the CdTe

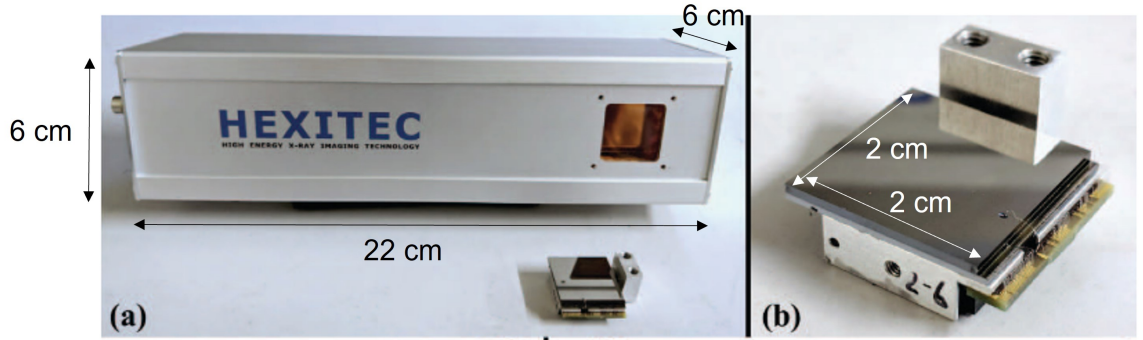


Figure 3.2.1. Photographs of the HEXITEC hyperspectral detector. (a) Complete HEXITEC unit, with the CdTe sensor removed. Measurements of the full detector device are included. (b) Close-up of the CdTe sensor with scale included [4].

semiconductor crystal, a number of electron-hole (e-h) pairs are generated, in the form of a 'charge cloud'. For a CdTe sensor, an e-h pair is produced for every 4.4 eV of the incident X-ray photon energy [9]. In the case of the HEXITEC, a 'bias voltage' of -500 V is applied across the detector to create an external electric field, enabling the charge cloud to drift towards the electrodes. Due to their improved charge mobility, it is the electrons which are measured to form the detector signal, as is true for most CdTe-based detectors [9]. In order to extract energy-based information, the key component of the HEXITEC is the ASIC, designed to match the layout of the sensor chip (6400 pixellated elements over the 80×80 array). The CdTe material is bump-bonded to the ASIC using gold stud and silver epoxy flip-chip bonding. Each pixel of the ASIC has its own electronics, with a diagram shown in Fig. 3.2.2. The circuit uses a charge sensitive pre-amplifier in order to integrate the current signal and generate a proportional voltage. The output signal is shaped with a shaping amplifier and, following high-frequency noise filtration, the peak signal is held until measured by the readout circuit. The total peaking time of the signal is approximately 2 μ s. As the signal in each pixel is processed and measured, a 'frame' of data is built across the pixel array. The stored analogue signals are then read out for each row of the detector, at a frame rate of up to 8.9 kHz, and converted to digitised values [4]. Once transferred to the control PC via Ethernet connection, the software represents the data as a histogram in each pixel, distributing photon events into narrow energy channels, based on the calculated energies in the detector ASIC.

Semiconductor Material	Pixel Size (μm^2)	Pixel Number	Detection Efficiency
1 mm CdTe	250×250	80×80	\approx 100% at 40 keV \approx 40% at 140 keV
Max Counts (Mcps/Pixel)	Energy Channels	Working Energy Range (keV)	Energy Resolution
0.001	~200-800	4-200 keV	~800 eV at 59.9 keV ~1.5 keV at 141 keV

Table 3.2.1. Summary of the technical specifications for the HEXITEC detector system. Detector specification values obtained from the HEXITEC data sheet [5] and relevant published literature on the device development [4, 6–8].

As described above, the HEXITEC was installed in both the Colour Bay and HFB systems, based on the samples under investigation and X-ray settings required. The HFB X-ray source offered up to 10× lower beam current, and therefore the system was prefer-

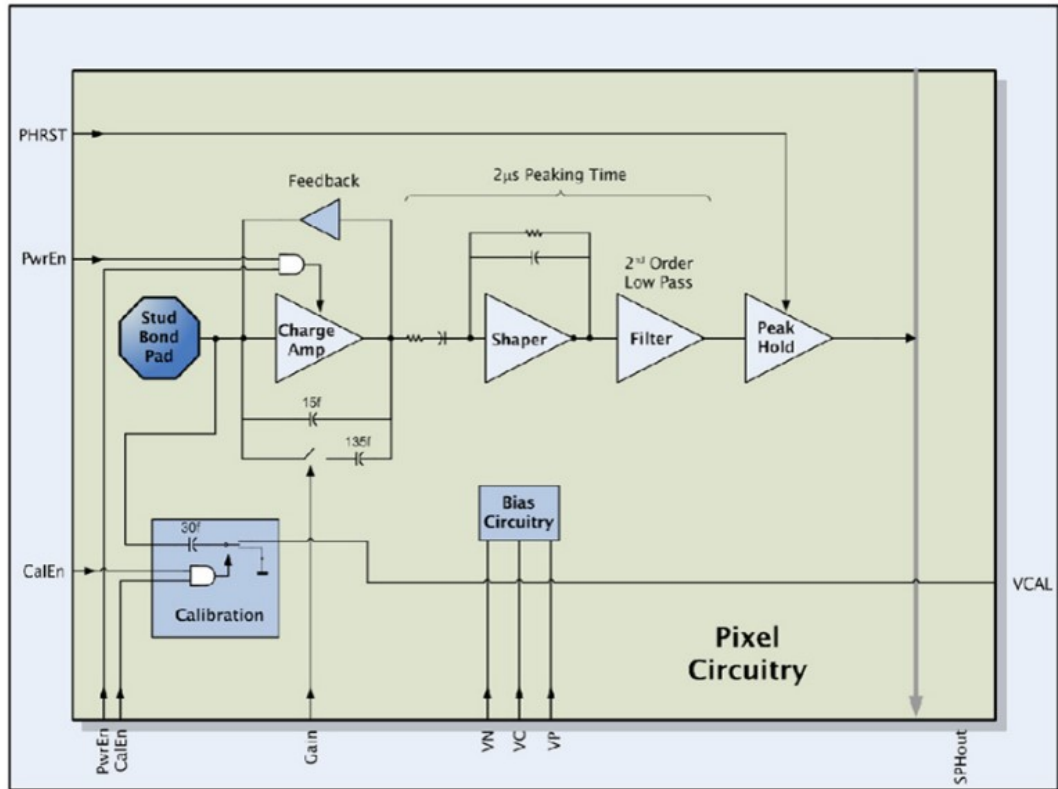


Figure 3.2.2. Diagram of the circuitry in each pixel of the HEXITEC ASIC. All core components, including the pre-amplifier, shaping, and filter electronics, as well as the peak-hold system, are labelled. In addition, the bias circuitry enables the detector to be held at a pre-defined voltage. A calibration circuit allows characterisation of the pixel electronics [10].

able for the study of biological specimens, given their lower overall attenuation in soft tissue regions, even after chemical staining with contrast enhancers. In order to conduct a full CT scan, the HEXITEC required the use of a 'triggering' system in order to synchronise the start/stop acquisition points for the detector, and the corresponding rotation of the sample stage to the next angular position. This is in contrast to most commercial devices, whereby the detector is integrated into the experimental system and automatically enables synchronicity between all components. Triggering of the HEXITEC was enabled through a transistor-logic USB input cable and controller box [11], as shown in Fig. 3.2.3. The cable was connected between the desired input of the trigger controller, which connects to the HEXITEC device, and the sample stage motor control PC by USB connection. By entering triggering mode through the HEXITEC software, synchronicity between acquisition and sample rotation was achieved based on exposure time. For each acquisition, a trigger signal was sent to the HEXITEC, informing the device to record an image for a duration equal to the selected exposure time (Input 2 mechanism). Following the end of the exposure, the sample stage would rotate the sample to the next position, and a new trigger was sent. The process was repeated until a full CT scan was complete. For the Colour Bay system, the triggering system was controlled using the same script as the MATLAB-controlled sample stages.

For the HFB system, an adapted routine was required given that manipulation of the sample rotation/translation stage was controlled by Nikon's Inspect-X software. Therefore, a link between the trigger system and Inspect-X was developed through the use of Nikon's Inter

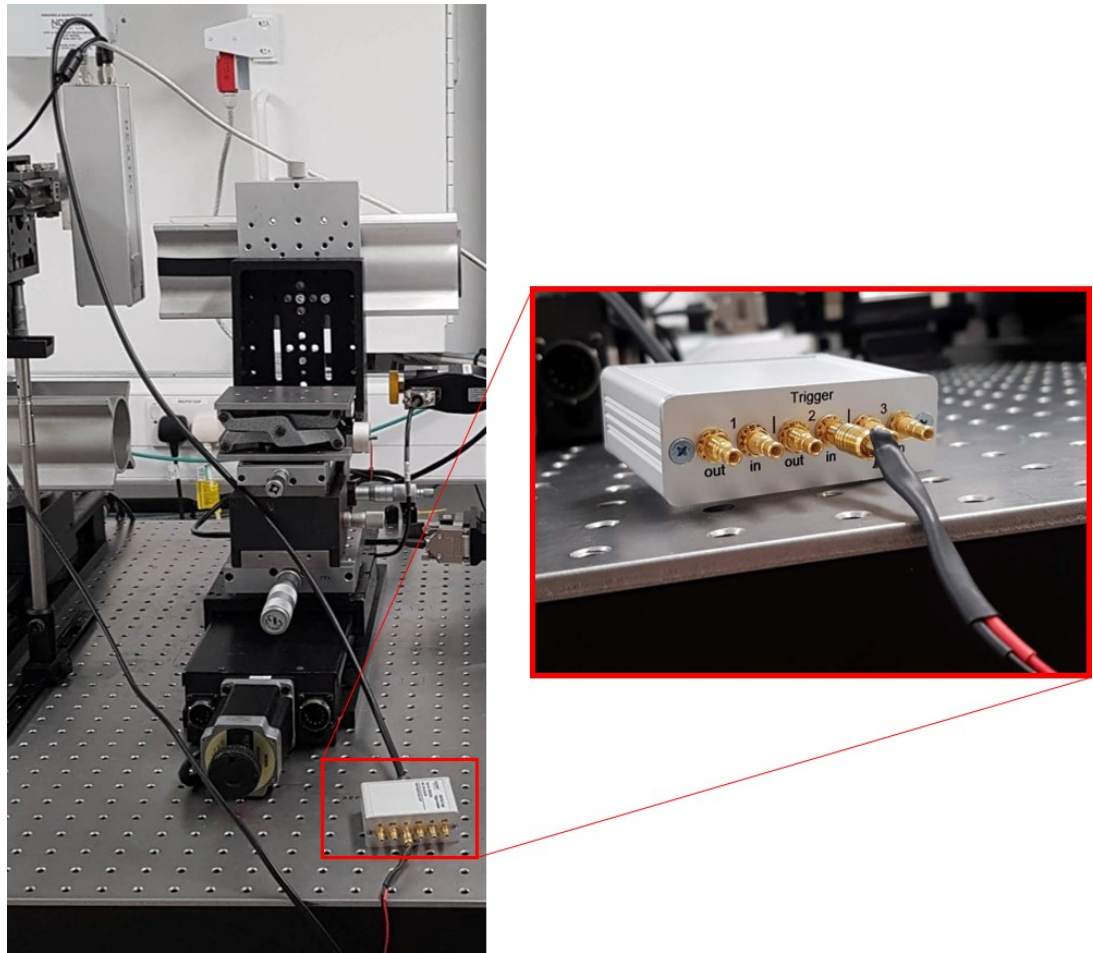


Figure 3.2.3. Photo of the HEXITEC system with the trigger controller installed. The cable connects directly to the HEXITEC, and runs through the trigger controller, before then connecting via USB to the sample stage PC. A magnified image of the triggering system (red box) is shown, with variable input based on trigger system. For all experiments, Input 2 was used.

Process Communication (IPC) tool. IPC allows users to control the Nikon system through a custom-built application. Here, IPC was used to enable the automatic acquisition of energy-sensitive images for a full CT scan, using the HEXITEC as opposed to the pre-installed flat panel detector. The application was developed using the Microsoft .NET platform, with software written in the C# programming language. Similar scripts were previously written to explore non-standard geometries and imaging routines within Nikon systems, including laminography [12] and temporal CT [13]. For the imaging work in this dissertation, the author adapted these scripts and built a workflow to alter the functionality for hyperspectral acquisition using the HEXITEC detector. A graphical user interface (GUI) was built to allow full tracking of the X-ray settings (source and sample stage), and set the parameters of the CT acquisition. By selecting the desired number of projections and exposure time, the triggering system and Inspect-X were synchronised to enable sequential acquisitions for the correct angular positions. An output log tracked the progress of each radiograph, and provided related metadata following scan completion. A representation of the X-ray CT set-up using the HEXITEC and the HFB is shown in Fig. 3.2.4, as well as the author's final design of the developed GUI.

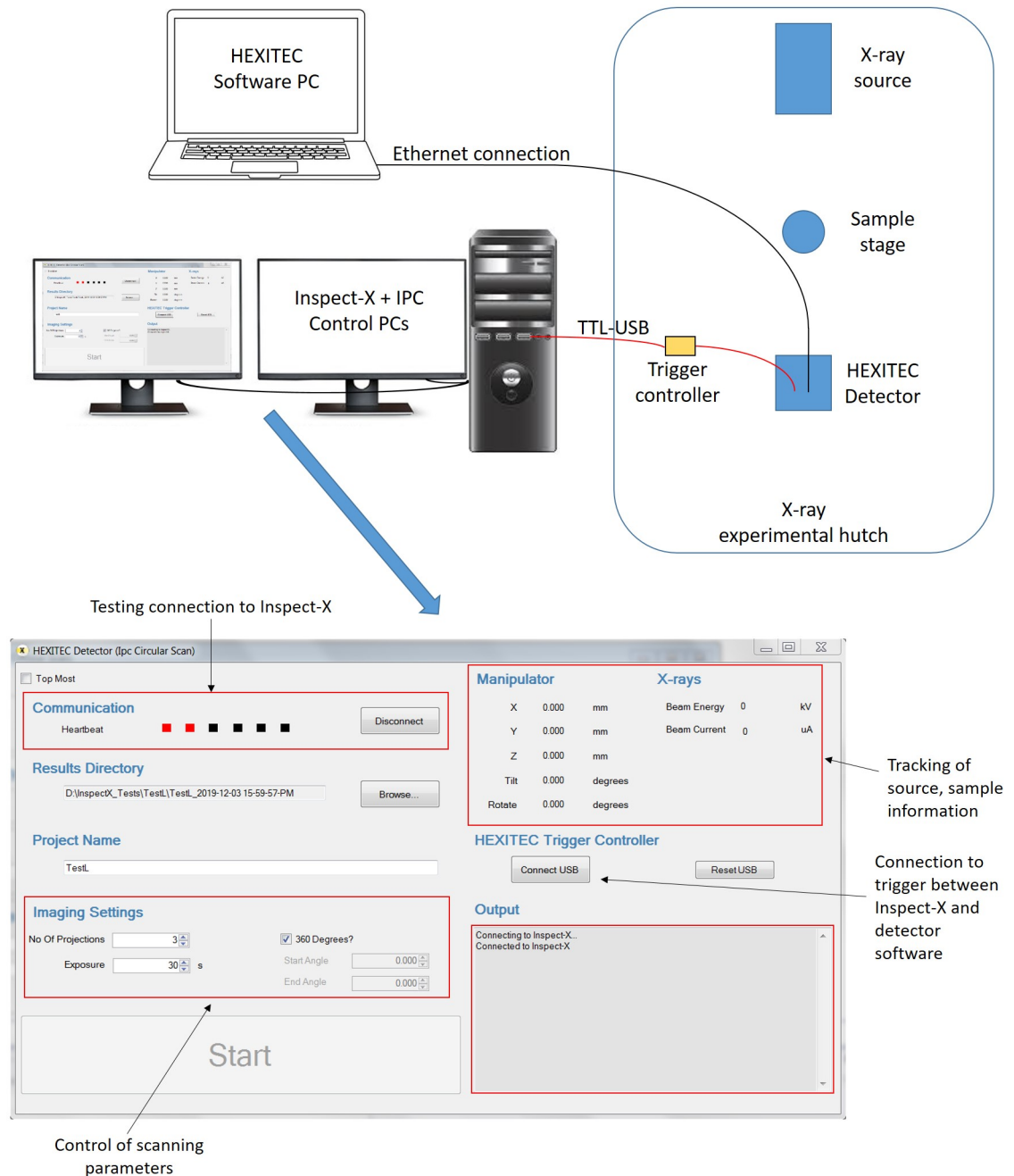


Figure 3.2.4. Design of the experimental set-up for CT imaging using the HEXITEC in the commercial Nikon system. (Top) Ethernet connection from the HEXITEC transferred data to a computer, to be stored and viewed in the HEXITEC software. The trigger controller cable was connected between the HEXITEC and the HFB computer, containing the Inspect-X software (source and motor control) and IPC application linking all equipment. (Bottom) Interface developed using IPC, allowing the user to connect directly to Inspect-X and control the settings for the CT scan, as well as monitor source and sample settings. The output logged the progression of the full CT scan.

3.2.1 HEXITEC calibration

In order to identify spectral distortions, noisy or ineffective pixels within the HEXITEC detector, a calibration was performed prior to the collection of new datasets. In addition, the calibration enabled the direct relationship between hyperspectral channel number and photon energy to be determined, as well as to assess the current energy resolution of the system. Calibration was conducted using a sealed radioactive source of ^{241}Am . The source

contained an adjustable ‘dial’ of six metal foils, namely: Cu, Rb, Mo, Ag, Ba, and Tb. The ^{241}Am source emits radiation, which impinged onto a user-selected metal foil, resulting in the emittance of characteristic fluorescent X-rays. The source was housed in a brass and tungsten enclosure. For each calibration, foils of Ba and Tb were chosen, producing fluorescence corresponding to their respective K_α and K_β peaks. Further to this, the ^{241}Am source also emitted some gamma radiation which can also be detected and used as a characteristic signal (γ photopeak at 59.54 keV). The detector was placed 2 cm away from the source as an optimum position for high count rate and uniform exposure over the full pixel array. Prior to exposure, the detector acquired a set of offsets (images acquired with no radiation source), used as a form of dark current subtraction for all future data collected. Using the HEXITEC GUI, data collection was set for 60 minutes. Each of the two chosen metal foils were exposed to the ^{241}Am source for 30 minutes, producing energy spectra in each pixel containing characteristic peaks corresponding to each foil. A total of 300 channels were included in the histogram, with all spectral information up to the highest energy peak ($^{241}\text{Am}_\gamma - 59.54 \text{ keV}$) captured within this channel range. Figure 3.2.5 shows a global spectrum for the total acquisition across all pixels, with indicators given for the peaks of: $^{241}\text{Am}_\gamma$, Tb K_α and K_β , and Ba K_α and K_β .

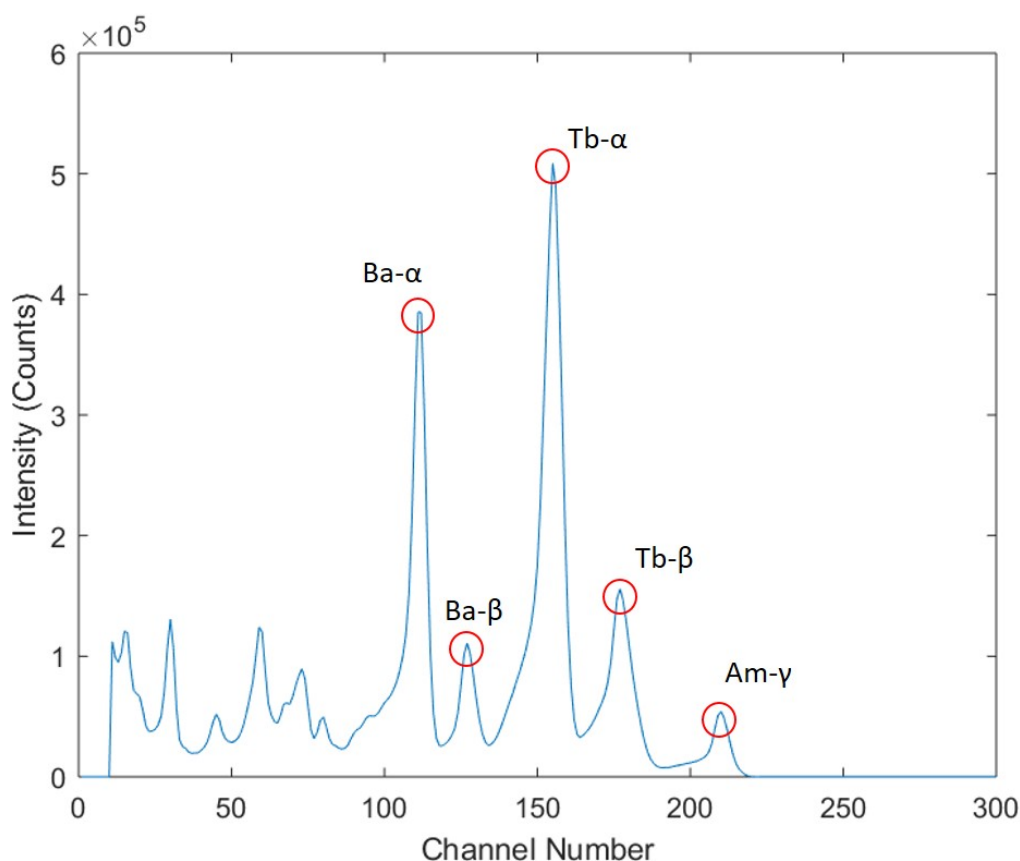


Figure 3.2.5. Global spectrum for emissions of ^{241}Am on to the metal foils of Ba and Tb. Peaks are highlighted and labelled for the relevant characteristic peaks of Ba and Tb, along with the photopeak from ^{241}Am .

Measurement of the energy-channel calibration was calculated using a custom MATLAB programming script. An interactive GUI enabled the user to select the peaks of interest, and match them to the corresponding energies of the known fluorescence peaks. The known

values (taken from the NIST database [14]) of the fluorescence peaks are:

- Ba K_{α} - 32.19 keV, K_{β} - 36.38 keV
- Tb K_{α} - 44.48 keV, K_{β} - 50.39 keV

Combined with the ^{241}Am peak, these spectral markers were plotted as channel number versus known peak energy, enabling a linear fit to be determined. Fig. 3.2.6 shows an example of a fitted relationship based on selected peak positions. The calibration of the HEXITEC showed strong alignment, with an R^2 value of 0.99 for the linear fit. A linear fitting function was then applied to extract the linear equation of the calibration, such that all channel number values may immediately be transformed into photon energies. For the fit in Fig. 3.2.6, the resulting fitting equation was:

$$\text{Energy (keV)} = 0.278 \times \text{Channel Number} + 1.23 \quad (3.1)$$

For each calibration test performed, it was confirmed that the R^2 value remained at 0.99 or above to ensure a correct linear relationship, otherwise the full calibration was repeated.

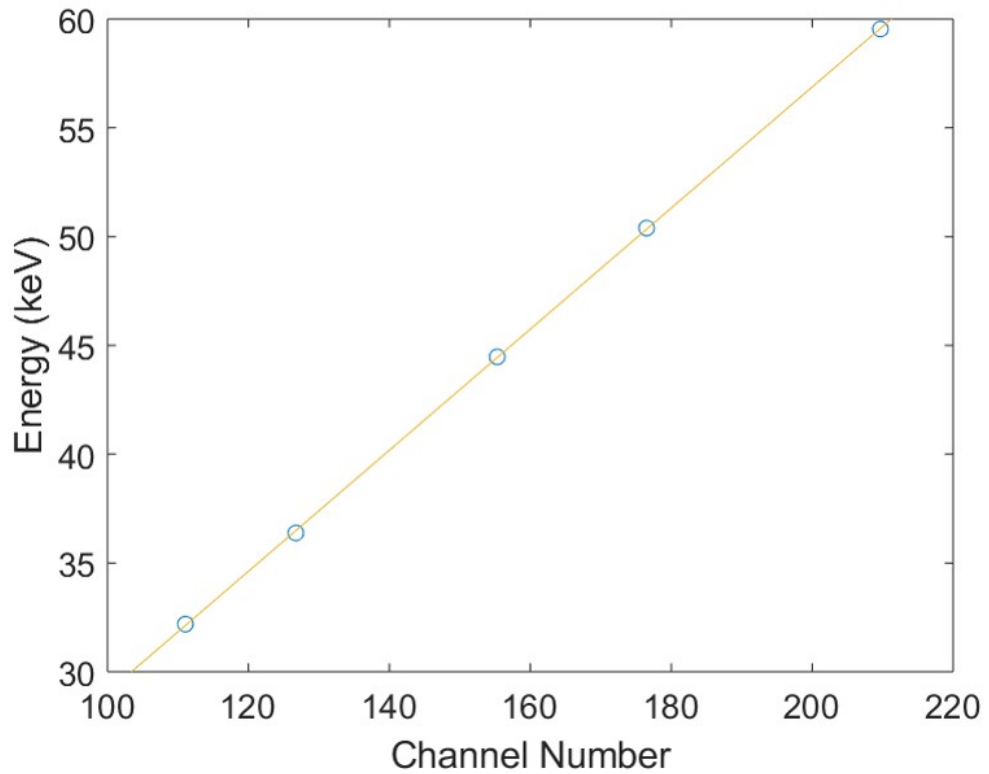


Figure 3.2.6. Linear fit calibration between channel number and energy for the identified characteristic peaks. In total, 5 data points were fitted with a linear fitting routine.

A further gain calibration procedure was applied to the HEXITEC spectra, in order to account for general inhomogeneities in individual pixel elements. These differences typically lead to variations in spectral performance, and can lead to gain shifts, whereby spectra between pixels can appear to be offset in energy, or suffer from degraded energy resolution

or sensitivity, with broadening in the FWHM of peaks in a global spectrum. To correct for this, the method proposed by Egan *et al.* [15] was implemented, which uses the concept of correlation optimised warping (COW). The principle of COW uses linear stretching and compressing of each pixel spectrum to best align with a choice of reference spectrum. Further information on the MATLAB toolbox developed for COW can be found elsewhere [16]. Here the COW method was applied to the calibration dataset, which works well due to its high photon intensity and uniform distribution over all detector pixels. Through prior assessment of several pixel spectra, looking for good energy response and little peak broadening, a reference was chosen each time. All pixels were then adjusted on a pixel-by-pixel basis aimed at matching the gain of the reference pixel. The result of one such implementation of COW is shown in Fig. 3.2.7, where two pixel spectra are compared before and after the gain correction. The output of the routine produces an 80×80 matrix of 'warping' values, indicating the gain shift required for each pixel, which may be applied during processing of any real dataset.

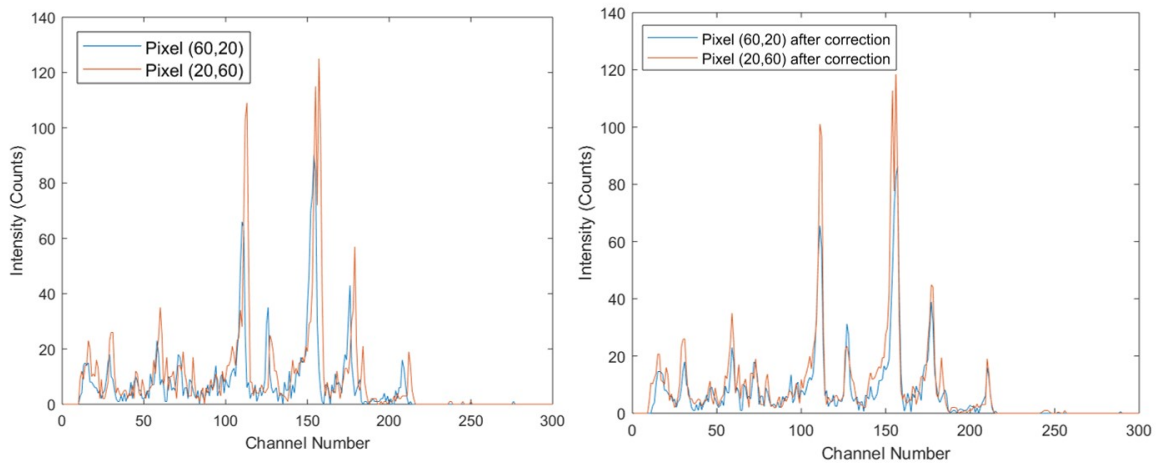


Figure 3.2.7. Effect of the COW method on the calibration dataset, containing spectral signals from Ba, Tb, and ^{241}Am . Pixels (60,20) and (20,60) were used to highlight initial differences with regards to spectral gain shift (Left), along with the same spectra after application of the COW method, showing better alignment (Right).

Finally, a 'bad pixel' map was assembled, highlighting any pixels showing erroneous values due to dead or ineffective pixels. Such pixels typically appear with a 'condensed spectrum', with all photon counts registering at lower energies than surrounding pixels. Similar defects can appear due to the absence of a bond between the sensor material and underlying ASIC, as described elsewhere [17]. Using a sample flatfield image, each individual pixel was analysed through a MATLAB script and bad pixels were identified by measuring the proportion of photon counts measured in the low energy channels. The result produced a bad pixel map, as shown in Fig. 3.2.8, in the form of a binary 80×80 matrix for 'good' (value = 0) and 'bad' (value = 1) pixels. Also shown is an example flatfield image both before and after bad pixel correction, acquired with a X-ray beam voltage of 50 kV. In order to correct bad pixels, the method interpolates over all nearest neighbours of the bad pixel (that are also 'good' pixels) and averages their energy spectra, with the bad pixel allocated the new mean spectrum values. The routine works well for improving uniformity of the image. It should also be noted that typically pixels close to the detector edges are more prone to re-

duced spectral performance, due to defects or impurities in the CdTe crystal [4, 18]. Finally, the figure shows an example of a plot in the case of a good pixel response, and the effect of correction on an ineffective pixel with poor spectral response.

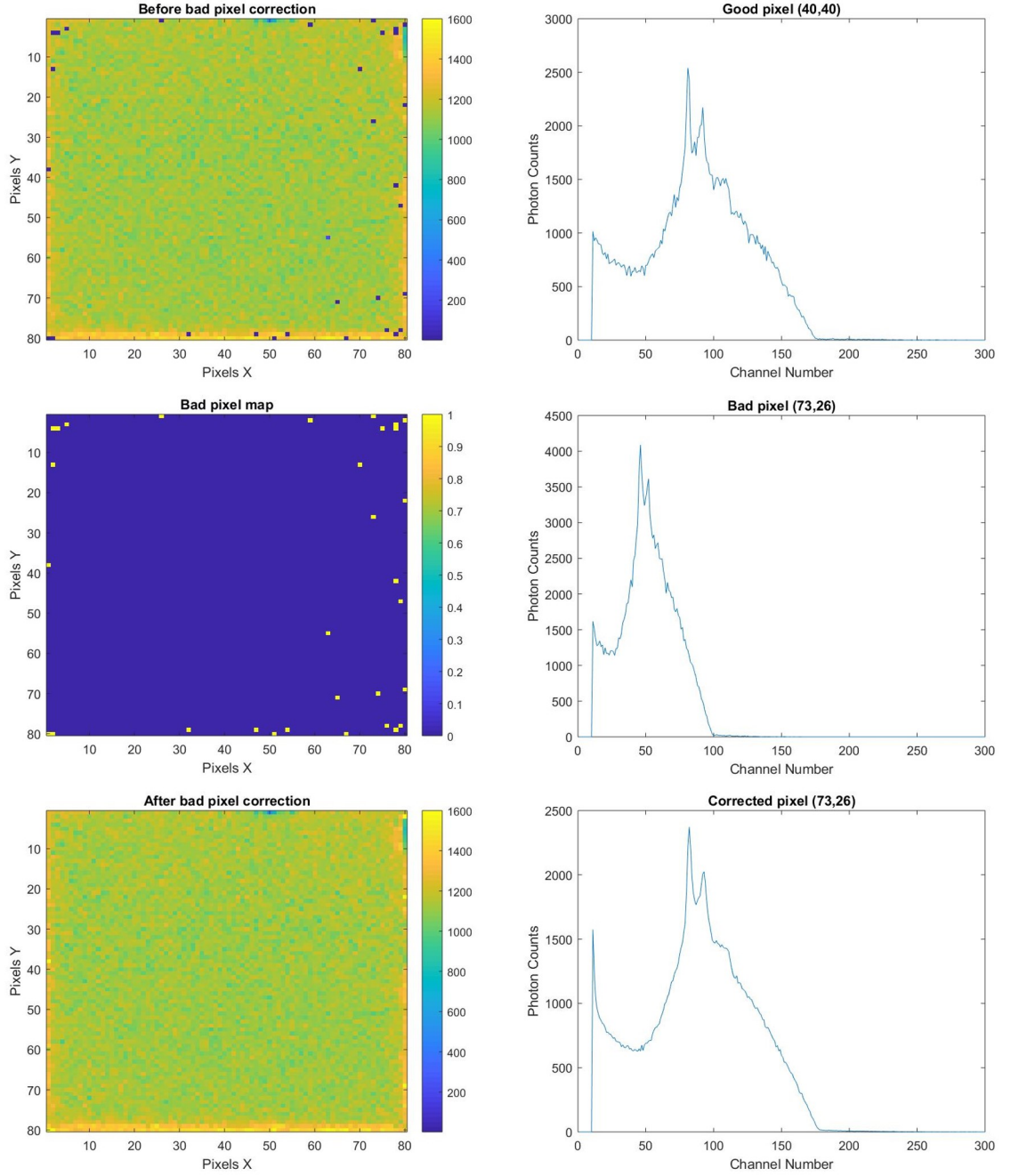


Figure 3.2.8. Demonstration of the bad pixel correction routine. Left Column: Top - Example flatfield image acquired at 50 kV, shown for a single energy channel (channel 120). Colour bar measures photon counts. Bad pixels appear as very low photon numbers for the given channel. Middle - Bad pixel map identifying all ineffective pixels that require correction. Bottom - The same flatfield image following correction of bad pixels. Right Column: Top - Example of a fully functioning pixel with good spectral response. Middle - Example of a poorly responding detector pixel. Bottom - The same ineffective pixel after correction.

3.2.2 Evaluation of HEXITEC characteristics

Using the same calibration dataset described above, an evaluation of the energy resolution for each pixel was performed. As performed elsewhere [10], measurement of the full width at half maximum (FWHM) of characteristic peaks provides a clear indicator of the spectral

resolution in a given pixel. Here, an evaluation of the resolution was made through analysis of the ^{241}Am peak at 59.54 keV. Identification of all peaks present was performed via a peak-search algorithm in MATLAB, with the highest energy peak found corresponding referring to ^{241}Am . The FWHM was measured using a standard procedure of parabolic fitting and interpolation [19]. Poorly-functioning or dead pixels were identified by means of setting a count threshold, below which pixels were considered non-functioning. Fig. 3.2.9 shows an example distribution of the FWHM values measured for all functioning pixels. The distribution is also shown in the form of a pixel map, revealing the locations of any pixels with a poorer spectral resolution. All pixels identified as non-functioning were labelled as zero in the pixel grid, and were excluded from the final calculations of average FWHM for the peak. A number of pixels with poor spectral response, as well as those highlighted as 'dead', were close to the edges of the detector. This was attributed to the effect of leakage current, observed most strongly at the detector perimeter. In addition, material defects and bonding issues to the underlying ASIC contribute to the presence of erroneous pixel response [10]. For the peak evaluated in Fig. 3.2.9, the energy resolution of the system, as determined by the mean FWHM value, was 1.27 ± 0.47 keV.

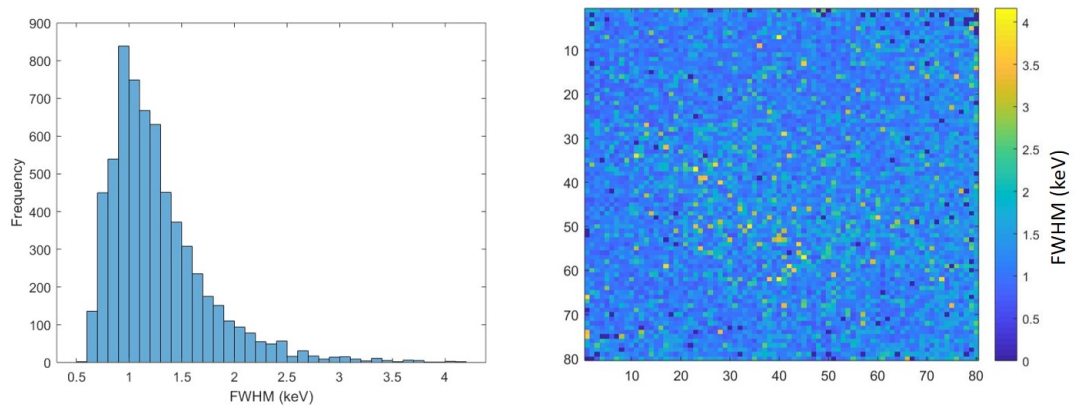


Figure 3.2.9. Spectral resolution statistics based on the ^{241}Am photopeak. (Left) Histogram depicting the frequency distribution of FWHM values of the peak, measured for each pixel. Dead pixels were not included. (Right) Pixel map distribution of the FWHM values. Dead pixels were labelled as zeros. Many non-functioning pixels emerge at the detector edges due to leakage current and poor pixel bonding.

Further investigations were conducted on the difference in spectral resolution, both as a function of peak energy, but also as a function of time. Though new calibrations of the HEXITEC were performed prior to each experimental acquisition, it was important to consider changes in the resolution of the system in each case also. Therefore, each factor was evaluated, with results shown in Fig. 3.2.10. For the analysis of resolution as a function of energy, mean FWHM are shown, along with error bars corresponding to one standard deviation, based on FWHM values measured over all functioning pixels. The poorer spectral resolution of the Ba K_β peak was attributed to a failure of the peak search algorithm to consistently identify the fluorescence signal. The Ba K_β peak appears at a much lower intensity than surrounding peaks, as observed in the global spectra in Fig. 3.2.5, and thus at a single pixel level the lower intensity peak becomes harder to identify amongst any background noise fluctuations. The failure of this algorithm for the Ba K_β peak is highlighted by the fact that a total of almost 1900 pixels were identified as dead, around 30% of all pix-

els. This is in contrast to an average of 83 dead pixels (1.3%) for the other four peaks. As such, the resolution determined through the Ba K_β signal was identified as an outlier. Considering only the remaining four peaks, the spectral resolution varied by approximately 40% between the lowest average FWHM (1.27 keV for ^{241}Am) and the highest FWHM (1.78 keV for Tb K_α).

When considering the same single peak across multiple calibration datasets, strong consistency was observed over several years of detector resolution measurements. Using the ^{241}Am photopeak as the reference, as performed elsewhere with similar radioactive samples [4, 6, 10], spectral resolution at 59.5 keV differs by just 7% between the lowest and highest FWHM values, as detailed in the table included in Fig. 3.2.10. Also included are the number of dead pixels identified in each case, showing a gradual increase in non-functioning pixels between calibrations. This was expected given the significant use of the detector, resulting in increased likelihood of additional issues with pixel bonding or leakage.

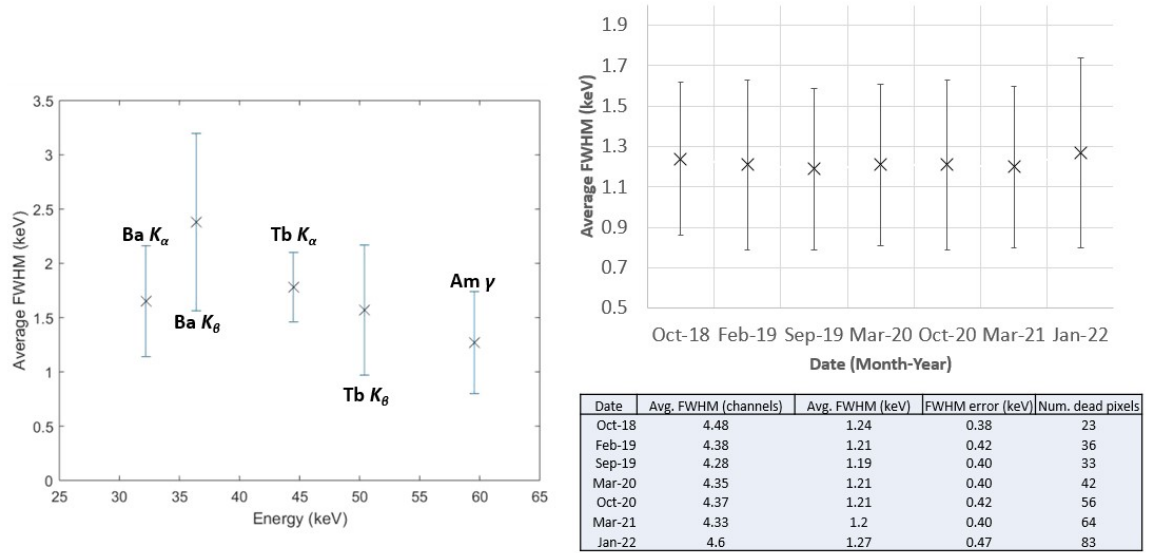


Figure 3.2.10. Variation in energy resolution as a function of peak energy and time. (Left) Average FWHM values for the five peaks considered in the calibration dataset. Error bars show one standard deviation. The Ba K_β peak shows poorer spectral response due to inconsistencies in the peak search algorithm. (Right) Energy resolution based on the ^{241}Am photopeak for several calibration datasets acquired over several years. Strong consistency in spectral resolution was observed. Full details on peak statistics, including the number of dead pixels identified, are included.

Finally, analysis of the degree of detector 'cross-talk' was evaluated, based on spectral distortion due to both pulse pile-up and charge-sharing. Each phenomenon was previously detailed in Section 2.2.3.

Due to the large pixel size of the HEXITEC detector, in comparison to other spectral systems and the majority of energy-integrating detectors, pulse pile-up was a common occurrence for the bright-field imaging modality. Beyond improvements in the detector hardware, minimisation of the pulse pile-up is achieved through reduced X-ray flux, reducing the likelihood of simultaneously recorded photon events, or through an increase in detector frame rate to process each single photon more quickly. In reducing X-ray flux, the beam voltage or current must be lowered. Beam voltage adjustment for bright-field imaging was limited, given that the mean energy of X-ray photons in the polychromatic spectrum must be suffi-

ciently high to produce visible K-edges of the material phases under investigation. As such, where applicable the X-ray current was reduced to minimise photon flux. For the Colour Bay system used, as described in Section 3.1, a minimum X-ray current of 0.1 mA resulted in limited flexibility in reduced flux, resulting in more prominent cases of pulse pile-up. An example single pixel flatfield spectrum is shown in Fig. 3.2.11, taken under the scanning conditions of 60 kV and 0.1 mA. The settings described match those used for the investigation of a multi-phase phantom sample studied in Chapter 4, and described further below in Section 3.3.2. As stated, the X-ray current was at its lower limit, while beam voltage was chosen to ensure capture of known absorption edges present. However, significant pulse pile-up occurred, resulting in a significantly distorted spectrum, far from the conventional Bremsstrahlung shape expected. The presence of pulse pile-up was clearly identified by two key features of the spectrum (as labelled in Fig. 3.2.11):

1. The lack of low photon energy events. Due to the high percentage of co-incident photon events, the majority of low energy photons were measured simultaneously with additional photons, registering each time as a single event of higher energy.
2. Photon events beyond the selected beam voltage. As expected with any polychromatic spectrum, the selected beam voltage defines the maximum energy of any incident photon, therefore no photon energies beyond this limit should be identified. Due to pulse pile-up, a number of photon counts were registered at an energy beyond the voltage limit.

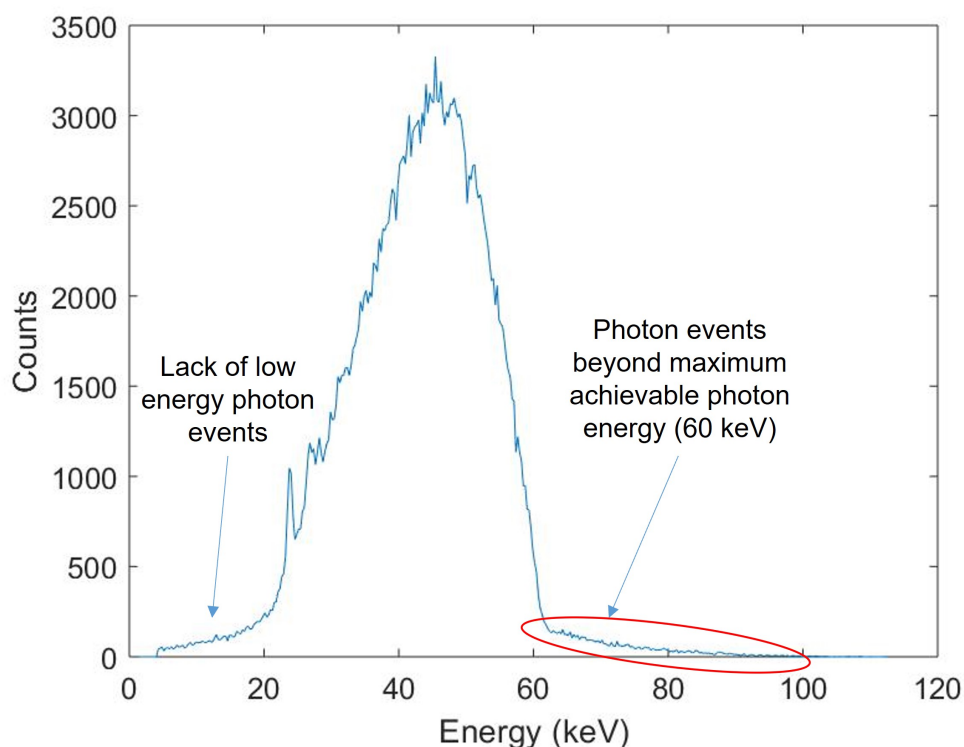


Figure 3.2.11. Single pixel (40,40) spectrum for a flatfield acquired at the scan settings of 60 kV and 0.1 mA. Significant pulse pile-up occurred, with very few low energy photon events recorded, and a number of events incorrectly assigned an initial photon energy beyond the maximum of 60 keV. Such effects are labelled and highlighted on the spectrum.

Where flux could not be reduced further, changes in the detector frame rate were investigated. In the HEXITEC software settings, the frame rate may be manually adjusted for faster readout, up to the maximum rate of 8.9 kHz. Due to stability and software limitations, the maximum frame rate was not achievable for the existing experimental set-up. Therefore, a set of tests were performed, acquiring flatfield spectra under the same source settings, adjusting the frame rate in each case. With reduced pile-up, the total counts measured in the spectrum would rise, given that more photon events were being measured individually, as opposed to simultaneously. However, if the frame rate was too high, a drop in counts would be observed as the acquisition PC could not maintain its readout rate. Therefore, total counts recorded was used as a stopping criteria for identifying the upper frame rate limit of the experimental system under given conditions.

Fig. 3.2.12 shows the global spectra (all pixels summed) for a series of flatfields, acquired at the same settings (60 kV, 0.1 mA) and geometrical configuration of the source and detector in the Colour Bay system. All spectra were obtained for a total of 180 seconds. The frame rates, as labelled, were the only parameter altered. Following acquisition, total counts registered in the spectrum were determined by analysis of the raw data, summed over all pixels. As observed in each spectrum, the severity of pulse pile-up reduced with increasing frame rate, up to the maximum frame rate achievable in the HEXITEC settings for this system at 8.0 kHz. An additional plot was included in the figure to map the rate of change of global counts, indicating that detected photon events continued to rise with frame rate. The diminishing returns at increasingly higher frame rates suggested that close to all photon events were being individually recorded. It should be noted however that, even at the highest frame rate for the HEXITEC, the scan settings used in this instance still resulted in minor pulse pile-up, as highlighted by the presence of some counts beyond the 60 kV upper limit. For all biological specimens studied, due to the lower attenuation soft tissue phases present, all scans were conducted using the HFB system, where greater flexibility in X-ray flux was available. Beam current was set closer to the 10 μ A limit, such that higher beam voltages could be utilised to capture the absorption edges of higher attenuation chemical stains.

Calibration spectra were once more used to evaluate the degree of charge sharing observed for the HEXITEC, and assess the degree to which the built-in charge sharing discrimination regime counteracts this. Fig. 3.2.13 shows two global calibration spectra acquired over the same time period, with 30 minute exposures to the Tb and Ba metal foils from the ^{241}Am source. Following the application of charge-sharing discrimination (CSD), global counts fell from 3.8×10^7 to 1.8×10^7 , equating to approximately 53% of events deleted by the CSD correction scheme, due to photons registering in more than one pixel. The effect of the CSD method was clear, with the low energy background greatly reduced, with only 8% of global counts registered below an energy of 10 keV, compared to 22% of global counts prior to application of CSD. Despite the removal of a significant proportion of photon events, the counts recorded in the characteristic peaks all increased, respectively by 15%, 13%, and 44% for the Ba K_α , Tb K_α , and ^{241}Am peaks. As such, the application of CSD,

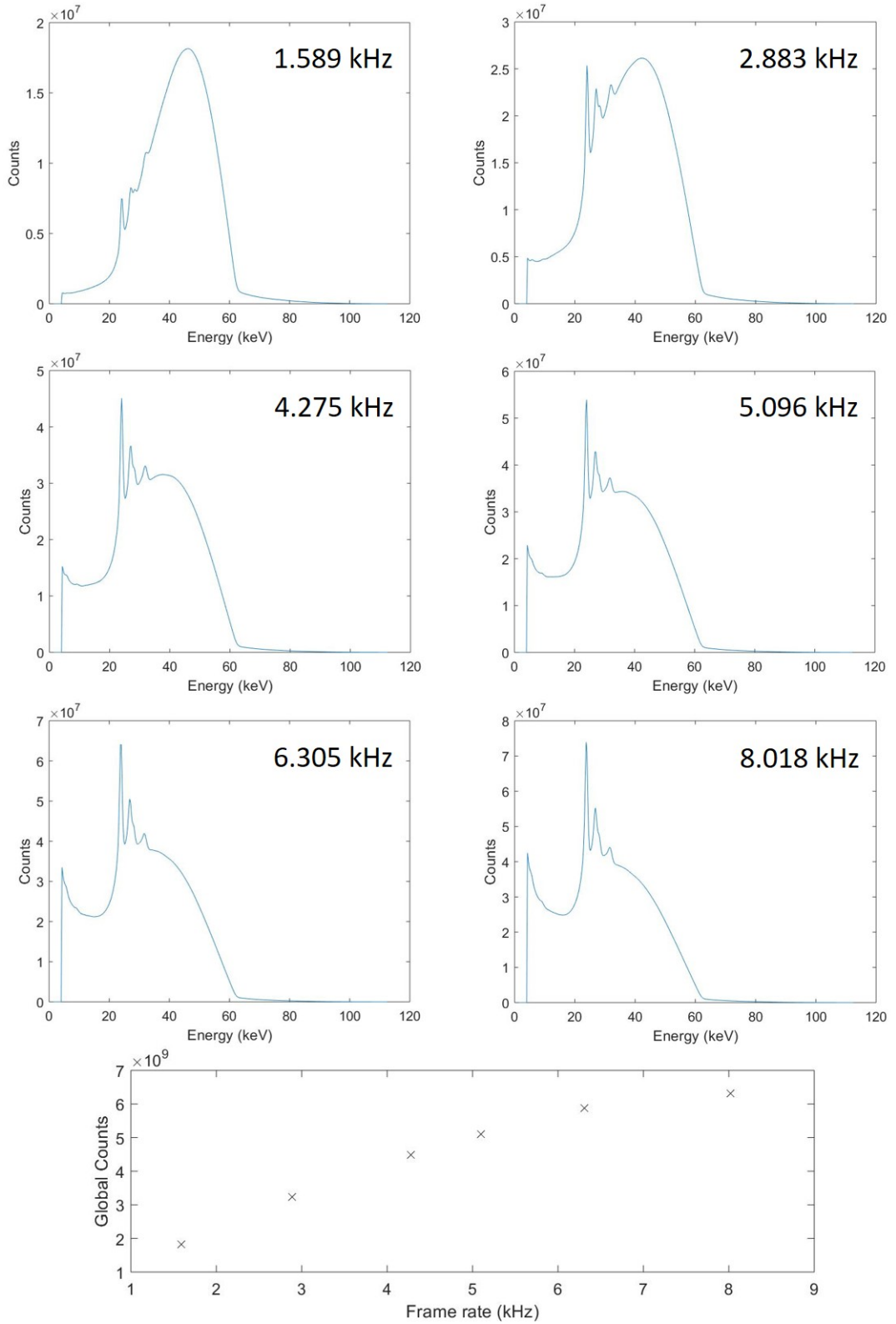


Figure 3.2.12. Reduction in pulse pile-up through changes in frame rate. A series of six flatfield images were acquired at 60 kV and 0.1 mA, with the global spectra for each flatfield shown. The frame rate used for each dataset is labelled. Also included is a plot comparing the global count rates as a function of frame rate.

where applicable, offered improved spectral resolution. However, as described in Section 2.2.3 and elsewhere [4], CSD worked effectively only when occupancy did not exceed more than a single photon event in a block of 3×3 pixels, equivalent to 11%. For the investigation of bright-field imaging, the high X-ray fluxes utilised prevented the use of CSD from offering such benefits to the resulting spectral analysis. The figure shows a number of addi-

tional peaks, at energies below the characteristic XRF signals from the calibration dataset ($\text{Ba } K_{\alpha}$, K_{β} , $\text{Tb } K_{\alpha}$, K_{β} , $^{241}\text{Am}_{\gamma}$) and above the low energy background. As labelled in Fig. 3.2.13, fluorescent peaks of Cd and Te are identified, owing to interaction of the incident photons with the detector materials. Origins of the lower energy signals cannot be absolutely confirmed, but a possible cause is the presence of escape peaks due to the gamma radiation of the ^{241}Am source producing XRF excitation of the metal foils, as opposed to the alpha radiation. Such interactions would produce signals in the range of 9-27 keV (gamma photopeak at 59.54 keV minus the energy of the XRF photon) and therefore could produce the observed low energy peaks.

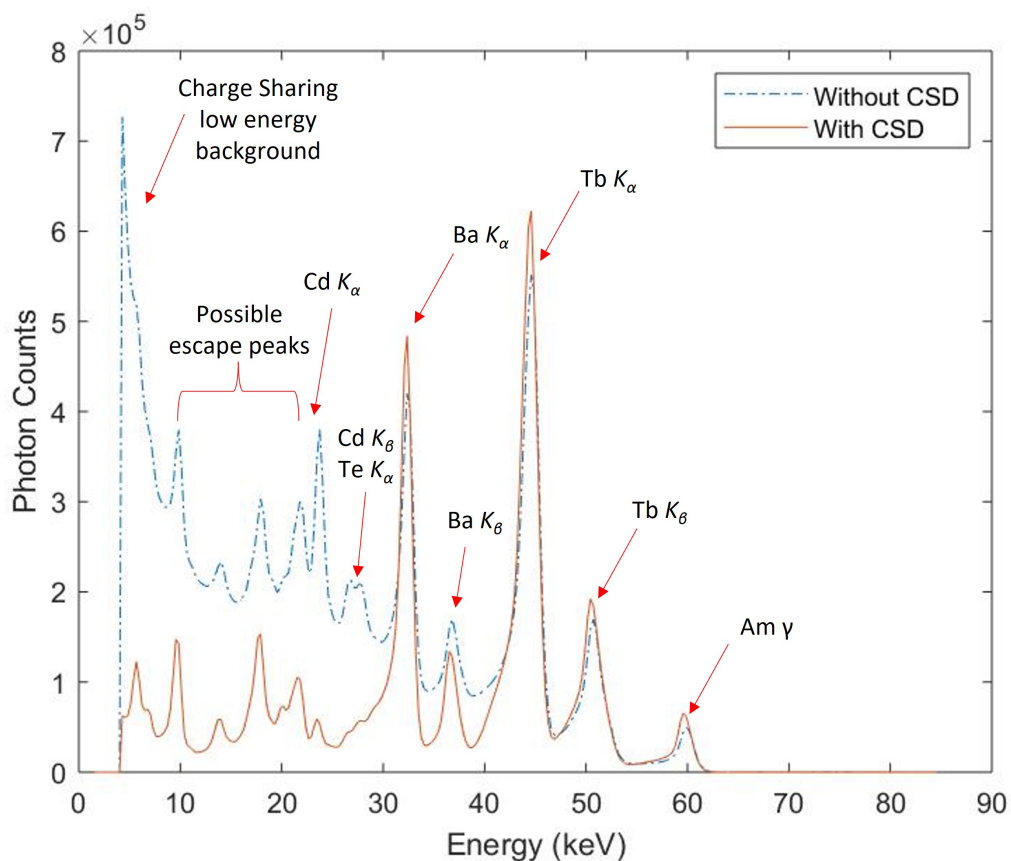


Figure 3.2.13. Evaluation of the charge sharing discrimination (CSD) correction on a calibration dataset. Significant reduction in the low energy background was observed following CSD correction. Despite a large number of deleted events, the characteristic peaks (labelled) all increase in total counts registered. Other peaks have been labelled, including characteristic XRF signals from the detector materials (CdTe), as well as possible escape peaks due to the gamma emissions from the ^{241}Am source followed by XRF emissions of Tb and Ba.

3.3 Sample preparation

For the studies discussed in Chapters 4 and 5, a number of stained biological specimens were created and produced. In Section 3.3.1, a breakdown is provided on the samples produced, containing images and explanation on the specimens chosen. Full details on the staining procedure are provided in the respective Methods sections of each paper in Chapters 4 and 5.

All of the research projects in this thesis also involved the use of multi-phase phantoms. In Chapter 4, the phantom offered a simple test case for evaluating the results of novel reconstruction methods, in a situation where full sample composition and dimensions were known. In Chapter 5, the phantoms form a crucial part of the quantitative analysis by acting as a means of spectral calibration. In Section 3.3.2 details are provided on how each sample was produced and prepared for imaging, as well as the reasoning behind their creation. To avoid excessive repetition, it should be stated that the delivery and storage process for all biological and phantom samples was identical. All samples (unless stated otherwise) were prepared at the University of Veterinary Medicine in Vienna, and followed animal care guidelines approved by the Administrative Panel on Laboratory Animal Care of the University of Veterinary Medicine in Vienna. Following preparation, the fixed specimens and chemical phantoms were shipped to the University of Manchester, UK, where they were then stored in a refrigerator at the HMXIF, at approximately 4°C. Once experimental time was available, samples were removed from refrigeration as needed, and mounted to the sample stage in the relevant experimental hutch. Following imaging, each sample was then returned to its storage container in the refrigeration unit. In each case, scanning of samples was aimed to be completed within 2-3 months of initial arrival at the HMXIF, in order to avoid any long-term deterioration of the biological specimens, or spreading of the contrast agents outside of the desired soft tissue regions. The exception is the single-stained lizard head specimen, which was produced in 2017, as detailed in the section below.

3.3.1 Biological staining procedures

Figure 3.3.1 provides a set of photos of the three biological specimens used across the two research studies described in Chapters 4 and 5. For each sample, sample type and size was chosen to suit imaging with the small detection area of the HEXITEC. The labels included in the figure show the full length of the sample, where it could not be fully captured within the detector FOV. The imaged section, which in the case of the lizard head covered the full sample, is shown as a dashed region.

In Chapter 4, a single, iodine-stained lizard head specimen was used as a simple biological case study to analyse the capability of hyperspectral imaging to identify and map a chemical contrast agent distributed inhomogeneously across multiple soft tissue regions. The lizard head sample (a species of the *Anolis* genus) was purchased as a fully-prepared, fixed and preserved specimen from Nasco Education (USA) [20] in January 2017 for previous

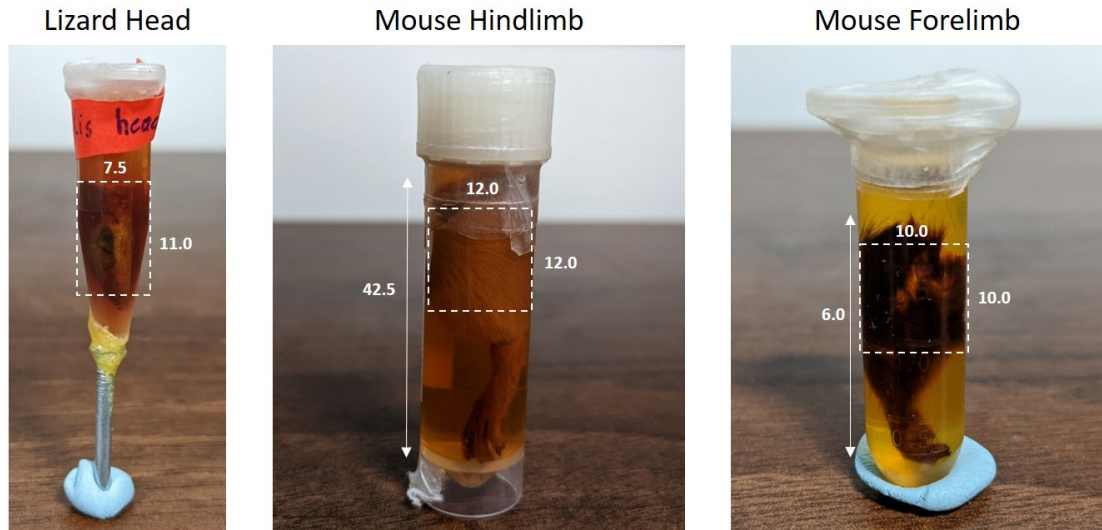


Figure 3.3.1. Photographs of the stained biological specimens, each of which were chemically fixed and held in individual containers. Sample dimensions are overlaid. An approximation of the imaged section of each sample is highlighted (dashed box). All measurements are in mm.

experimental work outside of this thesis. As described in the corresponding Methods section of Chapter 4, in order to aid long-term stability, the sample was fixed in formalin and stored in 70% ethanol, before heavy metal staining took place. The chemical fixation is typically performed as a first step to minimise sample shrinkage [21].

The mouse hindlimb and forelimb specimens shown were fully prepared at the University of Veterinary Medicine, Vienna. Adult mice were euthanized as part of the research, complying with animal care guidelines. The first staining procedure was that of the vasculature, whereby staining was achieved by the perfusion of the contrast agent through the blood vessels. This technique has been shown to offer fast staining across the full body of murine samples [22]. Upon removal of the desired limbs, staining of the soft tissue was performed. For the hindlimb, elemental iodine in absolute ethanol was used, while the forelimb used the commonly applied Lugol's iodine (I_2KI), both of which have been shown to provide rapid tissue penetration and strong contrast to multiple soft tissue structures. The triple-stained forelimb was also stained with PTA prior to the Lugol's solution, given its much slower penetration rate [23, 24]. The final samples were stored in polypropylene tubes, which provided little attenuation under X-ray imaging and therefore did not affect experimental results. Further, the samples were fixed such that sample movement during scanning was not a concern.

3.3.2 Phantom sample preparation

The study in Chapter 4 uses a multi-phase powder phantom, with an aluminium exterior, as a test sample for studying the efficacy of novel spectral reconstruction algorithms. Design specifications of the phantom are shown in Fig. 3.3.2, along with a photograph of the sample. The phantom was produced at The University of Manchester, UK, with the external aluminium matrix formed as an initial step, and then sequentially filled with a single metal-based powder in each drilled region by the author. The drilled regions in the phantom

reached a 75% depth of the total phantom height, ensuring all powders could be observed over several reconstructed vertical slices. The powders were filled sequentially by hand, and tapped to improve homogeneity through the sample depth. Finally the top of the sample was sealed with an epoxy adhesive to prevent loss or cross-contamination of powders.

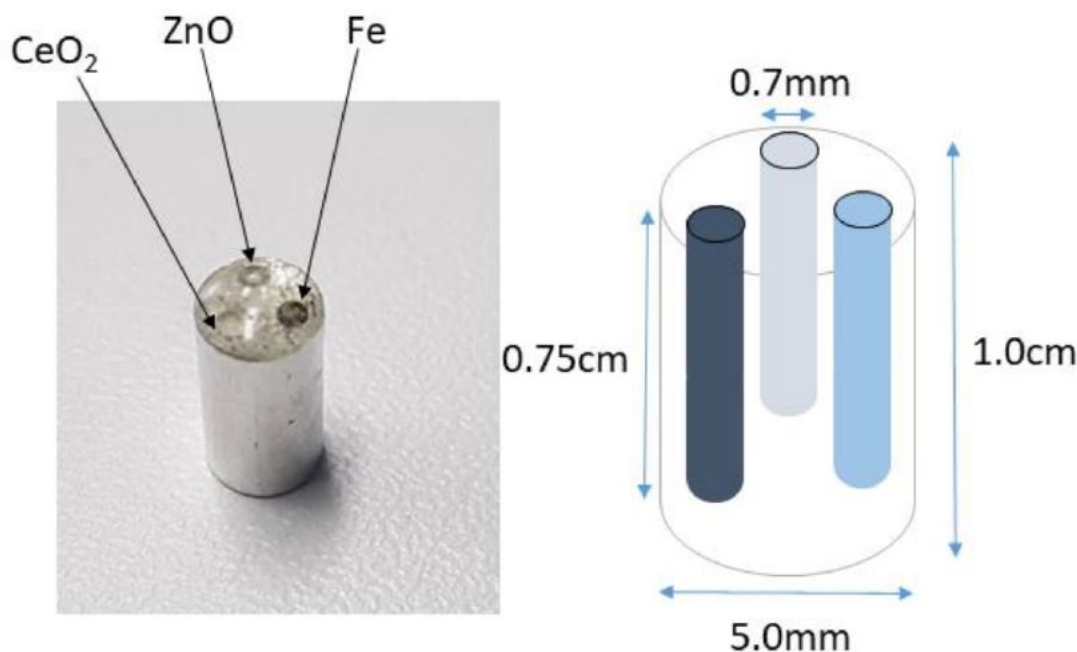


Figure 3.3.2. (Left) Photograph of the multi-phase powder phantom, with each metal-based powder labelled. The external metal of the phantom is aluminium. (Right) Schematic of the phantom sample, with dimensions included.

The sample was designed as an ideal case for imaging with each modality of the HEXITEC system. The small dimensions of the sample allowed it to easily fit within the detector FOV, allowing for increased geometric magnification for improved spatial resolution. Although only used as a bright-field sample in this thesis, the use of metal powders was chosen such that future dark-field work could be conducted with energy-dispersive diffraction. In this case, powders make an ideal choice for a simple, known phantom study for evaluating diffraction patterns and extracting crystallographic properties.

The chemical phantoms were formed to provide a baseline calibration for the measurement of spectral markers in hyperspectral imaging, namely in the evaluation of absorption K-edges. Each phantom contained chemicals commonly used as biological staining agents, aligning with those chosen for the corresponding biological specimens described in Section 3.3.1. In order to determine direct relationships between the concentration of the chemical and the size of the observed spectral marker, a minimum of three concentrations were required for each contrast agent. Shown in Fig. 3.3.3 are photographs of the assembled phantoms, including all external dimensions of the low-attenuation plastic containers. In the case of the BaSO_4 and PTA phantoms, the 5 ml containers were held together in an additional external tube with the use of agarose, which solidified at room temperature and prevented sample movement during scanning. The iodine phantom had an interchangeable set-up, with Lego-style connectors allowing the use of less than four concentrations if required

(due to its larger sample size and FOV limitations).

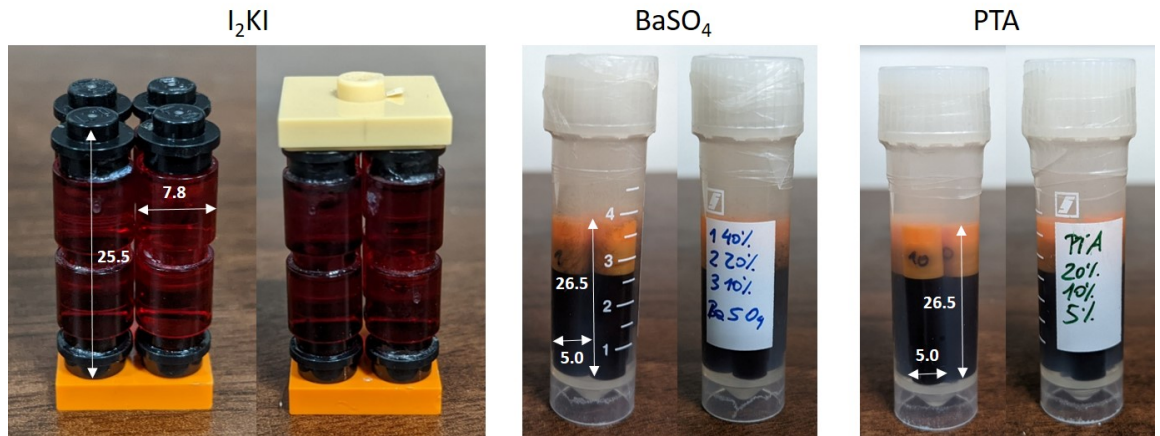


Figure 3.3.3. Photographs of the chemical phantoms produced for spectral calibration using known chemical concentrations. Sample dimensions are overlaid, and are measured in mm. (Left) Two images of the iodine-based phantom, containing four interchangeable rods of differing concentration of the I_3^- ion (25.3, 50.6, 76.0 and 101.2 mg/ml). The second photograph shows the optional connector plate to hold the four containers in position. (Middle) The $BaSO_4$ phantom, containing three concentrations (100, 200, and 400 mg/ml), with corresponding concentration percentages labelled. (Right) The PTA phantom, with three concentrations (50, 100, and 200 mg/ml) as labelled on the container.

3.4 Data processing, reconstruction and analysis: Software and Hardware

Below is a summary of the steps taken to transform the raw hyperspectral datasets into the final reconstructed 4D volumes, enabling different spectral analyses to then be conducted. Included are the main software programs and hardware devices required to achieve this. Where necessary, the software developed by the author is stated explicitly, and referenced otherwise.

3.4.1 Raw data processing

For all hyperspectral datasets, processing of the raw data, reconstruction of the sinograms and final spectral analysis and volumetric mapping was performed on devices at the HMXIF. Due to the unique nature of the hyperspectral data files, each raw projection was stored initially as a pre-defined '.hxt' file, which required conversion to a more useable format for reconstruction. Correction of the dark current (due to any leakage current in the detector) was applied automatically within the HEXITEC software, prior to data transfer. Initial processing steps of the raw data were performed locally from a laptop. The work was performed using MATLAB scripts adapted from those first built by Egan *et al.* for previous hyperspectral research [15, 25]. Minor adaptations by the author included updates to the data reading process, and corrections in the rare instances of erroneous angular projections through nearest-neighbour interpolation. In general, all preprocessing followed the same step-by-step workflow:

1. Reading in .hxt projection files
2. Application of corrections for gain shift and bad pixels
3. Flatfield correction and negative-log transforms of projection, building them into a 4D sinogram
4. Application of corrections for ring artefacts (and centre-of-rotation if required).

For all datasets, step 2 was necessary due to the aforementioned presence of spectral distortion and defective pixels observed with the HEXITEC detector (see Fig. 3.2.7 and 3.2.8). In step 3, rearrangement of the Beer-Lambert law, as described by Equation 2.6, converted 'transmission' images into 'projection' images, such that the sinogram was now described in terms of attenuation coefficient values for each pixel. Here, the sinogram values were also scaled by the voxel size, creating the dimensionless 'voxel optical density' values, as it has been termed in similar hyperspectral work [25–28]. Therefore, following reconstruction, the values were evaluated directly in terms of attenuation by removing the voxel size scaling. Step 3 also involved the use of flatfield correction, to negate any non-uniformity in the detector pixel response or X-ray source inhomogeneity. Typically 4–8 flatfields were acquired prior to X-ray scanning of a sample, with another set captured once the scan was complete. This was to account for any variations in the source over the total scan time. These flatfields were then averaged, and the correction was applied.

Finally, step 4 was necessary for any final corrections needed to minimise potential artefacts and improve image contrast, before reconstruction. In the case where the bad pixel correction was ineffective or did not sufficiently restore a typical spectrum, a further ring artefact correction was applied to the dataset. The method used a combined wavelet and Fourier analysis approach, developed by Münch *et al.* [29], to eliminate stripes in images, such as the vertical stripes in a sinogram caused by poorly-performing pixels in an X-ray CT scan. The stripes appear due to the same pixel registering an erroneous value for each projection, therefore as the sample rotates, the same error is observed at each angle, creating the vertical stripe which forms a ring artefact after image reconstruction. The effect is easily seen as the sinogram looks more 'blocky' and discontinuous between pixel columns. An example hyperspectral sinogram is shown in Fig. 3.4.1, with vertical stripes present. Also shown is the same sinogram following the application of the stripe removal filter. The images show the effect of the correction in creating a more natural transition in optical density values between the pixel columns.

Finally the centre-of-rotation correction, written in MATLAB by Egan in 2012 and based off the method proposed by Azevedo *et al.* [30], was an optional correction in MATLAB to account for misalignment of the sample on the rotation axis of the sample stage during scanning. In most cases, the correction was negligible, with a maximum offset on the order of ± 0.2 pixels.

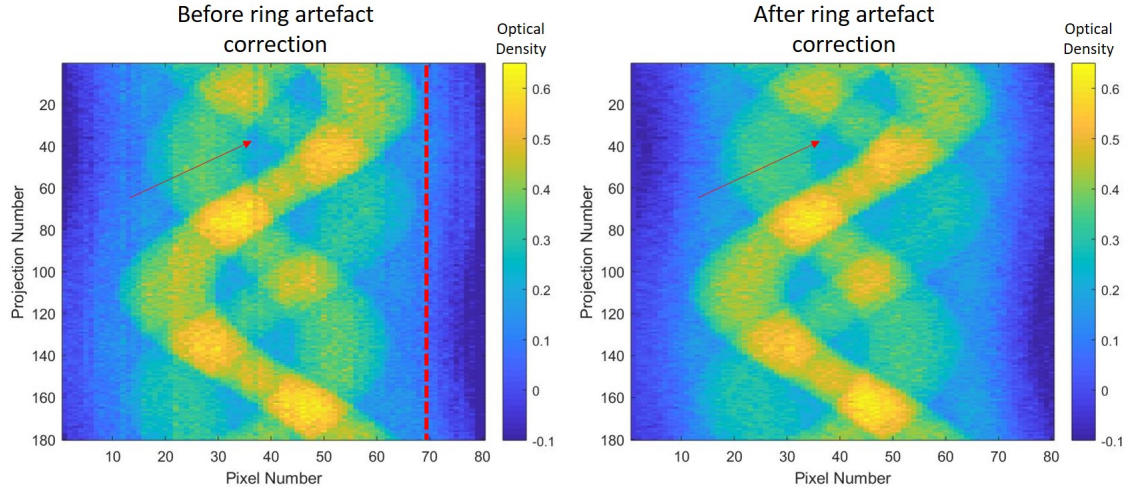


Figure 3.4.1. Implementation of the stripe reduction filter to minimise ring artefacts in hyperspectral imaging. (Left) Raw sinogram of the central image pixel, shown for a single energy channel, prior to any corrections. Stripes appear vertically (red dashed line) due to the same ineffective pixel in each projection. (Right) The same sinogram following ring artefact correction. A smooth, more natural sinogram is achieved, with less sharp changes between pixel columns. An example of a clear improvement in stripe reduction is highlighted (red arrow). Optical density values at the edge appear negative due to charge sharing effects.

3.4.2 Image reconstruction: The Core Imaging Library

As described in Chapter 1, one of the key aims for the PhD was the creation, optimisation and evaluation of novel hyperspectral reconstruction routines. In particular, this involved the implementation of iterative algorithms, offering greater flexibility in design to deal with low SNR and common artefacts observed in spectral acquisitions. In Section 2.3.5, a list of the considerations required to produce flexible and efficient algorithms for cone-beam hyperspectral were discussed. Compared to the simple, industry-standard FDK method found in most commercial systems for standard X-ray CT, very few spectral algorithms are readily available and easy to implement with lab-based hyperspectral datasets. Therefore, a crucial element of the research conducted in this thesis was a collaboration with the developers of the open source, Python-based software framework known as the Core Imaging Library (CIL - <http://www.ccpi.ac.uk/CIL>). The software tool is designed to offer a fully configurable set of modules that aid the workflow from raw data, through image reconstruction, to volume visualisation. Crucially, CIL offers a wide range of reconstruction algorithms for both standard and non-traditional imaging modalities, such as spectral (4D) datasets. Emphasis has been placed on the availability of a number of iterative algorithms, with the capability to "plug-and-play" with additional regularising parameters for noise suppression, edge preservation, non-negativity constraints, etc. Two articles on the CIL software (co-authored) have been published providing more detail on what the framework offers, including for multi-channel imaging applications [31, 32].

Given the computational cost of iterative algorithms, particularly in the case of spectral 4D algorithms, a high performance workstation was used for all hyperspectral reconstructions. A remotely-accessed, Linux-based workstation was utilised, with 256 GB of RAM and two Nvidia graphics cards, providing the GPU required to run the iterative routines. The full CIL framework was installed in a Python environment.

3.5 References

- ¹General Electric Company, *The ISOVOLT Titan E X-ray Generator*, tech. rep. (2009).
- ²Comet X-ray, *Mxr-225hp/11 Product Specifications*, tech. rep. 915371 (2018).
- ³Galil, *Motion Controllers* | Galil, 2020.
- ⁴M. C. Veale, P. Seller, M. Wilson, and E. Liotti, “HEXITEC: A High-Energy X-ray Spectroscopic Imaging Detector for Synchrotron Applications”, *Synchrotron Radiation News* **31**, 28–32 (2018).
- ⁵Q. Detectors, *HEXITEC Technical Datasheet*, tech. rep. (Quantum Detectors, 2022), pp. 1–4.
- ⁶P. Seller, S. Bell, R. J. Cernik, C. Christodoulou, C. K. Egan, J. A. Gaskin, S. Jacques, S. Pani, B. D. Ramsey, C. Reid, P. J. Sellin, J. W. Scuffham, R. D. Speller, M. D. Wilson, and M. C. Veale, “Pixellated Cd(Zn)Te high-energy X-ray instrument”, *Journal of Instrumentation* **6**, 1–11 (2011).
- ⁷Y. J. Lee, S. J. Park, S. W. Lee, D. H. Kim, Y. S. Kim, B. D. Jo, and H. J. Kim, “A monte carlo simulation study of the feasibility of a high resolution parallel-hole collimator with a cdte pixelated semiconductor spect system”, *Journal of Instrumentation* **8**, 10 . 1088 / 1748-0221/8/03/T03009 (2013).
- ⁸R. Ballabriga, J. Alozy, M. Campbell, E. Frojdh, E. H. Heijne, T. Koenig, X. Llopart, J. Marchal, D. Pennicard, T. Poikela, L. Tlustos, P. Valerio, W. Wong, and M. Zuber, “Review of hybrid pixel detector readout ASICs for spectroscopic X-ray imaging”, *Journal of Instrumentation* **11**, 1–31 (2016).
- ⁹A. Owens and A. Peacock, “Compound semiconductor radiation detectors”, *Nuclear Instruments and Methods in Physics Research, Section A: Accelerators, Spectrometers, Detectors and Associated Equipment* **531**, 18–37 (2004).
- ¹⁰M. D. Wilson, R. Cernik, H. Chen, C. Hansson, K. Iniewski, L. L. Jones, P. Seller, and M. C. Veale, “Small pixel CZT detector for hard X-ray spectroscopy”, *Nuclear Instruments and Methods in Physics Research, Section A: Accelerators, Spectrometers, Detectors and Associated Equipment* **652**, 158–161 (2011).
- ¹¹F. T. D. I. Ltd, *TTL-232R TTL TO USB SERIAL CONVERTER RANGE OF CABLES Datasheet*, tech. rep. (2022).
- ¹²S. L. Fisher, D. J. Holmes, J. S. Jørgensen, P. Gajjar, J. Behnsen, W. R. Lionheart, and P. J. Withers, “Laminography in the lab: Imaging planar objects using a conventional x-ray CT scanner”, *Measurement Science and Technology* **30**, 10 . 1088 / 1361 - 6501 / aafcae (2019).

- ¹³P. Gajjar, J. S. Jørgensen, J. R. Godinho, C. G. Johnson, A. Ramsey, and P. J. Withers, “New software protocols for enabling laboratory based temporal CT”, *Review of Scientific Instruments* **89**, 10.1063/1.5044393 (2018).
- ¹⁴R. D. Deslattes, E. G. Kassler, P. Indelicato, L. De Billy, E. Lindroth, and J. Anton, “X-ray transition energies: New approach to a comprehensive evaluation”, *Reviews of Modern Physics* **75**, 35–99 (2003).
- ¹⁵C. K. Egan, J. W. Scuffham, M. C. Veale, M. D. Wilson, P. Seller, and R. J. Cernik, “Energy calibration and gain correction of pixelated spectroscopic x-ray detectors using correlation optimised warping”, *Measurement Science and Technology* **28**, 10.1088/1361-6501/28/1/017001 (2017).
- ¹⁶G. Tomasi, F. Van Den Berg, and C. Andersson, “Correlation optimized warping and dynamic time warping as preprocessing methods for chromatographic data”, *Journal of Chemometrics* **18**, 231–241 (2004).
- ¹⁷B. Cline, M. Bullough, K. Richardson, H. Thorpe, M. C. Veale, and M. Wilson, “Characterisation of the performance of p-type Si detectors for hard X-ray spectroscopy”, *Journal of Instrumentation* **17**, 1–11 (2022).
- ¹⁸D. D. Duarte, S. J. Bell, J. Lipp, A. Schneider, P. Seller, M. C. Veale, M. D. Wilson, M. A. Baker, P. J. Sellin, V. Kachkanov, and K. J. Sawhney, “Edge effects in a small pixel CdTe for X-ray imaging”, *Journal of Instrumentation* **8**, 10.1088/1748-0221/8/10/P10018 (2013).
- ¹⁹G. Muehllehner, R. H. Wake, and R. Sano, “Standards for performance measurements in scintillation cameras”, *Journal of Nuclear Medicine* **22**, 72–77 (1981).
- ²⁰Nasco Education, *Nasco | Preserved Vertebrates*.
- ²¹S. D. Rawson, J. Maksimcuka, P. J. Withers, and S. H. Cartmell, “X-ray computed tomography in life sciences”, *BMC Biology* **18**, 1–15 (2020).
- ²²P. J. Dunmore-Buyze, C. Cruje, Z. Nong, J. J. Lee, J. A. Kiernan, J. G. Pickering, and M. Drangova, “3D vessel-wall virtual histology of whole-body perfused mice using a novel heavy element stain”, *Scientific Reports* **9**, 1–10 (2019).
- ²³B. D. Metscher, “Micro CT for comparative morphology: Simple staining methods allow high-contrast 3D imaging of diverse non-mineralized animal tissues”, *BMC Physiology* **9**, 10.1186/1472-6793-9-11 (2009).
- ²⁴B. D. Metscher, “MicroCT for developmental biology: A versatile tool for high-contrast 3D imaging at histological resolutions”, *Developmental Dynamics* **238**, 632–640 (2009).

- ²⁵C. K. Egan, S. D. M. Jacques, M. D. Wilson, M. C. Veale, P. Seller, A. M. Beale, R. A. D. Pattrick, P. J. Withers, and R. J. Cernik, “3D chemical imaging in the laboratory by hyperspectral X-ray computed tomography”, *Scientific Reports* **5**, 1–9 (2015).
- ²⁶C. K. Egan, S. D. M. Jacques, and R. J. Cernik, “Multivariate analysis of hyperspectral hard X-ray images”, *X-Ray Spectrometry* **42**, 151–157 (2013).
- ²⁷C. K. Egan, M. D. Wilson, M. C. Veale, P. Seller, S. D. M. Jacques, and R. J. Cernik, “Material specific X-ray imaging using an energy-dispersive pixel detector”, *Nuclear Instruments and Methods in Physics Research, Section B: Beam Interactions with Materials and Atoms* **324**, 25–28 (2014).
- ²⁸C. K. Egan, S. D. M. Jacques, M. D. Wilson, M. C. Veale, P. Seller, R. A. Pattrick, P. J. Withers, and R. J. Cernik, “3D elemental mapping of materials and structures by laboratory scale spectroscopic X-ray tomography”, *Journal of Physics: Conference Series* **849**, doi.org/10.1088/1742-6596/849/1/012013 (2017).
- ²⁹B. Münch, P. Trtik, F. Marone, and M. Stampanoni, “Stripe and ring artifact removal with combined wavelet-Fourier filtering”, *Optical Society of America* **17**, 8567–8591 (2009).
- ³⁰S. G. Azevedo, D. J. Schneberk, J. P. Fitch, and H. E. Martz, “Calculation of the Rotational Centers in Computed Tomography Sinograms”, *IEEE Transactions on Nuclear Science* **37**, 1525–1540 (1990).
- ³¹J. S. Jørgensen, E. Ametova, G. Burca, G. Fardell, E. Papoutsellis, E. Pasca, K. Thielemans, M. Turner, R. Warr, W. R. Lionheart, and P. J. Withers, “Core Imaging Library - Part I: A versatile Python framework for tomographic imaging”, *Philosophical Transactions of the Royal Society A: Mathematical, Physical and Engineering Sciences* **379**, 10.1098/rsta.2020.0192 (2021).
- ³²E. Papoutsellis, E. Ametova, C. Delplancke, G. Fardell, J. S. Jørgensen, E. Pasca, M. Turner, R. Warr, W. R. Lionheart, and P. J. Withers, “Core Imaging Library - Part II: Multichannel reconstruction for dynamic and spectral tomography”, *Philosophical Transactions of the Royal Society A: Mathematical, Physical and Engineering Sciences* **379**, 10.1098/rsta.2020.0193 (2021).

Chapter 4

Enhanced hyperspectral tomography for bioimaging by spatio-spectral reconstruction

¹Ryan Warr, ^{1,2}Evelina Ametova (E.A.), ¹Robert J. Cernik (R.J.C.), ³Gemma Fardell (G.F.),
⁴Stephan Handschuh (S.H.), ^{5,6}Jakob S. Jørgensen (J.J.), ^{1,3}Evangelos Papoutsellis (E.Pap.),
³Edoardo Pasca (E.Pas.), ¹Philip J. Withers (P.J.W.)

¹Henry Royce Institute, Department of Materials, The University of Manchester, Manchester, M13 9PL, UK

²Laboratory for Applications of Synchrotron Radiation, Karlsruhe Institute of Technology, Kaiserstr. 12, D-76131, Karlsruhe, Germany

³Scientific Computing Department, Science Technology Facilities Council, UK Research and Innovation, Rutherford Appleton Laboratory, Chilton, Didcot, OX11 0QX, UK

⁴VetCore Facility for Research, University of Veterinary Medicine Vienna, Vienna, Austria

⁵Department of Applied Mathematics and Computer Science, Technical University of Denmark, Denmark

⁶Department of Mathematics, The University of Manchester, Manchester, M13 9PL, UK

In this chapter, an investigation was conducted to evaluate the application of a novel, regularised, iterative reconstruction algorithm to improve the image quality of datasets acquired using a lab-based, hyperspectral X-ray CT system. We set out to analyse the key advantages of this new algorithm, compared to the filtered back-projection (FDK) method that is commonly used as a fast reconstruction routine in conventional XCT, and as the standard for many commercial XCT systems. Application of the novel routine to both a phantom sample and real-world, stained biological specimen enabled the clear benefits over FDK to be demonstrated for hyperspectral imaging, where noisy data is common. The work offered a first step into the ways in which higher quality spectral analysis and chemical mapping may be performed with hyperspectral X-ray CT.

Contribution Statement

The research project was conceived by myself, along with my supervisors (P.J.W. and R.J.C.). I led the overall organisation of the project, collaborating with the other co-authors to bring in their expertise for each element of the work. I worked with S.H who provided and stained the biological sample studied in this paper. S.H. also provided complementary dual-energy CT results for direct comparison with the hyperspectral images. The remaining authors (E.Pas, E.Pap., E.A., G.F., and J.J) were the main developers of the Core Imaging Library (CIL) software into which the hyperspectral reconstruction methods were built and optimised. I developed the design and arranged the manufacture of the multi-phase phantom. Further, I designed the experimental approach for the hyperspectral X-ray CT scans of both samples, including initial testing to determine optimum imaging geometries, scan time and X-ray source settings. These were performed by myself over a series of testing days on the two X-ray systems used in the research. I acquired all the hyperspectral datasets. The X-ray acquisitions on each machine were performed using pre-built programming scripts in both MATLAB and C#, modified by myself to work for CT acquisitions using the HEXITEC detector (full details provided in Section 3.2). The scripts were designed in such a way to allow full flexibility in scan settings, as well as track scan progress and log all relevant metadata for data processing.

For the initial preprocessing, all steps were conducted by myself in MATLAB, converting the raw data into a format ready for reconstruction in CIL. The data reconstruction, utilising the two algorithms discussed in the article, were applied using the open-source CIL module available through Python. The analytic FDK method was readily available as previously developed by the members of the CIL development team. The novel iterative method was specifically developed for this article, as well as a secondary article (in which I am a co-author) focusing on the use of the reconstruction algorithm in Bragg-edge neutron tomography [1]. As such, development of the algorithm was a core part of the research project, in both its software development and also the optimisation of the parameters within the reconstruction method. The Python programming of the novel method was predominantly developed by the aforementioned CIL team, as reported in [2, 3], while I regularly held meetings with them to discuss how best this could be implemented in hyperspectral CT. My datasets were used as test cases to refine the reconstruction algorithm and evaluate a range of regularisation parameters, This workflow was fed back into creating the optimum version of the CIL software, as well as enabling the best reconstructed output for the datasets produced in this research.

The majority of the manuscript was written by myself, including the initial draft versions and all subsequent edits as it was prepared for submission. Further, as the corresponding author of the paper, I led the review process when responding to comments from the journal referees.

This chapter has been published in Scientific Reports.

Warr, R., Ametova, E., Cernik, R.J. *et al.* Enhanced hyperspectral tomography for bioimaging by spatio-spectral reconstruction. *Sci Rep* **11**, 20818 (2021). <https://doi.org/10.1038/s41598-021-00146-4>

Abstract

Here we apply hyperspectral bright field imaging to collect computed tomographic images with excellent energy resolution (~ 1 keV), applying it for the first time to map the distribution of stain in a fixed biological sample through its characteristic K-edge. Conventionally, because the photons detected at each pixel are distributed across as many as 200 energy channels, energy-selective images are characterised by low count-rates and poor signal-to-noise ratio. This means high X-ray exposures, long scan times and high doses are required to image unique spectral markers. Here, we achieve high quality energy-dispersive tomograms from low dose, noisy datasets using a dedicated iterative reconstruction algorithm. This exploits the spatial smoothness and inter-channel structural correlation in the spectral domain using two carefully chosen regularisation terms. For a multi-phase phantom, a reduction in scan time of 36 times is demonstrated. Spectral analysis methods including K-edge subtraction and absorption step-size fitting are evaluated for an *ex vivo*, single (iodine)-stained biological sample, where low chemical concentration and inhomogeneous distribution can affect soft tissue segmentation and visualisation. The reconstruction algorithms are available through the open-source Core Imaging Library. Taken together, these tools offer new capabilities for visualisation and elemental mapping, with promising applications for multiply-stained biological specimens.

4.1 Introduction

With the increasing development in X-ray detector technology, the interest in energy-selective tomography has grown in recent years, particularly for medical imaging. In conventional X-ray absorption computed tomography (CT), each detector pixel records the total number of detected photons, irrespective of their energy, building up a single radiograph for each projection angle. Contrast is hence solely provided by differences in attenuation based on a sample's local material composition. Issues may then arise in post-processing segmentation, particularly for phases or structures of similar electron density, such as different types of soft tissue. In addition, due to the use of polychromatic radiation in laboratory X-ray imaging, beam-hardening artefacts are common, as the non-linear nature of attenuation as a function of energy is ignored without energy discrimination [4]. The introduction of spectroscopic detectors have enabled an additional dimension of information to be acquired, by measuring both the energy and position of each incident photon. Given that every element has a unique attenuation profile, these may be used as spectral 'fingerprints' in energy-sensitive CT imaging, such that full 3D elemental mapping may be performed from a single CT scan.

Recent spectral detectors take two main forms, differing mainly in their measurement processes, and number of energy 'channels' used for photon binning. Multispectral detectors use a set of 4-8 threshold (reference) channels, to which each incident photon is allocated based on the electrical signal generated upon detection. Such detectors have found use in the field of medical imaging for soft tissue differentiation [5–9]. While the low channel number enables high count-rates similar to conventional CT imaging [10], multispectral imaging provides coarse energy resolution ($\sim 5\text{--}10\text{ keV}$), thus for spectrally similar species, the threshold positions require specific pre-selection, as well as *a priori* knowledge of sample composition. In contrast, hyperspectral detectors can achieve very fine energy resolution ($\sim 1\text{ keV}$), with the ability to store photons into hundreds of narrow energy channels. The result is that, for every pixel, we acquire a 'pixel spectrum', containing a full absorption profile, for studying changes in attenuation as a function of energy. A key factor for chemical fingerprinting is the presence of absorption edges, observed as sharp discontinuities at the energies equivalent to the binding energies of the core-electron states (e.g. K-edges). Absorption edges act as characteristic markers for chemical identification, with many of these edges falling within the hard X-ray range ($> 10\text{ keV}$) used for imaging. One method that utilises the absorption edges is dual-energy CT (DECT). Following two sequential scans taken at different energies, DECT decomposes materials by virtue of their differing attenuation as a function of energy [11]. In biological and medical imaging, contrast-enhanced investigations in DECT use highly attenuating chemical tracers which preferentially bind to specific tissue structures. Numerous studies have previously reviewed the advantages of various contrast agents (e.g. I_2 , PMA/PTA) in both DECT and conventional CT for *in vivo* and *ex vivo* biological imaging [12–16]. A common limitation of DECT, however, is its time-consuming nature and the dose considerations required in some cases [17, 18]. Further, the technique struggles in the differentiation of materials with

spectrally similar characteristics, and therefore cannot unequivocally distinguish all materials. Hyperspectral imaging has, on the other hand, previously been demonstrated for the separation of closely-spaced K-edges, for example in the non-destructive evaluation of mineralised ore samples [19].

The capability of identifying spectral markers from the detailed absorption profile of each detector pixel comes at the cost of increased signal processing during data acquisition. Because the detected photons are distributed across hundreds of energy channels, the count-rate is limited to levels far below that of conventional CT [10]. Any individual energy bin is therefore subject to low signal-to-noise ratio (SNR) for each measured pixel spectrum. The issue of low SNR can create problems in chemical identification, particularly in the case of low concentration, where weaker signals may be hidden amongst the surrounding noise. Increased exposure time is one solution for improving SNR, however this is not always possible. Alternatively, the choice of reconstruction algorithm may be optimised for improved image quality. A conventional cone-beam reconstruction algorithm, such as Feldkamp-Davis-Kress (FDK - the 3D form of filtered back-projection for cone-beam imaging [20]) often fails to accurately reconstruct features for low count or undersampled data [21]. An advantage of hyperspectral imaging is the strong structural correlations between channels. Due to the fine energy resolution of the detectors, narrow channels result in a high degree of similarity between neighbouring energy bins. It is therefore possible to exploit the 'channel-wise' nature of the dataset as part of the reconstruction process, by employing dedicated algorithms. In the case of spectral imaging, this correlative nature may be used to, for example, provide both noise suppression and feature preservation in the spatial or spectral domains [22]. A number of methods have previously been evaluated for their effectiveness in spectral image reconstruction, including both undersampled and noisy datasets [23–25]. However, the availability of advanced, spectral reconstruction methods is still currently limited and inconsistent across the field. A set of modules have recently been developed in the form of open source software - the Core Imaging Library (CIL: <http://www.ccpi.ac.uk/CIL>) - to aid the complete workflow of CT datasets, including for 4D acquisition modalities like spectral imaging. Each method has been optimised for fast, simple use across a range of geometries and techniques. A detailed description of CIL may be found elsewhere, for both the overall software [2] and for its hyperspectral capabilities [3].

In this paper, we examine the capability of advanced spectral reconstruction methods in providing high quality results from undersampled, noisy 4D datasets, to enable elemental mapping. Using the HEXITEC hyperspectral detector [26] in a lab-based setting, we set out two main aims. Firstly, we assess the impact of implementing a dedicated, iterative reconstruction algorithm, compared to the conventional FDK method, using a physical, multi-phase phantom. By directly comparing reconstructions following a significant reduction in scan time, we evaluate the extent of feature restoration both in the spatial and spectral domains. Secondly, we evaluate reconstruction quality on a biological sample by means of different spectral analyses, including segmentation by K-edge subtraction, and measurement

of relative chemical concentration. Once more, a correlated reconstruction algorithm is applied, and used to highlight the vulnerabilities of the FDK method for noisy datasets. A single-stained lizard head was considered for mapping of tissue structures, and compared to equivalent results obtained following DECT. The work evaluates the advantages of hyperspectral imaging, compared to DECT and multispectral CT, where poorer energy resolution limits further analysis. This study also opens the way for further investigations into simultaneous staining of multiple contrast agents, where little work has previously been performed outside of DECT [13], or phantom studies for multispectral imaging [7, 27, 28].

4.2 Results

Firstly we examine a simple aluminium phantom test sample, measuring 0.5 cm in diameter, and 1 cm in height. Three cylindrical holes (diameter 0.7 mm) were drilled to a sample depth of 75% (0.75 cm), and filled with a different powder (CeO_2 , ZnO and Fe). Comprising different elements, each powder has different absorption properties for analysis. The phantom was imaged using a micro-focus source at 60 kV with beam power 6 W. Two scans were acquired using different exposure times, with an effective voxel size of 98 μm . The full dimensions of the sample were captured within the 80×80 detector field of view (FOV). The number of channels used in hyperspectral imaging are determined by two system characteristics - the tube voltage and the energy-channel calibration. For the 60 kV tube voltage applied, the full spectral profile was segmented across 200 energy channels for each pixel, with a measured single energy channel width of 1.2 keV. Given we have *a priori* knowledge of sample composition and, thus, absorption edge position in this case, a reduced subset of channels were selected for both datasets (corresponding to channel numbers 100 - 200, or energy range 28 - 56 keV), in order to increase the speed of reconstruction. To evaluate the capabilities of the iterative method in handling low count and under-sampled datasets, a comparison was made between two acquisition schemes: Scan A was taken with 180 projections and 180 s exposure time, and Scan B was taken with 30 projections and 30 s exposure time. Through prior testing, it was found that the conditions used for Scan A produced sufficiently low noise and strong feature definition, such that it may be treated as a 'ground truth', optimum state, when using conventional channel-wise FDK reconstruction. All results obtained under the conditions of Scan B were then compared directly to this reference case. Given the nature of spectral datasets, each channel may be analysed on an individual basis, akin to a set of multiple monochromatic scans. Figure 4.2.1a illustrates a set of sinograms for Scan A, corresponding to four equally spaced energy channels, combined with the corresponding central slice FDK reconstructions showing changes in attenuation value, μ as a function of energy. An important factor to note, however, is that we cannot directly identify chemicals through matching the absolute value of μ in each voxel to theoretical values for different elements. This is because non-linear effects, such as 'charge-sharing' between pixels, can lead to erroneous photon energies (and number of events) during scanning. For instances of lower X-ray flux, charge-sharing may be corrected for, as detailed elsewhere [19]. In this study, we show that, even without correc-

tion, we may still perform chemical identification and mapping through the identification of absorption edges, which remain clearly visible at their theoretical energy positions.

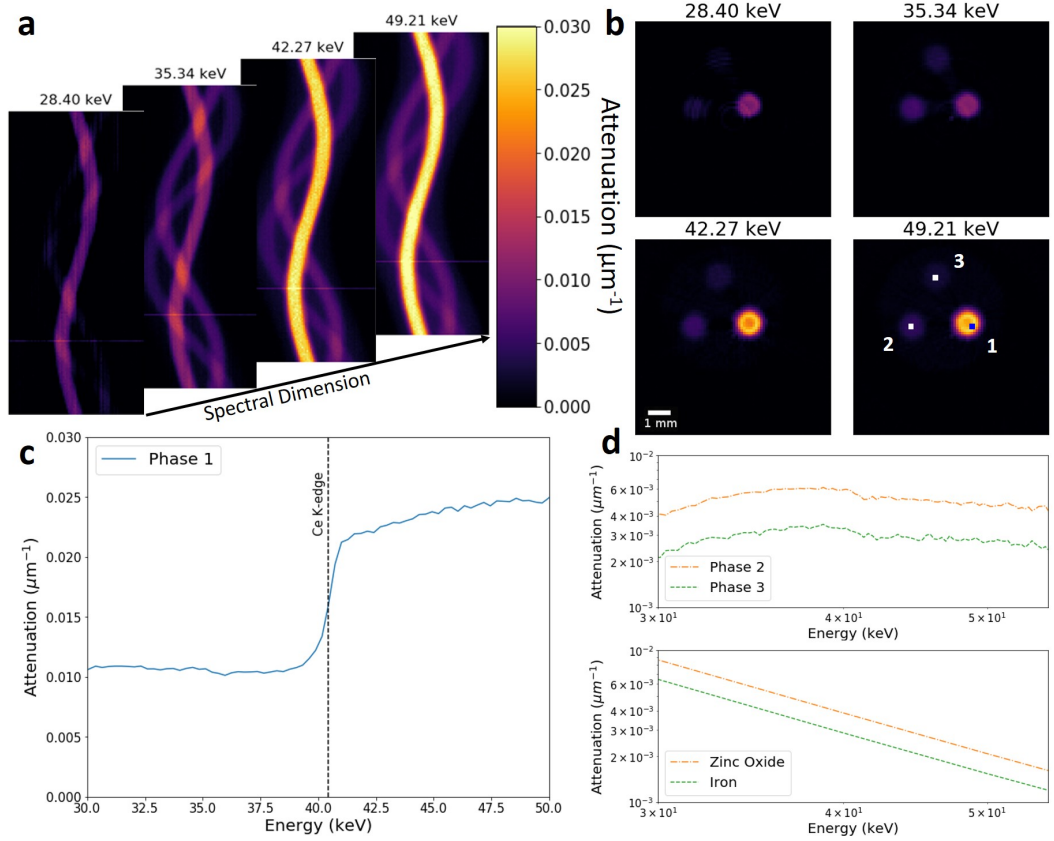


Figure 4.2.1. **Attenuation variation in the spectral dimension for a multi-phase powder phantom.** (a) Set of four sinograms taken between channels 100-175 at equal spacing of 25 channels (corresponding average energies are shown - channel width 1.2 keV) for Scan A. A single discontinuity in the sinograms appears due to an interrupted scan. (b) The corresponding FDK reconstructions for each energy channel of the sinograms in (a). Three distinct regions are observed, corresponding to the three metal-based powders. The colour scale measures the attenuation, and is consistent across both images. Three ROIs are highlighted (white/blue squares, marked by numbers for each respective powder phase). (c) Average voxel spectra of powder phase ROI 1. A line signifying the theoretical position of the cerium K-edge is overlaid for comparison. (d) Comparison of measured absorption spectra (top) for ROIs 2 and 3 located in the zinc oxide and iron phases respectively, and the theoretical values (bottom) over the same spectral range.

Through examination of the monochromatic reconstructions in Fig. 4.2.1b (covering the energy range 28 - 49 keV), we observe a significant rise in attenuation for one such phase, indicative of a spectrally significant elemental marker. By analysing voxel absorption spectra, chemical insight on sample composition can be obtained by examining changes in attenuation as a function of energy. Three regions of interest (ROIs) were selected in Fig. 4.2.1b covering each powder phase. The spectra shown in Fig. 4.2.1c corresponds to phase 1 where, as expected, an absorption edge is observed at 40.4 keV. Owing to the high energy resolution of the system, one may conclusively confirm that such an edge corresponds to that of cerium (40.443 keV). For the two remaining material phases in Fig. 4.2.1d, little variation in attenuation is observed. In addition, no absorption edges belonging to these materials (ZnO, Fe) were seen, as they fall below the sensitivity of the hyperspectral system (< 10 keV). Other methods may be employed to segment such materials, for instance through measuring the relative change in attenuation as a function of energy, as has been shown elsewhere [19]. Here we note that the rate of change of μ with increasing energy

does not precisely match the theoretical predictions. This may be due to effects such as pulse pile-up, which can distort the spectral profile due to the miscounting of coincident photon events [29]. A full investigation of the detector system electronics and signal acquisition properties, as a function of flux and energy range, is required to identify the precise cause. However, such detailed analysis is beyond the scope of this paper, with the observations not affecting results in terms of K-edge imaging. Unsurprisingly, the conditions of Scan A provide high quality reconstructions, with sharp feature definition, and little noise fluctuations across the full spectral range. Next we explore differences when reconstructing the low count and undersampled dataset of Scan B.

As previously discussed, analytic reconstruction methods, such as FDK, often fail to adequately reconstruct features for low SNR data. Here we explore the extent to which noisy, few projection data can be reconstructed, through the use of a spatio-spectral reconstruction algorithm. The reconstruction problem is typically formulated as a combination of a data fitting term between measured and reconstructed data, and one or more regularisation terms which encode desirable image characteristics. The problem is then solved using an iterative optimisation algorithm. CIL provides a number of building blocks to formulate the optimisation problems, and solvers to find a numerical solution. In this case we used a combination of two regularisation terms, known as the Total Variation (TV) and Total Generalised Variation (TGV), implemented along the spatial and spectral dimensions respectively. Further details of the regularisation terms, and how they were applied to the dataset, can be found in the methods section. The joint regularisation method, referred to here onwards as TV-TGV, is a novel method, chosen based on the prior knowledge that we expect noisy images, combined with the presence of an absorption edge. The CIL software enables such a method to be constructed and applied, and its advantages over other state-of-the-art methods has been demonstrated elsewhere in the case of Bragg-edge neutron tomography [1].

For the reconstruction of Scan B, TV-TGV was applied simultaneously across the full set of energy channels. By doing so, we exploit the correlations between neighbouring channels, compared to FDK, which is applied channel-by-channel and therefore cannot make use of such structural similarities. As described in Equation 4.1 (see methods section), three regularisation parameters (α for TV, $\beta_{1,2}$ for TGV) were optimised. Final parameters were determined to be 0.002, 0.18 and 0.25 for α , β_1 and β_2 respectively. A range of iteration numbers were tested, with no discernible improvements in image quality observed beyond 1000 iterations. Final reconstruction of the full volume was achieved with a runtime of 25 minutes for 1000 iterations of the algorithm.

Figure 4.2.2a shows a comparison of FDK and TV-TGV, through direct comparisons of reconstructed slices in the transverse and frontal planes. From the FDK reconstruction for Scan A, a distinct variation in attenuation is observed across the CeO_2 powder region, suggesting inhomogeneity in the powder. The frontal view confirms the non-uniform distribution, illustrating a consistently higher attenuation in the outer perimeter throughout the full depth of the sample. The slight 'cupping' feature is also reminiscent of beam hardening en-

countered for white beam imaging, which was not expected because of the high (1.2 keV) energy discrimination in this case, and is discussed further in the Supplementary Information (Fig. S3). Both reconstructed views illustrate the sufficiently high count and sampling of the dataset, with minimal noise and strong feature edge definition. In contrast, the undersampled reconstructions of Scan B highlight the limitations of FDK for low projection number and exposure time. Significant streak artefacts, projecting outwards from the CeO_2 powder phase, are observed, attributed to photon starvation due to the reduced photon counts stored in each energy channel, under the faster scan conditions. These artefacts are in addition to any further streaks caused by undersampling, combined with increased noise across the reconstructed slices.

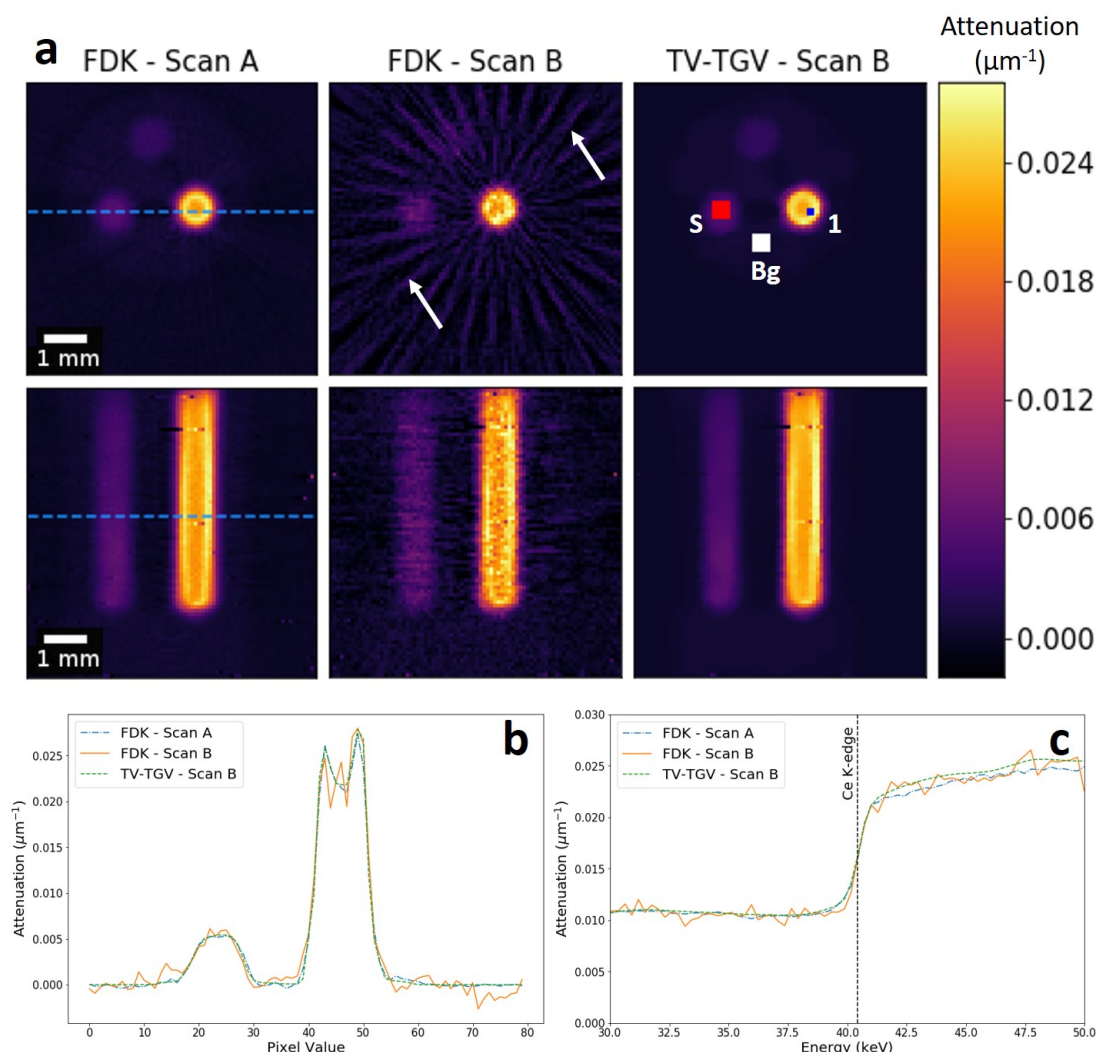


Figure 4.2.2. Comparison of reconstruction algorithms. (a) Transverse and frontal slices, showing reconstructions for FDK of sample Scan A (left column), followed by Scan B reconstructions with FDK (middle column), and TV-TGV (right column). All reconstructed slices are shown for a single energy channel (42.27 keV - channel width 1.2 keV). Dashed lines indicate the positions from which spatial profiles were measured for each reconstruction. White arrows mark examples of streak artefacts due to photon starvation. ROIs in the ZnO phase (red - S) and the Al phase (white - Bg) are highlighted for use in CNR calculations. (b) Spatial profile across two powder phases for the same energy channel. (c) Absorption spectra for ROI 1 within the cerium powder region (blue square in (a)).

Upon application of the TV-TGV method for Scan B, however, the data is recovered well, with the use of TV in the spatial domain providing enough smoothing to remove all streak artefacts, while maintaining edge preservation, restoring an image quality comparable to

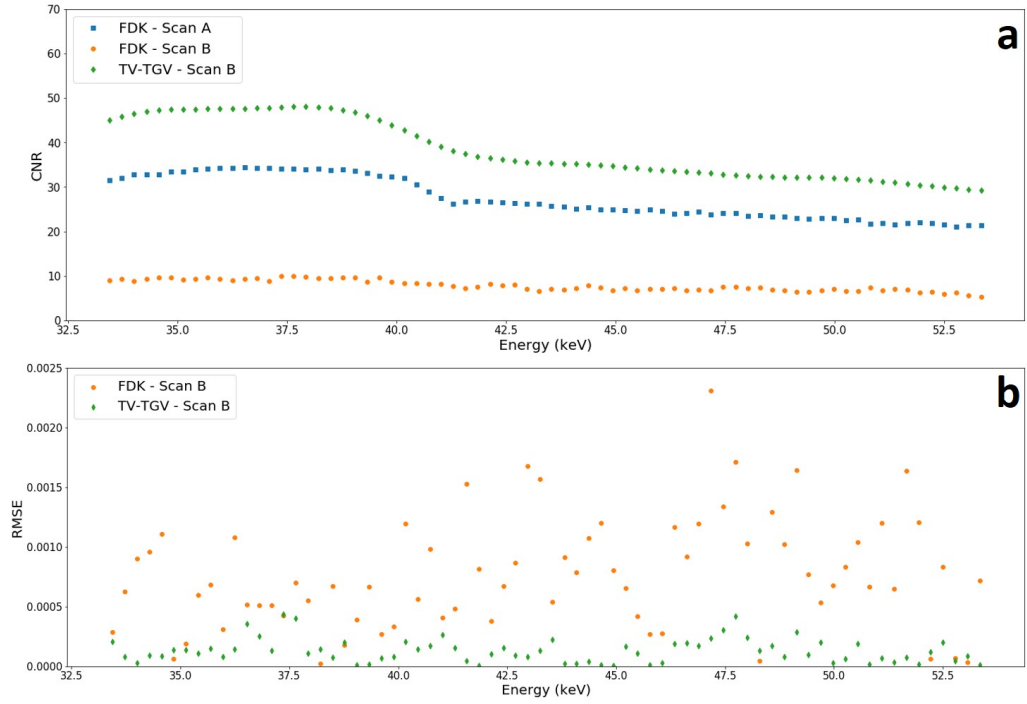


Figure 4.2.3. **Reconstruction comparison using different image quality metrics.** (a) Channelwise CNR calculations between the ZnO and the Al phase ROIs for an image slice in the transverse plane. Average values across the energy range were 27.44, 7.81 and 38.26 for FDK Scan A, FDK and TV-TGV Scan B respectively. (b) Channelwise RMSE values calculated using ROI 1 within the cerium phase. Values are calculated for all channels through comparison between Scan A and each respective Scan B reconstruction.

that of Scan A. We quantify this noise suppression through calculation of the contrast-to-noise ratio (CNR). Here, we apply the method employed by Bian et al., where the standard deviations of both the signal and background ROIs are taken into account [30]. In addition, we average out random variations both in the spatial and spectral domains through two steps: larger ROIs covering a greater range of pixels (5x5) average out spatial variations, while spectral fluctuations are reduced by computing the average standard deviation value for each ROI across all channels, and applying this to the CNR calculation for each individual channel. We use the ROIs marked in Fig. 4.2.2a (ROI S, ROI Bg) and calculate the CNR between the ZnO and Al phases in every channel. The result, shown in Fig. 4.2.3a, emphasises the successful feature restoration of the TV-TGV algorithm, with higher CNR measured in all channels, compared to both the Scan A and Scan B FDK reconstructions. As expected, with increasing energy, CNR gradually declines, with the difference in CNR values between TV-TGV and FDK Scan B narrowing, but still maintaining an average improvement of approximately 390% over the energy range. Additional quantitative analysis is shown in Fig. 4.2.3b in the form of channelwise root-mean-square-error (RMSE) measurements. Calculations are made by quantifying the difference in pixel values between ROI 1 of the cerium phase in Scan A, and the same ROI in each respective Scan B reconstruction. The residuals were then squared, averaged and square-rooted to determine an RMSE value for the energy channel. The method was then applied across all channels. The significant reduction in image error following TV-TGV reconstruction is highlighted, with RMSE values consistently lower than the FDK Scan B equivalent, across the full energy range. An additional single channel example of the RMSE calculation is shown in Supple-

mentary Fig. S4 to map spatial errors across different image planes. The application of TV-TGV can be analysed further by comparing spatial and spectral profiles for each method, as shown in Figures 4.2.2b and 4.2.2c respectively. For the spatial profile, measured across two of the powder phases (Fig. 4.2.2b), the advantages of the TV-TGV method for low count data are evident. Noise levels are significantly reduced for Scan B, compared to the equivalent FDK profile, with the TV-TGV method almost completely replicating the profile acquired for Scan A. For the spectral profile (Fig. 4.2.2c), TGV regularisation improves the linearity of the regions either side of the cerium K-edge for Scan B. It should be noted that, for such a simple phantom, identification of the absorption edge is not an issue here, regardless of reconstruction algorithm. However, the results demonstrate the capability of handling noisy, few projection data, and achieving high image quality in fast scan acquisitions. In this case, a reduction in scan time by a factor of 36 has been shown.

We next explore a more realistic sample in the field of biological imaging, where low SNR may pose problems in material identification and feature segmentation. An iodine-stained lizard head (*Anolis* sp.), measuring approximately 17 mm in length, and 10 mm in width, was scanned at a beam voltage of 50 kV, at a maximum power of 0.7 W, reconstructed with a voxel size of 137 μm . A spectral subset of channels from 60-160 (energy range 17.3 - 45.0 keV) was chosen given the prior knowledge of the single iodine stain, eliminating the need to reconstruct the full spectral range for identification of key elemental signals. A reduced projection dataset was used, such that only 60 projections (at 120 s exposures) were reconstructed over the full 360° rotation, to test the capabilities of the reconstruction algorithms. The need to limit X-ray dose is more prevalent in the life sciences field and, as such, the ability to extract high quality information from low count and/or undersampled data is crucial. Once more, TV-TGV reconstruction was applied, with the results compared to the conventional FDK method. Here, initial parameter estimates were based on the optimal conditions achieved in the reconstruction of the phantom sample, allowing faster identification of the optimal parameters. Final reconstruction was performed with parameters of 0.002, 0.25 and 0.35 for α , β_1 and β_2 respectively, with a total runtime of 40 minutes following 1000 iterations. Figure 4.2.4 demonstrates the smoothing effects in both the spatial and spectral domains, with the lens and jaw adductor muscles highlighted as key regions of interest. For both the axial and sagittal reconstructed slices (Fig. 4.2.4a), spatial smoothing provided improved edge definition of the exterior head shape, as well as the outer eye and jaw regions. The presence of the iodine contrast agent is easily confirmed with the precise matching of the theoretical edge position (33.169 keV) in each spectral profile (Fig. 4.2.4b). The benefit of noise suppression in the energy domain is demonstrated, allowing the presence of absorption edges to be more clearly defined, where they can often be lost within noisier reconstructions like FDK. Areas of lower iodine uptake, such as that of the jaw adductor muscles, may therefore be confidently identified as iodine-containing structures. As we have no ground truth reconstruction available for RMSE evaluation, we use only CNR calculations for a quantitative image metric, validated by the strong alignment between the RMSE and CNR metrics for the powder phantom. Figure 4.2.4c shows the channelwise CNR calculation for ROIs marked in Fig. 4.2.4a (ROI S, ROI Bg), which cover the jaw

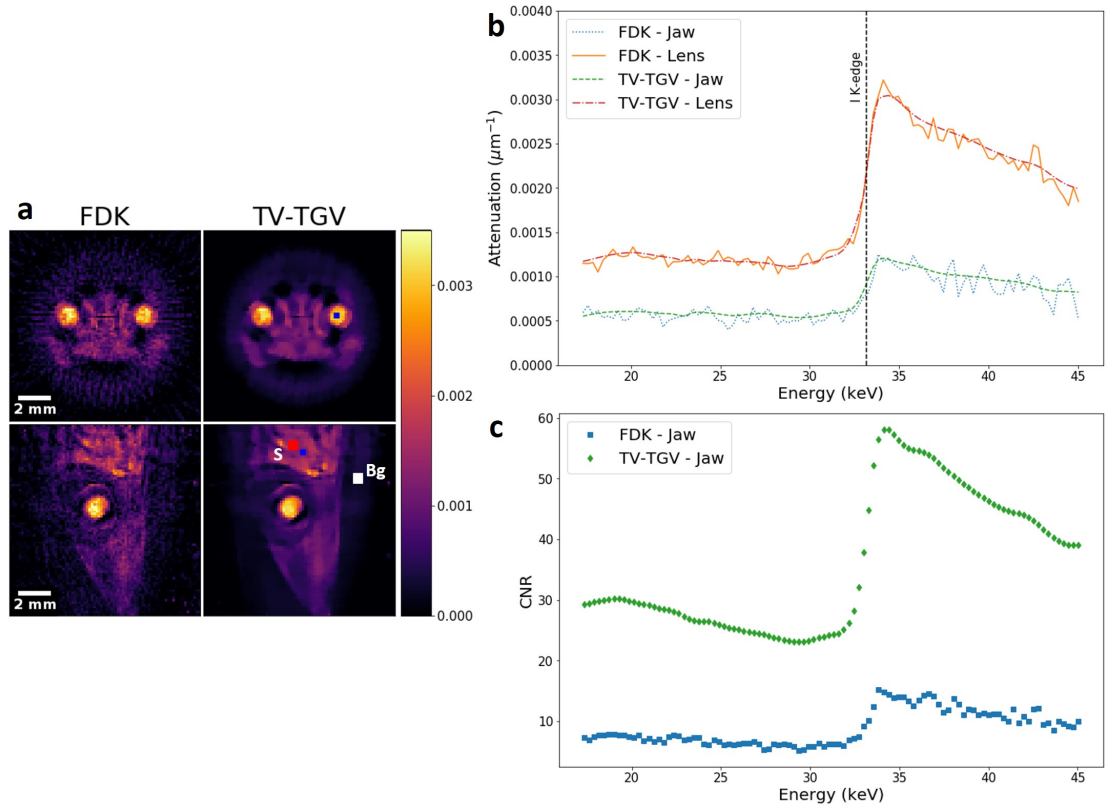


Figure 4.2.4. **Biological feature identification via regularised reconstruction.** (a) Reconstructed slices for channel 120 (33.95 keV - channel width 1.2 keV), along both the axial and sagittal dimensions, following FDK (left column) and TV-TGV (right column) reconstruction. General noise reduction and smoothing due to TV regularisation is observed over all spatial regions. (b) Absorption spectra measured for a ROI in two sections of the sample (blue squares in (a) - lens and jaw). A line signifying the theoretical position of the iodine K-edge is overlaid for comparison. (c) Channelwise CNR calculations of the stained jaw using the signal ROI (red - S) and the background ROI (white - Bg), for the image slice shown in the sagittal plane. Average CNR values across the energy range were 8.91 and 35.97 for FDK and TV-TGV respectively.

muscle and background respectively. Increased contrast using TV-TGV is found in every channel over the reconstructed range, compared to FDK. The impact of the iodine K-edge is also clear in its ability to sharply improve image contrast, and as such CNR, relative to the background material. The impact of TV-TGV is significant, producing an average CNR improvement of approximately 300% compared to the standard FDK algorithm.

Given the presence of an absorption edge, spectral analyses may be performed to provide information on iodine distribution throughout the biological specimen. Firstly we utilise the availability of a spectral profile in each voxel to measure relative iodine concentration, by virtue of spectral profile fitting. As shown in Fig. 4.2.5, linear least squares fitting was applied to regions before and after the absorption edge step for both the FDK and TV-TGV reconstructed volumes. By extrapolating and evaluating these fits at the known position of the K-edge (33.169 keV), we can precisely measure the size of the step change, $\Delta\mu_0$ [19]. Repeating this process at every voxel provides us with a map of $\Delta\mu_0$, which is directly proportional to the concentration of iodine present in the sample. Calculated values of $\Delta\mu_0$ are shown for both reconstructed volumes in Fig. 4.2.5a. Significant noise distortions in the FDK spectra lead to erroneous linear fitting, and consequently inaccurate measurements of $\Delta\mu_0$, as shown in Fig. 4.2.5b. Spectral smoothing due to TV-TGV, however, ensures improved precision in calculation of relative iodine concentration across the volume. Results

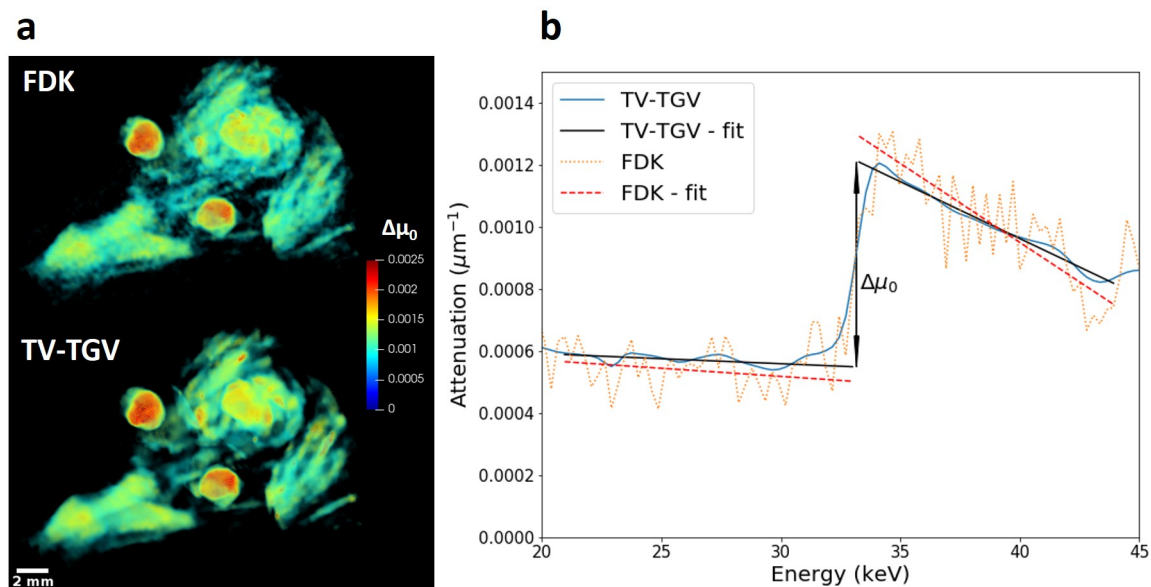


Figure 4.2.5. **Attenuation step size analysis for the iodine K-edge.** (a) 3D visualisations of the step size in the absorption edge, $\Delta\mu_0$, corresponding to relative iodine concentration. Images are shown for the lizard head sample following both FDK (upper left) and TV-TGV (lower left) reconstruction. (b) Absorption spectra acquired within the jaw adductor muscle for the same ROI in each reconstructed volume. Linear fits were acquired and extrapolated to the extremities of the absorption edge, where the relative change in attenuation values were measured.

indicate the diffusion of iodine fully into the lens, with high concentrations at the interior, and slightly lower levels on the exterior surface. Further, the increased reliability of $\Delta\mu_0$ measurements allows us to confidently identify 'hot spots' of higher iodine uptake, appearing on the brain and sections of the jaw muscles. The results are in good agreement with expected uptake regions of iodine contrast agent [14, 15].

Our second analysis uses the absorption edge as a means of segmenting iodine-containing material from the remaining structures. For this, we used K-edge subtraction (KES). That is, spectral information is extracted from energy channels before the edge of interest, and subtracted from an equivalent set after the edge. The result is a dataset containing only the contrasting material, eliminating other structures where attenuation is slight across this energy range. The method of KES has previously been applied for monochromatic imaging either side of absorption edges for segmentation [31, 32], as well as in hyperspectral cases, highlighting its potential for segmenting materials where more than one K-edge is present [19]. A detailed description of the method is provided in Supplementary Information (see Fig. S5). Here, KES also offers an opportunity to evaluate reconstruction quality by direct comparison of tissue segmentation for both the FDK and TV-TGV methods.

In order to measure the success of correct tissue segmentation, we match our hyperspectral reconstructed volumes against a DECT scan acquired of the same sample, reduced to the same spatial resolution ($137\ \mu\text{m}$) as that of the hyperspectral data. DECT has long been regarded as the 'gold standard' of biological stain imaging, and thus works well both as a measure of where hyperspectral X-ray CT stands in comparison, as well as an evaluation tool for each case of our spectral KES method. Segmented views of the sample are shown in Fig. 4.2.6 for both the TV-TGV regularised method, as well as the FDK reconstructed

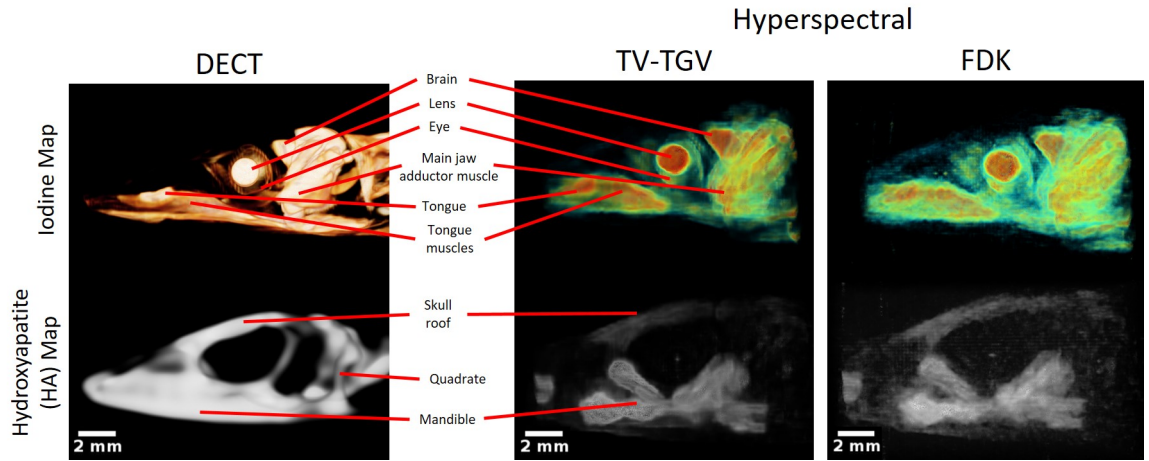


Figure 4.2.6. **Lizard head segmentation comparison for hyperspectral and dual-energy imaging.** Sagittal views of the segmented sample, producing maps of iodine-stained soft tissue (top row) and remaining hydroxyapatite (bottom row) bone structures. Results following K-edge subtraction for the TV-TGV reconstructed dataset (middle column) are directly compared to those following DECT acquisition of the same sample (left column), reduced to the same spatial resolution ($137\ \mu\text{m}$). Labels indicate the successful segmentation of several iodine-stained soft tissue regions for the hyperspectral dataset, with similar structures identified in the DECT equivalent image. A comparison of HA maps show distinct bone structures observed across both datasets, as well as the accumulation of bone mineral in particular regions due to long term sample storage. Included is an example of a bone structure (quadrate) unidentified in TV-TGV segmentation. (Right column) Equivalent maps following FDK reconstruction of the hyperspectral dataset are also shown, with significant noise hiding a number of key features.

volume. The resulting 3D visualisations are shown upon hyperspectral KES around the iodine edge. Using the DECT segmentation as reference for identifying key soft tissue features, the advantages of TV-TGV over FDK become clear. The increased level of noise due to FDK leads to reduced visibility, particularly in regions of lower iodine concentration, such as the tongue and jaw adductor muscles. In contrast, following KES of the TV-TGV volume, clear separation is observed for regions to which the iodine has diffused. Structures including the brain, lens, tongue and jaw muscle all show strong X-ray signal enhancement due to sufficient staining by elemental iodine. Segmentation of the remaining material offers the ability to observe 'non-contrast-enhanced' structures. In this case, the external skull structure, consisting mostly of hydroxyapatite (HA), remains. As confirmed by the DECT results, visualisation of certain bone structures, including the skull roof and mandible region, are achieved. Full definition of the skull structure is lost however, and this is attributed to the long-term storage of the sample prior to imaging. As such, bone mineral has accumulated in some regions, while having dissipated in others. Therefore, precise segmentation of HA material was not expected. Nevertheless, the advantage of combined hyperspectral imaging and advanced reconstruction algorithms is provided through the successful segmentation of iodine in the biological structure. Moreover, while 60 projections with 120 s exposures were taken, results from our phantom sample suggest a further reduction in exposure time is possible with minimal loss in reconstruction quality, owing to the application of regularised algorithms.

4.3 Discussion

The above case studies have highlighted the current state of the art for hyperspectral imaging in a lab-based setting and shown that, given an appropriate reconstruction algorithm, comparable levels of feature definition and characterisation of tissues and structures can be obtained to those in dual-energy and multispectral CT. However, our work is not without limitations. Spatial resolution is still far behind the standard set in conventional, and dual-energy, CT, emphasised by the downsampling of the aforementioned DECT results from their initial $9\text{ }\mu\text{m}$ voxel size. While currently limiting in the range of samples and features that may be observed, spatial resolution is only expected to improve with new detector technology. The use of an iodine contrast agent did not fully test the capability of chemical detection in hyperspectral imaging, given its high affinity for multiple soft tissue regions. A reasonable extension to the experiment is the use of additional chemical tracers, which bind to specific biological structures at varying concentrations. Given the high energy resolution of the hyperspectral (HEXITEC) detector, visualisation and segmentation of multiply-stained structures may be easily performed by virtue of measuring several spectral fingerprints. It has also previously been shown that absolute values of concentration may be determined in spectral imaging, given the use of an appropriate calibration phantom [33], offering potential diagnostic insight on tracer concentration and distribution as a function of time. The use of an *ex vivo* biological sample here may also be used as a step towards *in vivo* structure analysis in the future. Biological scans performed *in vivo* are limited more severely in terms of allowable X-ray dose and chemical concentration, hence the analysis performed in this work offers a solution in the form of regularised reconstruction for noisy, short exposure cases. Alternatively, there is a case to be made for the applicability of hyperspectral imaging in the absence of distinct spectral markers. With the availability of full spectral profiles at each pixel, beam-hardening artefacts may be eliminated now that changes in attenuation may be discriminated as a function of energy. In addition, while methods like K-edge subtraction are no longer applicable, measurement of relative attenuation changes over the energy range enables segmentation of poorly contrasting materials, which otherwise cannot be differentiated in conventional X-ray CT [19]. Previous work on bone densitometry and soft tissue segmentation has been shown to be possible with few channel spectroscopic imaging, without the need for contrast agents [34].

The use of advanced iterative reconstructions, in particular with application of regularisation terms, is also in its early stage development. The chosen method here of TV-TGV in the spatial-spectral domains is applicable given the composite materials producing sharp absorption edges, however optimisation of the regularised parameters for each dimension can be a slow process, due to the decoupled nature of the reconstruction algorithm. While every individual dataset will require specific tuning of each parameter, further development in the reconstruction protocols, combined with software packages like CIL to enable them, continues to allow these processes to be performed more quickly, while also laying a foundation upon which future methods may be based. In addition, the above studies have demonstrated the reduction in overall scan time enabled by the algorithms in CIL, offset-

ting the time taken to optimise reconstructed image quality. We predict that these methods will continue to allow further reductions in scan time, as well as limiting overall X-ray dose, without suffering significant losses in image quality, an advantage that may prove to be hugely beneficial to imaging in the biological field.

4.4 Conclusion

This paper has applied hyperspectral imaging to a simple test phantom, as well as, for the first time, mapping the location of staining in a biological sample, using as many as two hundred energy channels (~ 1 keV resolution). We have highlighted the vulnerabilities of conventional reconstruction methods for lab-based hyperspectral X-ray imaging. Through the use of a novel, spatio-spectral reconstruction algorithm, we have enabled precise chemical identification and mapping at the micrometer scale. Examination of a multi-phase phantom emphasised the significant reductions (36 times shorter) in scan time achievable by implementing regularised reconstruction to compensate for noisy datasets. In performing an *ex vivo* spectral CT scan of an iodine-stained lizard head sample, we have shown the capability of hyperspectral CT to have the elemental sensitivity to compete with existing techniques, such as DECT, in soft tissue segmentation and structural analysis, but with definitive identification of the iodine location through its characteristic K-edge. While here a single stain was measured and visualised, the exploration of multi-labelled biological samples is possible, given the high spectral resolution of the detector. Further, the weaknesses of analytic regimes such as FDK have been highlighted for spectral imaging, particularly for short scan acquisitions, reinforcing the need for standardised, iterative algorithms such as those provided in CIL. Together with the reduced scan times they enable, the correlated reconstruction methods open up the potential for hyperspectral studies in fields including non-destructive testing, security scanning and chemical catalysis. With improving detector technology and multi-staining methods, we conclude that lab-based hyperspectral CT offers great future prospects for biological research, among a number of other fields, such as chemical engineering, geology, materials science and cultural heritage.

4.5 Materials and methods

4.5.1 Phantom sample preparation

An aluminium cylinder was used as the matrix for three internal powders, due to its low attenuation relative to other metals. The choice of CeO_2 offered a clear example of a characteristic spectral marker (absorption edge), while the remaining two materials were used to evaluate the ability to restore lower attenuating structures following severe noise distortion. In addition, they enable discussion to be made on the identification of phases, absent of spectral markers.

4.5.2 Biological sample preparation

For this experiment the head of a lizard (*Anolis* sp.) was scanned and analysed. No live animals were used as part of the study. The sample was purchased as a fixed/preserved specimen from Nasco Education (USA). For long-term stability, the sample was fixed in formalin and stored in 70% ethanol, prior to staining. The sample was then dehydrated to 100% ethanol, before staining with 1% elemental iodine in absolute ethanol (I₂E). It has previously been shown that I₂E offers strong contrast in soft tissue, allowing for discrimination from bone and teeth (hydroxyapatite) structures [13, 14]. After staining, the sample was washed with 100% ethanol. Finally the biological specimen was mounted in 1.5% Agarose.

4.5.3 X-ray detector

The hyperspectral imaging was performed using an energy-sensitive HEXITEC detector [26], consisting of a 1 mm thick CdTe single-crystal semiconductor, bump-bonded to an ASIC producing a 2 cm × 2 cm detection area. The system is split into an 80 × 80 pixel array, with a 250 μm pitch. The detector offers an energy resolution of up to 800 eV at 59.5 keV and 1.5 keV at 141 keV. All raw data was acquired on an event-by-event basis using the HEXITEC detector software.

4.5.4 Data acquisition routines

For imaging of the phantom sample, a parallel source-sample-detector configuration was implemented in the custom-built Colour Bay, part of the Henry Moseley X-ray Imaging Facility (HMXIF) at The University of Manchester. The walk-in X-ray bay contains a 225 kV source, and full manipulator control is available via MATLAB scripts. Two scans of the phantom were acquired. Identical scanning conditions were implemented, at a geometrical magnification of 2.54, with the polychromatic X-ray source operating at a tube voltage of 60 kV with beam power 6 W. The chosen parameters ensured sufficient counts for energies close to measured absorption edges, optimised image contrast, while remaining within the count-rate limit of the detector. Further, X-ray flux was kept as low as possible to minimise the issue of photon saturation for the detector (X-ray source profile shown in Supplementary Information, Fig. S1). Exposure time, however, was varied, from 30 s up to 180 s per projection. In total, 180 projections were acquired per scan, with 2° step size over a full 360° rotation, resulting in total scan times of 2.5 and 11 hours, accounting for buffer times and bias voltage refreshing between projections in single photon detection [26]. Prior to reconstruction, one dataset was downsampled to 30 projections with 30 s exposure time to evaluate reconstruction quality on undersampled data.

As a further demonstration of the flexibility in lab-based hyperspectral imaging, the HEXITEC was next combined with the Nikon High Flux Bay system at the HMXIF. Once more a 225 kV source was utilised, however improved contrast was possible due to lower flux

capabilities, necessary for imaging of soft tissue within the biological sample. Source and sample manipulation were controlled by Nikon's proprietary software Inspect-X. A software module was created using the IPC interface to Inspect-X [35, 36], enabling communication between Nikon software and the spectral detector. The biological sample was secured to the rotation stage, held in place such that the specimen was suspended vertically during the acquisition. A geometric magnification of 1.81 was determined to project the sample fully in the detection area. The polychromatic X-ray beam was operated at a peak voltage of 50 kV, at a maximum power of 0.7 W (X-ray source profile shown in Supplementary Information, Fig. S1). Projection images were recorded at an angular step size of 2° over a full rotation, with exposure times of 120 s for each of the 180 projections, for an 8 hour total scan time. A reduced subset of the dataset was later taken for reconstruction, as described in the main text.

For all scans throughout the study, sets of four flat-field projections were acquired both before and after scanning for fixed-pattern noise subtraction, while a further dark current correction was applied during set-up, to minimise reduced spectral response due to increased leakage current, typically found at the edges of the detector [37]. Detected events were binned into a set of spectral channels, with the number determined by the maximum X-ray energy.

Prior to scanning, a preliminary energy calibration procedure was performed through the measurement of characteristic fluorescence signals from a series of metals [38]. The calibration procedure provides a direct transition between energy channels and their corresponding energies. Further, an inter-pixel gain correction was applied through the use of a correlative optimised warping algorithm using the same data [39, 40]. A calibration dataset was acquired before scanning of each sample, with the energy resolution of the system determined by measuring the distribution of FWHM values for characteristic peaks (see Supplementary Information, Fig. S2). Calibration values were consistent across each sample dataset. In each case, the energy resolution of the detector at 59.5 keV was found to be 1.21 ± 0.40 keV.

The accompanying DECT scan was conducted using a Zeiss Xradia XRM-400. The dual-energy acquisition performed scans at 40 kV and 80 kV, with a 0.17 mm glass filter and 0.4x optical lens. A total of 1051 projections were acquired over 210° rotation, with 15 s exposure times. The final reconstructed volume had a voxel size of $9.4 \mu\text{m}$.

4.5.5 Spectral CT data reconstruction

Initial processing of the acquired datasets was handled via MATLAB routines. In the case of the biological sample, a combined wavelet-based Fourier filter was applied in every channel for the removal of ring artefacts across the dataset [41]. For each dataset, the resulting 4D matrix (3 spatial dimensions, 1 spectral dimension) was then reconstructed using the CIL software. Full functionality and operation of the Python-based framework has been

discussed elsewhere [2, 3]. Given its traditional use in conventional cone-beam reconstruction, the FDK method formed the baseline from which all other results were compared and evaluated. For comparison, an iterative reconstruction algorithm was chosen, combining data fitting with spatial and spectral regularisation terms. The iterative algorithm took the form:

$$\min_u ||Au - b||_2^2 + \alpha \text{TV}_{x,y,z}(u) + \beta_{1,2} \text{TGV}_c(u) \quad (4.1)$$

where our first term concerns classic least-squares data fitting, with hyperspectral projection data, b , related to voxel value, u through the operator, A , based on the system geometry and properties. The latter terms concern the addition of spatial and spectral regularisation. Since 4D datasets exhibit different image properties in the spatial and spectral dimensions, two different regularisation terms were applied for their noise reduction capabilities. The result is a 'decoupled' regularisation algorithm. We define $\text{TV}_{x,y,z}(u)$ as the Total Variation (TV), applied across each spatial dimension [42] for a single channel, before summing over all channels (channel-wise). TV is one of the most widely used regularisers, as it favours piece-wise constant images, with sharp edge boundaries. The application of TV therefore allows for noise suppression of flat signal regions, while maintaining the local discontinuities at structure edges. The TV model fits well for CT images and has been successfully used previously for undersampled CT data [43], as well as noise suppression purposes [42, 44]. The use of TV regularisation has also previously demonstrated its benefits in spectral image reconstruction over analytic methods like FDK [24, 25]. However, TV is known for introducing 'staircasing' artefacts for piece-wise affine or smooth signals, for example ramp structures, which can result in patchy, unnatural reconstructed images [44]. Further, as the aim of TV regularisation is to reduce unwanted signal variations such as noise, the final reconstruction can suffer from a loss of contrast due to reductions in intensity [44]. For the spectral domain, we define $\text{TGV}_c(u)$ as the Total Generalised Variation (TGV), based on the method proposed by Bredies et al. [45]. Here we apply TGV regularisation along the channel direction, for each individual voxel in the image. TGV becomes applicable in the case of K-edge imaging, where we expect a smoothed step shape to our energy profiles across the edge position, spanning a few channels. TGV is able to reduce noise variations while maintaining the definition of any absorption edges present. Further, TGV avoids the staircasing effects experienced with TV. CIL provides a number of iterative algorithms to solve Equation 4.1, here we applied the primal dual hybrid gradient (PDHG) method [46]. Three regularisation parameters (α for TV, $\beta_{1,2}$ for TGV) were used to control the strength of penalisation for each regulariser, and must be optimised for each dataset. Therefore parameter values were chosen to suppress noise while preserving edge definition of reconstructed images and spectral profiles. In the case of noise suppression, optimal parameters vary based on the noise level in the dataset. Values of $\alpha > 1$ have previously been used images of significantly lower SNR [47], while for TGV regularization, selected values of the $\beta_{1,2}$ parameters are often based on a ratio between the two, with similar work on denoising suggesting this ratio, $\frac{\beta_2}{\beta_1}$ be either $\sqrt{2}$ or 2 [47–49]. These factors were therefore used to determine limits for initial parameter estimates. For the phantom sample, optimal values were determined based on three factors: visual comparison with reconstructed slices

of Scan A, precision of absorption edge position, and minimum obtained 'primal-dual gap'. The latter is a quantitative measure of convergence for the PDHG method, and has previously been used as a stopping criterion for the iterative method [46, 50].

4.6 Acknowledgements

We acknowledge the following EPSRC grants for funding that have enabled this project: "A Reconstruction Toolkit for Multichannel CT" (EP/P02226X/1) and "CCPi: Collaborative Computational Project in Tomographic Imaging" (EP/M022498/1 and EP/T026677/1). PJW and RW acknowledge support from the European Research Council grant No. 695638 CORREL-CT. JSJ was partially supported by The Villum Foundation (grant no. 25893). EA was partially funded by the Federal Ministry of Education and Research (BMBF) and the Baden-Württemberg Ministry of Science as part of the Excellence Strategy of the German Federal and State Governments. The Manchester (Henry Moseley) X-ray Imaging Facility was funded in part by the EPSRC (grants EP/F007906/1, EP/F001452/1 and EP/M010619/1). This work makes use of computational support by CoSeC, the Computational Science Centre for Research Communities, through CCPi.

4.7 References

- ¹E. Ametova, G. Burca, S. Chilingaryan, G. Fardell, J. S. Jørgensen, E. Papoutsellis, E. Pasca, R. Warr, M. Turner, W. R. Lionheart, and P. J. Withers, "Crystalline phase discriminating neutron tomography using advanced reconstruction methods", *Journal of Physics D: Applied Physics* **54**, 10.1088/1361-6463/ac02f9 (2021).
- ²J. S. Jørgensen, E. Ametova, G. Burca, G. Fardell, E. Papoutsellis, E. Pasca, K. Thielemans, M. Turner, R. Warr, W. R. Lionheart, and P. J. Withers, "Core Imaging Library - Part I: A versatile Python framework for tomographic imaging", *Philosophical Transactions of the Royal Society A: Mathematical, Physical and Engineering Sciences* **379**, 10.1098/rsta.2020.0192 (2021).
- ³E. Papoutsellis, E. Ametova, C. Delplancke, G. Fardell, J. S. Jørgensen, E. Pasca, M. Turner, R. Warr, W. R. Lionheart, and P. J. Withers, "Core Imaging Library - Part II: Multichannel reconstruction for dynamic and spectral tomography", *Philosophical Transactions of the Royal Society A: Mathematical, Physical and Engineering Sciences* **379**, 10.1098/rsta.2020.0193 (2021).
- ⁴G. Davis, N. Jain, and J. Elliott, "A modelling approach to beam hardening correction", *Developments in X-Ray Tomography VI* **7078**, 70781E (2008).

- ⁵H. Prebble, S. Cross, E. Marks, J. Healy, E. Searle, R. Aamir, A. Butler, J. Roake, B. Hock, N. Anderson, and S. P. Gieseg, “Induced macrophage activation in live excised atherosclerotic plaque”, *Immunobiology* **223**, 526–535 (2018).
- ⁶R. Aamir, A. Chernoglazov, C. J. Bateman, A. P. Butler, P. H. Butler, N. G. Anderson, S. T. Bell, R. K. Panta, J. L. Healy, J. L. Mohr, K. Rajendran, M. F. Walsh, N. De Ruiter, S. P. Gieseg, T. Woodfield, P. F. Renaud, L. Brooke, S. Abdul-Majid, M. Clyne, R. Glendenning, P. J. Bones, M. Billingham, C. Bartneck, H. Mandalika, R. Grasset, N. Schleich, N. Scott, S. J. Nik, A. Opie, T. Janmale, D. N. Tang, D. Kim, R. M. Doesburg, R. Zainon, J. P. Ronaldson, N. J. Cook, D. J. Smithies, and K. Hodge, “MARS spectral molecular imaging of lamb tissue: Data collection and image analysis”, *Journal of Instrumentation* **9**, 10.1088/1748-0221/9/02/P02005 (2014).
- ⁷N. G. Anderson, A. P. Butler, N. J. Scott, N. J. Cook, J. S. Butzer, N. Schleich, M. Firsching, R. Grasset, N. De Ruiter, M. Campbell, and P. H. Butler, “Spectroscopic (multi-energy) CT distinguishes iodine and barium contrast material in MICE”, *European Radiology* **20**, 2126–2134 (2010).
- ⁸N. G. Anderson and A. P. Butler, “Clinical applications of spectral molecular imaging: Potential and challenges”, *Contrast Media and Molecular Imaging* **9**, 3–12 (2014).
- ⁹R. K. Roeder, T. E. Curtis, P. D. Nallathamby, L. E. Irinata, T. L. McGinnity, L. E. Cole, T. Vargo-Gogola, and K. D. Cowden Dahl, “Nanoparticle imaging probes for molecular imaging with computed tomography and application to cancer imaging”, *Medical Imaging 2017: Physics of Medical Imaging* **10132**, 101320X (2017).
- ¹⁰R. Ballabriga, J. Alozy, M. Campbell, E. Frojdh, E. H. Heijne, T. Koenig, X. Llopart, J. Marchal, D. Pennicard, T. Poikela, L. Tlustos, P. Valerio, W. Wong, and M. Zuber, “Review of hybrid pixel detector readout ASICs for spectroscopic X-ray imaging”, *Journal of Instrumentation* **11**, 1–31 (2016).
- ¹¹T. R. Johnson, “Dual-energy CT: general principles”, *American journal of roentgenology* **199**, 3–8 (2012).
- ¹²E. Descamps, A. Sochacka, B. de Kegel, D. V. Loo, L. Hoorebeke, and D. Adriaens, “Soft tissue discrimination with contrast agents using micro-ct scanning”, *Belgian Journal of Zoology* **144**, 20–40 (2014).
- ¹³S. Handschuh, C. J. Beisser, B. Ruthensteiner, and B. D. Metscher, “Microscopic dual-energy CT (microDECT): a flexible tool for multichannel ex vivo 3D imaging of biological specimens”, *Journal of Microscopy* **267**, 3–26 (2017).

- ¹⁴B. D. Metscher, “Micro CT for comparative morphology: Simple staining methods allow high-contrast 3D imaging of diverse non-mineralized animal tissues”, *BMC Physiology* **9**, 10.1186/1472-6793-9-11 (2009).
- ¹⁵P. M. Gignac, N. J. Kley, J. A. Clarke, M. W. Colbert, A. C. Morhardt, D. Cerio, I. N. Cost, P. G. Cox, J. D. Daza, C. M. Early, M. S. Echols, R. M. Henkelman, A. N. Herdina, C. M. Holliday, Z. Li, K. Mahlow, S. Merchant, J. Müller, C. P. Orsbon, D. J. Paluh, M. L. Thies, H. P. Tsai, and L. M. Witmer, “Diffusible iodine-based contrast-enhanced computed tomography (diceCT): An emerging tool for rapid, high-resolution, 3-D imaging of metazoan soft tissues”, *Journal of Anatomy* **228**, 889–909 (2016).
- ¹⁶C. T. Badea, X. Guo, D. Clark, S. M. Johnston, C. D. Marshall, and C. A. Piantadosi, “Dual-energy micro-CT of the rodent lung”, *American Journal of Physiology - Lung Cellular and Molecular Physiology* **302**, 1088–1097 (2012).
- ¹⁷S. Achenbach, K. Anders, and W. A. Kalender, “Dual-source cardiac computed tomography: Image quality and dose considerations”, *European Radiology* **18**, 1188–1198 (2008).
- ¹⁸J. C. Schenzle, W. H. Sommer, K. Neumaier, G. Michalski, U. Lechel, K. Nikolaou, C. R. Becker, M. F. Reiser, and T. R. Johnson, “Dual energy CT of the chest: How about the dose?”, *Investigative Radiology* **45**, 347–353 (2010).
- ¹⁹C. K. Egan, S. D. M. Jacques, M. D. Wilson, M. C. Veale, P. Seller, A. M. Beale, R. A. D. Patrick, P. J. Withers, and R. J. Cernik, “3D chemical imaging in the laboratory by hyperspectral X-ray computed tomography”, *Scientific Reports* **5**, 1–9 (2015).
- ²⁰L. Feldkamp, L. C. Davis, and J. Kress, “Practical cone-beam algorithm”, *Journal of the Optical Society of America* **1**, 612–619 (1984).
- ²¹T. M. Buzug, *Computed Tomography: From Photon Statistics to Modern Cone-Beam CT*, 1st (Springer-Verlag, Berlin, 2008), pp. 32–48, 201–207.
- ²²C. K. Egan, S. D. M. Jacques, M. D. Wilson, M. C. Veale, P. Seller, R. A. Patrick, P. J. Withers, and R. J. Cernik, “3D elemental mapping of materials and structures by laboratory scale spectroscopic X-ray tomography”, *Journal of Physics: Conference Series* **849**, doi.org/10.1088/1742-6596/849/1/012013 (2017).
- ²³D. Kazantsev, J. S. Jørgensen, M. S. Andersen, W. R. Lionheart, P. D. Lee, and P. J. Withers, “Joint image reconstruction method with correlative multi-channel prior for x-ray spectral computed tomography”, *Inverse Problems* **34**, 1–27 (2018).
- ²⁴D. S. Rigie and P. J. La Rivière, “Joint reconstruction of multi-channel, spectral CT data via constrained total nuclear variation minimization”, *Physics in Medicine and Biology* **60**, 1741–1762 (2015).

- ²⁵Q. Xu, A. Sawatzky, M. A. Anastasio, and C. O. Schirra, “Sparsity-regularized image reconstruction of decomposed K-edge data in spectral CT”, *Physics in Medicine and Biology* **59**, 64–79 (2014).
- ²⁶P. Seller, S. Bell, R. J. Cernik, C. Christodoulou, C. K. Egan, J. A. Gaskin, S. Jacques, S. Pani, B. D. Ramsey, C. Reid, P. J. Sellin, J. W. Scuffham, R. D. Speller, M. D. Wilson, and M. C. Veale, “Pixellated Cd(Zn)Te high-energy X-ray instrument”, *Journal of Instrumentation* **6**, 1–11 (2011).
- ²⁷M. Mahdiah, R. Aamir, R. K. Panta, N. de Ruiter, A. Chernoglazov, J. L. Healy, A. P. H. Butler, and N. G. Anderson, “Discrimination of Multiple High-Z Materials by Discrimination of Multiple High-Z Materials by Multi-Energy Spectral CT – A Phantom Study”, *JSM Biomed Imaging Data Pap* **3**, 1–7 (2016).
- ²⁸R. Panta, S. T. Bell, J. L. Healy, R. Aamir, C. J. Bateman, M. Moghiseh, A. P. H. Butlera, and N. G. Anderson, “Element-specific spectral imaging of multiple contrast agents: A phantom study”, *Journal of Instrumentation* **13**, 10.1088/1748-0221/13/02/T02001 (2018).
- ²⁹K. Taguchi, E. C. Frey, X. Wang, J. S. Iwanczyk, and W. C. Barber, “An analytical model of the effects of pulse pileup on the energy spectrum recorded by energy resolved photon counting x-ray detectors”, *Medical Physics* **37**, 3957–3969 (2010).
- ³⁰J. Bian, J. H. Siewerdsen, X. Han, E. Y. Sidky, J. L. Prince, C. A. Pelizzari, and X. Pan, “Evaluation of sparse-view reconstruction from flat-panel-detector cone-beam CT”, *Physics in Medicine and Biology* **55**, 6575–6599 (2010).
- ³¹A. Panahifar, N. Samadi, T. M. Swanston, L. D. Chapman, and D. M. Cooper, “Spectral K-edge subtraction imaging of experimental non-radioactive barium uptake in bone”, *Physica Medica* **32**, 1765–1770 (2016).
- ³²S. Kulpe, M. Dierolf, B. Günther, M. Busse, K. Achterhold, B. Gleich, J. Herzen, E. Rummeny, F. Pfeiffer, and D. Pfeiffer, “K-edge Subtraction Computed Tomography with a Compact Synchrotron X-ray Source”, *Scientific Reports* **9**, 1–8 (2019).
- ³³A. De Vries, E. Roessl, E. Kneepkens, A. Thran, B. Brendel, G. Martens, R. Proska, K. Nicolay, and H. Gröll, “Quantitative spectral K-edge imaging in preclinical photon-counting X-ray computed tomography”, *Investigative Radiology* **50**, 297–304 (2015).
- ³⁴V. S. K. Yokhana, B. D. Arhatari, T. E. Gureyev, and B. Abbey, “Soft-tissue differentiation and bone densitometry via energy-discriminating X-ray microCT”, *Optics Express* **25**, 29328 (2017).
- ³⁵P. Gajjar, *IPC Quick Start Guide*, tech. rep. (The University of Manchester and Nikon Metrology, Tring, 2017).

- ³⁶P. Gajjar, J. S. Jørgensen, J. R. Godinho, C. G. Johnson, A. Ramsey, and P. J. Withers, “New software protocols for enabling laboratory based temporal CT”, *Review of Scientific Instruments* **89**, 10.1063/1.5044393 (2018).
- ³⁷M. D. Wilson, R. Cernik, H. Chen, C. Hansson, K. Iniewski, L. L. Jones, P. Seller, and M. C. Veale, “Small pixel CZT detector for hard X-ray spectroscopy”, *Nuclear Instruments and Methods in Physics Research, Section A: Accelerators, Spectrometers, Detectors and Associated Equipment* **652**, 158–161 (2011).
- ³⁸S. M. Alkhateeb, M. H. Abdelkader, D. A. Bradley, P. Seller, M. C. Veale, M. D. Wilson, and S. Pani, “Energy dispersive X-ray diffraction computed tomography of breast-simulating phantoms and a tissue sample”, *Medical Imaging 2013: Physics of Medical Imaging* **8668**, 1–11 (2013).
- ³⁹G. Tomasi, F. Van Den Berg, and C. Andersson, “Correlation optimized warping and dynamic time warping as preprocessing methods for chromatographic data”, *Journal of Chemometrics* **18**, 231–241 (2004).
- ⁴⁰C. K. Egan, J. W. Scuffham, M. C. Veale, M. D. Wilson, P. Seller, and R. J. Cernik, “Energy calibration and gain correction of pixelated spectroscopic x-ray detectors using correlation optimised warping”, *Measurement Science and Technology* **28**, 10.1088/1361-6501/28/1/017001 (2017).
- ⁴¹B. Münch, P. Trtik, F. Marone, and M. Stampanoni, “Stripe and ring artifact removal with combined wavelet-Fourier filtering”, *Optical Society of America* **17**, 8567–8591 (2009).
- ⁴²L. I. Rudin, S. Osher, and E. Fatemi, “Nonlinear total variation based noise removal algorithms”, *Physica D* **60**, 259–268 (1992).
- ⁴³E. Y. Sidky, C. M. Kao, and X. Pan, “Accurate image reconstruction from few-views and limited-angle data in divergent-beam CT”, *Journal of X-Ray Science and Technology* **14**, 119–139 (2006).
- ⁴⁴T. Chan, S. Esedoglu, F. Park, and A. Yip, “Recent Developments in Total Variation Image Restoration”, in *Mathematical methods in scattering theory and biomedical engineering: proc. of the 7th int. workshop (nymphaio, greece, 8–11 september 2005)* (2005), pp. 1–8.
- ⁴⁵K. Bredies, K. Kunisch, and T. Pock, “Total generalized variation”, *SIAM Journal on Imaging Sciences* **3**, 492–526 (2010).
- ⁴⁶A. Chambolle and T. Pock, “A first-order primal-dual algorithm for convex problems with applications to imaging”, *Journal of Mathematical Imaging and Vision* **40**, 120–145 (2011).

- ⁴⁷M. Holler and K. Kunisch, “On infimal convolution of TV-type functionals and applications to video and image reconstruction”, *SIAM Journal on Imaging Sciences* **7**, 2258–2300 (2014).
- ⁴⁸F. Knoll, K. Bredies, T. Pock, and R. Stollberger, “Second Order Total Generalized Variation (TGV) for MRI”, *Magnetic Resonance in Medicine* **65**, 480–491 (2011).
- ⁴⁹J. C. De los Reyes, C. B. Schönlieb, and T. Valkonen, “Bilevel Parameter Learning for Higher-Order Total Variation Regularisation Models”, *Journal of Mathematical Imaging and Vision* **57**, 1–25 (2017).
- ⁵⁰M. Zhu and T. Chan, “An efficient primal-dual hybrid gradient algorithm for total variation image restoration”, *UCLA CAM Report*, 1–29 (2008).

4.8 Supplementary Information

4.8.1 X-ray source properties

Figure S1 shows typical incident source spectra measured by a single pixel of the detector, taken from flatfield projections acquired prior to scanning the lizard head and powder phantom samples respectively. For the lizard head flatfield, X-ray fluence rate was calculated to be 2.1×10^6 photons $\text{cm}^{-2} \text{s}^{-1}$. For the powder phantom flatfield, the X-ray fluence rate was 6.2×10^6 photons $\text{cm}^{-2} \text{s}^{-1}$. Distinct peaks are observed in the 20 – 30 keV range, due to fluorescence of the Cd and Te semiconductor materials within the hyperspectral detector. In addition, different levels of scattering directly affect the proportion of fluorescent events, altering the expected count distribution in the lower energy regions. These changes to the flatfield spectra, compared to those acquired when the samples are in place, directly affect the resulting spectrum in each pixel as flatfield correction is applied. The low-energy tails for each flatfield spectra in Fig. S1 can be attributed to the charge sharing effect.

4.8.2 Spectral detector calibration

For both datasets, a calibration was performed using a ‘dial source’, whereby a ^{241}Am sealed source emits radiation which impinges onto various metal foils. This results in the emittance of X-ray fluorescence photons, which are characteristic of the metals, measured by the detector. Linear fitting of theoretical peak energies to ‘channel number’ can then be performed, to produce our calibration values. For this study, calibration was performed using the ^{241}Am γ -ray photopeak, as well as the $K_{\alpha,\beta}$ fluorescence peaks of Tb and Ba. Figure S2 (left) shows a typical spectrum measured from a single pixel of the detector, with markers identifying the peaks used for calibration. Calibration values were calculated prior to scanning of each sample, with consistent energy-channel conversions across datasets. In addition, the calibration data enables the energy resolution of the detector to be measured,

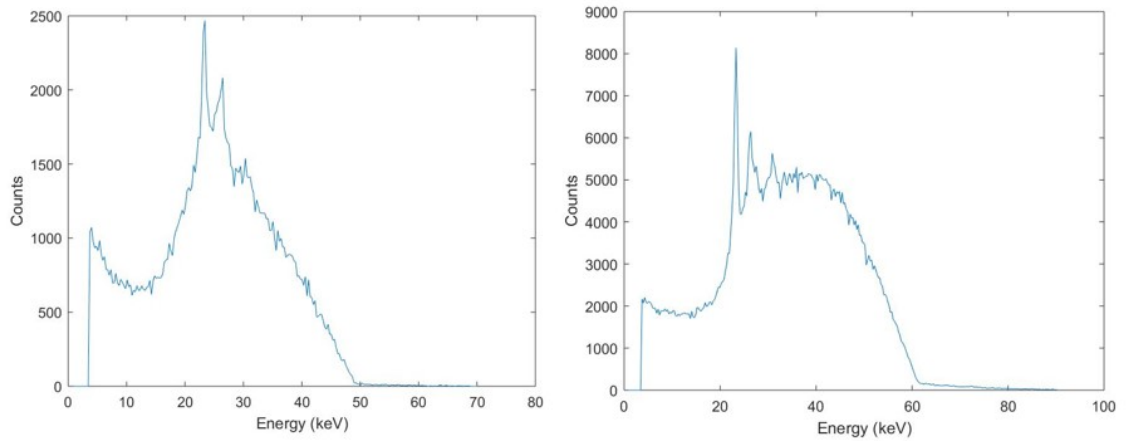


Figure S1. Example incident source spectra measured by a single pixel of the hyperspectral detector. For each flatfield, a low-energy tail is observed due to the effect of charge sharing. (Left) Single flatfield projection measured prior to scanning the lizard head sample (50 kV, 0.7 W, and 120 s exposure time.) Sharp peaks appear due to the fluorescence of the Cd and Te materials within the detector. (Right) Single flatfield projection measured prior to scanning the long exposure powder phantom (60 kV, 6W, and 180 s exposure time).

by measuring the FWHM of the peaks. Here, we measured the FWHM of the ^{241}Am photopeak (59.5 keV), for every pixel on the detector. Figure S2 (right) shows the distribution of FWHM values, with the energy resolution at 59.5 keV found to be 1.21 ± 0.40 keV. The increased energy resolution, compared to the ideal resolution of 800 eV at 59.5 keV, is attributed to the effect of charge sharing. As seen in Fig. S2 (left), this results in a high number of measured events in the low energy range, as measured charge is distributed between neighbouring pixels, causing a low-energy tail. In addition, the fluorescence of the Cd and Te semiconductor materials can result in additional charge sharing effects.

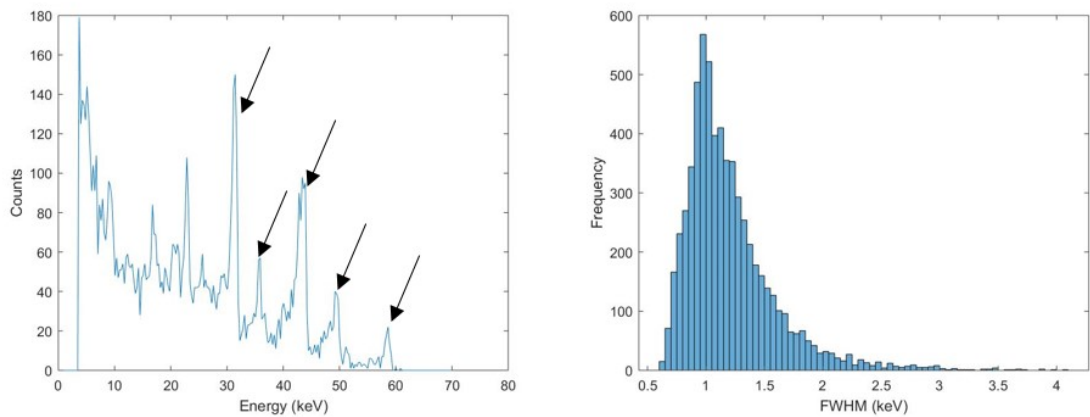


Figure S2. (Left) Example spectrum, measured in a single pixel, from the calibration source. Five arrows mark the peaks used for linear fitting, ranging from the $K_{\alpha,\beta}$ fluorescence peaks of Ba (farthest left) to the ^{241}Am γ -ray photopeak (farthest right). A large, low-energy tail is observed due to charge sharing. (Right) Distribution of FWHM values for the ^{241}Am peak, measured at 59.5 keV. Dead pixels were not considered.

4.8.3 Powder phantom - phase 1 artefacts

Following reconstruction of each dataset for the metal phantom, it is observed that phase 1 (the CeO_2 powder), produces slightly higher levels of attenuation at the edges of the cylinder, with a consistently lower level at the centre extending along the full depth of the cylin-

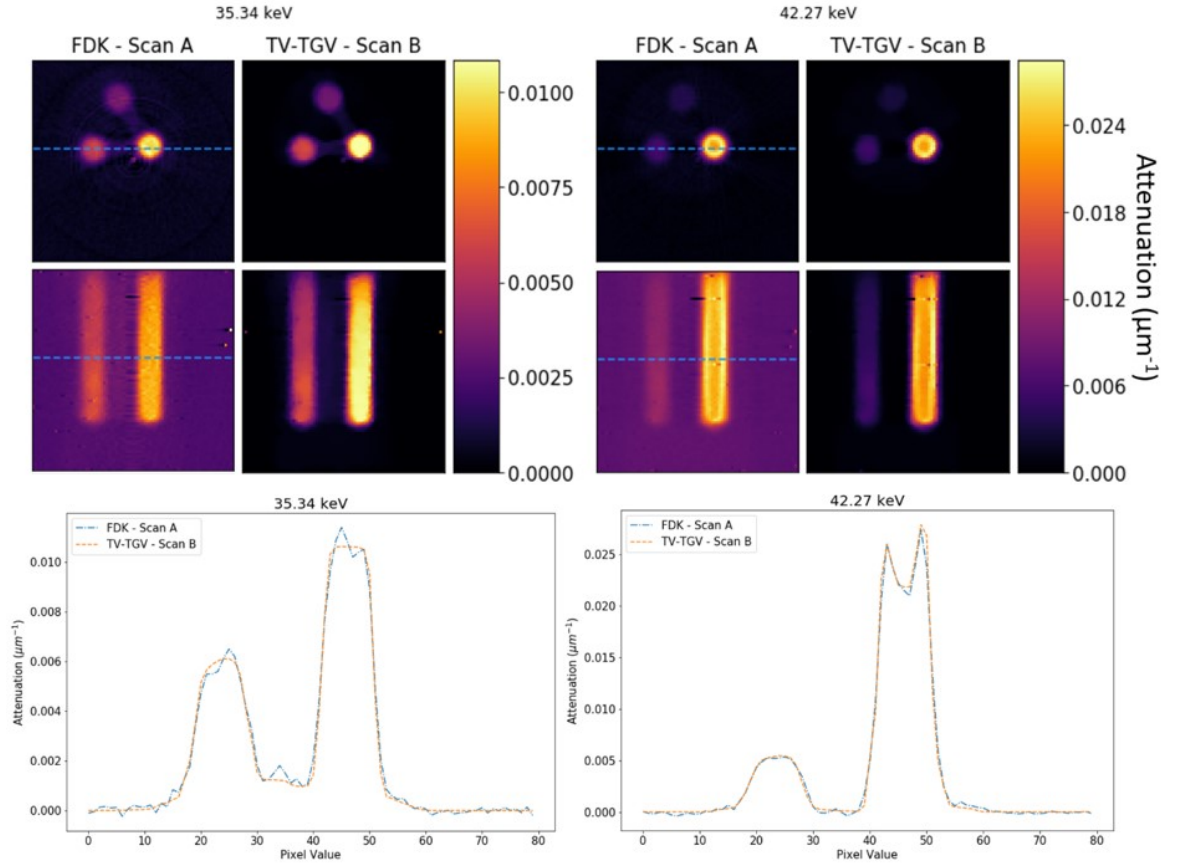


Figure S3. (Top) Spatial images of the FDK and TV-TGV reconstructions taken for Scan A and Scan B respectively. Images are shown for single energy channels, both before (top left) and after (top right) the Ce K-edge (40.443 keV). (Bottom) Line profiles taken across two phases, as marked on the spatial images (blue dotted line).

der (see Fig. 4.2.1b, 4.2.2a,b). In conventional white beam CT this ‘cupping’ contrast is characteristic of beam hardening, but could have a number of causes, for example, uneven filling of the cylinder by the CeO_2 powder. To investigate this further we scanned a solid tungsten rod and saw the same cupping contrast. This would rule out the effect of uneven packing. Regarding beam hardening, the energy resolution of the system is approximately 1.2 keV, and therefore, while not truly ‘monochromatic’, the width of each energy channel is very narrow, and it would be expected that the effect of beam hardening would be negligible for any single channel. Nevertheless, the artefact does appear to be much more prominent after the CeO_2 absorption edge than before it (Fig. S3). Consequently, while beam hardening seems unlikely it cannot be unequivocally ruled out. Alternative explanations may lie in the energy detector response and we will continue to investigate this effect.

4.8.4 Powder phantom - noise suppression

Given the low noise and clear feature definition of the FDK Scan A reconstruction, we treat this as a ground truth dataset, and as such we may quantify the improvement in reconstruction quality of Scan B by direct comparison with this data. In addition to the CNR values noted in the manuscript, here we also show spatial comparisons of the root-mean-square-error (RMSE) between our Scan B reconstructions and the Scan A dataset. Figure S4 shows RMSE values calculated across two image slices, in the transverse and frontal

planes, following FDK and TV-TGV reconstructions of Scan B. RMSE values are shown at a channel just beyond the Ce K-edge, where attenuation is at its highest for this phase, and as such errors are at their highest. As expected, significant deviations are observed in the RMSE values of Scan B following FDK reconstruction, due to the severity of artefacts and noise present. Such differences are almost entirely removed following TV-TGV reconstruction of Scan B, with only small deviations on the boundaries of the cerium phase, as well as a few erroneously high pixel values.

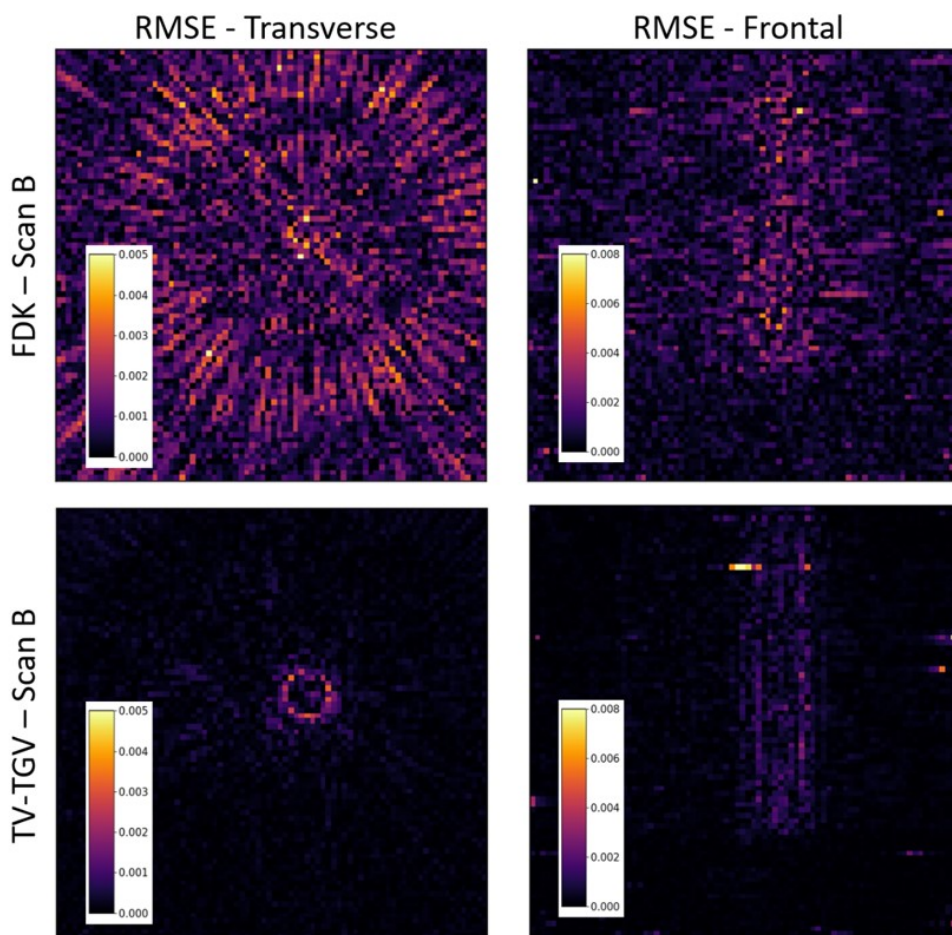


Figure S4. RMSE values calculated by comparison of the Scan B reconstructions with the results of Scan A. Images shown are taken for single slices in the transverse (left) and frontal (right) planes, at energy 42.27 keV. Colour bars quantify the RMSE in each image, with scaling consistent within image planes for comparison.

4.8.5 K-edge subtraction

When the presence of an absorption edge is known, K-edge subtraction (KES) may be used to isolate chemical information due to the element corresponding to the edge. In order for KES to be performed, the energy position of the edge must be known, either through prior knowledge of the sample composition, or visualisation of the acquired spectral profile. Two parameters are then required to determine the data extracted for subtraction either side of the edge: 'Separation' and 'Width', which identify the distance from the edge and the range of energy channels integrated respectively. As illustrated in Fig. S5, the values of each parameter may be adjusted based on the size and shape of the measured absorption step. In

the case of the iodine-stained lizard head, optimum values of 5 and 2 channels were found for width and separation respectively.

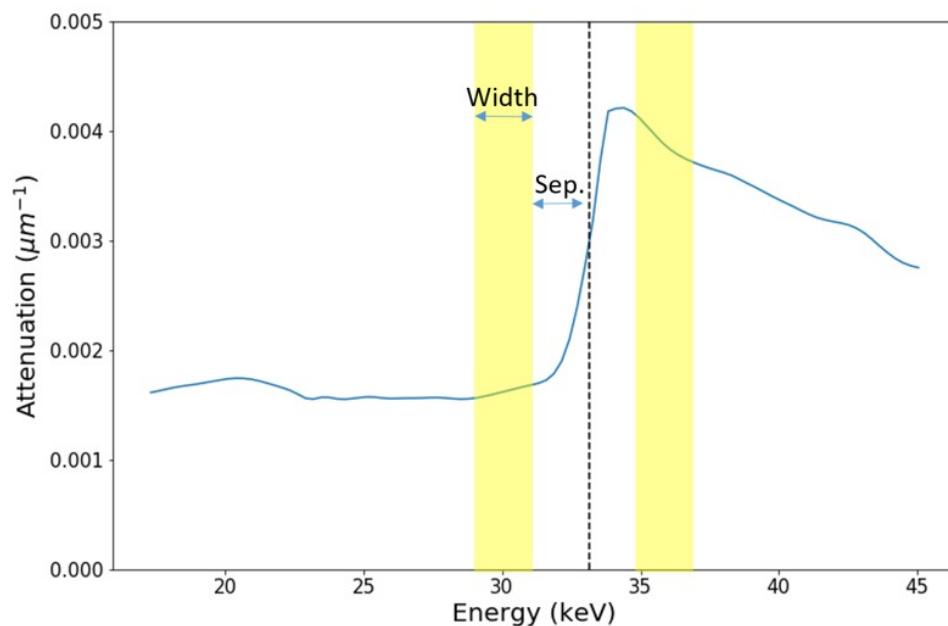


Figure S5. Example profile illustrating K-edge subtraction around the iodine absorption edge for a voxel in the stained lizard head. The theoretical position of the edge is marked for comparison (dotted line). The 'separation' (Sep.) determines the distance in energy (channels) away from the edge position, while the 'width' measures the energy (channel) range across which data is extracted (yellow bars). Identical values are used either side of the edge. Sizes of each parameter are not to scale.

Chapter 5

Quantifying multiple stain distributions in bioimaging by hyperspectral X-ray tomography

¹Ryan Warr, ²Stephan Handschuh (S.H.), ²Martin Glösmann (M.G.), ¹Robert J. Cernik (R.J.C.), ¹Philip J. Withers (P.J.W.)

¹Henry Royce Institute, Department of Materials, The University of Manchester, Manchester, M13 9PL, UK

²VetCore Facility for Research, University of Veterinary Medicine Vienna, Vienna, Austria

In this chapter, a study was conducted to evaluate the extent of quantitative information that could be extracted on the chemical distribution of contrast agents within stained biological specimens, through the use of hyperspectral X-ray CT. Typically, the chemical information within a sample extracted using spectral imaging can be largely qualitative. For example, the use of K-edge subtraction as a segmentation tool simply maps out the separate chemical regions, but provides no quantitative information on the relative uptake of the chemical throughout the sample. However, by using a set of chemical phantoms, of varying concentration, this study performed a first instance of measuring the relationship between chemical concentration, and the size of the absorption edge spectral marker identified. In doing so, hyperspectral imaging would allow the non-destructive measurement of chemical stain distribution as a function of position across a full sample volume. The study uses a set of two multiply-stained biological specimens to analyse both the energy-discriminating properties of hyperspectral X-ray CT, as well as the chemical concentration mapping capabilities.

Contribution Statement

This research project was conceived between myself and S.H. with the intention to perform further work on biological staining, expanding on the initial results obtained in Chapter 4. Following further meetings with my supervisors (P.J.W. and R.J.C.), a range of biological samples were assessed for their applicability to hyperspectral study and multi-staining regimes, with expertise provided by S.H. First experimental tests were conducted by myself on several stained biological specimens, with differing double- and triple-staining regimes. All samples were provided by S.H. alongside his colleague M.G., given the substantial time required to prepare and stain each specimen. I acquired all the data reported in this study, processed and reconstructed the data using the same workflow as in Chapter 4, and evaluated the results. All X-ray CT scans were conducted by myself using scripts designed in the C# programming language. Significant preliminary testing was required to strike a balance between high image contrast in the soft tissue structures, and using X-ray source settings capable of capturing the spectral signals of each high-attenuation stain in the samples. Such tests were conducted by myself over the course of several months, with multiple days of X-ray beam time. Upon determining the best biological samples for the research project through discussions with all co-authors, further phantom samples were prepared by S.H. and M.G. in order to conduct the quantitative measurements shown in the final manuscript.

All data processing, corrections, reconstruction and analysis of the hyperspectral data were conducted by myself using both MATLAB and Python. A similar workflow to that used in Chapter 4 enabled the same scripts to be adapted for the parameters of the latest datasets for faster processing from raw 2D images to reconstructed volumes. Additional scripts were written by myself for the novel quantitative calibration of the phantom samples, and the corresponding calculations of stain distribution in the biological specimens.

The complementary datasets of the samples, acquired using high-resolution XCT and dual-energy CT, were conducted, reconstructed and analysed by S.H. to provide direct comparisons to the hyperspectral equivalent datasets. S.H. also performed the volume registration of the datasets to enable a correlative, multi-modal approach for identifying and mapping spectral features in the biological specimens.

I wrote the majority of the manuscript, including several draft versions as comments were provided each time by all co-authors. The Methods sections on biological and phantom preparation were written by S.H. and M.G. All supplementary information, including all figures and videos, were produced by myself. Following submission, I took the lead as the corresponding author to handle all reviewer comments and make edits accordingly.

Quantifying multiple stain distributions in bioimaging by hyperspectral X-ray tomography

This chapter has been published in Scientific Reports.

Warr, R., Handschuh, S., *et al.* Quantifying multiple stain distributions in bioimaging by hyperspectral X-ray tomography. *Sci Rep* **12**, 21945 (2022).
<https://doi.org/10.1038/s41598-022-23592-0>

Abstract

Chemical staining of biological specimens is commonly utilised to boost contrast in various soft tissue structures, but unambiguous identification of staining location and distribution is difficult without confirmation of the elemental signature, especially for chemicals of similar contrast. Hyperspectral X-ray computed tomography (CT) enables the non-destructive identification, segmentation and mapping of elemental composition within a sample. With the availability of hundreds of narrow, high resolution (~ 1 keV) energy channels, the technique allows the simultaneous detection of multiple contrast agents across different tissue structures. Here we describe a hyperspectral imaging routine for distinguishing multiple chemical agents, regardless of contrast similarity. Using a set of elemental calibration phantoms, we perform a first instance of direct stain concentration measurement using spectral absorption edge markers. Applied to a set of double- and triple-stained biological specimens, the study analyses the extent of stain overlap and uptake regions for commonly used contrast markers. An improved understanding of stain concentration as a function of position, and the interaction between multiple stains, would help inform future studies on multi-staining procedures, as well as enable future exploration of heavy metal uptake across medical, agricultural and ecological fields.

5.1 Introduction

X-ray computed tomography (XCT) has long been used to analyse the internal structure and composition of samples non-invasively across a wide range of fields, including the study of biological soft tissue structures. Compared to destructive techniques, such as microscopic histology, the use of XCT enables whole samples to be examined in 3D in a single scan, to obtain insight on the internal organisation of the full specimen. Achieving strong contrast is a key aspect of XCT in order to confidently resolve structures and segment distinct regions. Contrast between material phases is dependent on their relative absorption (attenuation) of X-rays. Every element and material substance has a unique, energy-dependent attenuation profile, with materials of higher density such as bone (calcium) more readily absorbing of X-rays than say, unmineralised (soft) tissue. Some examples of attenuation profiles for chemical elements, as well as that of soft tissue, are shown in Fig. 5.1.1. With increased X-ray energy, differences in attenuation narrow, and therefore contrast is reduced. As such, for the hard X-ray energy range (> 20 keV), feature separation can be difficult, particularly for soft tissue imaging of biological samples with XCT [1].

One method of improved tissue characterisation is through the addition of contrast agents. These chemical stains, composed of highly-attenuating elements such as iodine or tungsten, offer a form of localised contrast enhancement, due to their differing affinities to soft tissue structures, increasing tissue attenuation. Popular stains include the use of iodine-based compounds (for deep and rapid staining of multiple tissues [2–5]) as well as phosphomolybdic and phosphotungstic acid (PMA, PTA) for their slower, but strong binding to proteins and connective tissue [1, 6, 7].

XCT enables the imaging of stained soft tissues at high contrast, however it cannot readily discriminate two or more highly-absorbing materials present in the same sample. Material differentiation can instead be accomplished by the evaluation of attenuation values at multiple energies. Common X-ray contrast agents display sharp discontinuities in X-ray attenuation at specific X-ray energies for chemical elements. The sharp jumps in attenuation, as observed in Fig. 5.1.1, correspond to K-edges, occurring at the binding energy of an element's K-shell electrons. By measuring the attenuation at a number of points, the aforementioned differences in absorption for soft tissues may be exploited to discriminate between them. Dual-energy CT (DECT) utilises this comparison of relative attenuation by exposing the tissues to X-ray spectra at two different energies. Multiple DECT geometries have been created, such as rapid voltage-switching, dual source systems or even dual-layer detector technologies [8], however the principle is still the same. By evaluating the attenuation response of the sample at two different X-ray energies, any differences in relative attenuation may be exposed and used as a means of material discrimination [9]. If a contrast agent is also added, then by selecting X-ray spectra at energies before and after the K-edge value, attenuation differences between stained and unstained regions are exaggerated, improving soft tissue identification. Biological applications of DECT have included imaging of vasculature [10], gout [11] and atherosclerotic plaque [12, 13]. The method of DECT is

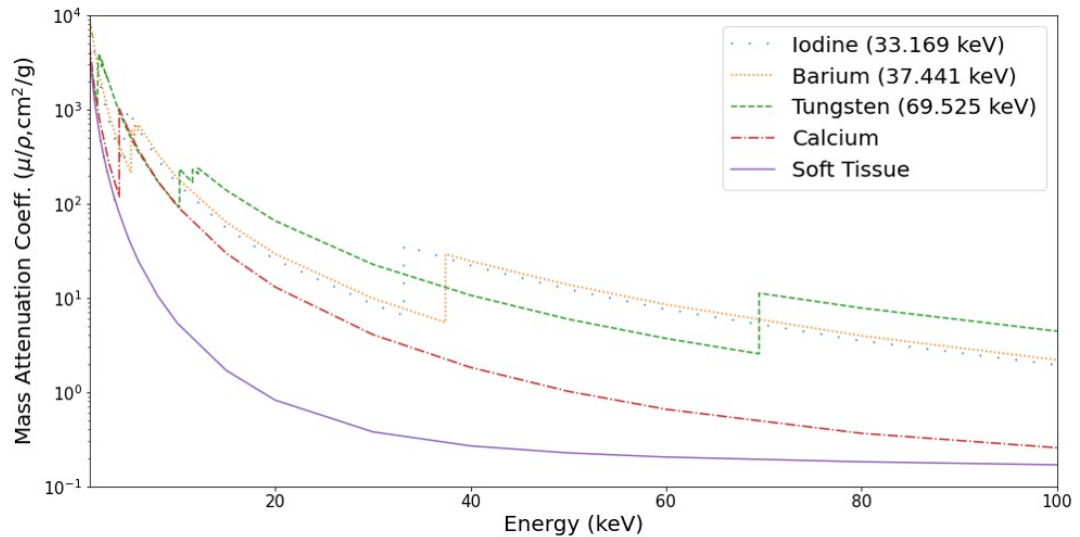


Figure 5.1.1. **Attenuation variation as a function of energy.** Known values of the mass attenuation coefficient shown for a number of materials. Across the hard X-ray energy range, many elements exhibit sharp rises in attenuation at their absorption edge positions (K-edge energies given in legend), providing strong contrast relative to soft tissue or calcium (bone) structures. Values extracted from the NIST online database [15].

disadvantaged however by the increased dose required [14], as well as the difficulty in unambiguously differentiating spectrally similar chemicals, such as that of barium and iodine contrast agents.

Developments in single photon-counting detector systems have aimed to bridge the gap between conventional absorption X-ray CT/DECT and full chemical characterisation modalities, by enabling the simultaneous acquisition and measurement of photon energy and position at each respective pixel. A key advantage to such systems is the ability to directly capture spectral markers, such as K-edges and X-ray fluorescence (XRF) peaks. The creation of detector systems with high spectral sensitivity over a very narrow bandwidth (≤ 1 keV), termed ‘hyperspectral’ detectors, have enabled full access to these markers, with the energy precision required to unambiguously match them to their elemental origins. With imaging possible over the hard X-ray range, the system is also well-suited for lab-based CT imaging, where a polychromatic spectrum may be captured in full, and recorded over hundreds of energy channels. As such, hyperspectral imaging facilitates the simultaneous recording, and mapping, of a wide range of chemical elements, to provide complete 4D spatspectral insight. Previous applications of hyperspectral CT have explored elemental segmentation with K-edges in geology [16] and single-stain bioimaging [17], XRF imaging of nanoparticles [18] and alloy melting/solidification [19], as well as spectral diffraction studies of brain amyloid plaque [20].

As shown elsewhere [16, 17], the size of an absorption edge may be measured to determine relative chemical concentration as a function of spatial position in the sample. However, with the addition of a suitable calibration phantom, it is possible to precisely extract the direct relationship between absorption step size and chemical concentration, to produce maps of absolute concentration. As such, for multiply-stained biological specimens, hyperspectral imaging provides a unique ability to further understand and quantify the interaction and

distribution of simultaneous contrast agents over a variety of soft tissue regions.

Testing popular and commonly used contrast agents, here we evaluate the ability to segment similarly-attenuating chemicals, and measure their concentration distribution across skin, muscle, connective tissue and vasculature in murine specimens. In order to investigate the efficacy of hyperspectral tomography for multi-stain bioimaging we examine a mouse hindlimb stained with two contrast agents (barium and iodine) and a mouse forelimb stained with three (barium, iodine and tungsten). In addition, we establish a calibration routine using a set of idealised phantoms of the same chemical stains. The spectroscopic imaging routine, here using the hyperspectral HEXITEC detector system, is verified against results achieved in conventional XCT and DECT, providing a foundation for automated elemental concentration measurement across a range of samples and research fields in the future. The unique ability to directly identify, quantify and map heavy elements shown in this study demonstrates the powerful potential of hyperspectral X-ray CT as a tool for non-destructive, 3D chemical analysis, applicable to research including medical biopsies and heavy metal poisoning.

5.2 Methods

As detailed below, all methods and procedures are reported in accordance with the ARRIVE guidelines, and the relevant legislation.

5.2.1 Biological sample and phantom preparation

All procedures followed animal care guidelines approved by the Administrative Panel on Laboratory Animal Care of the University of Veterinary Medicine in Vienna. No experimental procedures were carried out on living animals. Tissues for contrast-staining were collected from a single male, adult C57BL/6N mouse. The animal was specific pathogen-free (SPF) according to FELASA recommendations [21] and maintained in a barrier rodent facility. For mice that are not genetically modified (such as C57BL/6N), breeding as well as euthanasia for the mere purpose of tissue harvesting is not subject to permission by license according to national legislation of Austria and EU directive 2010/63/EU. Inhalation euthanasia was performed by an overdose of Isoflurane in accordance with international standards and recommendations for humane euthanasia [22, 23]. The mouse was placed in a closed receptacle containing gauze soaked with 5 ml Isoflurane. Inside the receptacle, a barrier of dry paper tissue ensured that the animal was only exposed to anaesthetic vapour and did not get in contact with the liquid Isoflurane. The animal was kept in the closed receptacle for ten minutes. Cessation of heartbeat and breathing occurred within less than five minutes. After ten minutes, the mouse was taken out of the receptacle and successful euthanasia was verified by the absence of heartbeat, breathing and toe pinch reflex. All perfusion and tissue preparation procedures were carried out post-mortem and thus also were

not subject to permission by license according to national legislation of Austria and EU directive 2010/63/EU.

Mouse hindlimb containing two high-Z contrast agents (barium, iodine) The mouse was perfused into the left ventricle with isotonic saline containing 10 UI/ml Heparin to remove blood from the vasculature, followed by perfusion fixation with 4% neutral buffered formalin. Subsequently, the vasculature was perfused with 30% Micropaque® barium sulphate (w/v) in 3% gelatine in phosphate buffered saline (PBS). After perfusion, the whole mouse was immersed in 4% neutral buffered formalin at 4°C for 72h. After fixation, the head, limbs and inner organs were harvested and stored in PBS at 4°C. A hindlimb was dehydrated to absolute ethanol through a graded series of ethanol concentrations (70%, 85%, 95%, 100%, 1h per step). The dehydrated hindlimb was stained using 1% elemental iodine (I_2) in absolute ethanol for six days at room temperature (RT) using gentle horizontal shaking. After staining, the hindlimb was washed in absolute ethanol and mounted in a polypropylene tube again in absolute ethanol.

Mouse forelimb containing three high-Z contrast agents (barium, iodine, tungsten) Details on fixation and perfusion have been reported above. A forelimb was transferred to 70% ethanol. In the first staining step, the forelimb was immersed in 1% (w/v) phosphotungstic acid hydrate (PTA) in 70% ethanol for 11 days at RT using gentle horizontal shaking. Subsequently, the sample was transferred to an acidic (pH 2.8, pH adapted using HCl) low concentration I_2 KI solution containing 0.25% (w/v) I_2 and 0.5% (w/v) KI in distilled water and stained for six days at RT using gentle horizontal shaking. Finally, the forelimb was mounted in the same acidic (pH 2.8) low concentration I_2 KI solution inside a polypropylene tube. Staining times used for the sample enable a complete staining from the cut surface to the elbow including all soft tissues of the upper arm, which was the main ROI in the present investigation. However, a longer PTA staining time would be required to completely stain soft tissues of the lower arm and paw.

BaSO₄ phantom Three mixtures of commercial Micropaque® barium sulphate suspension (1g BaSO₄ / ml) with 2% agarose gel were made. First, the agarose was heated to 70°C. Then, the respective amount of BaSO₄ and agarose was mixed with a Vortex Mixer, and pipetted into small plastic containers, followed by immediate cooling to avoid sinking of the BaSO₄ crystals. In total three concentrations of BaSO₄ were prepared, equating to 100 mg/ml, 200 mg/ml, and 400 mg/ml, respectively. The three plastic containers were put into a 5 ml polypropylene tube, and the space around the three containers was filled with 2% agarose that solidified at RT.

Iodine phantom Four containers of aqueous I_2 KI were prepared, with concentrations of 25.3, 50.6, 76.0 and 101.2 mg of I_3^- per ml respectively. The containers were held in an interchangeable setup to enable the locations of each concentration to be switched as required.

PTA phantom Three concentrations of aqueous PTA solutions were prepared, containing 50, 100, and 200 mg of phosphotungstic acid hydrate per ml. The three plastic contain-

ers were put into a 5 ml polypropylene tube, and the space around the three containers was filled with 2% agarose that solidified at RT.

5.2.2 Hyperspectral X-ray microCT imaging

All samples were scanned with a 225 kV Nikon X-ray source, based within the High Flux walk-in bay at the Henry Moseley X-ray Imaging Facility (HMXIF), University of Manchester. The experimental set-up for hyperspectral image acquisition follows that of a conventional system. The cone-beam source, sample rotation stage and detector are oriented in a parallel configuration along the same imaging plane. The key difference is that here we replace the standard energy-integrating detector with an energy-sensitive, hyperspectral imaging detector. In this case we use the high-energy HEXITEC hyperspectral detector [24, 25]. The HEXITEC detector is capable of measuring both incident photon position and energy, to build an attenuation profile across hundreds of narrow energy channels in each pixel. The result is that any single radiograph may be viewed at a single energy channel, directly exposing changes in attenuation as a function of energy. The HEXITEC consists of an 80×80 pixel array at a $250 \mu\text{m}$ pixel pitch, with a 1 mm thick CdTe sensor bump-bonded to an ASIC to produce a $2 \text{ cm} \times 2 \text{ cm}$ detection area. The detector has an achievable energy resolution of 800 eV at 60 kV and $< 1.5 \text{ keV}$ up to 160 kV. Due to the small FOV, all samples investigated in the study were chosen such that all key features could be seen in a single CT acquisition. In addition, the samples only contained features with sizes of $\geq 100 \mu\text{m}$, given the relatively poor spatial resolution of the HEXITEC. Prior to scanning of the samples, calibration of the detector was performed by acquiring fluorescent X-ray signals from a series of metal foils, emitted upon exposure to a radioactive ^{241}Am source. Matching of the theoretical X-ray fluorescence peak energies to their measured energy channel position enabled a linear fitting to be determined, providing a direct energy-to-channel conversion [26] (see Supplementary Fig. S1). The energy resolution of the system was determined based on the FWHM of the ^{241}Am photopeak at 59.5 keV, averaged over every pixel [17, 24], with resolution measured as $1.27 \pm 0.47 \text{ keV}$ (see Supplementary Fig. S2). An inter-pixel gain correction was also applied to account for differences in spectral response across the pixel array [27].

For each sample, the X-ray settings were chosen to strike a balance between measuring the spectral signal from each distinct chemical stain, while also ensuring strong image contrast was obtained. As such, the mean X-ray energy was increased high enough to capture a significant number of photons at each known chemical absorption edge. Table 5.3.1 shows the selected scan settings for each of the biological samples, as well as the individual chemical phantoms.

Raw data processing: For each sample, additional processing of the raw data was applied following creation of the 4D sinogram. A common artefact observed following CT reconstruction is that of ring artefacts, due to poorly functioning or miscalibrated detector pixels. Applying the method developed by Münch et al. [28], which uses a combined wavelet-

Fourier based approach, reduces the presence of such artefacts in the final reconstructed volume. In addition, a centre-of-rotation correction was applied to sample datasets where there existed a misalignment from the true centre during scanning. Pre-processing was performed using scripts in MATLAB.

High resolution XCT/DECT Imaging: For the mouse hindlimb and forelimb, respective XCT and DECT scans were performed to provide high spatial resolution comparative datasets to those acquired with hyperspectral imaging. For the hindlimb, the XCT scan used a MicroXCT-400 (Carl Zeiss X-Ray Microscopy, Pleasanton, CA, USA), with a $0.4\times$ detector assembly, at source settings of 80 kVp, 100 μ A. The reconstructed voxel size was 13.63 μ m. The forelimb was scanned using the same system and $0.4\times$ detector assembly, but as a dual-energy set-up. Two scans were acquired at 40 kVp/200 μ A and 80 kVp/100 μ A, with a reconstructed voxel size of 7.97 μ m. Three material fractions were calculated using a post-reconstruction basis material decomposition approach, as described elsewhere [9]. Joint dual energy profiles of bone (hydroxyapatite) and iodine-stained soft tissue were measured using ROIs in the registered dual energy data. Using an energy pair of 40kVp/80kVp, bone and PTA, as well as iodine and barium, show almost identical dual energy profiles. This is because the mean energy of each spectra (~ 27 keV for 40 kVp and ~ 42 keV for 80 kVp) produce similar attenuation around the K-edges of iodine and barium (33.17 keV and 37.44 keV, respectively), but are both far from the K-edges of calcium and tungsten (4.04 keV and 69.53 keV, respectively). The result of the basis material decomposition were three image channels ('materials'): channel 1 = bone + PTA, channel 2 = iodine + barium, channel 3 = water).

5.2.3 Reconstruction routine

A regularised iterative approach was adopted, using the Primal-Dual Hybrid Gradient (PDHG) algorithm [29], combined with separate regularising parameters applied to the spatial and spectral dimensions. In this case, we used a method known as TV-TGV regularisation, based on different forms of the Total (Generalised) Variation regularising routine. The algorithm has previously been applied successfully to improve reconstructed image quality for hyperspectral X-ray and neutron tomography [17, 30]. Variations of the TV method are known to be efficient at suppressing noise [31, 32], and using a split approach of applying TV and TGV to spatial and spectral domains respectively enabled optimisation for the differing levels of noise in each dimension. Optimisation of weighting parameters plays a crucial role in obtaining high signal-to-noise ratio and for performing precise analysis of the spectral attenuation profiles. Under- or over-estimation of the parameters can lead to little noise suppression or over-smoothing, affecting the identification of weak spectral markers. Therefore, parameters for spatial and spectral regularisation were optimised by trialling a range of values for each dataset, until values were selected to obtain a balance between sufficient noise suppression and strong feature contrast. The reconstruction method was implemented using the open-source Core Imaging Library (CIL) software [33, 34], and fully programmed through Python. All samples were reconstructed with 1000 iterations of

the algorithm, which has proven to be sufficient for noise suppression in previous hyperspectral datasets [17].

5.2.4 Volume registration

In order to compare exactly corresponding slices between hyperspectral and XCT/DECT datasets, image volumes were imported into the 3D software package Amira 2021.1. (FEI Visualization Sciences Group, part of Thermo Fisher Scientific, Mérignac Cédex, FR). Co-registration of datasets was performed using the *Register Images* tool. The respective XCT/DECT dataset was registered to one energy channel (38.94 keV for double-stained hindlimb, 38.13 keV for triple-stained forelimb) of the hyperspectral data based on normalized mutual information and using a rigid body transformation (six degrees of freedom, translation and rotation in X-Y-Z). After co-registration of image volumes, the corresponding slice was generated with the *Resample Transformed Image* tool using Lanczos interpolation.

5.2.5 Spectral analysis routines

K-edge subtraction: In order to segment and visualise different stained tissue phases, the spectral analysis method of K-edge subtraction (KES) was applied. The method used two key parameters: width and separation. Width determined how many energy channels were integrated either side of the absorption edge, while separation measured the gap between the channel of the known edge position, and the regions either side over which channels are integrated and subtracted. The separation value was determined based on the minimum number of channels needed to span the full absorption edge for each element. A value above zero is often required as experimentally measured absorption edges show a rise in attenuation over a narrow range of channels, compared to the sharp discontinuity observed in theoretical data. For the iodine and barium K-edges in the study, optimal width and separation values of 5 and 2 channels were used, respectively. The separation was increased to 10 channels for the tungsten K-edge in the triple-stained specimen due to a broader absorption edge measured. The method was applied using Python code, producing elemental segmentation maps for each unique K-edge position [16].

Edge height analysis: Following measurement of individual voxel spectra and identification of an absorption edge, the relative size of the absorption edge step was calculated in Python. Linear fits were applied to the attenuation profile either side of the absorption edge, before extrapolating the fits to the known K-edge value. The difference in attenuation value ($\Delta\mu_0$) between the upper and lower bounds of the linear fit provide a relative measure of the change in phase attenuation.

Absolute concentration calculation: Applying linear fitting to the edge height analysis for the chemical phantoms, the relationship between concentration and step size was determined. The fitted relationship was then used as a baseline for determining absolute concen-

tration of staining agents in the soft tissue structures of each sample. For each sample, the equation corresponding to the linear fit for each contrast agent was used to directly convert edge height values to absolute concentration values. The method was applied iteratively in Python on a voxel-by-voxel basis to produce a 3D map of concentration values for each elemental stain.

5.3 Results

Elemental segmentation of multi-stain specimens Our first sample examines a case of double-staining within a mouse hindlimb. The sample was stained with elemental iodine (I_2) for general soft tissue contrast enhancement, while barium sulphate ($BaSO_4$) was added to improve the visualisation of the blood vessels within the limb [35, 36]. Despite the relatively poor spatial resolution achievable with the HEXITEC detector it is well suited for imaging the upper knee region of the hindlimb. Indeed, the larger blood vessels in the hindlimb vasculature can reach hundreds of microns in diameter [37]. Here, the use of these two stains represents an example of contrast agents difficult to spectrally separate with DECT due to their similar attenuation profiles and closely-spaced K-edges. A complete breakdown of the scanning parameters, for all biological specimens and phantom samples used in this study, is shown in Table 5.3.1. Following scanning, the datasets were reconstructed using an iterative algorithm catered towards optimising image quality for 4D hyperspectral imaging. Given the count-rate limitations of hyperspectral detector systems, a conventional CT reconstruction algorithm such as cone-beam filtered back-projection (FDK) is not well suited, as this algorithm often results in noisy 4D reconstructed volumes, as shown elsewhere [17, 30].

Sample	Stains	Beam voltage (kV)	Beam current (μA)	Exposure time (s)	Projections	Voxel size (μm)
Mouse Hindlimb	$I_2/BaSO_4$	60	13	120	180	151
Mouse Forelimb	$I_2KI/BaSO_4/PTA$	90	13	120	180	128
Phantom 1	I_2KI	60	13	120	180	223
Phantom 2	$BaSO_4$	60	13	120	180	196
Phantom 3	PTA	90	20	120	180	177

Table 5.3.1. Sample preparation and scan settings. A full list of the different contrast agents and scan settings for each biological sample and phantom included in this paper.

Figure 5.3.1A presents a set of reconstructed images corresponding to the same CT slice of the hindlimb, but recorded for three energy channels. A sharp rise in attenuation between the first two energy channels is consistent with the presence of the iodine K-edge (33.17 keV) between them. With approximately 99% of the soft tissue estimated to be stained by iodine, as expected the majority of the reconstructed cross-section shows a consistent attenuation increase. An additional benefit of evaluating quasi-monochromatic image slices is to qualitatively identify different phases, prior to spectral segmentation. The spectral profiles for three regions of interest (ROIs) in Fig. 5.3.1A are shown in Fig. 5.3.1B. The spectra for

ROI₁ indicates the presence of the iodine contrast agent, with a rise in attenuation at the energy corresponding to the iodine K-edge. Similarly, ROI₂ includes an absorption step at the energy corresponding to the K-edge of barium, as well as a small rise around the iodine K-edge. The magnified image in Fig. 5.3.1A highlights the marginal overlap of ROI₂ with material outside of the phase, due to the small feature size being analysed, which probably explains the presence of the iodine absorption step. Analysis of ROI₃, within the dense bone region, shows a minor increase due to the presence of iodine, which has been observed in similar staining studies based on DECT data (SH, personal observation).

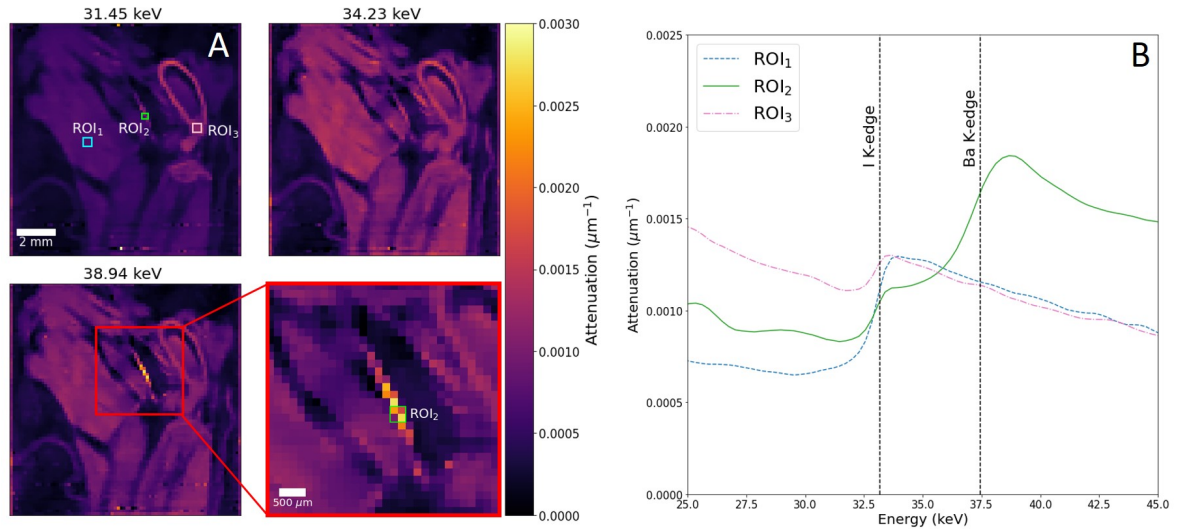


Figure 5.3.1. **Voxel spectra analysis for double-stained hindlimb specimen.** A) Single image slice in the sagittal plane across three monochromatic energy channels, following iterative reconstruction. A set of three regions-of-interest (ROIs) are highlighted for voxel spectra analysis. An enlarged image of a section of (A) - red box - is included to highlight ROI₂ taken over one of the distinct material phases. ROIs_{1,3} cover a 3×3 voxel region, while a 2×2 pixel region is used for ROI₂, partially overlapping with surrounding material outside of the phase. B) Voxel spectra for each ROI, showing clear steps in attenuation. Known absorption edge positions (black dotted lines) confirm the presence of iodine and barium in the ROIs, while ROI₃ shows a small iodine signal, having partially diffused into the calcium-containing bone.

In order to precisely map the distribution of chemical stain over soft tissue structures, the method of K-edge subtraction (KES) is applied. For each absorption edge, narrow channel ranges either side of the edge position were integrated and subtracted from one another. As a result, only information corresponding to the chosen element remains, enabling a form of elemental segmentation to be performed. Applying the KES method for iodine and barium produces the results shown in Fig. 5.3.2A, where we achieve clear segmentation of the iodine- and barium-stained structures. Included in Fig. 5.3.2B are a set of 3D volume renders for the segmented regions, where we also map the remaining material phase, following subtraction of iodine and barium (also see Supplementary Video 1). As expected, the structure of this phase over 3D is confirmed as calcium-containing bone. In order to reinforce the identification of each phase, an equivalent image slice acquired through conventional XCT for high spatial resolution comparison is shown in Fig. 5.3.2C. The scan was reconstructed with a voxel size of approximately 14 μm , providing clear structural insight which may be missing in the hyperspectral images. Exact image slices were identified and matched using volume registration. As seen in Fig. 5.3.2C, labelled regions for each stained structure matches those segmented using the KES method in the hyperspec-

tral dataset. Based on the XCT image shown, we can identify the soft tissue regions stained by iodine, with the barium contrast agent only filling the lumen of blood vessels in the mouse hindlimb. Though a small amount of iodine binds to the bone tissue as previously discussed, such differences are negligible relative to the soft tissue, and do not emerge in the elemental difference maps created.

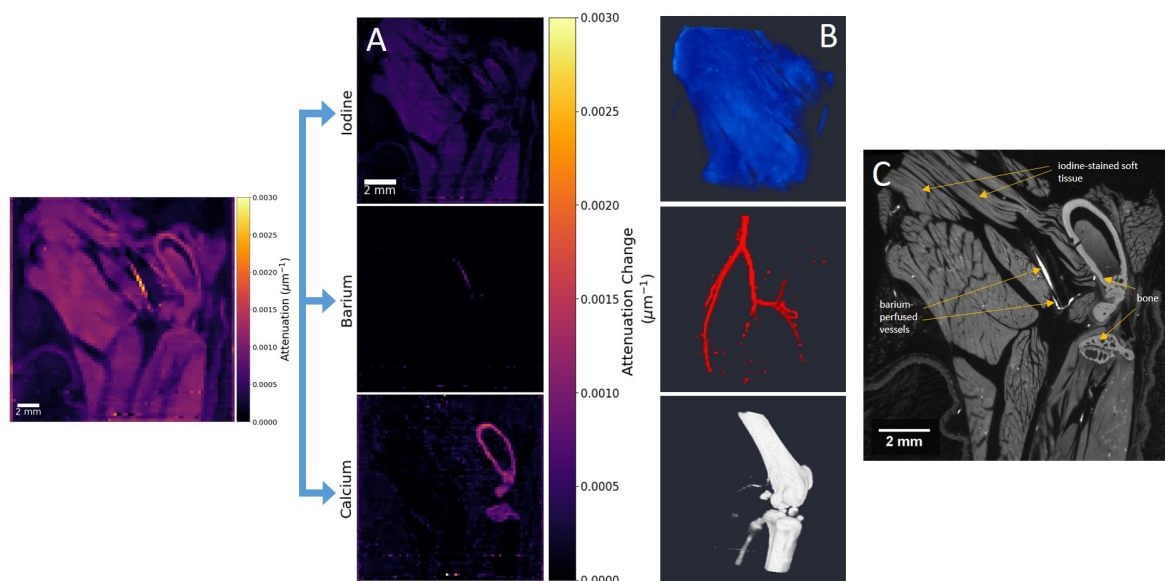


Figure 5.3.2. **Elemental segmentation of hindlimb by K-edge subtraction.** A) Elemental difference maps shown for the hyperspectral image slice shown in the sagittal plane (left). Colour bar for elemental difference maps is measured in terms of attenuation change, $\Delta\mu$, as determined by KES of narrow energy windows (5 channels, ~ 1.1 keV width total) either side of each absorption edge. B) 3D volume mapping for elemental maps of iodine-, barium- and calcium-containing regions (top, middle, bottom respectively). C) Virtual cross-section from a high spatial resolution XCT scan of the mouse hindlimb, showing the equivalent image slice following volume registration. Labels indicate the three material phases with expected stain uptake regions.

Our second sample, a triple-stained mouse forelimb, provides an opportunity to observe the effect of overlapping contrast agents. Here, we now have additional soft tissue staining provided through the tungsten-based phosphotungstic acid (PTA). While the use of PTA has been shown to provide strong contrast enhancement to regions such as connective tissue, it also enhances tissues overlapping with iodine-based agents, including muscles, while dual-staining in the skin is possible, though sometimes the skin is removed due to acting as a barrier for stain penetration [38]. Therefore the sample provides an opportunity to investigate stain interaction, and identify any double-stained regions or potential displacement of one chemical by another.

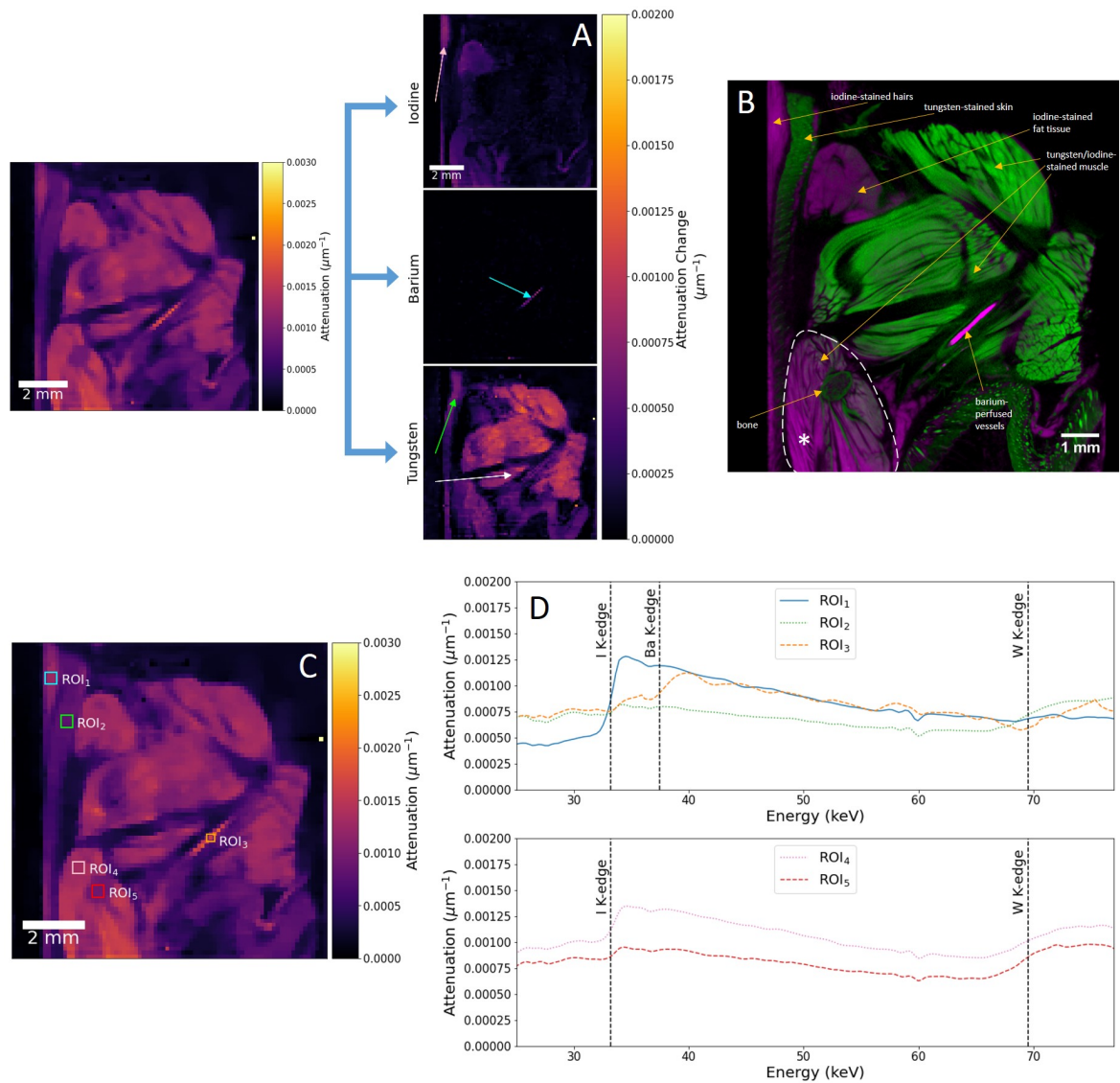


Figure 5.3.3. Spectral analysis for a triple-stained forelimb specimen. A) Elemental difference maps shown for the hyperspectral image slice shown in the coronal plane (left). Colour bar for elemental difference maps is measured in terms of attenuation change, $\Delta\mu$. Arrows are included to highlight distinct soft tissue regions stained by each chemical, confirmed as hair (pink), vasculature (blue), skin (green) and muscle (white). B) Reconstructed cross-section from a high spatial resolution DECT scan of the mouse forelimb, following basis material decomposition. The image slice matches that shown in the hyperspectral dataset, following volume registration. Labels indicate regions containing tungsten and calcium (green), as well as those containing iodine and barium (magenta). DECT decomposition fails to fully segment all elements into distinct phases. The dashed region and asterisk highlight the area below the elbow joint where PTA did not fully stain. C) Reconstructed cross-section slice in the coronal plane of the triple-stained mouse forelimb. ROIs are shown for five distinct regions of the specimen, to analyse average voxel spectra. All ROIs cover 3×3 pixels, apart from ROI₃, which covers a 2×2 region. D) Voxel spectra for the ROIs selected in (C). Known K-edge positions are overlaid, with ROIs 1, 2 and 3 matching the K-edges for iodine, barium and tungsten respectively (top). Two ROIs, 4 and 5, show the presence of both iodine and tungsten contrast agents (bottom).

Using the same reconstruction and analysis routine as for the double-stained specimen, we acquire a full spectral segmentation of the three contrast agents in the triple-stained mouse forelimb, as shown in Fig. 5.3.3A. It becomes immediately clear that PTA constitutes the dominant stain in the majority of the soft tissue, with significantly reduced iodine uptake compared to the double-stained hindlimb sample. Clear elemental segmentation is achieved despite the addition of a third elemental stain, owing to the unambiguous identification of each absorption edge with hyperspectral imaging, followed by KES for each spectral

marker (also see Supplementary Video 2). By analysing an equivalent DECT reconstructed dataset of the same sample, we can perform a direct comparison of imaging modalities, while using the high spatial resolution nature of the DECT method to identify and match soft tissue regions. As with the XCT comparison for the double-stained specimen, we once more perform volume registration to directly match the volume orientation. The DECT image slice shown in Fig. 5.3.3B, with a reconstructed voxel size of approximately $8\text{ }\mu\text{m}$, was segmented following basis material decomposition, a method of separating the individual contributions of each material to the overall attenuation of the X-ray beam [8], and has regularly been used as an effective method of chemical segmentation in DECT [9, 39]. The decomposition method for DECT is limited in its ability to fully segment each individual chemical phase. The higher attenuation tungsten-stained regions, along with the calcium-based bone can be segmented from the iodine- and barium-stained regions, but no further separation is possible. In part, this is due to the aforementioned similar spectral profiles of iodine and barium, with very similar attenuation and closely-spaced K-edges. Hyperspectral CT can overcome such issues due to the high energy resolution available, enabling segmentation through KES. We can therefore confirm the identification of iodine staining in the hair of the forelimb, as well as the fat tissue, between which a layer of skin is clearly stained only by the tungsten-based PTA. The intensity of the PTA staining shows clearly in the majority of the musculature, with very low levels of iodine present. This is reversed in the lower area below the elbow joint however, as highlighted by the dashed region in Fig. 5.3.3B, where iodine staining shows an equal, or greater intensity than the tungsten contrast agent. This is due to the staining time of the PTA, combined with its slow penetration speed, meaning the contrast agent only partially stained to this sample depth. This did however offer an excellent opportunity to evaluate the balance of stains in the same soft tissue structure. Finally, a small section of bone is noted by the DECT results, which appears as part of the tungsten segmentation in the hyperspectral KES analysis. As such, no calcium map is extracted following KES. The cause of this may be investigated through the analysis of several ROI voxel spectra, as shown in Fig. 5.3.3C and D. The results confirm the presence of iodine, barium and tungsten in the hairs, vessels and skin respectively, based on reference regions in the DECT dataset. The spectra of ROI₄, at the lower region of the forelimb, shows the overlap between I₂KI and PTA staining in the muscle tissue. A small step change at the K-edge of tungsten is also observed in ROI₅, taken over the feature identified as bone in the DECT cross-section. Therefore, partial binding of the PTA contrast agent to the bone tissue may have occurred, indicating why no calcium segmentation was possible. A slight rise in attenuation around the iodine K-edge was also present, though slightly offset from the known edge position. Combined with its small step size, the signal is likely due to noise, or possibly of sufficiently low concentration to not register as part of the iodine map in Fig. 5.3.3A.

Quantifying chemical stain distributions

While the use of KES confirms the presence of each stain, and allows us to build unambiguous individual elemental maps, this form of spectral analysis enables elemental seg-

mentation but provides no quantitative insight into the concentration distribution of the staining agents. The analysis may be taken a step further using 'step size' measurements, making use of the spectral markers available. By applying a fitting routine to the spectral profiles the height of the K-edge step may be extracted for every voxel. It has previously been shown that the height of the absorption edge step (referred to as $\Delta\mu_0$) is directly proportional to the concentration of the corresponding elemental species [16]. Therefore we can extract a map of $\Delta\mu_0$ values by performing this linear fitting routine across the entire reconstructed volume, as performed previously on a single-stained biological specimen [17]. However, on its own the use of this 'edge height' analysis can only provide relative concentration values, rather than absolute values. In order to extract a quantitative map of chemical staining, we require the use of calibration samples of known concentrations.

For this study, a set of three calibration phantoms were produced, containing various concentrations of the contrast agents used in our biological specimens: I_2KI , $BaSO_4$ and PTA. Figure 5.3.4A illustrates the layout of each phantom sample, and the chemical concentrations for each container. Also shown in Fig. 5.3.4A are reconstructed image slices for each phantom, acquired through conventional XCT. Signal intensity is measured in terms of 'standardised intensity', with higher values corresponding to a more strongly-attenuating (higher concentration) material. While typically CT number would be used to quantify signal intensity, we choose a different terminology to account for the fact that calibration was performed using a combination of agarose and air, as opposed to the standard water/air. The heterogeneous nature of the $BaSO_4$ phantoms are due to partial sinking and separation of the barium sulphate crystals from the agarose base during mixing and cooling.

Reconstructed image slices of the chemical phantoms are shown in Fig. 5.3.4A. Image slices are evaluated at two different energy channels, taken either side of the K-edge positions for the heavy elements found in each phantom (iodine - 33.17 keV, barium - 37.44 keV, tungsten - 69.53 keV). As expected, a rise in attenuation is observed across the appropriate energy threshold for the phases. The tungsten-based PTA phantom portrays some signal distortion due to minor ring artefacts. Spectral profiles are then extracted by selecting ROIs covering each distinct phase, and averaged to cancel out any differences due to chemical inhomogeneity. Figure 5.3.4B shows the ROI voxel spectra for each phase of the three phantoms. The profiles closely follow the expected trend of a sharp rise in attenuation at the K-edge position, with the overlaid edge energies demonstrating the precise matching with the measured experimental data. The step change at the K-edge varies in size for each phase, therefore a relationship between chemical concentration and absorption step size may be determined.

Using the aforementioned edge height analysis routine, the absorption edge size may be measured and plotted against the corresponding phase concentration. Further, by evaluating these values at a range of vertical heights through the sample depth, any changes due to inhomogeneity may be accounted for. For each phantom, a total of six slices through their vertical depth were measured and averaged. The fitted relationships are shown in Fig. 5.3.4C, with strong linear correlation found for each chemical phantom. Similar linear re-

relationships have previously been identified between concentration and CT number [9]. A linear fitting was also confirmed between concentration and standardised intensity for the XCT acquisition of the phantoms in this study, and is shown as a direct comparison in Fig. 5.3.4D.

With a linear relationship determined for each contrast agent, a direct conversion from relative to absolute concentration may be calculated for every voxel in the biological specimens. As a result, stain distribution as a function of position can be investigated. The results for both the double- and triple-stained mouse limbs are shown in Fig. 5.3.5A and C, which illustrate 3D maps measured in terms of concentration on a voxel-by-voxel basis. Analysing the results in 3D provides excellent insight into the level of staining at various depths of the tissue (see Supplementary Videos 3-7). In addition, Fig. 5.3.5B and D detail the statistics behind the concentration distribution, with histograms showing the concentration frequency across the entire volume. Analysis of the iodine staining in the double-stained specimen in shows nearly all voxels contain ≤ 300 mg/ml of iodine, with the highest concentrations observed on the exterior skin. For the vasculature, the largest vessels experience chemical uptake of up to 800 mg/ml of BaSO₄. For many smaller vessels, concentrations of below 200 mg/ml were typically observed. However, consideration must be taken for the partial volume effect. Given the relatively coarse spatial resolution (151 μ m) of the reconstructed volume, smaller vessels typically occupied a space below a single voxel. Therefore, the edge height analysis cannot precisely estimate the true concentration within such vessels. A number of voxels also portray a very low concentration of barium disconnected from the main vasculature structure. Some regions are attributed to noise and artefacts, though some cannot be ruled out as smaller regions of the vessel structure with sufficient barium signal to register on the chemical map. An improved spatial resolution would enable us to unambiguously identify and discriminate noisy regions from stained structures.

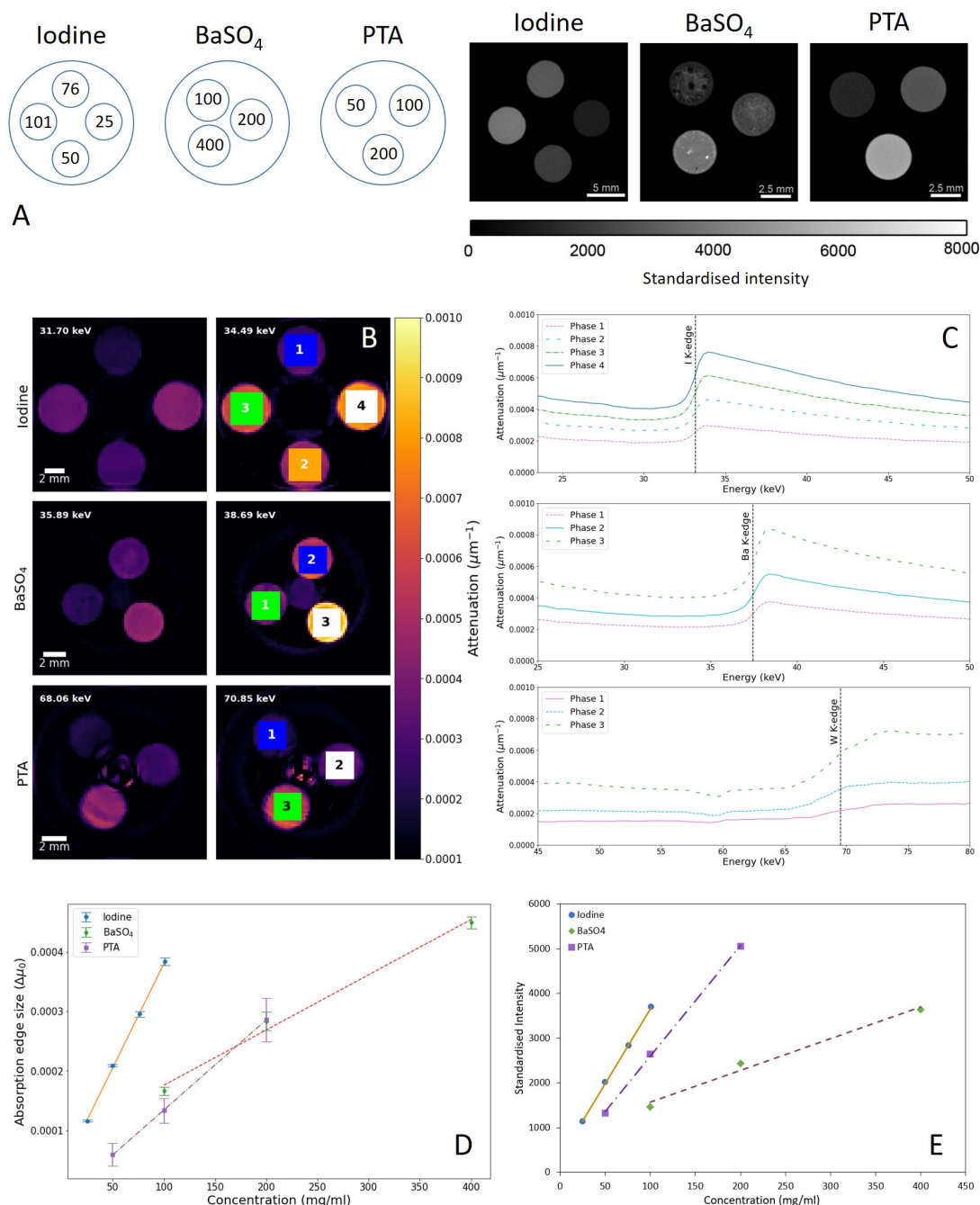


Figure 5.3.4. Design and spectral analysis of chemical phantoms. A) Illustration of the phantom layout for each contrast agent (left), with chemical concentrations labelled in units of mg/ml. The I₂KI phantom is labelled as iodine to highlight that the concentrations represent aqueous I₃⁻. Reconstructed image slices for each of the respective chemical phantoms (right), with concentrations matched to the concentrations labelled. The BaSO₄ phantoms appear heterogeneous due to partial sinking and separation of the barium sulphate crystals from the agarose base. Images are measured in terms of 'standardised intensity' value, with the same overall scaling range. B) Reconstructed slices of each chemical phantom, shown in the axial plane, for two energy channels, taken just before (left column) and just after (right column) the relevant K-edge position. ROIs covering each chemical phase are highlighted and numbered, from which spectral plots were extracted. Minor ring artefacts appear on the PTA reconstructed phantom. C) Voxel spectra showing attenuation as a function of energy for the ROIs highlighted in (B). The attenuation values were averaged over the full ROI. Known K-edge positions of the phantom's heavy element are overlaid. D) Fitted relationship for each chemical phantom, based on the average K-edge step change over six vertical slices through the sample depth. Error bars measure the standard deviation across the slices analysed. A line of best fit is applied for each phantom following linear interpolation. E) Fitted relationship between chemical concentration and 'standardised intensity' value in each phantom phase following conventional XCT imaging. Values were calculated for the central slice reconstruction. Phantom datasets were scanned at 80 kV and 100 μA with a Zeiss Xradia MicroXCT-400. Standardised intensity values are based on 2% agarose and air, as the barium phantom uses an agarose base.

The concentration information details for the triple-stained forelimb sample are shown in Fig. 5.3.5C and D. These results show the significantly lower concentration of iodine observed throughout the various soft tissue regions. With a maximum recorded concentration of approximately 250 mg/ml, the majority of iodine-stained tissue falls below 100 mg/ml. Using the images in Fig. 5.3.3 and 5.3.5, we observe that the iodine staining shows clearly in regions where there was no tungsten uptake, such as the external hairs, and layers of fat within the specimen. As expected, barium was only located within the blood vessels, with uptake averaging 100 mg/ml, but reaching as high as 800 mg/ml for very few voxels in the largest regions of the vessel. Less of the vasculature was observable for the triple-stained specimen, believed to be due to a larger number of vessels below the spatial resolution limit. The more highly-attenuating tungsten-based PTA contrast agent dominated the soft tissue staining, as seen in the elemental segmentation. Connective tissue and muscle regions are predominantly enhanced by tungsten staining, though some overlap is observed in the musculature with both iodine and tungsten. Particularly in the lower section of the forelimb, where the muscle tissue was only partially stained by PTA, we see a clear presence of both the iodine- and tungsten-based contrast agents.

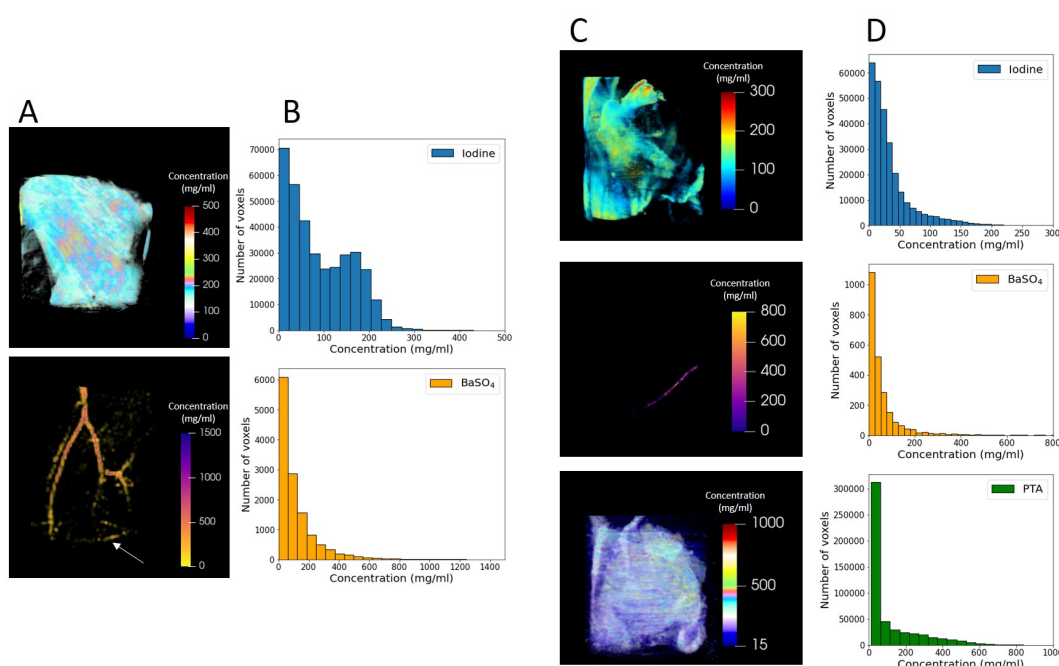


Figure 5.3.5. **Distribution and concentration of contrast agents.** A) 3D volume maps quantifying the stain distribution of iodine (top) and barium (bottom) in the soft tissue and blood vessels respectively within the double-stained mouse hindlimb. Some low concentrations regions (white arrow) with a systematic pattern of voxels are attributed to ring artefacts or general noise. B) Histogram detailing the statistical breakdown of concentration distribution on a voxel-by-voxel basis for each chemical stain of the sample in (A). C) Volume maps for the triple-stained mouse forelimb, showing absolute concentration values in each voxel for iodine (top), BaSO_4 (middle) and PTA (bottom). D) Concentration distribution histogram for each stain within the sample in (C).

The statistical analysis also provides a metric of the detectability of the hyperspectral system, with many voxels measured to contain iodine and barium concentrations of approximately 1% (w/v) for both mouse limb samples (see Supplementary Fig. S3 and S4 for extended histogram plots). However, caution must be taken in evaluating the low concentration sensitivity, as highlighted by the PTA statistics, where a heavier skew towards the

lower concentrations appears due to the presence of some ring artefacts remaining. The results of the calibration phantoms in Fig. 5.3.4 confirm that for an ideal, homogeneous sample, detection of K-edge markers is currently achievable down to concentrations of 2.5% (w/v), particularly when aided by iterative algorithms aimed at reducing noise fluctuations in the spectral domain.

5.4 Discussion

Using a set of chemical calibration phantoms, evaluation of double- and triple-stained biological specimens was achieved in this study by hyperspectral X-ray tomography. The work builds on previous studies involving hyperspectral imaging [16, 17], exploiting the variety of spectral analyses available to achieve elemental segmentation over a full 3D volume. Due to the high energy resolution of the HEXITEC detector, unambiguous chemical identification is achievable for a range of elements in the hard X-ray range simply by matching of the spectral fingerprints (absorption edges) to their unique positions. With the ability to identify multiple chemicals simultaneously, and determine the absolute concentration distribution as a function of position, the work offers great potential for investigations involving heavy metal uptake, even in cases where we have no *a priori* knowledge of initial chemical composition. In the research of ecology and agriculture, heavy metal uptake by soil and vegetation is of particular interest. Excessive uptake by soil and plants of heavy metals, including molybdenum (Mo), cadmium (Cd), and lead (Pb), can pose a serious threat to animals and humans, due to their toxic nature when consumed in high concentrations [40–42], on top of the damaging nature of such elements to vegetation yield and quality. Calculating similar calibration metrics for concentration of commonly-occurring elements in agriculture using hyperspectral tomography would enable future studies into uptake and distribution across soil, plant, animal and human samples to evaluate the level of contamination and poisoning risk. The feasibility of using hyperspectral imaging for such work requires further evaluation. X-ray CT as an imaging technique has an inherently low sensitivity, compared to alternative light-optical methods [43]. Therefore, given that biological systems typically exhibit heavy metal levels of parts-per-million [41], hardware improvements in spectroscopic systems require continued advancement to become a viable option. Nevertheless, this research offers a reference point for a workflow in potential future studies. In addition, the present study analysing iodine and PTA staining provides a means of better understanding tissue morphology following heavy element accumulation. This work enables improved interpretation of the tissue layers in which these elements accumulate, providing a useful tool for future toxicological research.

This work is the first of its kind to establish a relationship between K-edge height and chemical concentration, and in theory is capable of defining a baseline calibration for each element, translatable across research studies. Given that each calibration phantom only includes a single high-attenuation element, and each energy channel is quasi-monochromatic, it is believed that the linear relationships between K-edge height and chemical concentra-

tion are independent of both sample and incident X-ray spectra. Attenuation response, regardless of concentration, is consistent over the same subset of energy channels, and therefore alterations to the spectra only correspond to a change in photon statistics. Therefore, any changes are proportional, and the same linear relationship will emerge. Future work may validate this approach through imaging of the same calibration phantom under different beam voltages. Potential sources of error may include differences in spectral responses for other hyperspectral detectors, as well as the choice of reconstruction algorithm, given that these can directly impact voxel attenuation spectra due to noise or excessive smoothing of the K-edge. A wider discussion on factors affecting the accuracy of the method is included in the Supplementary Information.

A feature of spectral analysis covered in this work that could warrant further investigation is the concept of 'spectral unmixing' for multi-element voxels. That is, in instances where a single voxel registers multiple absorption edge markers, signifying the presence of more than one chemical element. For hyperspectral imaging, this is more likely given the large pixel size and coarse spatial resolution of the HEXITEC system. As such, precise quantification of the concentration distribution for these 'mixed' voxels may be affected, particularly in cases where the absorption edges are closely-spaced. While many voxels will likely contain a single element, this study has already identified some cases of such mixing, such as the overlap of PTA and iodine in the muscle tissue (see Fig. 5.3.3). A range of unmixing methods have previously been explored in other fields of spectral imaging [44], in order to better classify material composition and improve spatial resolution. The methods typically focus around linear unmixing routines, applied to fields such as energy-dispersive X-ray diffraction [45] and fluorescence microscopy [46], while more recently machine learning approaches have been studied for 'blind' spectral unmixing [47]. Such algorithms could easily be adapted to improve quantitative measurements in hyperspectral X-ray CT.

This research also highlights some of the existing limitations of hyperspectral imaging and the HEXITEC detector, the main aspect being the spatial resolution limits. With a pixel size of $250\text{ }\mu\text{m}$ and a $2\text{ cm} \times 2\text{ cm}$ detection area, magnification of samples is limited, with typical spatial resolutions $\sim 100\text{ }\mu\text{m}$. As such, the current detector technology may require a complementary high-resolution technique, followed by volume registration, to achieve optimum spatial feature definition and composition mapping in the low-micron range. Similarly, sample size is currently limited by the available field of view. It is anticipated that this limitation will be overcome as more sensitive and more pixellated detectors emerge. At present, the modality is restricted to smaller specimens, or magnified ROI studies.

The sensitivity of the detector is also an area for further investigation. Here, concentration levels on the order of 10^1 - 10^3 mg/ml or more were studied. For studies involving trace elements, detectability levels of 10 - $100\times$ greater may be required. Further quantitative studies could be conducted on the HEXITEC sensitivity limit using a set of heavy metal phantoms, decreasing in concentration until spectral markers may no longer be observed. It seems likely that future developments in hyperspectral detectors will improve the sensitivity further. Alongside this, additional developments in denoising algorithms could extend the

detection limit of trace elements yet beyond those currently achievable. It should also be noted that hyperspectral imaging offers the potential for trace analysis through other complementary imaging modalities. For example, the use of energy-dispersive X-ray fluorescence has been shown to offer successful elemental identification on the trace level, both for heavy metal elements, as well as those at the low-energy sensitivity limit of such detectors [48–50]. The effect of self-absorption often confines the XRF modality to studying small samples [51], however this limit was already apparent given the HEXITEC pixel size and field of view (FOV), and thus the multi-modal approach is achievable for small samples with large features. Alternatively, a two-step approach may be adopted, whereby hyperspectral CT offers non-destructive identification of ROIs, followed by cutting and extraction of the ROI, which may then be investigated under high-resolution, high spectral sensitivity XRF to overcome self-absorption concerns.

5.5 Conclusion

To conclude, we have evaluated the potential of hyperspectral X-ray tomography for the direct segmentation, measurement and mapping of absolute stain concentration. This research demonstrates the first instance of directly extracting elemental concentration from multi-stained biological specimens through evaluation of absorption edge height for several elemental markers. With an excellent energy resolution (~ 1 keV), hyperspectral CT overcomes the issues of spectrally similar attenuation profiles observed in DECT, shown here in the unambiguous discrimination between iodine- and barium-staining. Through a set of hindlimb and forelimb murine samples, the work has enabled a thorough examination of the interaction between multiple simultaneous chemical stains for double- and triple-staining procedures, providing insight into the level of stain overlap in the same soft tissue regions, and how this affects the overall concentration distribution. Evaluating the results against equivalent high-resolution XCT and DECT datasets, the advantages in the spectral domain become clear, yet the issues in the spatial domain are also highlighted, particularly with regards to the need for improved spatial resolution. However, through either the improvement in spectral detector technology, or the use of multi-modal acquisition for combined high spatio-spectral resolution, the methodology opens up the possibility of chemical investigations in a range of fields. Given sufficient sensitivity, exploring heavy metal uptake in ecological or environmental research, as well as contrast agent applications for medical biopsies, would be greatly enhanced by the ability to confirm the elements present, and even more so by quantifying the concentrations and how they are distributed. As such, the studies conducted in this work show a further step in the vast potential for hyperspectral imaging moving forward.

5.6 Acknowledgements

We thank Stefan Kummer for his support in building the calibration phantoms. This research was supported using resources of the VetCore Facility (VetImaging) of the University of Veterinary Medicine Vienna. PJW and RW acknowledge support from the European Research Council Grant No. 695638 CORREL-CT. We also acknowledge the following EPSRC grants for funding that have enabled this project: “A Reconstruction Toolkit for Multichannel CT” (EP/P02226X/1) and “CCPi: Collaborative Computational Project in Tomographic Imaging” (EP/M022498/1 and EP/T026677/1). The Manchester (Henry Moseley) X-ray Imaging Facility was funded in part by the EPSRC (Grants EP/ F007906/1, EP/F001452/1 and EP/M010619/1) and is part of the National Research Facility for lab X-ray CT (NXCT) funded by EPSRC (EP/T02593X/1). This work makes use of computational support by CoSeC, the Computational Science Centre for Research Communities, through CCPi.

5.7 References

- ¹S. D. Rawson, J. Maksimcuka, P. J. Withers, and S. H. Cartmell, “X-ray computed tomography in life sciences”, *BMC Biology* **18**, 1–15 (2020).
- ²P. M. Gignac, N. J. Kley, J. A. Clarke, M. W. Colbert, A. C. Morhardt, D. Cerio, I. N. Cost, P. G. Cox, J. D. Daza, C. M. Early, M. S. Echols, R. M. Henkelman, A. N. Herdina, C. M. Holliday, Z. Li, K. Mahlow, S. Merchant, J. Müller, C. P. Orsbon, D. J. Paluh, M. L. Thies, H. P. Tsai, and L. M. Witmer, “Diffusible iodine-based contrast-enhanced computed tomography (diceCT): An emerging tool for rapid, high-resolution, 3-D imaging of metazoan soft tissues”, *Journal of Anatomy* **228**, 889–909 (2016).
- ³M. M. Koç, N. Aslan, A. P. Kao, and A. H. Barber, “Evaluation of X-ray tomography contrast agents: A review of production, protocols, and biological applications”, *Microscopy Research and Technique* **82**, 812–848 (2019).
- ⁴B. D. Metscher, “Micro CT for comparative morphology: Simple staining methods allow high-contrast 3D imaging of diverse non-mineralized animal tissues”, *BMC Physiology* **9**, 10.1186/1472-6793-9-11 (2009).
- ⁵B. D. Metscher, “MicroCT for developmental biology: A versatile tool for high-contrast 3D imaging at histological resolutions”, *Developmental Dynamics* **238**, 632–640 (2009).
- ⁶S. Faulwetter, T. Dailianis, A. Vasileiadou, and C. Arvanitidis, “Contrast enhancing techniques for the application of micro-CT in marine biodiversity studies”, *Microscopy and analysis* **2**, S4–S7 (2013).

- ⁷E. Descamps, A. Sochacka, B. de Kegel, D. V. Loo, L. Hoorebeke, and D. Adriaens, “Soft tissue discrimination with contrast agents using micro-ct scanning”, *Belgian Journal of Zoology* **144**, 20–40 (2014).
- ⁸T. R. Johnson, “Dual-energy CT: general principles”, *American journal of roentgenology* **199**, 3–8 (2012).
- ⁹S. Handschuh, C. J. Beisser, B. Ruthensteiner, and B. D. Metscher, “Microscopic dual-energy CT (microDECT): a flexible tool for multichannel ex vivo 3D imaging of biological specimens”, *Journal of Microscopy* **267**, 3–26 (2017).
- ¹⁰D. P. Clark, K. Ghaghada, E. J. Moding, D. G. Kirsch, and C. T. Badea, “In vivo characterization of tumor vasculature using iodine and gold nanoparticles and dual energy micro-CT”, *Physics in Medicine and Biology* **58**, 1683–1704 (2013).
- ¹¹S. H. Barazani, W.-W. Chi, R. Pyzik, H. Chang, A. Jacobi, T. O’Donnell, Z. A. Fayad, Y. Ali, and V. Mani, “Quantification of uric acid in vasculature of patients with gout using dual-energy computed tomography”, *World Journal of Radiology* **12**, 184–194 (2020).
- ¹²T. Soeda, S. Uemura, Y. Morikawa, K. I. Ishigami, S. Okayama, S. J. Hee, T. Nishida, K. Onoue, S. Somekawa, Y. Takeda, H. Kawata, M. Horii, and Y. Saito, “Diagnostic accuracy of dual-source computed tomography in the characterization of coronary atherosclerotic plaques: Comparison with intravascular optical coherence tomography”, *International Journal of Cardiology* **148**, 313–318 (2011).
- ¹³S. Achenbach, F. Moselewski, D. Ropers, M. Ferencik, U. Hoffmann, B. MacNeill, K. Pohle, U. Baum, K. Anders, I. K. Jang, W. G. Daniel, and T. J. Brady, “Detection of Calcified and Noncalcified Coronary Atherosclerotic Plaque by Contrast-Enhanced, Submillimeter Multidetector Spiral Computed Tomography: A Segment-Based Comparison with Intravascular Ultrasound”, *Circulation* **109**, 14–17 (2004).
- ¹⁴J. C. Schenzle, W. H. Sommer, K. Neumaier, G. Michalski, U. Lechel, K. Nikolaou, C. R. Becker, M. F. Reiser, and T. R. Johnson, “Dual energy CT of the chest: How about the dose?”, *Investigative Radiology* **45**, 347–353 (2010).
- ¹⁵J. H. Hubbell and S. M. Seltzer, *Tables of x-ray mass attenuation coefficients and mass energy-absorption coefficient*, 2004.
- ¹⁶C. K. Egan, S. D. M. Jacques, M. D. Wilson, M. C. Veale, P. Seller, A. M. Beale, R. A. D. Patrick, P. J. Withers, and R. J. Cernik, “3D chemical imaging in the laboratory by hyperspectral X-ray computed tomography”, *Scientific Reports* **5**, 1–9 (2015).
- ¹⁷R. Warr, E. Ametova, R. J. Cernik, G. Fardell, S. Handschuh, J. S. Jørgensen, E. Papoutsellis, E. Pasca, and P. J. Withers, “Enhanced hyperspectral tomography for bioimaging by spatio-spectral reconstruction”, *Scientific Reports* **11**, 1–13 (2021).

- ¹⁸S. Jayarathna, M. F. Ahmed, L. O’Ryan, H. Moktan, Y. Cui, and S. H. Cho, “Characterization of a pixelated cadmium telluride detector system using a polychromatic X-ray source and gold nanoparticle-loaded phantoms for benchtop X-ray fluorescence imaging”, *IEEE Access* **9**, 49912–49919 (2021).
- ¹⁹E. Liotti, A. Lui, T. Connolley, I. P. Dolbnya, K. J. Sawhney, A. Malandain, M. D. Wilson, M. C. Veale, P. Seller, and P. S. Grant, “Mapping of multi-elements during melting and solidification using synchrotron X-rays and pixel-based spectroscopy”, *Scientific Reports* **5**, 3–8 (2015).
- ²⁰E. Dahal, B. Ghammraoui, M. Ye, J. C. Smith, and A. Badano, “Label-free X-ray estimation of brain amyloid burden”, *Scientific Reports* **10**, 1–6 (2020).
- ²¹M. Mähler, M. Berard, R. Feinstein, A. Gallagher, B. Illgen-Wilcke, K. Pritchett-Corning, and M. Raspa, “FELASA recommendations for the health monitoring of mouse, rat, hamster, guinea pig and rabbit colonies in breeding and experimental units”, *Laboratory Animals* **48**, 178–192 (2014).
- ²²B. Close, K. Banister, V. Baumans, E. M. Bernoth, N. Bromage, J. Bunyan, W. Erhardt, P. Flecknell, N. Gregory, H. Hackbarth, D. Morton, and C. Warwick, “Recommendations for euthanasia of experimental animals: Part 2”, *Laboratory Animals* **31**, 1–32 (1997).
- ²³S. L. Leary, *AVMA guidelines for the euthanasia of animals* (American Veterinary Medical Association, Schaumburg, IL, 2020), pp. 127–143.
- ²⁴P. Seller, S. Bell, R. J. Cernik, C. Christodoulou, C. K. Egan, J. A. Gaskin, S. Jacques, S. Pani, B. D. Ramsey, C. Reid, P. J. Sellin, J. W. Scuffham, R. D. Speller, M. D. Wilson, and M. C. Veale, “Pixelated Cd(Zn)Te high-energy X-ray instrument”, *Journal of Instrumentation* **6**, 1–11 (2011).
- ²⁵M. C. Veale, P. Seller, M. Wilson, and E. Liotti, “HEXITEC: A High-Energy X-ray Spectroscopic Imaging Detector for Synchrotron Applications”, *Synchrotron Radiation News* **31**, 28–32 (2018).
- ²⁶S. M. Alkhateeb, M. H. Abdelkader, D. A. Bradley, P. Seller, M. C. Veale, M. D. Wilson, and S. Pani, “Energy dispersive X-ray diffraction computed tomography of breast-simulating phantoms and a tissue sample”, *Medical Imaging 2013: Physics of Medical Imaging* **8668**, 1–11 (2013).
- ²⁷C. K. Egan, J. W. Scuffham, M. C. Veale, M. D. Wilson, P. Seller, and R. J. Cernik, “Energy calibration and gain correction of pixelated spectroscopic x-ray detectors using correlation optimised warping”, *Measurement Science and Technology* **28**, 10.1088/1361-6501/28/1/017001 (2017).

- ²⁸B. Münch, P. Trtik, F. Marone, and M. Stampanoni, “Stripe and ring artifact removal with combined wavelet-Fourier filtering”, *Optical Society of America* **17**, 8567–8591 (2009).
- ²⁹A. Chambolle and T. Pock, “A first-order primal-dual algorithm for convex problems with applications to imaging”, *Journal of Mathematical Imaging and Vision* **40**, 120–145 (2011).
- ³⁰E. Ametova, G. Burca, S. Chilingaryan, G. Fardell, J. S. Jørgensen, E. Papoutsellis, E. Pasca, R. Warr, M. Turner, W. R. Lionheart, and P. J. Withers, “Crystalline phase discriminating neutron tomography using advanced reconstruction methods”, *Journal of Physics D: Applied Physics* **54**, 10.1088/1361-6463/ac02f9 (2021).
- ³¹L. I. Rudin, S. Osher, and E. Fatemi, “Nonlinear total variation based noise removal algorithms”, *Physica D* **60**, 259–268 (1992).
- ³²K. Bredies, K. Kunisch, and T. Pock, “Total generalized variation”, *SIAM Journal on Imaging Sciences* **3**, 492–526 (2010).
- ³³J. S. Jørgensen, E. Ametova, G. Burca, G. Fardell, E. Papoutsellis, E. Pasca, K. Thielemans, M. Turner, R. Warr, W. R. Lionheart, and P. J. Withers, “Core Imaging Library - Part I: A versatile Python framework for tomographic imaging”, *Philosophical Transactions of the Royal Society A: Mathematical, Physical and Engineering Sciences* **379**, 10.1098/rsta.2020.0192 (2021).
- ³⁴E. Papoutsellis, E. Ametova, C. Delplancke, G. Fardell, J. S. Jørgensen, E. Pasca, M. Turner, R. Warr, W. R. Lionheart, and P. J. Withers, “Core Imaging Library - Part II: Multichannel reconstruction for dynamic and spectral tomography”, *Philosophical Transactions of the Royal Society A: Mathematical, Physical and Engineering Sciences* **379**, 10.1098/rsta.2020.0193 (2021).
- ³⁵P. Blery, P. Pilet, A. Vanden-Bossche, A. Thery, J. Guicheux, Y. Amouriq, F. Espitalier, N. Mathieu, and P. Weiss, “Vascular imaging with contrast agent in hard and soft tissues using microcomputed-tomography”, *Journal of Microscopy* **262**, 40–49 (2016).
- ³⁶P. Heimel, N. V. Swiadek, P. Slezak, M. Kerbl, C. Schneider, S. Nürnberger, H. Redl, A. H. Teuschl, and D. Hercher, “Iodine-Enhanced Micro-CT Imaging of Soft Tissue on the Example of Peripheral Nerve Regeneration”, *Contrast Media and Molecular Imaging* **2019**, 10.1155/2019/7483745 (2019).
- ³⁷G. Hong, J. C. Lee, A. Jha, S. Diao, K. H. Nakayama, L. Hou, T. C. Doyle, J. T. Robinson, A. L. Antaris, H. Dai, J. P. Cooke, and N. F. Huang, “Near-infrared II fluorescence for imaging hindlimb vessel regeneration with dynamic tissue perfusion measurement”, *Circulation: Cardiovascular Imaging* **7**, 517–525 (2014).

- ³⁸E. Pauwels, D. Van Loo, P. Cornillie, L. Brabant, and L. Van Hoorebeke, “An exploratory study of contrast agents for soft tissue visualization by means of high resolution X-ray computed tomography imaging”, *Journal of Microscopy* **250**, 21–31 (2013).
- ³⁹C. T. Badea, X. Guo, D. Clark, S. M. Johnston, C. D. Marshall, and C. A. Piantadosi, “Dual-energy micro-CT of the rodent lung”, *American Journal of Physiology - Lung Cellular and Molecular Physiology* **302**, 1088–1097 (2012).
- ⁴⁰F. li Li, W. Shi, Z. fang Jin, H. mei Wu, and G. D. Sheng, “Excessive uptake of heavy metals by greenhouse vegetables”, *Journal of Geochemical Exploration* **173**, 76–84 (2017).
- ⁴¹L. Reis, P. Pardo, A. Camargos, and E. Oba, “Mineral element and heavy metal poisoning in animals.”, *Journal of medicine and medical sciences* **1**, 560–579 (2010).
- ⁴²A. Emamverdian, Y. Ding, F. Mokhberdoran, and Y. Xie, “Heavy Metal Stress and Some Mechanisms of Plant Defense Response”, *The Scientific World Journal* **2015**, 1–18 (2015).
- ⁴³A. Walter, P. Paul-Gilloteaux, B. Plochberger, L. Sefc, P. Verkade, J. G. Mannheim, P. Slezak, A. Unterhuber, M. Marchetti-Deschmann, M. Ogris, K. Bühler, D. Fixler, S. H. Geyer, W. J. Weninger, M. Glösmann, S. Handschuh, and T. Wanek, “Correlated Multimodal Imaging in Life Sciences: Expanding the Biomedical Horizon”, *Frontiers in Physics* **8**, 10.3389/fphy.2020.00047 (2020).
- ⁴⁴J. Wei and X. Wang, “An Overview on Linear Unmixing of Hyperspectral Data”, *Mathematical Problems in Engineering* **2020**, 10.1155/2020/3735403 (2020).
- ⁴⁵T. YangDai and L. Zhang, “Spectral unmixing method for multi-pixel energy dispersive x-ray diffraction systems”, *Applied Optics* **56**, 907 (2017).
- ⁴⁶M. E. Dickinson, E. Simbuerger, B. Zimmermann, C. W. Waters, and S. E. Fraser, “Multiphoton excitation spectra in biological samples”, *Journal of Biomedical Optics* **8**, 329 (2003).
- ⁴⁷T. D. McRae, D. Oleksyn, J. Miller, and Y. R. Gao, “Robust blind spectral unmixing for fluorescence microscopy using unsupervised learning”, *PLoS ONE* **14**, 10.1371/journal.pone.0225410 (2019).
- ⁴⁸E. Marguá, M. Hidalgo, and I. Queralt, “XRF spectrometry for trace element analysis of vegetation samples”, *Spectroscopy Europe* **19**, 13–17 (2007).
- ⁴⁹K. Geraki, M. J. Farquharson, D. A. Bradley, and R. P. Hugtenburg, “A synchrotron XRF study on trace elements and potassium in breast tissue”, *Nuclear Instruments and Methods in Physics Research, Section B: Beam Interactions with Materials and Atoms* **213**, 564–568 (2004).

- ⁵⁰J. C. Larsson, C. Vogt, W. Vågberg, M. S. Toprak, J. Dzieran, M. Arsenian-Henriksson, and H. M. Hertz, “High-spatial-resolution x-ray fluorescence tomography with spectrally matched nanoparticles”, *Physics in Medicine and Biology* **63**, 1–11 (2018).
- ⁵¹M. D. De Jonge and S. Vogt, “Hard X-ray fluorescence tomography-an emerging tool for structural visualization”, *Current Opinion in Structural Biology* **20**, 606–614 (2010).
- ⁵²S. Seven, I. H. Karahan, and Ö. F. Bakkaloglu, “The measurement of total mass attenuation coefficients of cocuni alloys”, *Journal of Quantitative Spectroscopy and Radiative Transfer* **83**, 237–242 (2004).
- ⁵³J. H. Paterson and O. L. Krivanek, *Elnes of 3d transition-metal oxides h. variations with oxidation state and crystal sffucture* (1990), pp. 319–325.
- ⁵⁴H. Visser, E. Anxolabéhère-Mallart, U. Bergmann, P. Glatzel, J. H. Robblee, S. P. Cramer, J. J. Girerd, K. Sauer, M. P. Klein, and V. K. Yachandra, “Mn k-edge xanes and k β xes studies of two mn - oxo binuclear complexes: investigation of three different oxidation states relevant to the oxygen-evolving complex of photosystem ii”, *Journal of the American Chemical Society* **123**, 7031–7039 (2001).
- ⁵⁵J. Hubbell, “Photon cross section compilation activity in the u. s. in the range 1 kev to 100 gev”, *Journal de Physique Colloques* **32**, 10.1051/jphyscol:1971403i (1971).

5.8 Supplementary Information

5.8.1 Hyperspectral energy-channel calibration and resolution calculation

By convention, hyperspectral detectors store incident photons into hundreds of narrow energy ‘bins’ or ‘channels’. Through a calibration using spectral markers of known energy, it was possible to calibrate the system, and establish a relationship between channel number, and photon energy. The calibration data consisted of a series of fluorescent X-ray peaks, emitted from metal foils (Ba and Tb) that were exposed to a radioactive ²⁴¹Am source. Figure S1 shows the calibration dataset for a single pixel, with 5 peaks highlighted, corresponding to the K $_{\alpha}$ and K $_{\beta}$ fluorescence peaks of Ba and Tb, as well as the ²⁴¹Am photopeak. The channel number at which each peak occurred was determined using a peak-finding algorithm. The energy values of the peaks are known and well-established, and therefore by plotting channel number against energy (in keV), a relationship may be determined. Also shown in Fig. S1 is the linear fitting of the relationship, based on the 5 data points collected. An R² value of 0.99 for the fit confirms a strong linear relationship, with a polynomial fitting giving the equation of the fit as:

$$\text{Energy(keV)} = 0.278 \times \text{ChannelNumber} + 1.23 \quad (5.1)$$

To determine the energy resolution of the system, the same calibration dataset was used. By measuring the FWHM of the ^{241}Am peak for every pixel, the resolution of the system was calculated. Figure S2 shows the frequency distribution of FWHM values measured over every pixel. Dead pixels identified during pre-processing were not included in the plot. Also shown is a pixel map over the full HEXITEC array, showing the distribution of FWHM values. Here, dead pixels were set to a value of 0. Based on the average value of functioning pixels, the resolution of the detector at 59.5 keV was measured to be 1.27 ± 0.47 keV.

5.8.2 Considerations on HEXITEC low concentration sensitivity

In order to better evaluate the voxel frequency of concentrations at the low value range, Fig. S3 and S4 show extended histogram statistic plots, with a greater number of bins to reduce the average bin size, therefore providing a clearer pattern of concentration distribution. For the double-stained specimen (Fig. S3), the iodine bin size was around 4.5, while it was 12.4 for the BaSO_4 histogram.

Two clear trends are observed, with both iodine and BaSO_4 distribution gradually descending in voxel number as concentration is increased. The iodine distribution also exhibits a small peak around 180 mg/ml, suggesting a particular region of soft tissue with a consistent concentration of contrast agent. The results indicate that, while noise fluctuations may cause some low value voxels, the trends do not indicate any outliers, and therefore we may assume that our detectability limit lies in this low concentration range, at approximately 5-10 mg/ml, equivalent to a concentration of 0.5-1% (w/v).

For the triple-stained specimen (Fig. S4), however, this may be brought into question. 150 bins were used for the iodine and BaSO_4 distributions, reflecting the reduced total range of concentrations compared to the hindlimb sample. This gives a bin size of approximately 3.2 and 8.5 for iodine and BaSO_4 respectively. The PTA plot uses 250 bins as it covers a

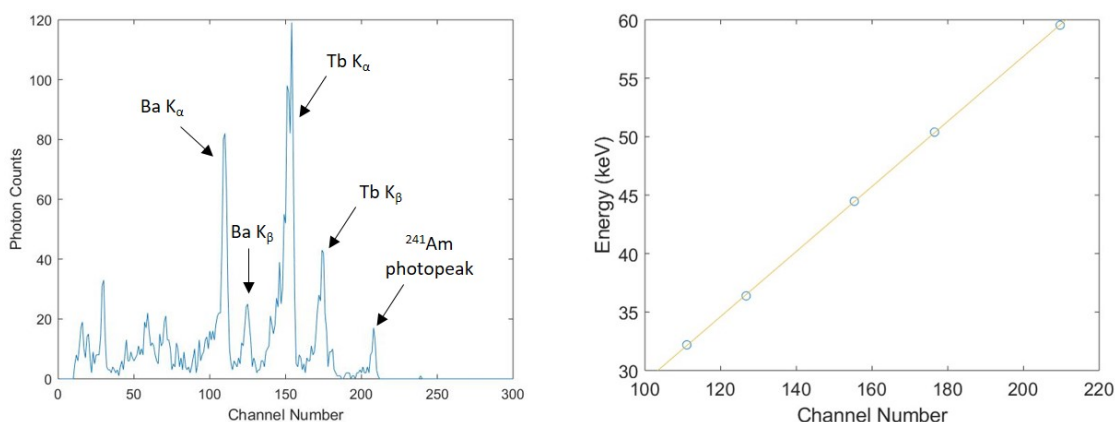


Figure S1. **Energy calibration using the ^{241}Am radioactive source.** (Left) Single pixel (40, 40) plot of the calibration spectra, measuring photon counts as a function of channel number. The highest energy peak at 59.5 keV ^{241}Am photopeak is labelled, as well as the XRF peaks produced from Ba and Tb metal foils upon exposure to the ^{241}Am source. (Right) Matching of the channel number for each XRF peak and the ^{241}Am photopeak to their known energy values, enabling a linear relationship between channel number and energy to be determined.

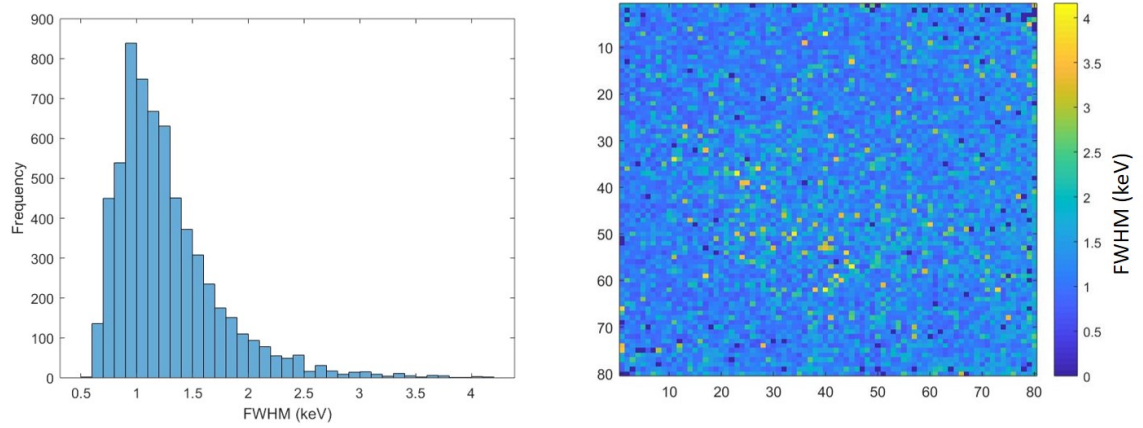


Figure S2. **Measurement of the resolution statistics using the ^{241}Am photopeak.** (Left) Histogram of the frequency distribution for FWHM values measured at 59.5 keV based on the ^{241}Am photopeak, over the full detector pixel array. Dead pixels were not included. (Right) Pixel map of the FWHM distribution. Dead pixels were set to a value of zero.

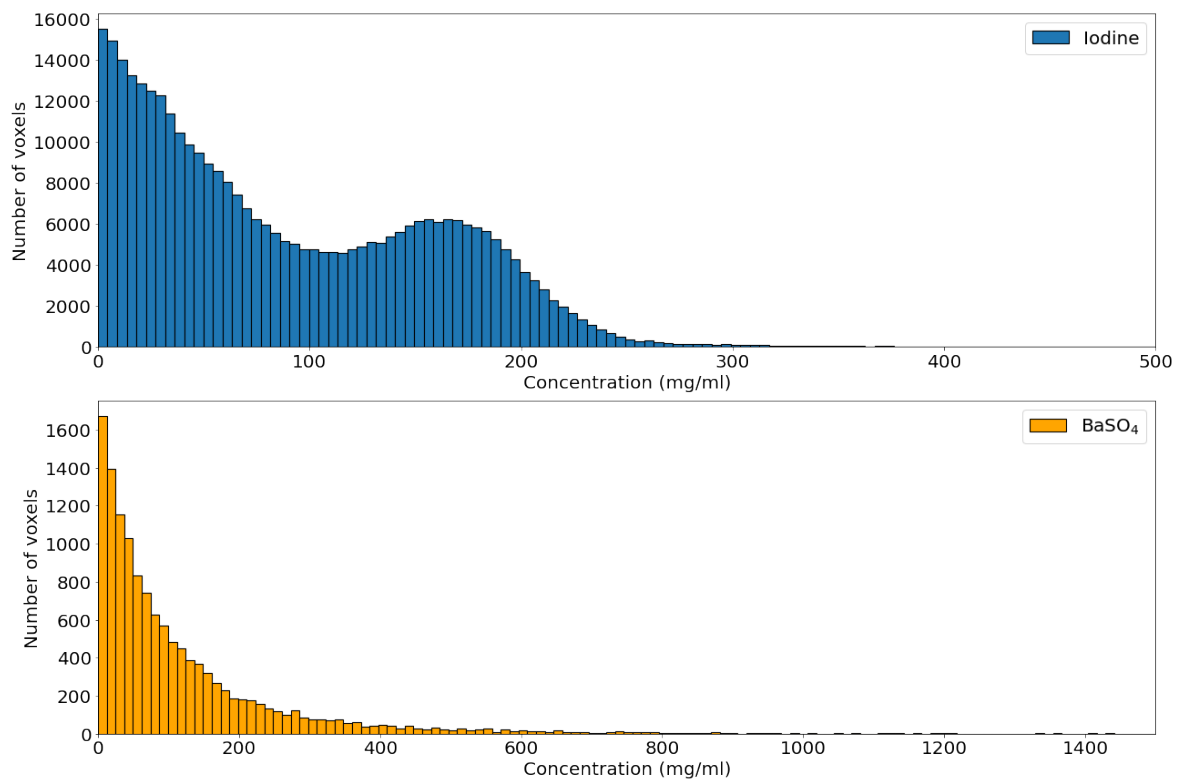


Figure S3. **Extended concentration statistics for double-stained mouse hindlimb specimen.** Histogram statistics are shown, detailing the concentration distribution of iodine (top) and BaSO_4 (bottom) over all voxels in the reconstructed volume. A total of 250 histogram bins are used over the full concentration range for both plots.

larger range, giving a bin size of roughly 10.2. While sensible trends are observed once more for iodine and BaSO_4 , a very sharp rise is observed for the lowest concentration bin for the PTA distribution, covering concentrations up to around 10 mg/ml (around 1% w/v). We attribute this to the presence of ring artefacts, distorting the voxel spectra and affecting the measured values of concentration. Therefore it is important we do not assume the detectability limit is as low as 1%, and caution must be taken when accounting for the effects of noise and artefacts. Given the results in the main manuscript for the calibration phantoms, concentrations of 2.5% and above appear much more reasonable as a lower limit esti-

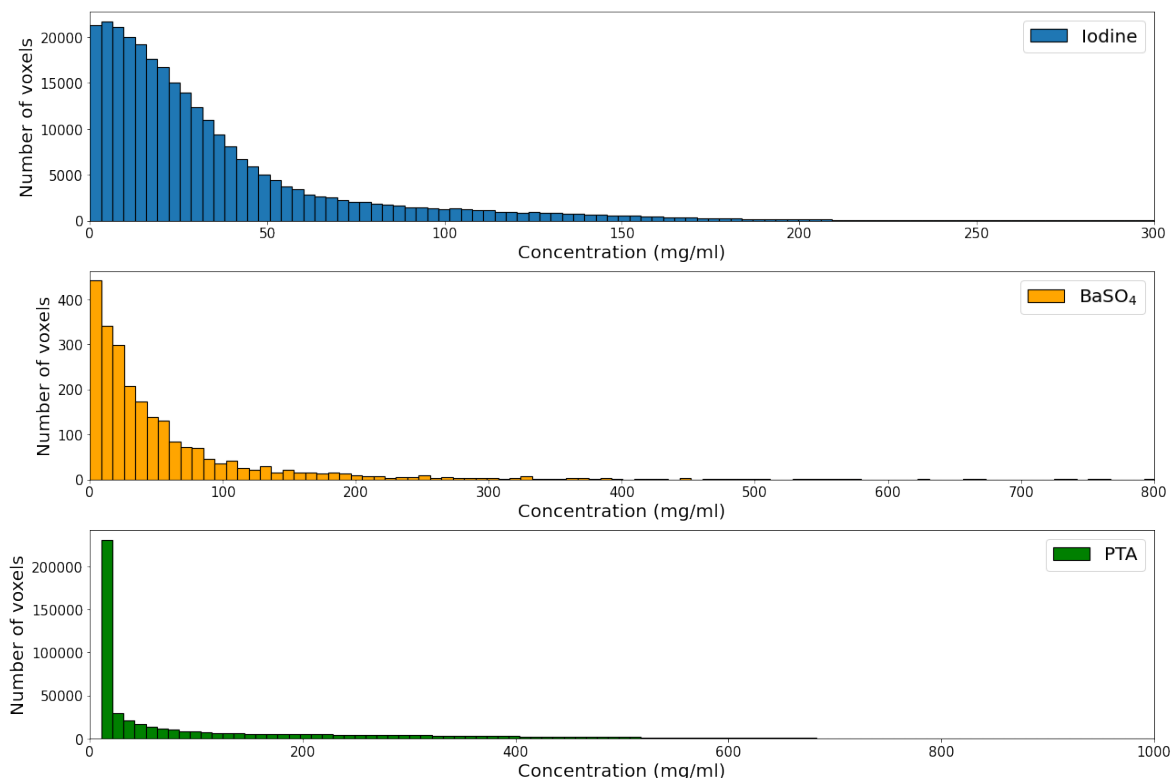


Figure S4. **Extended concentration statistics for triple-stained mouse forelimb specimen.** Histogram statistics are shown, detailing the concentration distribution of iodine (top), BaSO₄ (middle) and PTA (bottom) over all voxels in the reconstructed volume. A total of 150 histogram bins are used over the full concentration range for iodine and BaSO₄, while 250 bins are used for PTA. The sharp increase in voxel frequency for the lowest concentration bin in the PTA plot is attributed to the effect of ring artefacts within the final reconstructed volume.

mate of sensitivity for the HEXITEC.

5.8.3 Factors affecting the quantification of chemical concentration

In order to evaluate the accuracy of the method for quantifying chemical concentration using absorption edge height, and to understand the extent to which the method is translatable, several factors must be considered for their potential influence. Some are discussed below:

Chemical environment/Oxidation state - The chemical environment refers to the local arrangement of atoms and molecules around the elemental atom of interest, while the oxidation state measures the charge of an atom were all of its bonds to be ionic. In this study the mouse hindlimb was stained with elemental iodine, I₂ in ethanol, while the forelimb (and phantom) used I₂KI solution, therefore differing in the nature of their local chemical environment. It has previously been shown that higher oxidation states of a compound lead to a shift in the absorption edge position to a higher energy, owing to reduced shielding of the inner shell electrons by the outer shell electrons [52]. It has also been observed that the shape of the absorption edge can vary with the chemical environment, as demonstrated with Mn compounds [53, 54], while other studies have directly observed changes in edge height as a function of chemical environment [55]. For this study, calculation of chemical concentration relies on precise measurement of the absorption edge heights, and therefore

will be influenced by such environmental effects. For a calibration phantom with a single element/compound in the same oxidation state, a reliable relationship between edge height and concentration may be extracted. However, if the equivalent element/compound in the sample of interest occupies a different oxidation state, the corresponding K-edge position or shape may differ, and therefore an accurate translation from calibration sample to case sample cannot be assumed, and would require further investigation.

Matrix effects - The role of the chemical matrix should also be considered in the calibration and quantification of chemical concentration. In contrast to above, the matrix refers to the larger material/medium in which the given element under study is contained, as opposed to its local surroundings. For example, in the case of iodine staining, the surroundings vary if the contrast agent is intravenously distributed into soft tissue structures, compared to being administered orally. Regardless of the chemical matrix, the K-edge energy should not differ if oxidation state is consistent. However, other effects may distort the precision of K-edge measurement, such as higher attenuation in a particular matrix leading to fewer recorded counts in a given detector voxel. Such differences could lead to unreliability in obtaining consistent concentration calculation for every voxel for the 3D reconstructed volume.

X-ray signal saturation - An additional factor which should be considered is the assumption that the signal around the K-edge position is saturated, such that a full representation of the elemental attenuation pattern is captured. Any limitations in the flux would subsequently suppress the height of the measured K-edge, potentially affecting the calibration procedure if the level of saturation varies across chemical concentrations.

It is clear that a more detailed study of the various factors affecting the measurement of K-edge position and height is required to establish the reliability of such a protocol for quantifying concentration. Further investigation using a range of calibration phantoms, as recommended in the Discussion, varying in chemical environment and matrix, would offer a logical first step in this process.

Chapter 6

Conclusions and Future Work

6.1 Summary of Results and Conclusions

In this thesis, two major studies were conducted to advance various aspects of bright-field hyperspectral X-ray CT. In Chapter 4, a novel 4D reconstruction algorithm was described, and its ability to compensate for fast scan, noisy datasets was evaluated against the conventional reconstruction algorithm used as the standard of 3D datasets. A review of the current state of the art for spectroscopic reconstruction algorithms in Section 2.3.4 revealed the lack of comprehensive reconstruction algorithms available for hyperspectral CT, with no defined standard compared to what is available for XCT. In this thesis, the first steps towards filling this research gap were made. By studying both a phantom of known composition, as well as a single-stained biological specimen, three goals were achieved. First, the extent to which noisy, low SNR data may be overcome using regularised, iterative algorithms was evaluated. With a $36\times$ reduction in scan time, a successful restoration of image quality was shown for the multi-phase phantom, quantified using CNR and RMSE image metrics. Second, the use of a 'real-world' biological sample allowed a test of the reconstruction capabilities in the case of inhomogeneous chemical distribution. Improved elemental distribution mapping was attained over the conventional FDK algorithm, confirmed by significantly improved CNR metrics and reduced image noise in the reconstructed 3D volume. The work also enabled the two key forms of spectral analysis for bright-field hyperspectral imaging to be shown: K-edge subtraction and step size fitting. Finally, the biological sample offered a first step into the investigations of chemical mapping in stained specimens, with confirmation of the ease in which hyperspectral CT can precisely identify the elemental contrast agent.

The spectral analyses of stained biological specimens were brought to the fore in Chapter 5, as a natural extension to the progress made in the study of Chapter 4. While previously only the relative chemical distribution of the contrast agent was evaluated, this study performed a first instance of quantitative chemical concentration mapping using calibrations based on fitting of the spectral profiles in hyperspectral CT. The spectral separation capabilities of the HEXITEC detector was fully tested, with both double- and triple-stained specimens imaged and analysed. Separation of spectrally similar elements such as barium and iodine were achieved, enabling full 3D multi-phase elemental maps to be extracted using K-edge subtraction. Further, the measurement of absolute elemental accumulation was performed through calibrations against chemical phantoms of known concentration, enabling

linear fits to be extracted and conversion equations to be determined. As such, analysis of the interaction, overlap, and absolute concentration of each stain was assessed for multiple soft tissue structures. The work offered a unique insight into multi-staining procedures and could provide useful baseline for future research on stain accumulation.

From these studies, the main goals of the thesis have been achieved. The novel reconstruction algorithm used throughout both research studies moves the reconstruction phase of hyperspectral imaging in a positive direction, with the hope that this forms part of future standardised packages when reconstructing 4D datasets. Bright-field hyperspectral imaging has been demonstrated to be competent in the field of bioimaging and multiple elemental discrimination, enabling chemical analyses without the need for additional imaging modalities. The spectral analysis method of step size fitting has been expanded upon in hyperspectral CT, achieving quantitative metrics for the first time, only previously extracted with multi-spectral CT.

However, hyperspectral imaging is still in its relative infancy, and therefore significant progress can, and will, be made. The notable deficiency in spatial resolution will be aided by the rapid advancement of the sensor hardware, while similar improvements in count rate limits for devices like the HEXITEC will enable faster scans and higher image quality. While the dark-field capabilities of the HEXITEC were not tested in this work, the modalities highlight the flexibility of such systems, and present promising opportunities in further chemical and crystallographic analysis both as standalone and multi-modal techniques.

In summary, bright-field hyperspectral imaging has been advanced for lab-based applications in several phases of the imaging journey, including new applications in multi-stain bioimaging, novel reconstruction tools, and enhanced analysis of the spectral markers recorded in the bright-field regime.

6.2 Future Directions

This work begins to explore the numerous ways in which hyperspectral imaging can be advanced as a lab-based tomographic technique, in particular how it may be used in future biological applications. With the ever-developing hardware enabling a wider range of research, some areas of future investigation are discussed below.

6.2.1 Optimisation and standardisation of quantitative hyperspectral analyses

The spectral analyses used in the research studies of Chapters 4 and 5 demonstrate the potential of hyperspectral imaging for extracting both qualitative and quantitative chemical concentration parameters. However, optimisation of these metrics require further investigation. As discussed in Chapter 5, the absorption step size routine builds a baseline calibration for the contrast agents studied, and it is believed the calibration is both sample and spectra independent. Future research into this area offers an obvious extension to this work.

As recommended, studies of a series of phantoms under differing settings (X-ray sources, voltages, fluxes, etc.) will enable this claim to be tested. Establishing a set of requirements for such calibrations to be translatable across research would offer a significant step forward in enabling fast chemical concentration analysis of future hyperspectral datasets.

6.2.2 Investigation of beam hardening reduction with hyperspectral CT

As part of an exploration of the additional advantages offered by hyperspectral X-ray CT over conventional XCT, the representation of beam hardening artefacts offers a potential area for investigation outside of the study of characteristic markers. As described in Section 2.2.1, energy-integrating detectors weight each photon proportional to their energy, therefore higher energy photons contribute more than low-energy photons. In contrast, photon-counting systems weight all photons equally. The consequently better representation of beam hardening with spectral imaging has been shown previously [1]. Spectral CT has also been shown to be competent at reducing the beam hardening effect, through the manipulation of energy channel selection. Given that low energy photons cause the majority of the beam hardening effect, a 2014 study showed the artefacts may be reduced by selectively rejecting the lower energy windows using multispectral imaging [2]. In theory, hyperspectral CT can take this a step further, by eliminating beam hardening owing to the quasi-monochromatic energy channels available. By fine-tuning the acceptance and rejection of specific energy channels, an optimum balance may be found between improved image contrast and reduced beam hardening.

6.2.3 Expanded hyperspectral applications with multi-detector arrays

In this research, all samples under investigation were restricted in their overall size, and interior feature size, due to the limits of the current HEXITEC array. With an 80×80 pixel array and $250 \mu\text{m}$ pixel pitch, all phantoms and biological specimens selected were effectively restricted to a maximum size of 1-2 cm, and feature sizes on the order of 100s μm or greater, except in the cases of significant magnification for ROI studies. Therefore, a logical advancement of the current research is the development of a multi-detector array, producing a significant upgrade in the detection area and FOV. The HEXITEC detector offers a 3-side buttable design, with the fourth side reserved for wire connections between the ASIC and the readout printed circuit board. Therefore the detector system offers a modular design to enable scaling up to a much larger detection area. The principle has already been tested using a 5×5 HEXITEC array (approximately a $10 \text{ cm} \times 10 \text{ cm}$ detection area) capable of energy resolution similar to a single module (1-2 keV), with only minor corrections required for the inter-module spacing [3]. Installation of a 6×2 HEXITEC array (480×160 pixels) is underway at the X-ray imaging facility in Manchester, and would immediately expand the range of research available for lab-based hyperspectral investigations. For bioimaging, issues such as the identification of vasculature below $100 \mu\text{m}$ encountered in Chapter 5

would be overcome, as the freedom to magnify the sample would be greatly enhanced. Further to this, tiling of the sample in one direction could effectively extend the detection area, after appropriate stitching methods were implemented.

6.2.4 High spatio-spectral resolution through correlative techniques

While the ability to expand to larger detector arrays alleviates the issue of poor spatial resolution through offering an increased FOV, an alternative solution is the combination of hyperspectral imaging with a high spatial resolution X-ray technique. For example, scanning an object with the HEXITEC, followed by a second scan with a large, commercial flat panel detector, would provide two scans under the same geometry and sample orientation, each providing respectively high spectral and spatial resolution. Through mathematical alignment and feature matching, aided by the sequential scans, the resulting correlative approach would offer high resolution in both the spatial and spectral domains. Further, the method requires no new hardware, as the portable nature of the HEXITEC system means it can simply replace the existing detector in an X-ray system for a single scan in bright-field mode, and then be removed.

Alternatively, the multi-modal nature of the HEXITEC could be utilised to also achieve the same goal. Given that hyperspectral imaging offers the ability to examine dark-field characteristics such as fluorescence or diffraction by moving off-axis from the X-ray beam, a synchronous scan could instead be implemented with a high spatial resolution detector in the bright-field, and the HEXITEC in the dark-field. Multi-modal approaches have previously been shown using XCT + EDXRF [4] and XCT + EDD [5].

6.3 References

- ¹P. M. Shikhaliev, “Beam hardening artefacts in computed tomography with photon counting, charge integrating and energy weighting detectors: A simulation study”, *Physics in Medicine and Biology* **50**, 5813–5827 (2005).
- ²K. Rajendran, M. F. Walsh, N. J. De Ruiter, A. I. Chernoglazov, R. K. Panta, A. P. Butler, P. H. Butler, S. T. Bell, N. G. Anderson, T. B. Woodfield, S. J. Tredinnick, J. L. Healy, C. J. Bateman, R. Aamir, R. M. Doesburg, P. F. Renaud, S. P. Gieseg, D. J. Smithies, J. L. Mohr, V. B. Mandalika, A. M. Opie, N. J. Cook, J. P. Ronaldson, S. J. Nik, A. Atharifard, M. Clyne, P. J. Bones, C. Bartneck, R. Grasset, N. Schleich, and M. Billingham, “Reducing beam hardening effects and metal artefacts in spectral CT using Medipix3RX”, *Journal of Instrumentation* **9**, 1–11 (2014).

- ³M. D. Wilson, L. Dummott, D. D. Duarte, F. H. Green, S. Pani, A. Schneider, J. W. Scuffham, P. Seller, and M. C. Veale, “A 10 cm x 10 cm cdte spectroscopic imaging detector based on the hexitec asic”, *Journal of Instrumentation* **10**, 1–13 (2015).
- ⁴J. C. Larsson, C. Vogt, W. Vågberg, M. S. Toprak, J. Dzieran, M. Arsenian-Henriksson, and H. M. Hertz, “High-spatial-resolution x-ray fluorescence tomography with spectrally matched nanoparticles”, *Physics in Medicine and Biology* **63**, 1–11 (2018).
- ⁵T. Connolley, O. V. Magdysyuk, S. Michalik, P. K. Allan, M. Klaus, P. H. Kamm, F. G. Moreno, J. A. Nelson, M. C. Veale, and M. D. Wilson, “An operando spatially resolved study of alkaline battery discharge using a novel hyperspectral detector and x-ray tomography”, *Journal of Applied Crystallography* **53**, 1434–1443 (2020).